APPLIED COMPUTATIONAL ELECTROMAGNETICS SOCIETY JOURNAL

Special Issue on Antennas and Metrologies for 5G/B5G Communications

Guest Editors:
Yingsong Li, Harbin Engineering University
Xiaoming Chen, Xi'an Jiaotong University
Kwok L. Chung, Qingdao University of Technology

September 2021
Vol. 36 No. 9
ISSN 1054-4887

The ACES Journal is abstracted in INSPEC, in Engineering Index, DTIC, Science Citation Index Expanded, the Research Alert, and to Current Contents/Engineering, Computing & Technology.

The illustrations on the front cover have been obtained from the research groups at the Department of Electrical Engineering, The University of Mississippi

THE APPLIED COMPUTATIONAL ELECTROMAGNETICS SOCIETY
http://aces-society.org

EDITORS-IN-CHIEF

Atef Elsherbeni
Colorado School of Mines, EE Dept.
Golden, CO 80401, USA

Sami Barmada
University of Pisa, ESE Dept.
56122 Pisa, Italy

ASSOCIATE EDITORS

Mohammed Hadi
Kuwait University, EE Dept.
Safat, Kuwait

Alistair Duffy
De Montfort University
Leicester, UK

Wenxing Li
Harbin Engineering University
Harbin 150001, China

Maokun Li
Tsinghua University
Beijing 100084, China

Mauro Parise
University Campus Bio-Medico of Rome
00128 Rome, Italy

Yingsong Li
Harbin Engineering University
Harbin 150001, China

Riyadh Mansoor
Al-Muthanna University
Samawa, Al-Muthanna, Iraq

Lijun Jiang
University of Hong Kong, EEE Dept.
Hong, Kong

Shinishiro Ohnuki
Nihon University
Tokyo, Japan

Kubilay Sertel
The Ohio State University
Columbus, OH 43210, USA

Antonio Musolino
University of Pisa
56126 Pisa, Italy

Abdul A. Arkadan
Colorado School of Mines, EE Dept.
Golden, CO 80401, USA

Salvatore Campione
Sandia National Laboratories
Albuquerque, NM 87185, USA

Wei-Chung Weng
National Chi Nan University, EE Dept.
Puli, Nantou 54561, Taiwan

Alessandro Formisano
Seconda Universita di Napoli
81031 CE, Italy

Piotr Gas
AGH University of Science and Technology
30-059 Krakow, Poland

Long Li
Xidian University
Shaanxa, 710071, China

Steve J. Weiss
US Army Research Laboratoy
Adelphi Laboratory Center (RDRL-SER-M)
Adelphi, MD 20783, USA

Jiming Song
Iowa State University, ECE Dept.
Ames, IA 50011, USA

Maokun Li
Tsinghua University, EE Dept.
Beijing 100084, China

Marco Ajona López
La Laguna Institute of Technology
Torreon, Coahuila 27266, Mexico

Paolo Mezzanotte
University of Perugia
I-06125 Perugia, Italy

Luca Di Rienzo
Politecnico di Milano
20133 Milano, Italy

Lei Zhao
Jiangsu Normal University
Jiangsu 221116, China

Sima Noghanian
Commscope
Sunnyvale, CA 94089, USA

Qiang Ren
Beihang University
Beijing 100191, China

Nunzia Fontana
University of Pisa
56122 Pisa, Italy

Stefano Selleri
DINFO - University of Florence
50139 Florence, Italy

Amedeo Capozzoli
Univerita di Naoli Federico II, DIETI
I-80125 Napoli, Italy

Yu Mao Wu
Fudan University
Shanghai 200433, China

Atif Shamim
King Abdullah University of Science and Technology (KAUST)
Thuwal 23955, Saudi Arabia

EDITORIAL ASSISTANTS

Matthew J. Inman
University of Mississippi, EE Dept.
University, MS 38677, USA

Shanell Lopez
Colorado School of Mines, EE Dept.
Golden, CO 80401, USA

EMERITUS EDITORS-IN-CHIEF

Duncan C. Baker
EE Dept. U. of Pretoria
0002 Pretoria, South Africa

Allen Glisson
University of Mississippi, EE Dept.
University, MS 38677, USA

Ahmed Kishk
Concordia University, ECS Dept.
Montreal, QC H3G 1M8, Canada

Robert M. Bevensee
Box 812
Alamo, CA 94507-0516

Ozlem Kilic
Catholic University of America
Washington, DC 20064, USA

David E. Stein
USAF Scientific Advisory Board
Washington, DC 20330, USA

EMERITUS ASSOCIATE EDITORS

Yasushi Kanai
Niigata Inst. of Technology
Kashiwazaki, Japan

Alexander Yakovlev
University of Mississippi, EE Dept.
University, MS 38677, USA

Levent Gurel
Bilkent University
Ankara, Turkey

Mohamed Abouzahra
MIT Lincoln Laboratory
Lexington, MA, USA

Ozlem Kilic
Catholic University of America
Washington, DC 20064, USA

Erdem Topsakal
Mississippi State University, EE Dept.
Mississippi State, MS 39762, USA

Sami Barmada
University of Pisa, ESE Dept.
56122 Pisa, Italy

Fan Yang
Tsinghua University, EE Dept.
Beijing 100084, China

Rocco Rizzo
University of Pisa
56123 Pisa, Italy

William O'Keefe Coburn
US Army Research Laboratory
Adelphi, MD 20783, USA

EMERITUS EDITORIAL ASSISTANTS

Khaleb ElMaghoub
Trimble Navigation/MIT
Boston, MA 02125, USA

Kyle Patel
Colorado School of Mines, EE Dept.
Golden, CO 80401, USA

Christina Bonnigton
University of Mississippi, EE Dept.
University, MS 38677, USA

Anne Graham
University of Mississippi, EE Dept.
University, MS 38677, USA

Madison Lee
Colorado School of Mines, EE Dept.
Golen, CO 80401, USA

Allison Tanner
Colorado School of Mines, EE Dept.
Golden, CO 80401, USA

Mohamed Al Sharkawy
Arab Academy for Science and Technology, ECE Dept.
Alexandria, Egypt

SEPTEMBER 2021 REVIEWERS

Antonio Campos
Dileepan Dhanasekaran
Pere Ferrer
Xi Gao
Fan Jiang
Tianqi Jiao
Robin Kalyan
Neelam Sanjeev Kumar
Yeping Lai
Haotian Li
Jun Li
Long Li
Yingsong Li
Wen-Jiao Liao
Jau-Jr Lin
Shengyuan Luo
Panneer N.
Suriavel Rao R. S.
Khalil Sayidmarie
Yan Shi
Peiyu Wu
Qian Xu
Yan Zhang
Lei Zhao
Yong Jin Zhou
Zhibo Zhu

THE APPLIED COMPUTATIONAL ELECTROMAGNETICS SOCIETY JOURNAL

Vol. 36 No. 9 September 2021

TABLE OF CONTENTS – REGULAR PAPERS

Central-Symmetry Decoupling Technique for Circularly-Polarized MIMO System of Tightly Packed Chinese-character Shaped Patch Antennas

Kwok L. Chung [1], Aiqi Cui [1], Mingliang Ma [1], Botao Feng [2], and Yingsong Li [3*]

[1] Civionics Research Laboratory, School of Civil Engineering
Qingdao University of Technology, Qingdao, 266033, China
klchung@qut.edu.cn

[2] College of Electronic and Information Engineering, Shenzhen University, 518060, China
fengbotao@szu.edu.cn

[3] College of Information and Communication Engineering, Harbin Engineering University, Harbin, 15001, China
*liyingsong@ieee.org

Abstract **─** This article presents a novel decoupling technique for the circularly polarized multiple-input-multiple-output (CP-MIMO) system composed of *Guo*-shaped patch antennas. A comparative study has been conducted on antenna performance as a function of packing distance before and after applying the technique. A prototype of two-element *Guo*-shaped patch MIMO at a small inter-element spacing of 12.5 mm has devised aiming for the 5G new radio n38 (2.57-2.62 GHz) applications. Simulation reinforced with experimental results confirmed the effectiveness of the proposed technique, whereas the two *Guo*-shaped patch elements packed in such small spacing can be operated independently. Both the envelope correlation coefficient and diversity gain are approaching their ideal values.

Index Terms **─** Antenna isolation, artistic patch antenna, Chinese-character-shaped patch antenna, CP-MIMO, decoupling technique.

I. INTRODUCTION

Multiple-input-multiple-output (MIMO) antenna system becomes the key technology in current wireless communications addressing the demands of high channel capacity and anti-multipath interferences [1]. The circularly polarized (CP) antennas play a crucial role in space and indoor communications owing to the advantages of non-line-of-sight, better mobility and robust to polarization mismatching as compared with the linearly polarization (LP) counterparts [2-3]. As a result, the CP-MIMO antenna systems have been investigated and become popular in recent years. It has demonstrated that the achievable channel capacity of CP-MIMO outperforms the LP counterparts, especially when antennas are not perfectly aligned. Moreover, CP-MIMO allows yielding superior performance when its 3-dB axial-ratio beamwidth coverage reaches ~40° [4].

Suppression techniques of mutual coupling between antennas have long been the research topics in antenna array systems [3, 5-9]. Decoupling or isolation necessity is the primary design goal in MIMO systems. In [3], angular offset elements were used to reduce the mutual coupling and gain enhancement, this type of method is classified as the self-decoupled method. Various types of defected ground structure (DGS) [5-7] were employed to enhance the isolation between elements, whereas a wheel-like metamaterial decoupling structure was presented in [8]. In [9-12], different insertion techniques were used to enhance the isolation of MIMO antennas. For the aim of mutual coupling reduction, radial stub loaded resonator [9] and 3-D metamaterial structure [10] were inserted respectively in between the two elements of MIMOs. Also, the multi-layer electromagnetic bandgap structure and the single-layer metamaterial superstrate were added into the two-element source antennas in [11] and [12], respectively. In the recent CP-MIMO designs, a simple microstrip line was used as the decoupling structure [13], whereas a hybrid technique of parasitic patch with diagonal position of dielectric resonator antennas was presented for WiMAX application [14]. For 5G millimeter-wave bands, a high-gain wideband CP antenna with MIMO capabilities based on Fabry-Perot resonant cavity was proposed in [15], wherein a single-layered dielectric slab of half-wavelength thickness was utilized as a partially reflecting surface so that a high isolation of higher than 20 dB was obtained for an interelement spacing of half-wavelength. A dual CP-MIMO antenna using a hybrid technique was also reported in [16], wherein three grounded stubs plus mirrored F-shaped DGS were included between microstrip-line fed near-square-patch antennas to achieve high isolation. However, the use of DGS creates

Submitted On: March 29, 2021
Accepted On: September 2, 2021

https://doi.org/10.47037/2021.ACES.J.360901

backward radiation leading to low forward directivity. The inclusions of additional resonators and or reflecting (metamaterial) surface may increase the antenna volume as well as the insertion loss.

In this article, a novel decoupling technique is proposed for the isolation enhancement of a closely packed *Guo*-shaped patch antenna array, wherein the two *Guo*-shaped patch elements are placed at a center-to-center (C2C) distance of 80 mm (0.69 free-space wavelengths at 2.6 GHz). The technique uses no additional resonator(s), no defected ground structure(s) and or metasurface/metamaterial. Instead, we altered one of the *L*-shaped feeds with its position and orientation central-symmetrically with respect to the original one. The results demonstrated that the proposed technique is able to enhance the isolation by 5 dB at a shortest C2C distance of 70 mm. Therefore, the axial ratio and broadside gain can be independently established without mutually deteriorated by strong mutual coupling. The 2.6-GHz CP-MIMO is devised for use at 5G NR n38.

II. CLOSELY PACKED TWO-ELEMENT *GUO*-SHAPED PATCH MIMO ANTENNAS

A. Geometry of CP *Guo*-shaped patch antenna

This section introduces the geometry of the Chinese character-shaped patch antenna, which is a modification of the *Guo*-shaped patch [17] for left-hand CP (LHCP) propagation. Figure 1 shows the top- and side-view geometry, where a *L*-shaped feeding probe is placed at a coordinate (*m*, *n*) with respect to the patch center and its arm is faced downward for LHCP generation. The geometrical parameters are summarized in Table 1.

Table 1: Geometrical parameters (unit: mm)

L	M	w	H	a
71.8	67.5	35.5	15.5	10.5
b	c	d	e	f
9.1	8.9	6.7	7.7	6.2
g	m	n	F_h	F_v
8.6	20.0	13.4	13.5	11.5

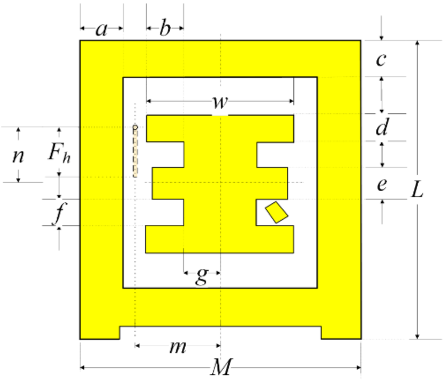

(a)

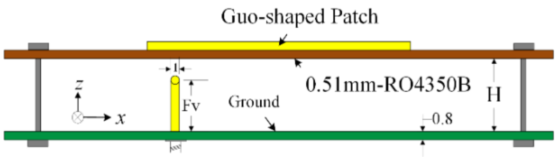

(b)

Fig. 1. Geometry of CP *Guo*-shaped element: (a) top view and (b) side view. The dielectric layer is 0.51mm thick RO4350B.

B. Impedance matching

Here, we present the effects of mutual coupling (MC), using Microwave Studio CST [18], when two identical *Guo*-shaped patch elements are closely packed at a C2C distance of *D*, namely, at an inter-element spacing of *g*, as shown in Fig. 2 (a). That is, when *D* is set at 70, 80, 90 and 100 mm, *g* is 2.5, 12.5, 22.5 and 32.5 mm, respectively. It is expected that the MC is very strong while the two elements are placing closely, say 70 mm, as a result, the impedance matching in terms of reflection coefficients ($|S_{11}|$ and $|S_{22}|$) of both the elements deteriorated as shown in Figs. 2 (b) to 2 (e). At $D = 70$ mm, the very strong MC causes S_{11} and S_{22} in dB to increase and be unequal. The mutual coupling logically reduced with *D* increasing. At last, the effect becomes minimal when $D = 100$ mm so that the S_{11} and S_{22} curves have overlapped each other.

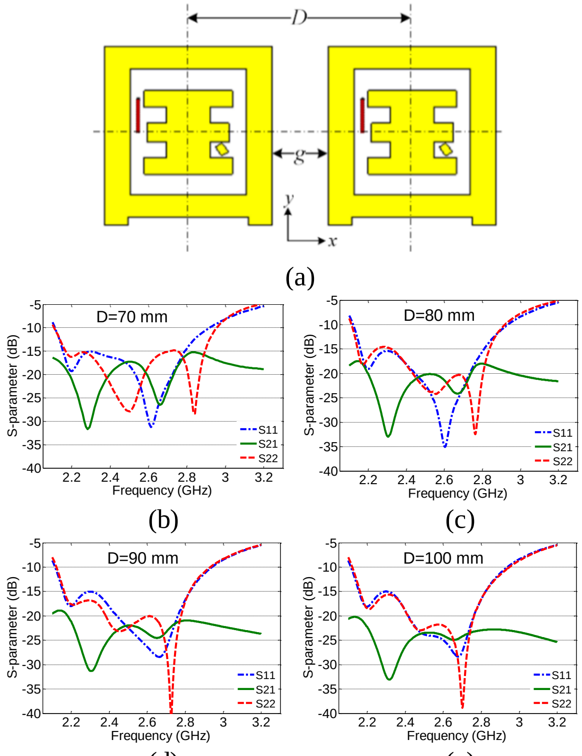

(a)

(b) (c)

(d) (e)

Fig. 2. Mutual coupling effect versus *D*.

C. Axial ratio and broadside gain performance

Strong MC not only affects the impedance matching but also the axial ratio (AR) and broadside gain (BG) performance of CP antennas. However, these were seldom fully addressed in the previous studies. Figure 3 demonstrates the comparison of AR and BG under two separation cases of 80 and 100 mm, respectively. At *D* = 80 mm, both the AR and BG curves deteriorated particularly, the deteriorations on the right-hand-side element (AR-R and BG-R) are more serious than the left-hand-side ones, which is attributed to the closer feed next to the left-element. Until the separation away at 100 mm, the situations are observed to be relieved. Therefore, a technique must be used to mitigate the mutual coupling effects at the closing space. An exploration of optimization issue arising during the modeling of *Guo*-shaped patch. The AR performance is very sensitive with the feed-probe location and orientation as compared with the BG and S-parameter performance. Therefore, a systematic tuning was used to obtain the best feed location by firstly aiming at AR performance.

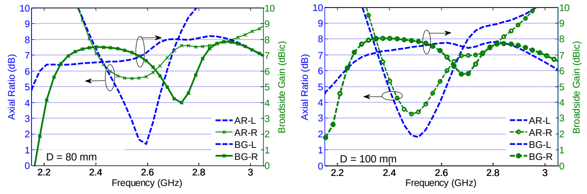

(a) (b)

Fig. 3. Simulated performance of axial ratio and broadside gain for (a) *D* = 80 mm and (b) *D* = 100 mm.

II. CENTRAL-SYMMETRICAL TECHNIQUE APPLIED FOR TWO-ELEMENT ARRAY

It is known that most of single-feed CP patch antennas have more than one optimal feed location to achieve the same sense (handedness) of CP operation at the broadside direction [19]. In particular, when the patch antenna has a symmetrical geometry [20]. Here, we make use of this knowledge and move one of the feeding probes of closely packed elements in such a way that the two probes are central-symmetrically (CS) placed, as shown in Fig. 4. Note that the probe orientation of the horizontal arm is also placed CS.

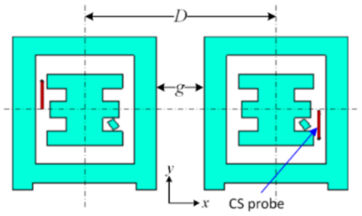

Fig. 4. Central-symmetrical technique is applied in the right-hand side element.

A. Effects on impedance matching

Figures 5 (a) to 5 (d) show the impedance matching in terms of S_{11} and S_{22} after applying the CS technique. As compared with Fig. 2, better reflection coefficients are obtained, particularly, in the closely packed case of *D* = 70 mm. One can see that the two elements are now almost isolated from each other. Besides, the mutual coupling reduced to below -20 dB for all separations.

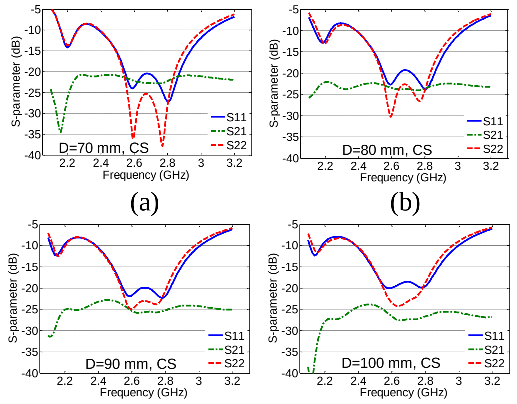

(a) (b)

(c) (d)

Fig. 5. Mutual coupling effects on reflection coefficients (S_{11}, S_{22}) as a function of separation *D*, after CS technique applied.

B. Isolation enhancement

The positive value of MC is the isolation between two input ports of the *Guo*-shaped patch element. We extracted that from Figs. 2 and 5, and make a comparison as a function of *D*, as shown in Figs. 6 (a) and 6 (b), respectively. Without using CS technique, the smaller the separation gives the more fluctuation on the isolation curves in the frequency range of 2-3 GHz. At the center frequency of 2.6 GHz, the isolation drops below 18 dB at 70 mm separation and enhanced to 23 dB at 100 mm. After applying CS, the isolation between *Guo*-shaped patch antennas is enhanced from 18 dB to a minimum of 22 dB at *D* = 80 mm across the whole frequency range. The simulated surface current distributions of the two closely packed *Guo*-shaped patch elements at 2.6 GHz shown in Fig. 7 are used to study the decoupling mechanism. In either case, the associated current with the *L*-probes are observed to be minimum.

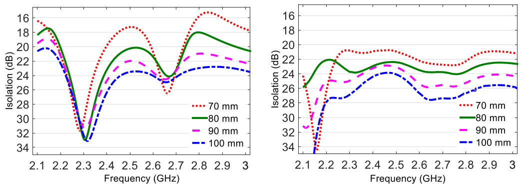

(a) (b)

Fig. 6. Isolation comparison (a) before and (b) after applying central-symmetrical feeding for a number of separations.

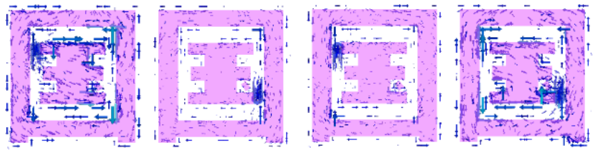

(a) (b)

Fig. 7. Surface current plots when (a) left-element is excited, and (b) right-element is excited.

C. Axial ratio and broadside gain performance

After applying the central-symmetrical technique, Figs. 8 (a) and 8 (b) show the simulated AR and BG for the two cases, D = 80 and 100 mm, respectively. With reference to Figs. 4 (a) and 4 (b), both the AR and BG improved significantly. In particular, the performance of the right-hand-side element has almost the same as the left-hand-side element in both the cases. These validate the effectiveness of the CS technique in the far-field performance.

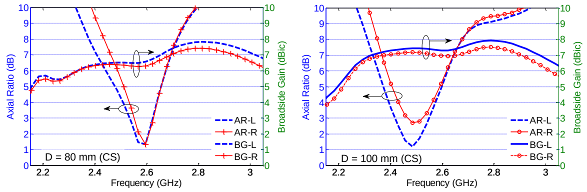

(a) (b)

Fig. 8. Simulated *on-axis* axial ratio and broadside gain after applying CS technique: (a) D = 80 mm and (b) D = 100 mm.

III. FABRICATION AND EXPERIMENTAL VERIFICATION

A. S-parameter performance measurement

Prototypes of closely packed *Guo*-shaped patch antennas at D = 80 mm (g = 12.5 mm, $0.10\lambda_0$) with and without central-symmetry decoupling were fabricated and measured. A photograph of the prototype is depicted in Fig. 9, whereas their measured S-parameters are shown in Fig. 10. It can be seen that the measured mutual coupling (S_{21}) is suppressed to –25 dB at 2.6 GHz whereas the reflection coefficients of both antennas (S_{11}, S_{22}) are almost identical. This means that the *Guo*-shaped patch antennas now own sufficient isolation that can be operated without mutual affections. When further comparing with the simulated results shown in Fig. 5 (b), we can conclude that excepting the minor frequency shifts of S_{11} and S_{22} curves, the experimental results have validated the effectiveness of the CS technique.

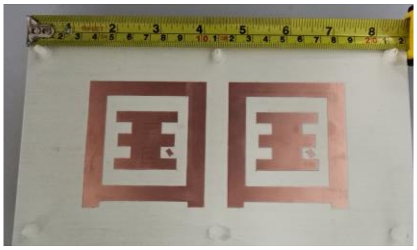

Fig. 9. Photograph of CP MIMO with closely packed (D = 80 mm) *Guo*-shaped patch antennas.

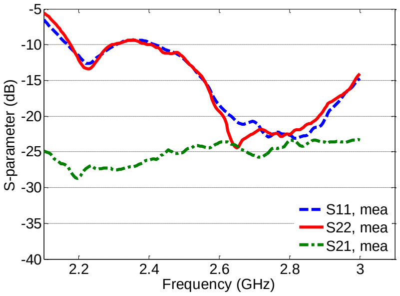

Fig. 10. Measured S-parameters of closely packed (D = 80 mm) *Guo*-shaped patch antennas after applying CS technique.

B. Measured axial ratio and broadside gain

The measurement of MIMO far-field performance was conducted inside a near-field SATIMO chamber, as depicted in Fig. 11. Besides, Fig. 12 displays the comparisons on AR and BG for both the left- and right-element. As verified before, the isolation is sufficiently high to cause the closely packed antennas to work independently. Both the ARs and BGs now also had very close performance. The measured 3-dB AR bandwidth is 2.56-2.64 GHz (3.1%), whereas the BG recorded as 6.5 dBic at 2.6 GHz. Moreover, the measured radiation patterns of both *Guo*-shaped elements at 2.6 GHz are plotted as shown in Fig. 13. As seen, the beam diversity can be achieved by using such novel probing technique.

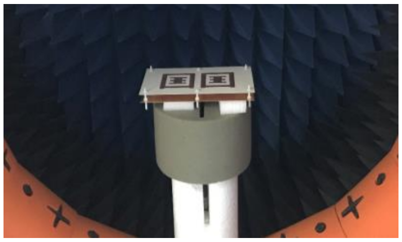

Fig. 11. Far-field measurement undertaken inside SATIMO.

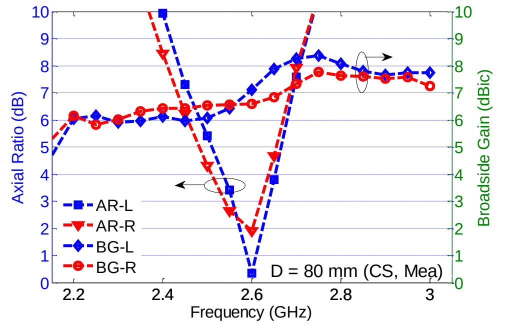

Fig. 12. Measured axial ratio and broadside gain after applying CS technique.

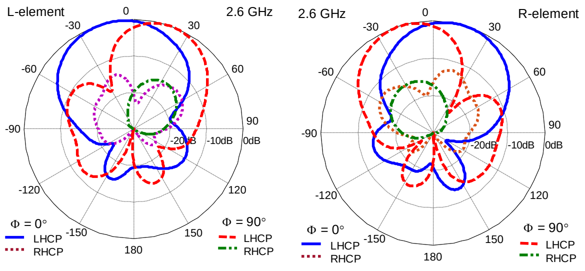

(a) (b)

Fig. 13. Simulated and measured envelope correlation.

C. MIMO performance verifications

The envelope correlation coefficient (ECC) is known as a primary diversity performance metric of the MIMO antenna system. When all elements are excited, ECC indicates the level of mutual influences and the far-field correlation among antenna elements, which is expressed in terms of S-parameters as [21]:

$$ECC = \frac{|S_{11}^{*}S_{12}+S_{21}^{*}S_{22}|^2}{(1-|S_{11}|^2-|S_{21}|^2)(1-|S_{21}|^2-|S_{22}|^2)}, \tag{1}$$

the value of diversity-gain (DG) can then be obtained by using (2),

$$DG = 10\sqrt{1-(ECC)^2}. \tag{2}$$

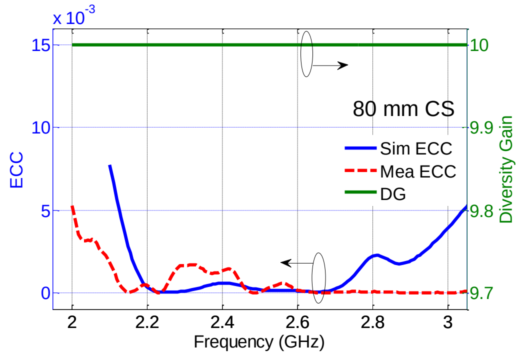

Fig. 14. Simulated and measured envelope correlation coefficients (ECCs) after applying CS technique.

Figure 14 shows the comparison of measured and simulated ECCs after using CS. As the ECCs are really small (0.002), the figure also shows that the diversity gains reach the upper limit of 10. Again, these values validate the effectiveness of the decoupling technique.

VI. CONCLUSION

A central-symmetrical technique is proposed for element decoupling in this paper. Two *Guo*-shaped patch elements, which were closely packed in a CP MIMO system at 2.6 GHz, were investigated. Simulated results, in terms of S-parameters, axial ratio and broadside gain have demonstrated that the proposed technique can effectively enhance the isolation so that the elements can be activated independently. Moreover, experimental results show that even at a small inter-element spacing of 12.5 mm (0.108λ_0 at 2.6 GHz), the measured ECC and DG approaching the ideal values of 0 and 10, respectively. Importantly, the technique uses no extra resonators or defected ground structures to achieve the results.

ACKNOWLEDGMENT

This work was supported by Funding of Key Laboratory of Advanced Marine Communication and Information Technology, MIIT, China (AMCIT2101-03) and the Fundamental Research Funds for the Central Universities (3072021CF0804) and the Open Project of State Key Laboratory of Millimeter Waves (K2020017).

REFERENCES

[1] M. A. Jensen and J. W. Wallace, “A review of antennas and propagation for MIMO wireless communications,” *IEEE Trans. Antennas Propag.*, vol. 52, no. 11, pp. 2810-2824, Nov. 2004.
[2] K. L. Chung, X. Yan, Y. Li, and Y. Li, “A Jia-shaped artistic patch antenna for dual-band circular polarization,” *Intern. J. Electronics and Comm. (AEÜ)*, vol. 120, 153207, June 2020.
[3] K. L. Chung and S. Kharkovsky, “Mutual coupling reduction and gain enhancement using angular offset elements in circularly polarized patch array,” *IEEE Antennas Wireless Propag. Lett.*, vol. 12, pp. 1122-1124, Sep. 2013.
[4] F. A. Dicandia, S. Genovesi, and A. Monorchio, “Analysis of the performance enhancement of MIMO systems employing circular polarization,” *IEEE Trans. Antennas Propag.*, vol. 65, no. 9, pp. 4824-4835, July 2017.
[5] R. Anitha, V. P. Sarin, P. Mohanan, and K. Vasudevan, “Enhanced isolation with defected ground structure in MIMO antenna,” *Electron. Lett.*, vol. 50, no. 24, pp. 1784-1786, 2014.
[6] G. Zhang and Q. Chen, “Mutual coupling reduction in Chinese character-shaped artistic MIMO antenna,” *Microw. Optical Tech. Lett.*, vol. 61, no. 7, pp. 2588-2594, July 2020.

[7] C.-M. Luo, J.-S. Hong, and L.-L. Zhong, "Isolation enhancement of a very compact UWB-MIMO slot antenna with two defected ground structures," *IEEE Antennas Wireless Propag. Lett.*, vol. 14, pp. 1766-1769, 2015.

[8] J. Jiang, Y. Xia, and Y. Li, "High isolated X-band MIMO array using novel wheel-like metamaterial decoupling structure," *Applied Computational Electromagnetics Society Journal*, vol. 34, no. 12, pp. 1829-1836, 2019.

[9] Y. Li, W. Li, and W. Yu, "A multi-band/UWB MIMO/diversity antenna with an enhanced isolation using radial stub loaded resonator," *Applied Computational Electromagnetics Society Journal*, vol. 28, no. 1, pp. 8-20, 2013.

[10] K. Yu, Y. Li, and X. Liu, "Mutual coupling reduction of a MIMO antenna array using 3-D novel metamaterial structures," *Applied Computational Electromagnetics Society Journal*, vol. 33, no. 7, pp. 758-763, 2018.

[11] T. Jiang, T. Jiao, and Y. Li, "A low mutual coupling MIMO antenna using periodic multi-layered electromagnetic band gap structures," *Applied Computational Electromagnetics Society Journal*, vol. 33, no. 3, pp. 305-311, 2018.

[12] J. Jiang, Y. Li, L. Zhao, and X. Liu, "Wideband MIMO directional antenna array with a simple metamaterial decoupling structure for X-band applications," *Applied Computational Electromagnetics Society Journal*, vol. 35, no. 5, pp. 556-566, 2020.

[13] I. Adam, M. N. M. Yasin, N. Ramli, M. Jusoh, H. A. Rahim, T. B. A. Latef, T. F. T. M. N. Izam, and T. Sabapathy, "Mutual coupling reduction of a wideband circularly polarized microstrip MIMO antenna," *IEEE Access*, vol. 7, pp. 97838-97845, July 2019.

[14] J. Iqbal, U. Illahi, M. I. Sulaiman, M. M. Alam, M. M. SU'UD, and M. N. M. Yasin, "Mutual coupling reduction using hybrid technique in wideband circularly polarized MIMO antenna for WiMAX application," *IEEE Access*, vol. 7, pp. 40951-40958, Apr. 2019.

[15] N. Hussain, M.-J. Jeong, J. Park, and N. Kim, "A broadband circularly polarized Fabry-Perot resonant antenna using a single-layered PRS for 5G MIMO application," *IEEE Access*, vol. 7, pp. 40897-42907, Apr. 2019.

[16] M. Y. Jamal, M. Li, and K. L. Yeung, "Isolation enhancement of closely packed dual circularly polarized MIMO antenna using hybrid technique," *IEEE Access*, vol. 8, pp. 11241-11247, Jan. 2020.

[17] K. L. Chung, A. Cui, and B. Feng, "A Guo-shaped patch antenna for hidden WLAN access points," *Int. J. RF & Microw. Comp. Aided Eng.*, mmce.22323, July 2, 2020.

[18] CST Microwave Studio, ver. 2017, Computer Simulation Technology, Framingham, MA, 2017.

[19] K. L. Chung, "A wideband circularly polarized H-shaped patch antenna," *IEEE Trans. Antennas Propag.*, vol. 58, no. 7, pp. 3379-3383, July 2010.

[20] K. L. Chung, W. Li, Y. Li, R. Liu, and P. Zhang, "Chinese character-shaped artistic patch antenna," *IEEE Antennas Wireless Propag. Lett.*, vol. 18, no. 8, pp. 1542-1546, Aug. 2019.

[21] S. Blanch, J. Romeu, and I. Corbella, "Exact representation of antenna system diversity performance from input parameter description," *Electron. Lett*., vol. 39, no. 9, p. 705, 2003.

Kwok L. Chung (Senior Member, IEEE) is a Research Professor and a Supervisor of Ph.D. students with Qingdao University of Technology (QUT). He is also a Director of Civionics Research Laboratory where he leads a cross-disciplinary research team at QUT. His current research interests include passive wireless sensors, cement-based materials design and characterization, microwave antennas, and metasurface. He is the Founding Chair of the IEEE Qingdao AP/MTT/COM joint chapter (CN10879) under Beijing Section. He has been an Associate Editor of IEEE ACCESS and an Associate Editor of Elsevier Alexandria Engineering Journal since 2016 and 2020, resepectively. He serves as a Reviewer for the numerous IEEE, IET, Elsevier, and other international journals.

Aiqi Cui was born in Jincheng, Shanxi, China in 1994. She received a degree in Packaging Engineering from Hunan University of Technology. She is currently pursuing a master's degree in Material Science and Engineering. Her research interests include electromagnetic shielding, material characterization, and artistic antennas.

Mingliang Ma received the B.S. degree from Ludong University in 2007, and received Ph.D. degree in Materials Science from North-western Polytechnical University in 2014. In late 2014, he joined the Qingdao University of Technology and now is an Associate Professor. His main research areas include design of multi-functional electromagnetic absorption materials, and disaster prevention mitigation and protection engineering.

Botao Feng (Senior Member, IEEE) received the Ph.D. degree in Communication and Information System from the Beijing University of Posts and Telecommunications (BUPT), Beijing, China, in 2015. He is currently a Postgraduate Advisor and a Postdoctoral Advisor with Shenzhen University, China, where he is also the Head of the Laboratory of Wireless Communication, Antennas and Propagation and the Deputy Director of the Department of Electronic Science and Technology.

Simulating Boundary Fields of Arbitrary-shaped Objects in a Reverberation Chamber

Qian Xu [1], **Kai Chen** [1,3], **Chun Ren** [2], **Xueqi Shen** [3], **and Yi Huang** [4]

[1] College of Electronic and Information Engineering
Nanjing University of Aeronautics and Astronautics, Nanjing 211106, China
emxu@foxmail.com, chenkay@nuaa.edu.cn

[2] Dassault Systèmes (Shanghai) Information Technology, co. Ltd. Beijing Branch, Beijing, 100025, China
chun.ren@3ds.com

[3] Nanjing Rongce Testing Technology Ltd, Nanjing 211112, China
george@emcdir.com

[4] Department of Electrical Engineering and Electronics
The University of Liverpool, Liverpool, L69 3GJ, United Kingdom
yi.huang@liverpool.ac.uk

Abstract **─** In a reverberation chamber, analytical solutions exist in very limited scenarios for the distribution of the boundary fields. For arbitrary-shaped objects, analytical solutions may not exist. To solve this problem, a general numerical method is proposed to obtain the mean field distribution near arbitrary-shaped objects in a random diffused-wave environment. The proposed method combines the full-wave method and the Monte-Carlo method; the numerical results are validated and compared with that from analytical equations. The proposed method can be applied to arbitrary-shaped objects with general material properties.

Index Terms **─** Boundary fields, Monte-Carlo simulation, plane wave model, reverberation chamber.

I. INTRODUCTION

Reverberation chambers (RCs) have been widely used in electromagnetic compatibility (EMC) [1] and over-the-air (OTA) testing [2-5] in recent years. New applications include antenna measurement [6], radar cross section measurement [7], and channel emulation [3]. Ideally, a statistically homogeneous and isotropic random multipath environment can be created in an RC. When the field point is far from the boundaries and stirrers (typically larger than $\lambda/4$ [1]), the field can be considered statistically uniform and isotropic. However, because of the boundary conditions (e.g., the tangential component of E-field is nearly zero $E_t = 0$ on the metallic boundaries), the field statistics close to the boundaries deviate from ideal values and is no longer uniform and isotropic [1, 3]. Generally, how the power density ($\langle|E_x|^2\rangle$, $\langle|E_y|^2\rangle$ or $\langle|E_z|^2\rangle$) distributes around an arbitrary-shaped object remains unsolved. This paper is aimed to solve this problem by applying the plane wave model (PWM) directly [3, 8].

Luckily, typical boundary fields such as planar, right-angle bend and right-angle corners have analytical solutions [9, 10]. In these cases, the distribution of the mean value of the boundary fields can be expressed analytically as a function of (x, y, z) coordinates. At high frequency limit, a very efficient model is proposed in [11, 12] by using the diffusion equation to obtain a system-level description. In this paper, we apply the PWM using the full-wave simulation and combine the results using the Monte-Carlo method [13-16]; the method is a direct method from the first principle and can be applied to arbitrary-shaped boundary shapes and material properties.

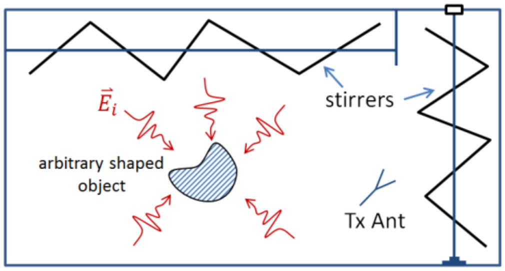

Fig. 1. An arbitrary shaped object in a random field environment (reverberation chamber).

The algorithm is detailed in Section II and the

Submitted On: July 29, 2021
Accepted On: August 22, 2021

https://doi.org/10.47037/2021.ACES.J.360902

simulated results are validated in Section III, general scenarios are investigated in Section IV and conclusions are summarized in Section V.

II. ALGORITHM

For an arbitrary-shaped object in an RC in Fig. 1, when the RC is well stirred, the random wave environment can be modeled using multiple plane waves. Each incident plane wave can be expressed as:

$$\vec{E}_i = \vec{A}_i e^{-j\vec{k}_i \cdot \vec{r}_i}, \qquad (1)$$

where i represents ith incident wave, k is the wave number, $\vec{r} = (x, y, z)^T$ represents the field point and $\vec{A}_i$ is a complex vector which represents the amplitude and initial phase of the plane wave. For many random incident waves we have [13]:

$$\vec{E}_{inc} = \sum_{i=1}^{N} \vec{E}_i = \sum_{i=1}^{N} \vec{A}_i e^{-j\vec{k}_i \cdot \vec{r}_i}, \qquad (2)$$

where the amplitude and phase of $\vec{A}_i$ are Rayleigh and uniform distributed, respectively. When the plane wave number N approaches to infinity, (2) is the well-known PWM which is also written as [3]:

$$\vec{E}_{inc} = \iint_{4\pi} \vec{A}(\Omega)\, e^{-j\vec{k}\cdot\vec{r}} \mathrm{d}\Omega\,, \qquad (3)$$

where $\iint_{4\pi}[\cdot]\,\mathrm{d}\Omega$ means the integral over a unit sphere. As we can only simulate finite N numerically, we start from (2) to detail the algorithm.

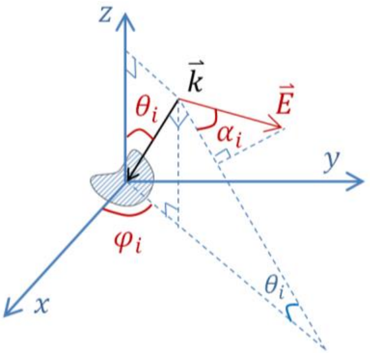

Fig. 2. Angle definitions of an incident plane wave.

For each plane wave, the wave propagation direction can be expressed as:

$$k_{xi} = -\sin(\theta_i)\cos(\varphi_i)$$
$$k_{yi} = -\sin(\theta_i)\sin(\varphi_i)$$
$$k_{zi} = -\cos(\theta_i), \qquad (4)$$

and the E-field direction can be expressed as:

$$E_{xi} = \cos(\varphi_i)\cos(\theta_i)\cos(\alpha_i) - \sin(\varphi_i)\sin(\alpha_i)$$
$$E_{yi} = \sin(\varphi_i)\cos(\theta_i)\cos(\alpha_i) + \cos(\varphi_i)\sin(\alpha_i)$$
$$E_{zi} = -\sin(\theta_i)\cos(\alpha_i), \qquad (5)$$

where θ_i and φ_i are the polar angle and azimuth angle respectively, α_i is the polarization angle. The definitions are illustrated in Fig. 2. Only two α values (0° and 90°) are necessary which represents TE and TM waves respectively.

For each incident wave $\vec{E}_i$, the scattering problem can be solved by using the Finite Integral Time Domain (FITD) method in CST, the E-field in the solving volume can be solved as $\vec{E}_{iTot}$ (normalized to 1 V/m incident wave). Simulations using FDTD and TLM method for RC performance analysis have been detailed in [17-21]. When the system is linear, the total field in the solving volume can be obtained as $\vec{E}_{Tot} = \sum_{i=1}^{N} A_i \exp(j\delta_i)\vec{E}_{iTot}$ for N plane waves incident simultaneously with random amplitude A_i and δ_i phase. By repeating this process M times with Monte-Carlo simulations, the mean value of the square of the total fields (power density) can be obtained. The probability density function (PDF) of the power density is still exponential distribution but with different mean parameters, thus we focus on the mean values in the simulation.

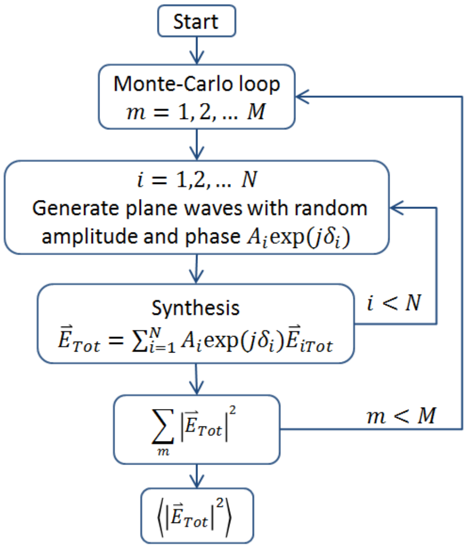

Fig. 3. The workflow of the full-wave Monte-Carlo simulation.

Table 1: Simulation scenarios

	Scenarios	Simulation Time FW+MC (hours)
Analytical scenarios	Vacuum cube	13.2+3.9
	Right-angle bend	6.1+3.9
	Right-corner	6.4+3.9
General scenarios	Arbitrary-angle bend	6.4+3.9
	Dielectric cube	17.8+3.9
	Receiving antenna	6.4+3.9
	Half-space aperture	4.6+3.9

The workflow of the full-wave Monte-Carlo simulation (FWMC) is illustrated in Fig. 3. Note that the FITD simulation only needs to be performed for N times, each $\vec{E}_{iTot}$ is saved in memory and no full-wave simulation is necessary in the Monte-Carlo simulation.

In the next section (Section III), we validate the proposed method using models with have analytical solutions. In Section IV, we apply the FWMC method to general scenarios. The simulation scenarios are given in Table 1, in which FW and MC represent full-wave simulation and Monte-Carlo simulation respectively. Since we use the same sampling number for $\vec{E}_{iTot}$ in all models, the MC simulation time are the same.

III. VALIDATIONS

In the FWMC simulation, we use 642 sets of (θ_i, φ_i) (illustrated in Fig. 4) for $\vec{k}$ vectors and each incident wave has two polarizations with $\alpha = 0°$ and $\alpha = 90°$, thus $N = 1284$ incident waves are simulated (the magnitude of the incident wave is normalized to 1 V/m). After each simulation, the total fields in the solving volume are saved as $E_{xiTot}(x, y, z)$, $E_{yiTot}(x, y, z)$ and $E_{ziTot}(x, y, z)$. After the full-wave simulation, the Monte-Carlo simulation in Fig. 3 is performed with $M = 10000$. The M value can be understood as the number of independent stirrer positions in an ideal RC, as for each value of M, a new set of A_i and δ_i are generated.

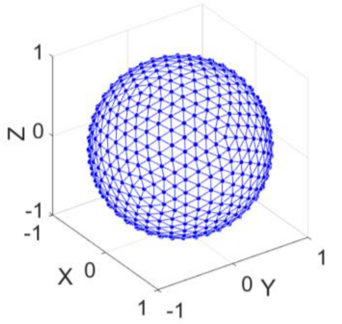

Fig. 4. 642 incident wave directions on a unit sphere are used in the full-wave simulation.

To normalize $\langle |E_{xTot}|^2 \rangle$ to 1 at fields far from boundaries, the magnitude of the incident plane wave A_i has a Rayleigh distribution and the PDF is [3]:

$$p_A(x) = \frac{x}{\sigma^2} e^{-\frac{x^2}{2\sigma^2}}, \qquad x = A_i, \qquad (6)$$

with $\sigma = \sqrt{3/2}/\sqrt{N}$. The initial phase δ_i has a uniform distribution in $(0, 2\pi]$. To verify the proposed method we simulate a vacuum cube, a right-angle bend and a right-angle corner as they have analytical solutions.

A. A vacuum cube

We first use a vacuum cube in Fig. 5 (a) to validate the method, the electrical dimensions are 4λ × 4λ × 4λ. Since there is no scatter in the solving volume, the error can be explained as the numerical noise level. The simulated $\langle |E_{xTot}|^2 \rangle$ is illustrated in Fig. 5 (b), as can be seen, the values are very close to 1 and the relative standard deviation (which is also the field uniformity (FU)) is about 1% (0.05 dB). This agrees well with the theoretical value from the central limit theorem which is $1/\sqrt{M}$. This also means that the statistical noise level is about -20 dB for $M = 10000$. The FU in the simulation volume is given in Fig. 6 for different M and N values. The unit sphere is decomposed uniformly with $4^{p-1} \times 10 + 2$ $(p = 1, 2, \ldots)$ points, and the plane wave number is $4^{p-1} \times 20 + 4$. The theoretical curve of $10\log_{10}(1 + 1/\sqrt{M})$ is also given. As can be seen, very good agreement is obtained; the FU is dominated by M and is not sensitive to N in free space.

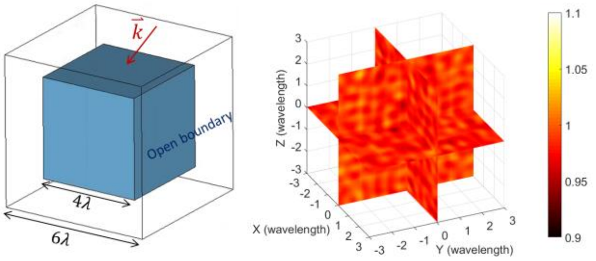

(a) (b)

Fig. 5. (a) A vacuum cube, and (b) simulated $\langle |E_{xTot}|^2 \rangle$, the plots for $\langle \left|E_{yTot}\right|^2 \rangle$ and $\langle |E_{zTot}|^2 \rangle$ are similar.

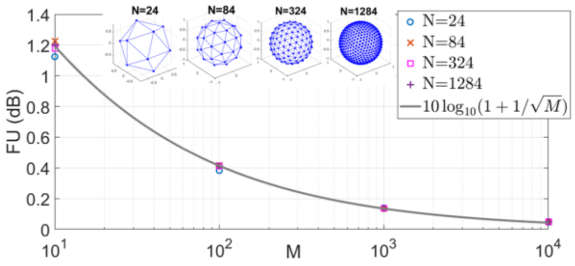

Fig. 6. Simulated FU with different M and N values.

B. A right-angle bend

A right-angle bend with two finite plates are presented in Fig. 7 (a), the edge length is 4λ. Note that when the plates are infinitely large, analytical solutions exist [3]:

$$\langle |E_{zTot}(x, y, z)|^2 \rangle = \frac{E_0^2}{3}\left[1 - \rho_t(2y) - \rho_t(2x) + \rho_t\left(2\sqrt{x^2 + y^2}\right)\right], \quad (7)$$

$$\langle |E_{xTot}(x, y, z)|^2 \rangle = \frac{E_0^2}{3}\Big[1 - \rho_t(2y) + \rho_l(2x) - \frac{y^2}{x^2 + y^2}\rho_t(2\sqrt{x^2 + y^2}) - \frac{x^2}{x^2 + y^2}\rho_l(2\sqrt{x^2 + y^2})\Big], \quad (8)$$

where $\rho_t(\cdot)$ and $\rho_l(\cdot)$ are defined as:

$$\rho_t(r) = \frac{3}{2}\left[\frac{\sin(kr)}{kr} - \frac{1}{(kr)^2}\left(\frac{\sin(kr)}{kr} - \cos(kr)\right)\right], \quad (9)$$

$$\rho_l(r) = \frac{3}{(kr)^2}\left[\frac{\sin(kr)}{kr} - \cos(kr)\right]. \quad (10)$$

The simulated results are illustrated in Figs. 7 (b)-(d). Comparisons between numerical and analytical results along the radial direction ($x = y$, $z = 0$) are given in Fig. 7 (d). As expected, the simulated results agree well with the analytical results, and the negative r represents the other side of right-angle bend. The plot for $\langle|E_{yTot}|^2\rangle$ is not shown as it is similar to $\langle|E_{xTot}|^2\rangle$.

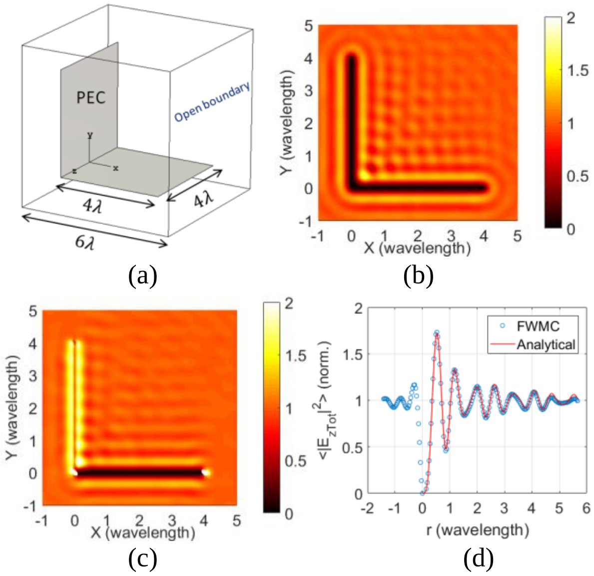

(a) (b)

(c) (d)

Fig. 7. (a) A right-angle bend, (b) simulated $\langle|E_{zTot}|^2\rangle$, (c) simulated $\langle|E_{xTot}|^2\rangle$, and (d) a comparison between results from FWMC and analytical equation.

C. A right-angle corner

A right-corner with 4-wavelength length is shown in Fig. 8 (a). When the plates are infinitely large, the analytical solution for $\langle|E_{zTot}|^2\rangle$ is [3]:

$$\begin{aligned}\langle|E_{zTot}(x,y,z)|^2\rangle = {}& \\ \frac{E_0^2}{3}[1 &- \rho_t(2x) - \rho_t(2y) + \rho_t\left(2\sqrt{x^2+y^2}\right) + \rho_l(2z) \\ &- \frac{x^2}{x^2+z^2}\rho_t\left(2\sqrt{x^2+z^2}\right) - \frac{z^2}{x^2+z^2}\rho_l\left(2\sqrt{x^2+z^2}\right) \\ &- \frac{y^2}{y^2+z^2}\rho_t\left(2\sqrt{y^2+z^2}\right) - \frac{z^2}{y^2+z^2}\rho_l\left(2\sqrt{y^2+z^2}\right) \\ &+ \frac{x^2+y^2}{x^2+y^2+z^2}\rho_t\left(2\sqrt{x^2+y^2+z^2}\right) \\ &+ \frac{z^2}{x^2+y^2+z^2}\rho_l\left(2\sqrt{x^2+y^2+z^2}\right)]. \quad (11)\end{aligned}$$

We apply the FWMC simulation and the results are illustrated in Fig. 8 (b). Comparisons between numerical and analytical results along the radial direction ($x = y = z = r/\sqrt{3}$) are given in Fig. 8 (c). Not surprisingly, good agreement is obtained. The plot for $\langle|E_{xTot}|^2\rangle$ and $\langle|E_{yTot}|^2\rangle$ are not shown as they are similar. It is interesting to note that for negative r close to 0, the field strength varies drastically because of the sharp corner.

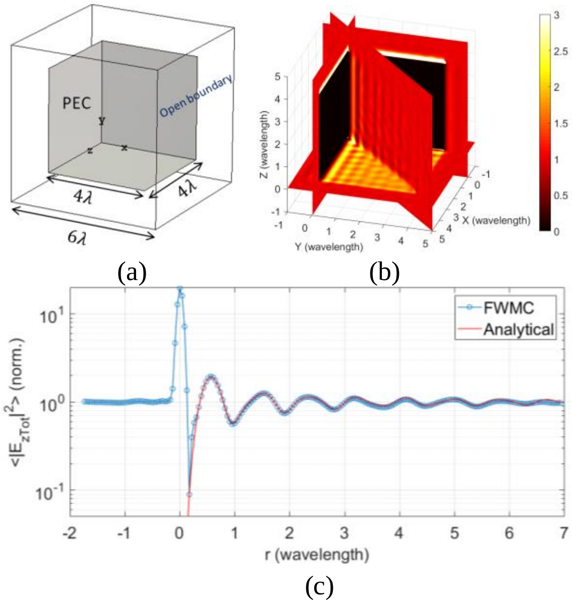

(a) (b)

(c)

Fig. 8. (a) A right-angle corner, (b) simulated $\langle|E_{zTot}|^2\rangle$, and (c) a comparison between results from FWMC and analytical equation, note that because of the finite mesh resolution, small error exist when r is close to zero.

We have verified the numerical results in three specific scenarios and the results are correct. In the next section, we apply this method to more general scenarios.

IV. GENERAL SCENARIOS

In this section we apply the FWMC method to general scenarios, in which four types of models are demonstrated: arbitrary angle bends, dielectric objects, a receiving antenna and a half-space aperture.

A. Arbitrary angle bends

For a right-angle bend, analytical solution exists. For a bend with an arbitrary angle γ, the results can be obtained by using the FWMC method which are illustrated in Figs. 9 (a)-(g). The simulation model is given in Fig. 9 (a) and the plots for $\langle|E_{xTot}|^2\rangle$, $\langle|E_{yTot}|^2\rangle$ and $\langle|E_{zTot}|^2\rangle$ in the cut plane $z = 0$ are illustrated in Figs. 9 (b)-(d) and Figs. 9 (e)-(g) with $\gamma = 30°$ and $\gamma = 60°$ respectively. Not surprisingly, when γ becomes smaller, the FU in the corner becomes poorer.

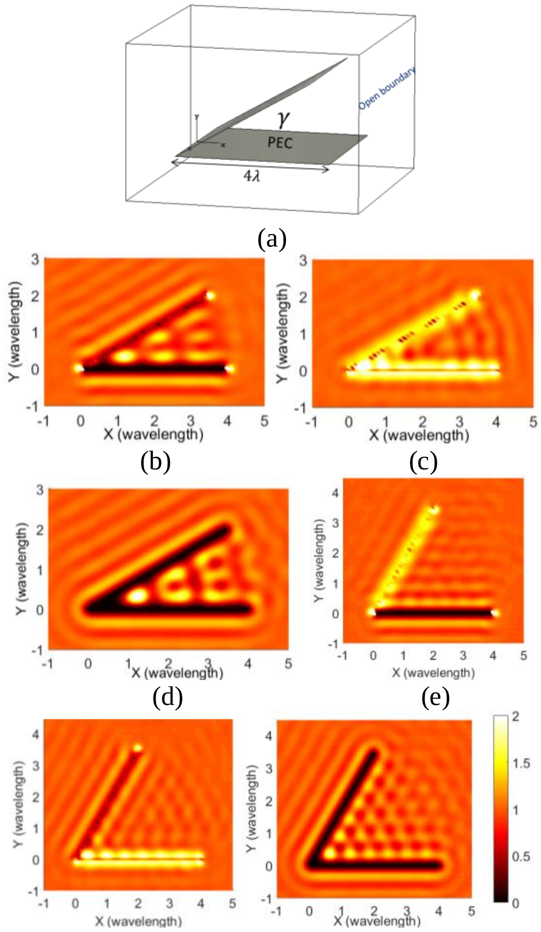

(f) (g)

Fig. 9. (a) A bend with angle α, (b) simulated $\langle |E_{xTot}|^2 \rangle$, $\gamma = 30°$, (c) simulated $\langle |E_{yTot}|^2 \rangle$, $\gamma = 30°$, (d) simulated $\langle |E_{zTot}|^2 \rangle$, $\gamma = 30°$, (e) simulated $\langle |E_{xTot}|^2 \rangle$, $\gamma = 60°$, (f) simulated $\langle |E_{yTot}|^2 \rangle$, $\gamma = 60°$, and (g) simulated $\langle |E_{zTot}|^2 \rangle$, $\gamma = 60°$.

B. Dielectric objects

A dielectric block is shown in Fig. 10 with relative permittivity ε_r, the dielectric block is placed in an ideal multipath environment. The simulated $\langle |E_{zTot}|^2 \rangle$ are illustrated in Figs. 10 (b)-(d) for $\varepsilon_r = 2$, 5 and 10 respectively. Because of the symmetry, only $\langle |E_{zTot}|^2 \rangle$ are plots in Figs. 10 (b)-(d). The fields on the line $y = 0$, $z = 0$ are extracted and given in Fig. 10 (e). It is interesting to note that the field inside the dielectric is not statistically uniform although the environment is statistically uniform. When ε_r increases, both the inside E-field and the nonunifomity increases. This model can be used to simulate the heating power distribution of an arbitrarily shaped object inside a microwave oven.

An interesting example is the sparking of grapes in a household microwave oven [22]. A similar model in [22] is shown in Fig. 11 (a) with two dielectric spheres gapped with 1mm. The power density of $\langle |E_{xTot}|^2 \rangle$ is illustrated in Figs. 11 (b) and (c). The interesting effect as in [22] is observed, the power density is enhanced greatly (more than 100 times) between the two spheres.

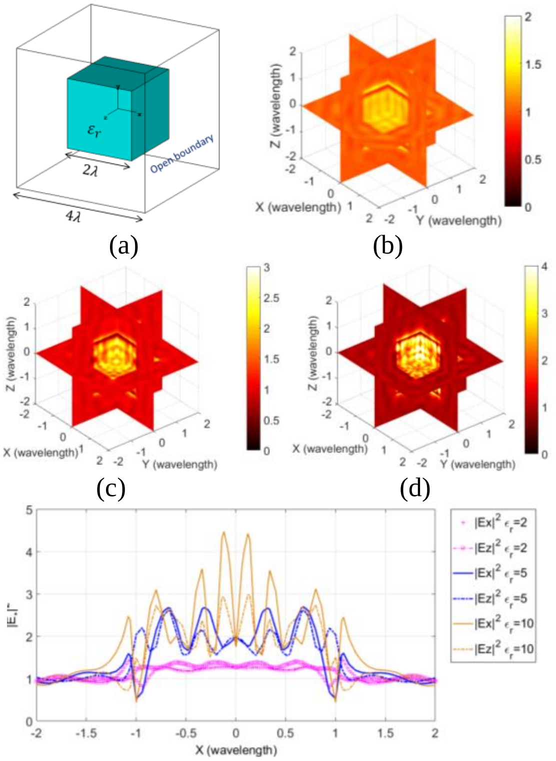

(e)

Fig. 10. (a) A dielectric block with relative permittivity ε_r, simulated $\langle |E_{zTot}|^2 \rangle$ for (b) $\varepsilon_r = 2$, (c) $\varepsilon_r = 5$, (d) $\varepsilon_r = 10$, and (e) extracted plots on the line $y = 0$, $z = 0$, $\langle |E_{yTot}|^2 \rangle$ are not shown as they are the same as $\langle |E_{zTot}|^2 \rangle$.

C. A receiving antenna

A horn antenna working in receiving mode is shown in Fig. 12 (a). The simulated mean power densities are illustrated in Figs. 12 (b)-(d). Since the horn antenna is y-polarized, $\langle |E_{yTot}|^2 \rangle$ gives smaller values than $\langle |E_{xTot}|^2 \rangle$ and $\langle |E_{zTot}|^2 \rangle$ in the horn.

D. A half-space aperture

When two RCs are contiguous or nested in to measure the shielding effectiveness of a planar material, we have a half-space aperture model. A half-space aperture with dimensions of $2\lambda \times 2\lambda$ is shown in Fig. 13 (a). The random incident waves are from $+z$ half space. In the FMWC simulation, we only need to generate half number of plane waves in Fig. 4. The simulated mean power densities are illustrated in Figs. 13 (b)-(c) in which we can identify how random waves diffused through an aperture and apply this method to arbitrary shaped apertures [23].

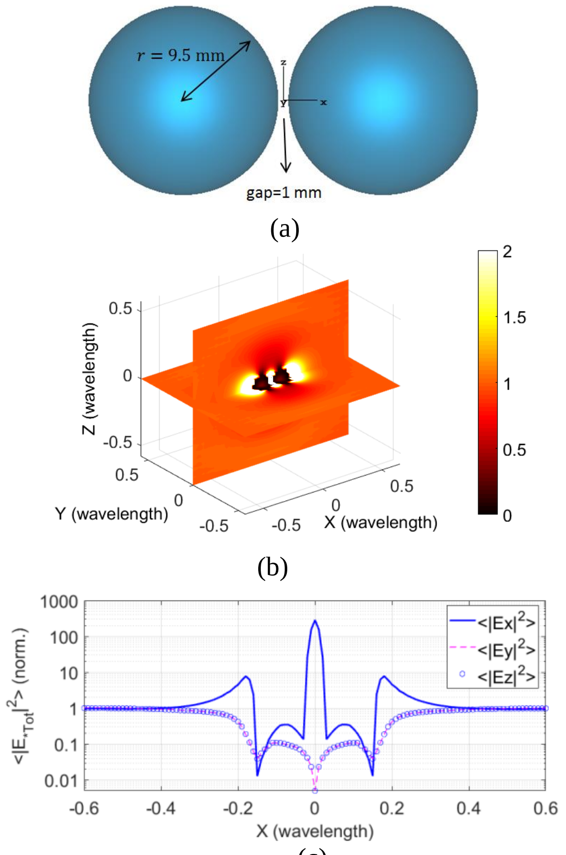

(a)

(b)

(c)

Fig. 11. (a) Two spheres gapped with 1 mm, the material is set as sea water, (b) simulated $\langle|E_{xTot}|^2\rangle$, and (c) extracted plots on the line $y = 0$, $z = 0$.

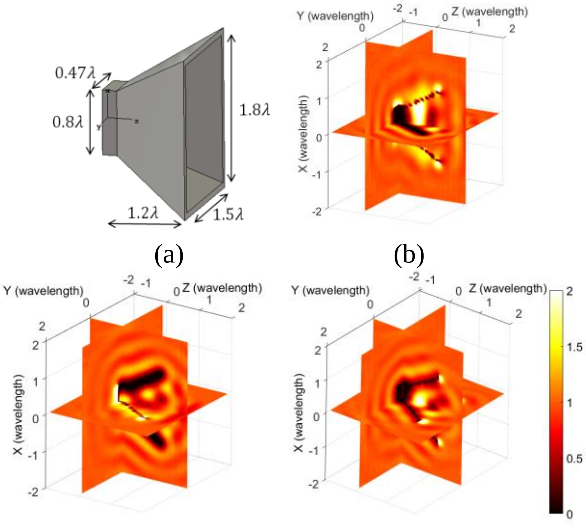

(a)

(b)

(c)

(d)

Fig. 12. (a) A horn antenna, (b) simulated $\langle|E_{xTot}|^2\rangle$, (c) $\langle|E_{yTot}|^2\rangle$, and (d) $\langle|E_{zTot}|^2\rangle$.

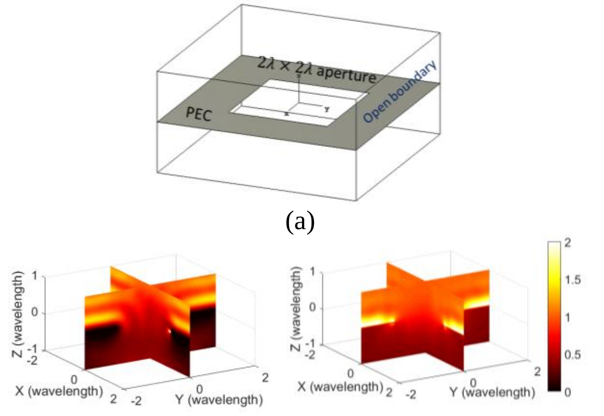

(a)

(b)

(c)

Fig. 13. (a) A half-space aperture, (b) simulated $\langle|E_{xTot}|^2\rangle$, and (c) simulated $\langle|E_{zTot}|^2\rangle$.

V. CONCLUSIONS

We have proposed the FWMC method in this paper and validated the results with analytical equations. The method is from the first principle of PWM and has been applied to general scenarios with arbitrary angle bends, dielectric materials, a receiving antenna and a half-space problem.

For the models in this paper, the simulation time for each plane wave incident is less than 2 minutes and the total simulation times for 1284 incident waves are less than 43 hours (on a computer workstation). The Monte-Carlo simulation consumes less than 4 hours for $M = 10000$. Since each plane wave is independent with others, the parameter sweep process (for each plane wave) can be parallelized with more computers.

Compared with the diffusion equation model, although the accuracy of this method is very high, the memory consumption for electrically large objects is significant. However, for waves far from scatterers, the mean power density becomes uniform in a well-stirred condition and the simulation could be unnecessary. A typical distance of at least $\lambda/4$ from any scatterers is suggested for EMC applications [1]. For non-ideal reverberant environment, this method could be combined with the diffusion equation model to provide more accurate boundary conditions.

ACKNOWLEDGMENT

This work was supported in part by the National Natural Science Foundation of China under Grants 61701224 and in part by Nanjing Rongce Testing Technology Ltd.

REFERENCES

[1] IEC 61000-4-21, *Electromagnetic compatibility (EMC) – Part 4-21: Testing and measurement*

techniques – Reverberation chamber test methods, IEC Standard, Ed 2.0, 2011-01.

[2] CTIA, *Test Plan for Wireless Large-Form-Factor Device Over-the-Air Performance*, ver. 1.2.1, Feb. 2019.

[3] D. A. Hill, *Electromagnetic Fields in Cavities: Deterministic and Statistical Theories*. Wiley-IEEE Press, USA, 2009.

[4] X. Chen, J. Tang, T. Li, S. Zhu, Y. Ren, Z. Zhang, and A. Zhang, “Reverberation chambers for over-the-air tests: An overview of two decades of research,” *IEEE Access*, vol. 6, pp. 49129-49143, 2018.

[5] Q. Xu and Y. Huang, *Anechoic and Reverberation Chambers: Theory Design and Measurements*. Wiley-IEEE Press, USA, 2019.

[6] M. S. Castañer, “Review of recent advances and future challenges in antenna measurement,” *Applied Computational Electromagnetics Society Journal*, vol. 33, no. 2, pp. 99-102, Jan. 2018.

[7] A. Sorrentino, G. Ferrara, M. Migliaccio, and S. Cappa, “Measurements of backscattering from a dihedral corner in a reverberation chamber,” *Applied Computational Electromagnetics Society Journal*, vol. 33, no. 1, pp. 91-93, Jan. 2018.

[8] D. A. Hill, “Plane wave integral representation for fields in reverberation chambers,” *IEEE Trans. Electromagn. Compat.*, vol. 40, no. 3, pp. 209-217, Aug. 1998.

[9] D. A. Hill, “Boundary fields in reverberation chambers,” *IEEE Trans. Electromagn. Compat.*, vol. 47, no. 2, pp. 281-290, May 2005.

[10] A. Somani, S. Gorla, M. Magdowski, and R. Vick, “Measurement of boundary fields in a reverberation chamber,” *10th International Symposium on Electromagnetic Compatibility*, pp. 123-127, 2011.

[11] I. D. Flintoft and J. F. Dawson, “3D electromagnetic diffusion models for reverberant environments,” *International Conference on Electromagnetics in Advanced Applications (ICEAA)*, pp. 511-514, 2017.

[12] I. D. Flintoft, A. C. Marvin, F. I. Funn, L. Dawson, X. Zhang, M. P. Robinson, and J. F. Dawson, “Evaluation of the diffusion equation for modeling reverberant electromagnetic fields,” *IEEE Trans. Electromagn. Compat.*, vol. 59, no. 3, pp. 760-769, June 2017.

[13] J. M. Ladbury, “Monte Carlo simulation of reverberation chambers,” *Gateway to the New Millennium. 18th Digital Avionics Systems Conference. Proceedings (Cat. No.99CH37033)*, pp. 10.C.1-10.C.1, 1999.

[14] Y. Li, X. Zhao, L. Yan, K. Huang, and H. Zhou, “Probabilistic-statistical model based on mode expansion of the EM field of a reverberation chamber and its Monte Carlo simulation,” *Asia-Pacific International Symposium on Electromagnetic Compatibility (APEMC)*, pp. 779-781, 2016.

[15] Y. Zhao, X. Zhao, L. Yan, C. Liu, K. Huang, Q. Liu, and H. Zhou “Analysis of field-to-transmission line coupling inside a reverberation chamber based on mode expansion method,” *IEEE International Symposium on Electromagnetic Compatibility and IEEE Asia-Pacific Symposium on Electromagnetic Compatibility (EMC/APEMC)*, pp. 84-87, 2018.

[16] I. Flintoft, A. Marvin, and L. Dawson, “Statistical response of nonlinear equipment in a reverberation chamber,” *IEEE International Symposium on Electromagnetic Compatibility*, pp. 1-6, 2008.

[17] Y. Cui, H. G. Wei, S. Wang, and L. Fan, “Efficient method of optimizing reverberation chamber using FDTD and genetic algorithm method,” *Applied Computational Electromagnetics Society Journal*, vol. 28, no. 4, pp. 293-299, Apr. 2013.

[18] J. Clegg, A. C. Marvin, J. F. Dawson, and S. J. Porter, “Optimization of stirrer designs in a reverberation chamber,” *IEEE Trans. Electromagn. Compat.*, vol. 47, no. 4, pp. 824-832, Nov. 2005.

[19] L. Bastianelli, V. M. Primiani, and F. Moglie, “Stirrer efficiency as a function of its axis orientation,” *IEEE Trans. Electromagn. Compat.*, vol. 57, no. 6, pp. 1732-1735, Dec. 2015.

[20] V. Mariani Primiani and F. Moglie, “Reverberation chamber performance varying the position of the stirrer rotation axis,” *IEEE Trans. Electromagn. Compat.*, vol. 56, no. 2, pp. 486-489, Apr. 2014.

[21] G. Bosco, C. Picciani, V. M. Primiani, and F. Moglie, “Numerical and experimental analysis of the performance of a reduced surface stirrer for reverberation chambers,” *IEEE International Symposium on Electromagnetic Compatibility*, pp. 156-161, 2012.

[22] H. K. Khattak, P. Bianucci, and A. D. Slepkov, “Linking plasma formation in grapes to microwave resonances of aqueous dimers,” *Proceedings of the National Academy of Sciences*, vol. 116, no. 10, pp. 4000-4005, Mar. 2019.

[23] G. Gradoni, T. M. Antonsen, S. M. Anlage, and E. Ott, “A statistical model for the excitation of cavities through apertures,” *IEEE Trans. Electromagn. Compat.*, vol. 57, no. 5, pp. 1049-1061, Oct. 2015.

Accuracy Comparisons of Channel Emulation Methods for Two-dimensional Uniform and Three-dimensional Sectored Multi-probe Anechoic Chamber

Xiaoyu Huang [1], Xiaoming Chen [1], Huiling Pei [1], and Yingsong Li [2,3]

[1] School of Information and Communications Engineering
Xi'an Jiaotong University, Xi'an, 710049, China
xiaoming.chen@mail.xjtu.edu.cn

[2] College of Information and Communication Engineering
Harbin Engineering University, Harbin, 150001, China

[3] Key Laboratory of Microwave Remote Sensing
National Space Science Center, Chinese Academy of Sciences, Beijing, 100190, China

Abstract **─** Multiple-input-multiple-output (MIMO) over-the-air (OTA) testing has been seen as a promising solution for evaluation of the radio performance of MIMO devices. In this work, we compare the accuracy of two channel emulation methods, i.e., the prefaded signal synthesis (PFS) and the plane wave synthesis (PWS), in two-dimensional (2D) uniform and 3D sectored multi-probe anechoic chamber (MPAC), respectively. The PWS method is proven to be more accurate than the PFS for 2D uniform MPAC system. However, for 3D sectored MPAC system, the PFS method emerged to be better than the PWS method. To explain these seemingly contradicting findings, both the required number of active probes and the leakage of power spectrum are considered in this paper. It is found that the PWS method has higher emulation accuracy than the PFS method when the number of active probes becomes sufficiently large, whereas the PFS is more robust to the undersampling due to the limited number of active probes in practical 3D sectored MPAC system. Moreover, when the number of active probes is particularly small (less than the number of clusters in the probe panel), the emulation accuracy of the PWS method outperform its counterpart.

Index Terms **─**Multi-probe anechoic chamber (MPAC), over-the-air (OTA), pre-faded signal synthesis (PFS), plane wave synthesis (PWS).

I. INTRODUCTION

Multiple-input-multiple-output (MIMO) as the core technology of the new generation of mobile communication has been proposed and applied to long-term evolution (LTE), fifth generation (5G) and other wireless technologies [1]. Furthermore, with the application of millimeter wave (mm-Wave) and the reduction of antenna size, massive MIMO (M-MIMO) is widely used as a promising technology in 5G communication systems [2]-[5]. Before a MIMO device is put into use, it is important to test whether its radio performance meets the certification requirements. OTA testing has become the only feasible solution especially for mmWave M-MIMO devices. In recent years, three mainstream MIMO-OTA testing methods have been formed, including the multi-probe anechoic chamber (MPAC) method [6],[7], the reverberation chamber (RC) method [8],[9], and the radiated two-stage (RTS) method [10],[11]. The multi-probe anechoic chamber (MPAC) method, which is standardized by CTIA [12], can accurately reproduce various standard 2D radio propagation channels [13]-[15].

The main idea of the MPAC is to control the physical position and signal intensity of the probe antennas, so that the transmitted signals of multiple probes superimposed in the test area are consistent with the characteristics of the target channel [16],[17]. There are two common channel emulation methods, which are usually adopted in channel reconstruction of MPAC, i.e., the prefaded signal synthesis (PFS) and the plane wave synthesis (PWS) [18]. The basic idea of the PFS method is to reproduce the spatial characteristics of the target channel environment in the test area by controlling the power weights of the probe antennas, whereas the PWS method assigns appropriate complex weights to the probe antennas to synthesize a static plane wave field in any direction in the test area.

In this work, we make a comprehensive comparison of the emulation accuracies of the PFS and PWS techniques for both two-dimensional (2D) user equipment (UE) MIMO OTA testing and 3D massive base station (BS) OTA testing. The results show that in the traditional 2D MPAC setups, the PWS method has higher emulation accuracy than the PFS method, which is consistent with

Submitted On: March 30, 2021
Accepted On: May 16, 2021

https://doi.org/10.47037/2021.ACES.J.360903

the findings in [19]. However, when it turns to the 3D sectored MPAC system with limited active probes [20]-[22], the PFS method emerges superior performance compared to the PWS method. Then both the required number of probes and the leakage of power spectrum are considered to explain this contradicting finding. It is demonstrated that the number of active probes plays a key role in this problem. The PWS method can show superior emulation performance if there are enough required probes. In the case of limited probes, the PFS method is more accurate than the PWS method. However, when the number of probes is extremely small, the PWS method has better emulation accuracy than the PFS method again. The findings of this work not only explain contradicting finding in the literature, but also provide insight into optimal design of the 3D sectored MPAC system.

II. METHOD

A. Configuration of MPAC setups

Figure 1 illustrates the MPAC setup for the 2D UE OTA testing. The device under test (DUT) is located in the center of the anechoic chamber, surrounded by a horizontal ring composed of uniformly distributed probe antennas. The BS emulator generates the original test signal, which is transmitted to the channel emulator. The channel emulator simulates the multipath environment, including Doppler spread, delay spread and fast fading. Power amplifiers are necessary to compensate the path loss between the probe antennas and the DUT.

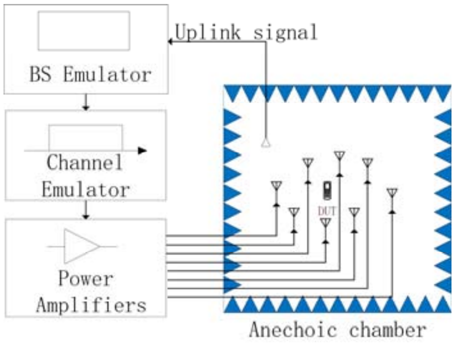

Fig. 1. Illustration of the 2D MPAC OTA setup.

Generally, the purpose of OTA testing is to accurately reproduce the power angular spectrum (PAS) of the target channel model. However, the actual PAS of the target is continuous while the emulation PAS is discrete, which is problematic to use PAS to evaluate the performance of OTA testing. The spatial correlation can be obtained from the PAS through the Fourier transform, so the spatial correlation metric can be used to evaluate the PAS indirectly [19]. In the sequel, the spatial correlation is used to evaluate the emulation performance of the PFS and PWS methods in the case of 2D UE OTA testing.

For the massive BS OTA testing, a 3D sectored MPAC setup was proposed [20], as shown in Fig. 2. The setup consists of an anechoic chamber, a DUT (i.e., a BS array), a probe panel covering a certain angle area, a switching network for selecting a specific number of active probe antennas from the probe panel, channel emulators, and UE emulators.

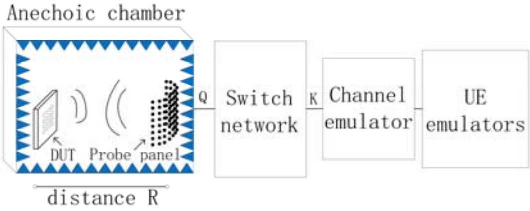

Fig. 2. Illustration of the 3D sectored MPAC OTA setup.

Different from the 2D UE OTA testing, the total variation distance of the PAS [20] is chosen as the evaluation metric to estimate the emulation performance of the PFS and PWS methods in the 3D BS OTA testing. The metric directly evaluates the ability of the two channel emulation methods to reproduce the target PAS under the 3D sectored MPAC setup.

B. Prerequisite

The spatial correlation is the second moment of the random wave field, which is defined as the statistical similarity between two signals received by two different antennas. For better illustration, we assume vertical polarization throughout this work, while the results can be readily extended to dual-polarized channels. The target spatial correlation can be expressed as:

$$\rho_{Tar} = \int a(\Omega)P(\Omega)a^H(\Omega)d\Omega\,, \tag{1}$$

where $a(\Omega)$ is the steering vector of the antenna array at the solid angle Ω (which reduces to the azimuth angle in the 2D case), $P(\Omega)$ is the continuous PAS of the target channel, and the superscript ^{H} denotes conjugate transpose. For simplicity, both probes and DUT antennas are assumed to be isotropic. For the PFS method, the corresponding spatial correlation of the MPAC based emulated channel can be expressed as:

$$\rho_{PFS} = \sum_{k=1}^{K} a(\Omega_k)w(\Omega_k)a^H(\Omega_k)\,, \tag{2}$$

where K is the total number of the active probes connected to the channel emulators and $w(\Omega_k)$ is the power weight of the kth active probe. The power weights of the K probes can be expressed as a vector $w=[w(\Omega_1),\cdots,w(\Omega_K)]^T$. Then the power weight vector w can be obtained by solving a convex optimization problem [23]:

$$\begin{aligned} &\arg\min_{w}\left\|\rho_{Tar}-\rho_{PFS}(w)\right\|_2^2 \\ &s.t. \left\|w\right\|_1 = 1, 0 \le w(\Omega_i) \le 1\left(\forall i \in [1,K]\right) \end{aligned} . \quad (3)$$

For the PWS method, the corresponding spatial correlation of the MPAC based emulated channel can be derived as [19]:

$$\rho_{PWS} = \frac{1}{\beta_0}\sum_{m=1}^{M}\cdot\sum_{k=1}^{K}F(\Omega_k)\omega_{m,k}\sum_{k'=1}^{K}F^H(\Omega_{k'})\omega^H_{m,k'} , \quad (4)$$

where M is the number of subpaths; $F(\Omega_k)$ is the field patterns of the DUT antennas; $\omega_{m,k}$ is the complex weight of the kth active probe for the mth subpath:

$$\begin{aligned} \beta_0 = &\sqrt{\sum_{m=1}^{M}\left\|\sum_{k=1}^{K}F(\Omega_k)\omega_{m,k}\right\|^2} \\ &\cdot\sqrt{\sum_{m=1}^{M}\left\|\sum_{k'=1}^{K}F(\Omega_{k'})\omega_{m,k'}\right\|^2} \end{aligned} , \quad (5)$$

is the normalization factor. In this work, the least square technique is used to calculate the complex weights.

Furthermore, the classic Bartlett beamformer [24] is utilized to estimate the PAS (for it is robust to channel emulation errors):

$$\begin{aligned} U(\Omega) &= a^H(\Omega)\rho_{Tar}a(\Omega) \\ \widehat{U}(\Omega) &= a^H(\Omega)\rho_{OTA}a(\Omega) \end{aligned} , \quad (6)$$

where $U(\Omega)$ and $\widehat{U}(\Omega)$ are the estimated PASs of the target channel and emulation channel, respectively, and ρ_{OTA} represents ρ_{PFS} and ρ_{PWS} , respectively. In this work, our main target is to optimize the weights of the OTA probes to reconstruct the spatial channel as close as possible to the target channel, i.e., $\boldsymbol{\rho_{OTA}} \approx \boldsymbol{\rho_{Tar}}$ and $\widehat{\boldsymbol{U}}(\boldsymbol{\Omega}) \approx \boldsymbol{U}(\boldsymbol{\Omega})$. Moreover, as mentioned before, the total variation distance of the PAS was chosen to evaluate the PAS similarity between the emulated and target channels. This metric reflects the PAS, as well as the size and resolution of the DUT. The Bartlett beamformer and the assumed DUT array are used to estimate the PAS, which is equivalent to observing the power angular distribution of the channel through the limited aperture of the DUT array. The total variation distance of the PAS is calculated as:

$$D_p = \frac{1}{2}\int\left|\frac{\widehat{U}(\Omega)}{\int\widehat{U}(\Omega')d\Omega'} - \frac{U(\Omega)}{\int U(\Omega')d\Omega'}\right|d\Omega , \quad (7)$$

that ranges from 0 (identical) to 1 (complete dissimilar).

III. SIMULATION AND RESULTS

In the 2D UE OTA testing, the 16 probes are evenly distributed in the horizontal ring. The target channel is set to have two clusters with angle of arrival (AoA) of 0° and 11.25°, respectively. As shown in Fig. 3, when the AoA is set to 0°, there is exactly a probe located at this angle (i.e., the best case), whereas when AoA is set to 11.25°, the incident wave is in between two adjacent probes (i.e., worst case). The angular spreads of arrival (ASA) of each cluster varies from 5° to 35° with 10° steps, and 20 subpaths are generated by each cluster with equal power. The performances of the PFS and PWS methods are evaluated by comparing the similarity of the spatial correlations between the emulated channel and the target channel.

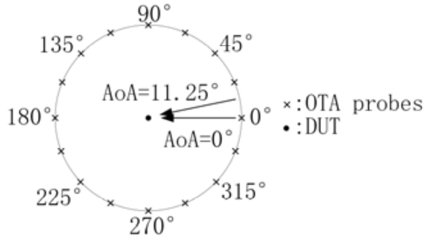

Fig. 3. OTA probe configuration for channel emulation.

The spatial correlations of the target channel and the emulation channel in the two cases are shown in Figs. 4 (a) and (b), respectively. It can be seen that with 16 probes, the test zone size can reach 1.6 λ (where λ is the operation wavelength). In both cases, the PWS method matches the spatial correlation of the target channel well, while the PFS method has poor emulation performance. Nevertheless, with the increase of the ASA, the deviation of the PFS method will gradually decrease, which indicates that the PFS method has poor regeneration ability for clusters with smaller ASA. Furthermore, in the case of large ASA, the spatial correlation of the two methods both well match the target channel, such as 25° and 35°. The results are in accordance with [19]. Therefore, we can speculate that, in the UE testing, the ASA is relatively large due to the abundant scatterers around. As a result, it can be considered that the emulation accuracy of the PFS and PWS methods are roughly the same in this case. However, for the BS testing, the ASA is relatively small because there are not too many scatterers around the BS. Therefore, the PWS method has better emulation performance than its counterpart.

Next, we extend the above analyses to the 3D massive MIMO OTA testing, as shown in Fig. 5. The DUT is assumed to be an 8×8 uniform square array with an inter-element spacing of 0.5 λ. The closest distance between the probe panel and the DUT is set to 2 meters. The probe panel contains 16 evenly distributed probes, and the angular spacing between the probes is 22.5° (which is the same as the 2D case). Figures 5 (a) and (b) correspond to the best case and worst case in the 2D scenario, respectively. Figure 5 (c) shows the four clusters in the best case. Here, the angular spread (AS) of the elevation and the AS of the azimuth of each cluster are set to 2° and 3°, respectively (corresponding to the CDL-C model [25]).

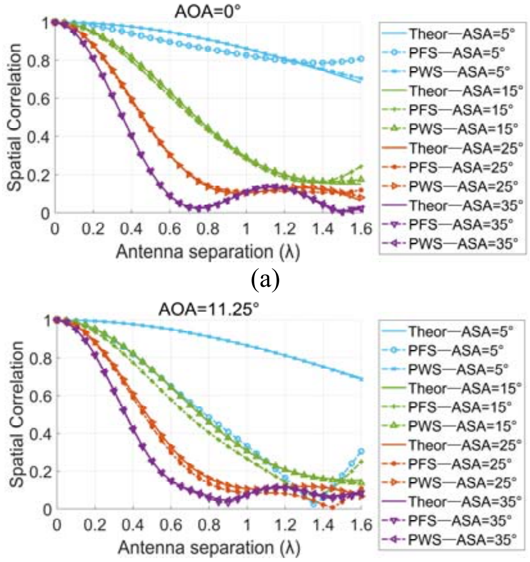

(a)

(b)

Fig. 4. Spatial correlations of the target and emulated channels when (a) AoA = 0° and (b) AoA = 11.25° (with different ASAs).

The total variation distances of the PAS of the PFS and PWS methods of the three cases (shown in Fig. 5) are listed in Table 1. The results show that, for both the best case and the worst case, the advantage of the PWS is obvious in the case of small AS. Moreover, if the angular spacing between the active probes is large, the increase of cluster will not change the observation that the PWS method is better than the PFS method.

More generally, the sectored MPAC setup is widely used in the 3D massive MIMO OTA testing, as shown in Fig. 2. As mentioned before, the DUT is assumed to be an 8 × 8 uniform square array with an inter-element spacing of 0.5 λ and the shortest distance between the probe panel and the DUT is set to 2 meters. The probe panel contains Q = 629 probes, covering 135° in azimuth and 60° in elevation (with a uniform angular spacing of 3.75°). Furthermore, to consider the influence of the leakage of power spectrum, we add another case where the probe panel contains Q = 1241 probes, covering 270° in azimuth and 60 ° in elevation. Figures 6 (a) and (b) show examples of these two cases with $K = 16$ active probes. In this work, the 3GPP clustered delay line (CDL) C model [25] has been chosen as the target channel model. Moreover, the spatial angle mapping (SAM) method [20] is taken as the probe selection scheme.

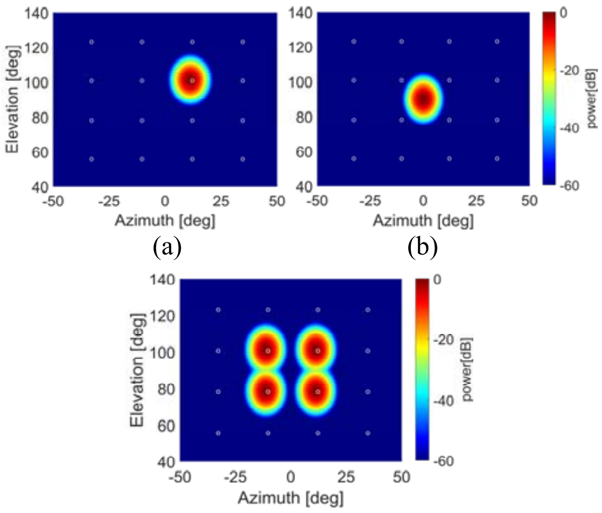

(a)

(b)

(c)

Fig. 5. Illustration of the OTA probe configuration for the PAS of different clusters: (a) the best case; (b) the worst case; (c) four clusters in the best case. White circles represent the active probes.

Table 1: Total variation distances of the PAS of the PFS and PWS methods in the three cases (shown in Fig. 5)

	Case 1	Case 2	Case 3
PFS	0.1628	0.7590	0.1211
PWS	0.1233	0.6826	0.0846

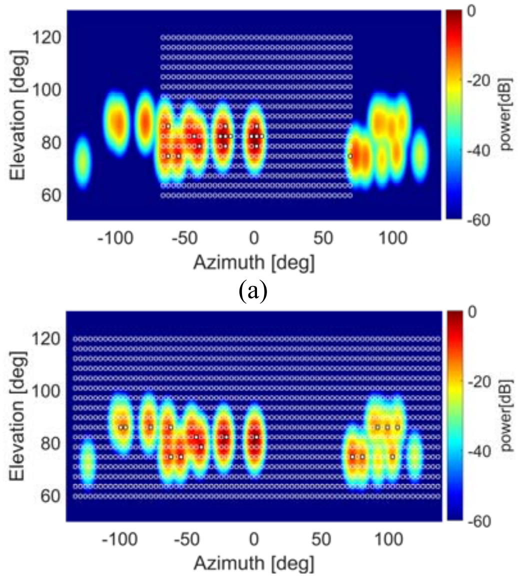

(a)

(b)

Fig. 6. Illustration of the probe selection for the PAS of the target channel: (a) the general scenario; (b) the full

coverage scenario. White circles represent the available probes and white dots denote the selected active probes.

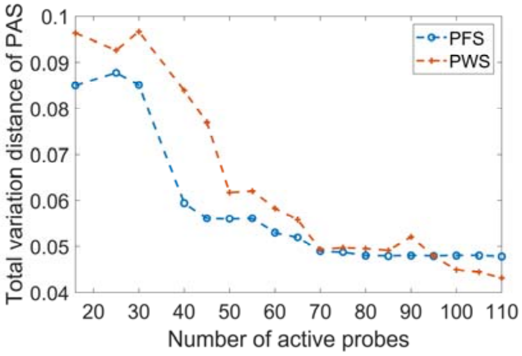

(a)

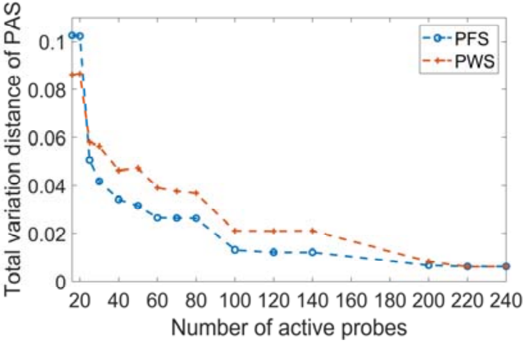

(b)

Fig. 7. Deviations of the PAS between PFS and PWS in (a) the general scenario and (b) the full coverage scenario with different number of active probes.

Figure 7 shows the results of the total variation distance of the PAS with different number of active probes of the two scenarios. As can be seen in Fig. 7 (b), when the number of active probes is extremely small (e.g., less than the number of clusters in the probe panel), the PWS method exhibits better performance than the PFS method. This is due to the small AS, which makes up for the disadvantages caused by the number of active probes (it can also be said that the performance of PFS is worse in this case), so that the PWS method has better emulation performance than PFS when the number of probes is particularly small (consistent with the conclusion in Table 1). However, with the increase of the number of active probes (exceeding the number of clusters in the probe panel), as shown in Figs. 7 (a) and (b), the advantages due to the small AS can no longer make up for the disadvantages due to the small number of active probes. Therefore, the PFS method shows better performance than the PWS method. In addition, as the number of active probes continues to increase, the emulation errors of the PFS and PWS methods become smaller, and then the PWS shows better performance.

To further confirm this finding, more simulations are carried out with $K = 629$ and $K = 1241$ active probes of the whole probe panel for the two scenarios. The results show that, in the general scenario, the total variation distance of the PFS is 0.0347, while that of the PWS is 0.0016. In the full coverage scenario, the total variation distance of the PFS is 0.0062, while that of the PWS is 0.00078. Thus, it is safe to conclude that the number of active probes plays a key role in the performance comparisons of the PFS and PWS methods compared with the leakage of the power spectrum. This is easy to understand, since it can be seen from Fig. 6 (a) that the clusters in the probe panel already contain more than 80% of the total power of the target model, so the angle selection of the probe panel in the general scenario is appropriate.

IV. CONCLUSION

In this paper, we studied the performance of two channel emulation methods in 2D uniform MPAC and 3D sectored MPAC, respectively. It is found that in the case of the traditional 2D MPAC, the PWS method has higher accuracy than the PFS method. In the case of 3D sectored MPAC, however, the results get complicated. It is proved that, compared to the leakage of the power spectrum, the number of active probes plays a more critical role in the performances of the PFS and PWS methods. Furthermore, it can be found that when the number of active probes is less than the number of clusters in the probe panel, the emulation accuracy of the PWS method is better than that of the PFS method. As the number of active probes increases to be greater than the number of clusters in the probe panel, the PFS method then shows better performance than the PWS method. As the number of active probes continues to increase, the deviation of the PFS and PWS methods gradually decrease, and then the PWS method becomes superior to the PFS method.

ACKNOWLEDGMENT

This work was supported in part by the National Natural Science Foundation of China under Grant 61801366 and the Natural Science Foundation of Shaanxi Province under Grant 2020JM-078, and also supported in part by the Key Research and Development Program of Heilongjiang under Grant GX17A016 and by the Open Project of State Key Laboratory of Millimeter Waves (K2020017).

REFERENCES

[1] M. Abdullah, Q. Li, W. Xue, G. Peng, Y. He, and X. Chen, "Isolation enhancement of MIMO antennas using shorting pins," *Journal of Electromagnetic Waves and Applications*, vol. 33, no. 10, pp. 1249-1263, July 2018.

[2] A. Zaidi, F. Athley, J. Medbo, U. Gustavsson, G. Durisi, and X. Chen, *5G Physical Layer: Principles, Models and Technology Components*,

Academic Press, 2018.

[3] Y. Li, W. Li, and W. Yu, “A multi-band/UWB MIMO/diversity antenna with an enhanced isolation using radial stub loaded resonator,” *Applied Computational Electromagnetics Society Journal*, vol. 28, no. 1, pp. 8-20, Jan. 2013.

[4] F. Faraz, X. Chen, Q. Li, J. Tang, J. Li, T. Khan, and X. Zhang, “Mutual coupling reduction of dual polarized low profile MIMO antenna using decoupling resonators,” *Applied Computational Electromagnetics Society Journal*, vol. 35, no. 1, pp. 38-43, Jan. 2020.

[5] K. Yu, Y. Li, and X. Liu, “Mutual coupling reduction of a MIMO antenna array using 3-D novel meta-material structures,” *Applied Computational Electromagnetics Society Journal*, vol. 33, no. 7, pp. 758-763, July 2018.

[6] W. Fan, P. Kyösti, Y. Ji, L. Hentilä, X. Chen, and G. F. Pedersen, “Experimental evaluation of user influence on test zone size in multi-probe anechoic chamber setups,” *IEEE Access*, vol. 5, pp. 18545-18556, Sep. 2017.

[7] W. Wang, H. Wang, H. Gao, Y. Wu, Y. Liu, and J. Gao, “Plane wave compensation technique for MIMO OTA testing in small multi-probe anechoic chamber,” *IET Microwaves Antennas & Propagation*, Apr. 2019.

[8] X. Chen, W. Xue, H. Shi, J. Yi, and W. E. I. Sha, “Orbital angular momentum multiplexing in highly reverberant environments,” *IEEE Microw. Wireless Compon. Lett.*, vol. 30, no. 1, pp. 112-115, Jan. 2020.

[9] J. Tang, F. Li, J. Zheng, X. Chen, Y. Li, and J. Chen, “A new mode stirrer design for the reverberation chamber,” *Applied Computational Electromagnetics Society Journal*, in press.

[10] W. Yu, Y. Qi, K. Liu, Y. Xu, and J. Fan, “Radiated two-stage method for LTE MIMO user equipment performance evaluation,” *IEEE Trans. Electromagn. Compat.*, vol. 56, no. 6, pp. 1691-1696, Dec. 2014.

[11] Y. Jing, H. Kong, and M. Rumney, “MIMO OTA test for a mobile station performance evaluation,” *IEEE Instrument. Meas. Mag.*, vol. 19, no. 3, pp. 43-50, June 2016.

[12] CTIA, “Test Plan for 2x2 Downlink MIMO and Transmit Diversity Over-the-Air Performance,” Tech. Rep. Version 1.1.1, Sep. 2017.

[13] W. Fan, X. Carreno, P. Kyosti, J. O. Nielsen, and G. F. Pedersen, “Over-the-air testing of MIMO-capable terminals: Evaluation of multiple-antenna systems in realistic multipath propagation environments using an OTA method,” *IEEE Veh. Technol. Mag.*, vol. 10, no. 2, pp. 38-46, June 2015.

[14] X. Chen, W. Fan, L. Hentilä, P. Kyösti, and G. F. Pedersen, “Throughput modeling and validations for MIMO-OTA testing with arbitrary multipath,” *IEEE Antennas Wireless Propag. Lett.*, vol. 17, no. 4, pp. 637-640, Apr. 2018.

[15] R. He, B. Ai, G. Wang, M. Yang, C. Huang, and Z. Zhong, “Wireless channel sparsity: Measurement, analysis, and exploitation in estimation,” *IEEE Wireless Communications*, in press.

[16] F. Zhang, W. Fan, Y. Ji, M. Gustafsson, T. Jamsa, G. Steinböck, P. Kyösti, and G. F. Pedersen, “Performance testing of massive MIMO base station with multi-probe anechoic setups,” *Proc. 12th Eur. Conf. Antennas Propag. (EUCAP)*, pp. 1-5, Apr. 2018.

[17] A. Khatun, V. M. Kolmonen, V. Hovinen, D. Parveg, M. Berg, K. Haneda, K. Nikoskinen, and E. Salonen, “Experimental verification of a plane-wave field synthesis technique for MIMO OTA antenna testing,” *IEEE Trans. Antennas Propag*., vol. 64, no. 7, pp. 3141-3150, July 2016.

[18] P. Kyösti, T. Jämsä, and J.-P. Nuutinen, “Channel modelling for multiprobe over-the-air MIMO testing,” *International Journal of Antennas and Propagation*, vol. 2012, Mar. 2012.

[19] Y. Ji, W. Fan, G. F. Pedersen, and X. Wu, “On channel emulation methods in multiprobe anechoic chamber setups for over-the-air testing,” *IEEE Trans. Veh. Technol.*, vol. 67, no. 8, pp. 6740-6751, Aug. 2018.

[20] W. Fan, P. Kyösti, M. Romney, X. Chen, and G. F. Pedersen, “Over-the-air radiated testing of millimeter-wave beam-steerable devices in a cost-effective measurement setup,” *IEEE Commun. Mag.*, vol. 56, no. 7, pp. 64-71, July 2018.

[21] H. Pei, X. Chen, W. Fan, M. Zhang, A. Zhang, and T. Svensson, “Comparisons of channel emulation methods for state-of-the-art multi-probe anechoic chamber based millimeter-wave over-the-air testing,” *IEEE VTC-Fall*, Honolulu, HI, Sep. 2019.

[22] Y. Li, L. Xin, and X. Zhang, “On probe weighting for massive MIMO OTA testing based on angular spectrum similarity,” *IEEE Antennas and Wireless Propagation Letters*, vol. 18, pp. 1497-1501, July 2019.

[23] S. Boyd and L. Vandenberghe, *Convex Optimization.* Cambridge University Press, Mar. 2004.

[24] P. Stoica and R. L. Moses, *Spectral Analysis of Signals*. Pearson/Prentice Hall Upper Saddle River, NJ, 2005.

[25] TR 38.901, “Study on channel model for frequencies from 0.5 to 100 GHz,” 3GPP, Tech. Rep. V14.1.1, July 2017.

Influence Analysis of mm-Wave DUT Mounting Fixture in 5G OTA Measurement

Xudong An [1], Meijun Qu [2], Siting Zhu [1], and Xiaochen Chen [1*]

[1] China Telecommunication Technology Labs
China Academy of Information and Communications Technology, Beijing 100191 China
*chenxiaochen@caict.ac.cn

[2] School of Information and Communication Engineering
Communication University of China, Beijing 100024 China
qumeijun@cuc.edu.cn

Abstract **─** All of the test cases in the current version of TR 38.810 in 3GPP and CTIA millimeter-Wave (mm-Wave) test plan are limited to the free space configuration. However, the truly free-space condition does not exist for mm-Wave testing of 5G user equipment since no device can float in the air. Mounting fixtures and supporting structures are needed to fix the device under test (DUT) and move it in two axes. The influence of mounting fixture on 5G mm-Wave wireless device performance is analyzed in this paper. First, a common 4×1 patch array at 28 GHz is simulated as the performance baseline. Various mounting fixture thickness & various spacing between the DUT and the mounting fixture are simulated to get a quick understanding of the mounting fixture's influence on DUT performance. In different configurations, the working frequency of the antenna would have different degrees of deviation, while the gain could decrease or increase accordingly. Then, to explain these phenomena, an equivalent circuit is extracted utilizing the transmission line theory. Finally, according to the findings, it is recommended that the thickness of the mounting structure should be equal to an integer time of 0.5 λg to minimize the impact of the fixture for practical mounting structure design.

Index Terms **─** 5G, effect, millimeter-wave, mounting fixture, OTA.

I. INTRODUCTION

The technology of mm-Wave is the key contributor to achieve high-data-rate transmission in 5G. The high channel capacity resulting from the high frequency could support the enhanced mobile broadband (eMBB) scenario [1-2]. Antenna size is inversely proportional to the frequency, thus high-gain phased array antennas with small element-element spacing can be tightly packed within the 5G mm-Wave wireless device. Note that completely integrated solutions with modems, antenna and radio frequency (RF) front-end become the cornerstones of 5G deployment [3-4]. Nevertheless, the antenna is inaccessible for connecting any physical cable to the test equipment due to the high level of integration [5-6]. Therefore, over-the-air (OTA) testing becomes mandatory for all 5G FR2 wireless devices.

Given the system constraints for both direct far field (DFF) and compact antenna test range (CATR) methods, the majority of mm-Wave OTA measurement systems are combined-axis systems which require a fixture to mount and rotate the device under test (DUT) to perform full spherical scans. For traditional sub-6 GHz OTA testing where the integrated power metrics of total radiated power (TRP) and total isotropic sensitivity (TIS) are the key performance indicators (KPIs) of interest, the impact of the mounting fixture can be ignored as long as it is made of low dielectric materials. For mm-Wave bands, cellular phones realize isotropic spherical coverage by using several beam-forming antenna modules, the OTA testing process and KPIs will be considerably different from that for traditional sub-6 GHz OTA testing. Since the size of the fixture is comparable with the wavelength in mm-Wave band, even if the mounting fixtures can be assumed to be lossless, the phase change introduced by propagating through even several millimeters of dielectric material can result in a significant change of the measured pattern. Due to the significantly different electromagnetic behaviors in mm-Wave band from those in LTE or sub-6 GHz ones, the current common dielectric materials used as "RF transparent" support structures should be rechecked and redesigned so that accurate measurements can be obtained. Typical KPIs for 5G mm-Wave wireless devices include radiation pattern, effective isotropic radiation power (EIRP), TRP, and effective isotropic sensitivity (EIS). These metrics are closely related.

In this paper, we mainly analyze the influence of mounting fixture on 5G mm-Wave wireless device

Submitted On: May 18, 2021
Accepted On: September 9, 2021

https://doi.org/10.47037/2021.ACES.J.360904

performance. The combination of various thicknesses and space between DUT and the mounting structure are simulated and the impacts of which are compared. The influence mechanism and principle are also explained in detail.

II. IMPACT ANALYSIS OF MILLIMETER-WAVE DUT MOUNTING FIXTURE

To analyze the impact of the mounting fixture on the mm-Wave DUT radiation performance, a common 4×1 patch antenna array working at 28 GHz is designed in Fig. 1 (b) as the performance baseline representing typical array sizes expected to be implemented in common cellular phones specified in 3GPP TR 38.810. The simulated antenna array is printed on a Rogers RO4003 substrate with the thickness of 0.35mm and size of 40×40 mm2. The center-to-center spacing between adjacent elements is set to half wavelength in free space (FS) at 28 GHz. A layer of medium with the same size as the array substrate and the dielectric constant of 3.0 is introduced to imitate the mounting fixture material so that the material loading effect on the radiation performance can be well investigated. Fixture and the gap between the fixture and the mm-Wave antenna can be modeled as 2-layered dielectric materials from Fig. 1 (a) with the thickness of T and D, dielectric constant of ε1 and ε2, respectively.

Combinations of various medium thickness and spacing between the antenna array and the fixture are considered and simulated for analysis. For better understanding, the fixture thicknesses (T) are set to 1.55 mm, 3.1 mm, 4.65 mm, and 6.2 mm, corresponding to 0.25 λg, 0.5 λg, 0.75 λg and 1 λg at 28 GHz, respectively. The spacing (D) is set to 0 mm, 2.68 mm, 5.35 mm, 8.0 mm, and 10.17 mm, corresponding to 0, 0.25 λ0, 0.5 λ0, 0.75 λ0 and 1 λ0 at 28 GHz, respectively. The phased array is set to radiate only in its normal direction for simplicity.

The reflection coefficients and radiation patterns for different thicknesses (T) and spacing (D) are shown in Figs. 2-6. The performance metrics in FS application, i.e., without the medium material, are also calculated, serving as the baseline for further comparison.

For the close contact scenario (D = 0), the loading of dielectric material shifts the resonant frequency of the array antenna to a lower frequency. The bigger the thickness, the larger the resonant frequency shifts. Hence, the degradation in radiation patterns can be observed in Fig. 2 clearly.

For most material loading scenarios, when the thickness of the material is approaching or equal to odd times of 0.25 λg, i.e., T = 0.25 and 0.75 λg in this study, there are obvious shifts in the resonant frequencies, degradations in the realized gain and distortions in the radiation patterns compared with those of FS scenarios.

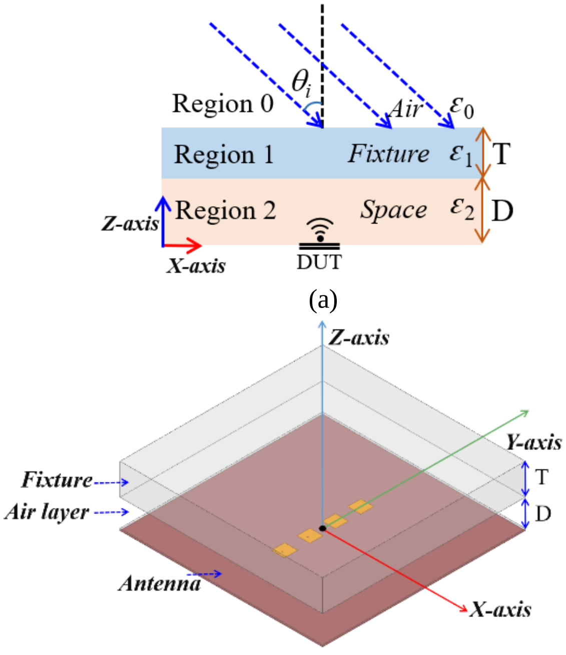

(a)

(b)

Fig. 1. (a) Schematic diagram of the fixture and DUT, and (b) tiled view of the antenna array and the fixture.

The material thickness around integer times of 0.5 λg, i.e., T = 0.5 and 1 λg in this study, can result in resonant frequency and realized gain performance very close to those of FS scenarios.

There is also a very interesting phenomenon for the case of spacing between the array antenna and dielectric material approaching integer times of 0.5 λ_0, i.e., D = 0.5 and 1 λ_0, and the thickness of the material is approaching or equal to odd times of 0.25 λg, i.e., T = 0.25 and 0.75 λg in this study, the focusing effect of noticeable higher realized gains and narrower main beams than those of FS case can be observed clearly. This can be explained that most rays emanating from the DUT going to free space will bend on the interface of different media and superpose in certain directions by proper arrangement of the layer parameters according to Snell's law.

The above findings can be extended that not only in the broadside direction, but in any direction satisfying the corresponding combination conditions, changes in radiation performance can be observed. The specific reasons for the above conclusions refer to the next section.

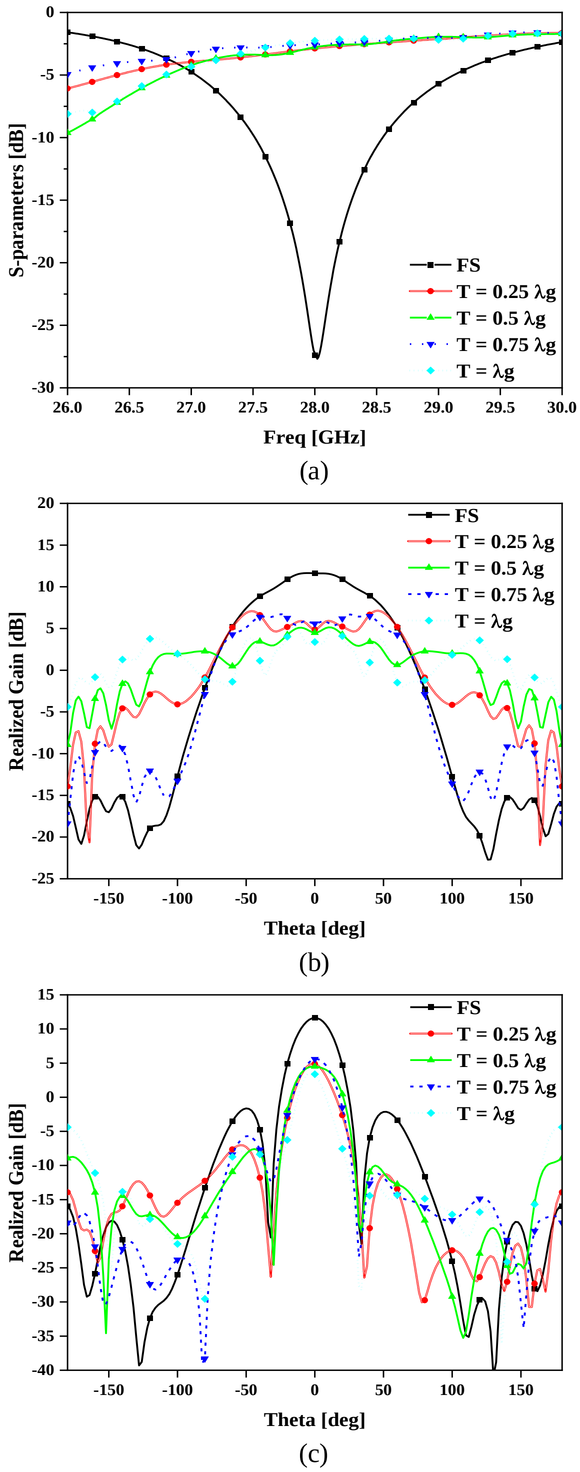

Fig. 2. Scattering parameters and radiation patterns for close contact (D = 0), (a) $|S_{11}|$, (b) pattern @ phi=0, and (c) pattern @ phi=90.

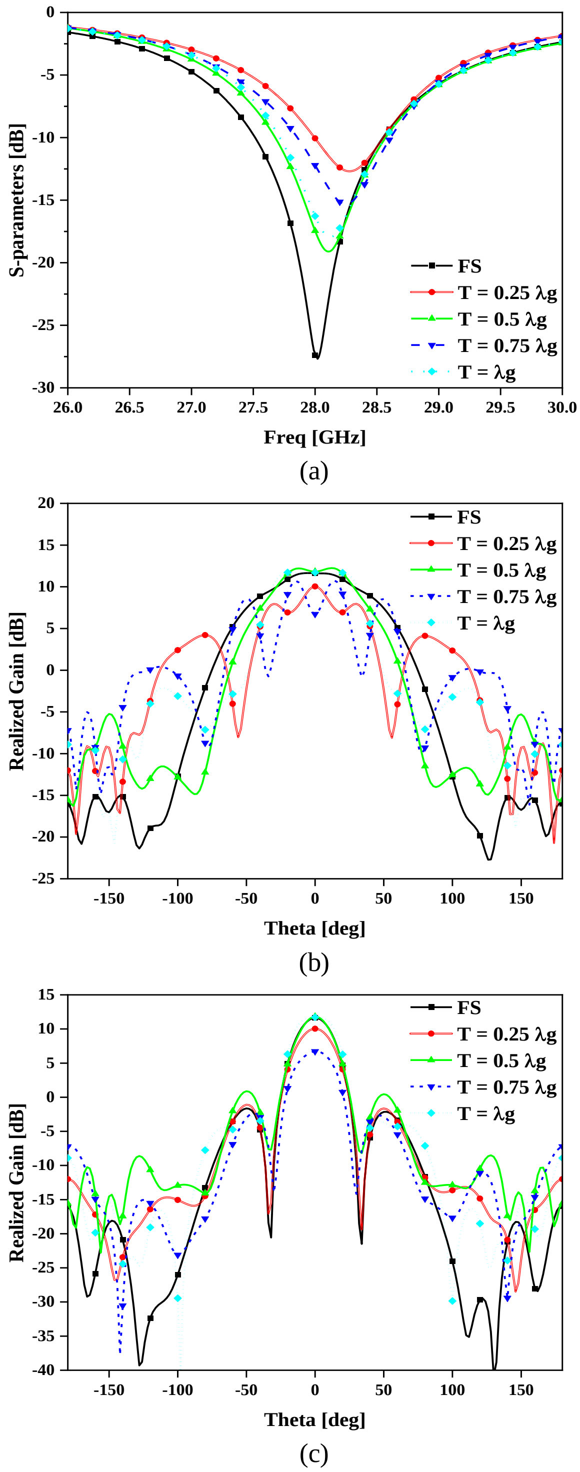

Fig. 3. Scattering parameters and radiation patterns for D = 0.25 λ_0, (a) $|S_{11}|$, (b) pattern @ phi=0, and (c) pattern @ phi=90.

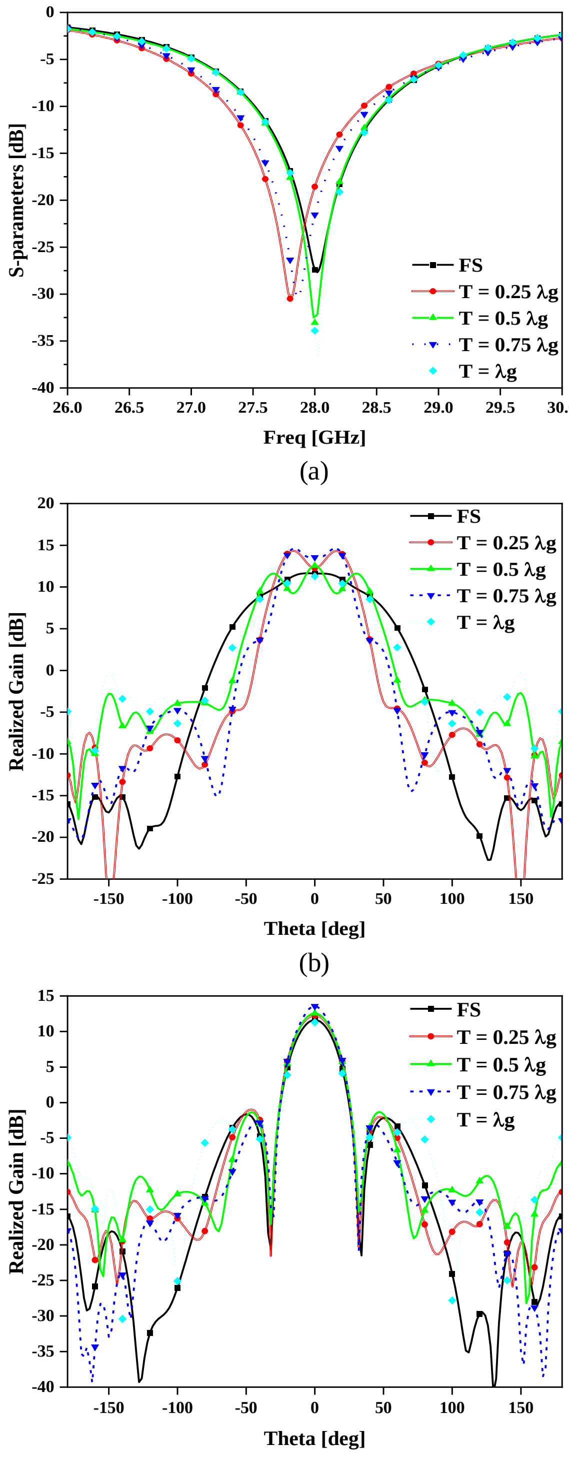

(a)

(b)

(c)

Fig. 4. Scattering parameters and radiation patterns for D = 0.5 λ_0, (a) $|S_{11}|$, (b) pattern @ phi=0, and (c) pattern @ phi=90.

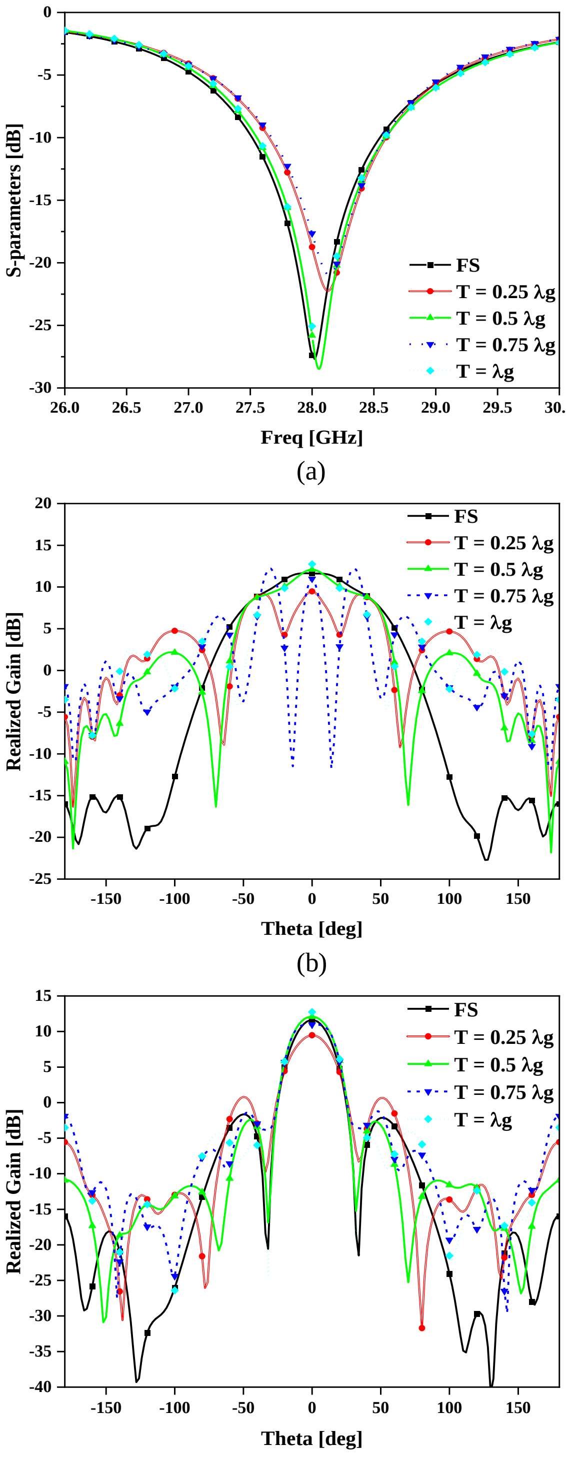

(a)

(b)

(c)

Fig. 5. Scattering parameters and radiation patterns for D = 0.75 λ_0, (a) $|S_{11}|$, (b) pattern @ phi=0, and (c) pattern @ phi=90.

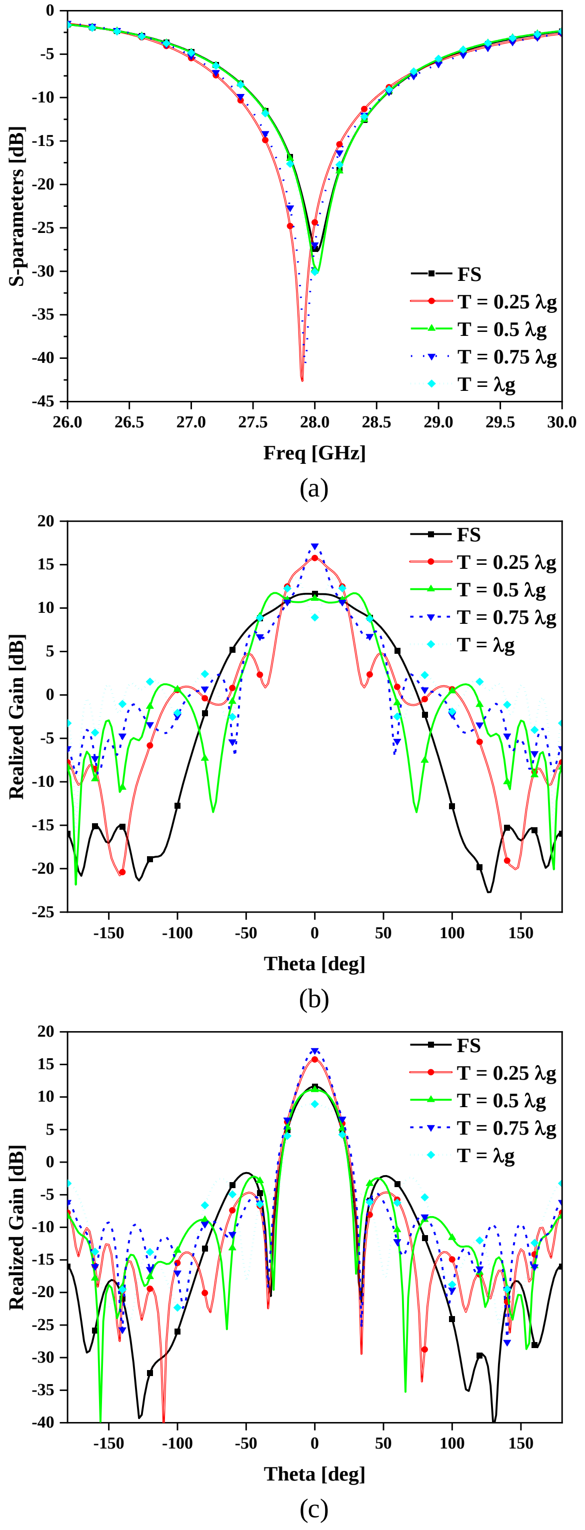

(a)

(b)

(c)

Fig. 6. Scattering parameters and radiation patterns for D = λ_0, (a) $|S_{11}|$, (b) pattern @ phi=0, and (c) pattern @ phi=90.

III. PRINCIPLE OF FIXTURE AFFECTING MILLIMETER-WAVE DUT BASED ON TRANSMISSION LINE THEORY

To further understand the impact of the fixture on mm-Wave DUT radiation performance, this section analyzes its principle based on transmission line theory.

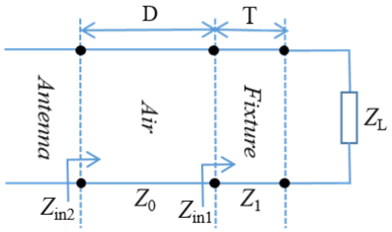

Fig. 7. Schematic diagram of the equivalent cascade transmission line.

Electromagnetic waves could propagate in the medium with a certain wave impedance which depends on the characteristic parameters of the medium (dielectric constant and permeability). The wave impedance of air is 377 Ω. The whole propagation process can be equivalent to the cascade of several transmission lines with different characteristic wave impedances as can be seen from Fig. 7. The load impedance ZL is equal to the wave impedance Z0 in FS.

Cascade transmission lines can be regarded as a multistage impedance converter. According to the theory of transmission line, when the length of a transmission line is T and the characteristic impedance is Z1, the input impedance Zin1 of the transmission line terminated with load ZL = Z0 could be calculated by:

$$Z_{\text{in1}}=Z_1\frac{Z_0\cos(\beta \mathrm{T})+jZ_1\sin(\beta \mathrm{T})}{Z_1\cos(\beta \mathrm{T})+jZ_0\sin(\beta \mathrm{T})}. \tag{1}$$

It can be derived:

$$\mathrm{T}=2\mathrm{k}\cdot\lambda/4,\ Z_{\text{in}}=Z_0, \tag{2}$$

$$\mathrm{T}=(2\mathrm{k}\text{-}1)\cdot\lambda/4,\ Z_{\text{in}}=Z_1^2/Z_0, \tag{3}$$

where β is a propagation constant, k is a nonzero integer. If the electromagnetic wave could propagate forward completely through the mounting structure and produce zero reflection, it is necessary to ensure impedance conjugate matching, that is, to meet the condition of Equation (2). At this time, the influence of the fixture on the electromagnetic wave is reduced to the minimum. Therefore, it is necessary to ensure that the electrical length of the transmission line is an integral multiple of π, that is to say, the thickness of the fixture (T) should be an integral multiple of the half dielectric wavelength, and the minimum thickness should be the half dielectric wavelength. This is consistent with the above simulated results in Section II. Based on this, we recommend that for practical mounting fixture design, the thickness of the fixture should be integer times of 0.5 λg.

When the length of T satisfies Equation (3), namely, T is odd times of 0.25 λg, the fixture could transform 377 Ω to Z12/Z0. At this time, the condition of impedance matching is no longer satisfied, that is to say, the fixture has a reflection effect on the electromagnetic wave greatly. The electromagnetic wave reflected by the antenna surface experiences a 180° phase shift due to the fixture, which greatly affects the working frequency and radiation pattern of the mm-Wave antenna. Therefore, when the thickness of the material is approaching or equal to odd times of 0.25 λg, the working frequency deviated seriously and the radiation pattern deteriorated clearly:

$$Z_{\text{in2}} = Z_0 \frac{Z_{\text{in1}} \cos(\beta \text{D}) + jZ_0 \sin(\beta \text{D})}{Z_0 \cos(\beta \text{D}) + jZ_{\text{in1}} \sin(\beta \text{D})} . \tag{4}$$

It can be calculated:

$$\text{D=2k} \cdot \lambda / 4,\ Z_{\text{in2}} = Z_{\text{in1}} , \tag{5}$$

$$\text{D=(2k-1)} \cdot \lambda / 4,\ Z_{\text{in2}} = Z_0^2 / Z_{\text{in1}} . \tag{6}$$

If the spacing between the array antenna and fixture (D) as well as the thickness of the fixture (T) are set to integer times of 0.5 λ_0 (meet Equations (2) and (5) in this case), under the condition of antenna resonance, each transmission component of the electromagnetic wave has the same phase value after passing through the fixture, which realizes in-phase superposition and continuous enhancement. At the same time, the reflection component decreases with the increase of reflection times due to the inverse effect [7-8].

We also analyze the phenomenon of antenna gain improvement (focusing) when the spacing between the array antenna and fixture (D) is integer times of 0.5 λ_0 and the thickness of fixture (T) is odd times of 0.25 λg (meet Equations (3) and (5) in this case), which is obtained in Section II. Since the air layer between the antenna and the fixture is an integral multiple of the half wavelength, this is equivalent to the case where there is no air layer between the antenna and the fixture and is close to each other. Importantly, it should be mentioned that there is no gain improvement in FS when D equals zero. Only when D is integer times of 0.5 λ_0 and T odd times of 0.25 λg, can the gain improvement be achieved. However, it should be noted that this is a test error and does not represent the true gain of the antenna. This configuration should be avoided. The reason is like Fabry-Perot cavity antenna theory which is explained as follows:

Assuming that the reflection coefficient of the fixture is ρejφ, the radiation pattern of the DUT is f(α), n is the number of reflections, θ_n is the total phase difference between the beam reflected n times and the initial beam. If there is no loss in the transmission between the fixture and the DUT, the amplitude of the electric field at the far field should be the vector superposition of multiple transmitted waves:

$$E = \sum_{n=0}^{\infty} f(\alpha) E_0 \rho^n \sqrt{1-\rho^2} e^{j\theta_n} . \tag{7}$$

Therefore, for the electromagnetic wave of antenna resonance frequency, the reflection is very small and the energy is almost transmitted. This phenomenon could improve the antenna gain, which could be applied to the design of high-gain antennas [9-12].

IV. CONCLUSION

To sum up, a truly FS configuration does not exist for 5G mm-Wave device OTA testing because they can't be floated in the air. It can be found that not only the property of the dielectric material imitating mounted fixtures, but also the spacing between DUT and fixtures, or the combination of them, will affect the measurements. We suggest that maybe white-box measurements are needed for mm-Wave DUTs in which the locations of mm-Wave modules are declared by manufacturers and the scanning ranges of which should not be covered or blocked by mounting fixtures. In addition, based on the findings in this study, for practical mounting fixture design, the thickness of the mounting structure should be close to integer times of 0.5 λg to minimize the impact of the fixture on DUTs. These proposals are for the original entrusted manufacturers (OEMs) and DUT mounting fixture vendors.

ACKNOWLEDGMENT

This research was funded in part by the Major State Basic Research Development Program (2019YFF0216600), and in part by the Fundamental Research Funds for the Central Universities (CUC210B012).

REFERENCES

[1] Y. Niu, Y. Li, D. Jin, L. Su, and A. V. Vasilakos, "A survey of millimeter wave communications (mmWave) for 5G: opportunities and challenges," *Wireless Networks*, vol. 21, pp. 2657-2676, 2015.

[2] H. Gamage, N. Rajatheva, and M. Latvaaho, "Channel coding for enhanced mobile broadband communication in 5G systems," *European Conference on Networks and Communications*, pp. 1-6, 2017.

[3] S. G. Pannala, "Feasibility and challenges of over-the-air testing for 5G millimeter wave devices," in *2018 IEEE 5G World Forum (5GWF)*, pp. 304-310, 2018.

[4] B. Derat, C. Rowell, and A. Tankielun, "Promises of near-field software and hardware transformations for 5G OTA," *IEEE Conference on Antenna Measurements Applications*, 2018.

[5] H. Huang, "Overview of 5G mm-wave antenna design solutions in cellular phones: AiP, AiA, and

AiAiP," *International Symposium on Antennas and Propagation*, 2019.

[6] CTIA, "Test Plan for Wireless Device Over-the-Air Performance," 2019.

[7] A. K. Gautam and M. Singh, "Design of gain enhanced stacked rectangular dielectric resonator antenna for C-band applications," in *International Conference on Computing for Sustainable Global Development*, pp. 119-123, 2016.

[8] Y. Pan and S. Y. Zheng, "A low-profile stacked dielectric resonator antenna with high-gain and wide bandwidth," *IEEE Antennas and Wireless Propagation Letters*, vol. 15, pp. 68-71, 2016.

[9] S. A. Muhammad, R. Sauleau, and H. Legay, "Purely metallic waveguide-fed Fabry–Perot cavity antenna with a polarizing frequency selective surface for compact solutions in circular polarization," *IEEE Antennas and Wireless Propagation Letters*, vol. 11, pp. 881-884, 2012.

[10] J. Ren, W. Jiang, K. Zhang, and S. Gong, "A high-gain circularly polarized Fabry–Perot antenna with wideband low-RCS property," *IEEE Antennas and Wireless Propagation Letters*, vol. 17, pp. 853-856, 2018.

[11] F. Deng and J. Qi, "Shrinking profile of Fabry–Perot cavity antennas with stratified metasurfaces: Accurate equivalent circuit design and broadband high-gain performance," *IEEE Antennas and Wireless Propagation Letters*, vol. 19, pp. 208-212, 2020.

[12] Y. Lv, X. Ding, and B. Wang, "Dual-wideband high-gain Fabry-Perot cavity antenna," *IEEE Access*, vol. 8, pp. 4754-4760, 2020.

Xudong An Senior Engineer, Director of Antenna and Positioning Department, China Academy of Information and Communications Technology. He has long been engaged in the research and standardization of cellular mobile communication (3G, 4G, 5G, etc.), 5G terminal test technology, large-scale array antenna system, position-based technology, gesture recognition and test system development. He has published more than ten papers and articles in journals and conferences at home and abroad, and applied for 6 patents related to mobile communication equipment testing.

Meijun Qu received the Ph.D. degree from the School of Information and Communication Engineering, Beijing University of Posts and Telecommunications (BUPT), Beijing, China, in 2020. She is currently a Lecturer at Communication University of China, China. Her research interests include microwave passive component, antenna, metamaterial, and electromagnetic compatibility.

Siting Zhu R & D Engineer, Antenna and Positioning Department, China Academy of Information and Communications Technology, is engaged in the research of MIMO OTA and 5G terminal test, standard setting and related technologies, participated in the National Science and Technology Major Special "R15-oriented 5G terminal test system and platform research and development," and other projects.

Xiaochen Chen Senior Engineer, Chinese Leaders of EU FP6 GO4IT, FP7 WALTER, is responsible for several national development and reform commission projects and major special sub-project research of the Ministry of Industry and Information Technology. He is responsible for formulating more than 20 domestic and foreign communication standards, applying for / owning 6 patents, and publishing more than 20 academic papers. Now, he works at China Telecommunication Technology Labs, China Academy of Information and Communication Technology, Beijing 100876 China.

Measurement Uncertainty of Antenna Efficiency Measured Using the Two-Antenna Method in a Reverberation Chamber

Wei Xue [1], Yuxin Ren [2], Xiaoming Chen [1], Zhengpeng Wang [3], Yingsong Li [4,5], and Yi Huang [6]

[1] School of Information and Communications Engineering
Xi'an Jiaotong University, Xi'an, 710049, China

[2] China Academy of Information and Communications Technology, Beijing, 100191, China
renyuxin@caict.ac.cn

[3] Electronics and Information Engineering
Beihang University, Beijing, 100191, China

[4] College of Information and Communication Engineering
Harbin Engineering University, Harbin, 150001, China

[5] Key Laboratory of Microwave Remote Sensing
National Space Science Center, Chinese Academy of Sciences, Beijing, 100190, China

[6] Department of Electrical Engineering and Electronics
University of Liverpool, Liverpool, L69 3GJ, UK.

Abstract **─** With decades of development, the reverberation chamber (RC) has been proven to be a popular facility to determine antenna efficiency. One-, two- and three- antenna methods have been proposed to measure antenna efficiency without the need of a reference antenna. Due to the stochastic nature of RC-based measurements, the statistical analysis of the uncertainty is indispensable. Recently, the statistical uncertainty models for the one- and three-antenna methods were derived, however, the statistical model for the two-antenna method is still unknown to date. In this paper, the statistical uncertainty model of the two-antenna method is proposed. The approximated relative uncertainty is also given. The derived statistical uncertainty is verified by both simulations and measurements. It is experimentally verified that the statistical model can cope with hybrid stirring and assess the measurement uncertainty with and without frequency stirring in an efficient and convenient way.

Index Terms **─** Antenna efficiency, measurement uncertainty, reverberation chamber, two-antenna method, hybrid stirring.

I. INTRODUCTION

The reverberation chamber (RC) is an electrically large and highly conductive enclosure, which is initially proposed for electromagnetic compatibility (EMC) testing in 1968 [1]. The electromagnetic (EM) fields within the RC can be regarded as a superposition of resonant cavity modes with different weights [2]. Various stirring techniques (e.g., mechanical stirring, source stirring, and frequency stirring) [3]-[5] are usually adopted to stir (redistribute) the EM modes, resulting in different combinations of the weights. From the viewpoint of statistics, the EM field averaged over all stirring states can be considered as uniform, isotropic, and homogeneous. Owning to RC's particular properties (e.g., cost-effectiveness, good repeatability, and high efficiency), its application has extended from EMC testing to other areas, including over-the-air (OTA) testing (e.g., total radiated power, total isotropic sensitivity, throughput, and adjacent channel leakage power ratio) [6]-[9], antenna measurements (e.g., free-space *S*-parameter [2], [9], efficiency [1], [10]-[13], radiation pattern [14]-[16], and diversity gain [17]) , material characterization (e.g., absorption cross section, permittivity, and shielding effectiveness) [1], [2], etc. In this work, we focus on the antenna efficiency measurements.

In order to determine the antenna efficiency in a more convenient and accurate way, a few RC-based methods have been proposed. Most of these methods need a reference antenna with known efficiency [1]. A reference antenna covering the desired band of interest may not be always available in practice, thus, three non-reference antenna methods, i.e., one-, two-, and three-

Submitted On: April 13, 2021
Accepted On: August 5, 2021

https://doi.org/10.47037/2021.ACES.J.360905

antenna methods, were proposed in [10] to overcome this problem. Knowing the enhanced backscattering effect in the RC [1], [10], meanwhile, utilizing the relationship between the quality factors in time-domain (Q_{TD}) and frequency-domain (Q_{FD}), the antenna efficiency can be determined without the need of a reference antenna. Due to the stochastic nature of RC-based measurements, the statistical analysis of measurement uncertainty is necessary and beneficial. The statistical uncertainty models of the standard reference antenna method and two non-reference antenna methods (i.e., one- and three-antenna methods) were presented in [18] and [19], respectively. However, the statistical uncertainty model of the two-antenna method is still unknown to date. It is worth stressing that these three non-reference antenna methods have different prerequisites and expressions, further different measurement uncertainties. Therefore, to achieve a rigorous uncertainty assessment, the statistical analysis must be performed independently for each non-reference antenna method.

In this paper, the statistical uncertainty model of the two-antenna method is proposed. The approximated relative uncertainty (when the number of independent samples is large) is also given. Simulations and measurements are performed to validate the proposed uncertainty model. Moreover, hybrid stirring (i.e., mechanical stirring and frequency stirring) is considered based on the proposed uncertainty model. Analytical and empirical uncertainties with and without frequency stirring are analyzed. Good agreements are observed.

The rest of this paper is organized as follows: Section II gives a brief introduction to the two-antenna method and exhibits the derivation of the statistical uncertainty. Simulations and measurements are conducted in Section III and IV, respectively. Hybrid stirring and comparisons of three non-reference antenna methods are also discussed in Section IV. Section V draws the conclusion.

II. THEORETICAL ANALYSIS

A common setup for antenna efficiency measurement using the two-antenna method is depicted in Fig. 1. Two antennas under test (i.e., Antenna 1 and Antenna 2) are both connected to the vector network analyzer (VNA). The mechanical stirrers are driven and controlled by the motor controller. At each stirring state, all the S-parameters are collected and stored by the VNA.

According to [10], once the measurement procedure is completed, the antenna efficiencies can be determined by:

$$\eta_1 = \sqrt{\frac{C_{RC}\langle |S_{11,s}|^2\rangle}{e_b Q_{\mathrm{TD}}}},\ \eta_2 = \sqrt{\frac{C_{RC}\langle |S_{22,s}|^2\rangle}{e_b Q_{\mathrm{TD}}}}\ , \qquad (1)$$

where $C_{RC} = 16\pi^2 V/\lambda^3$, V is the inner volume of the RC and λ is the wavelength, $Q_{\mathrm{TD}} = \omega\tau_{\mathrm{RC}}$ with ω being the angular frequency and τ_{RC} being the chamber decay time. $S_{ii,s} = S_{ii} - \langle S_{ii}\rangle$ (i = 1, 2) denotes the stirred part of S_{ii} , and $\langle \bullet \rangle$ represents the ensemble average over all stirring states. e_b represents the enhanced backscatter coefficient, which can be calculated using [10]:

$$e_b = \frac{\sqrt{\langle |S_{11,s}|^2\rangle\langle |S_{22,s}|^2\rangle}}{\langle |S_{21,s}|^2\rangle}. \qquad (2)$$

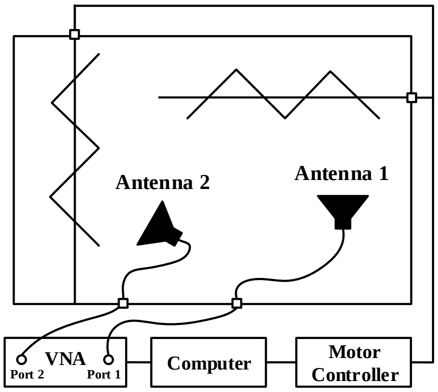

Fig. 1. Setup for antenna efficiency measurement using the two-antenna method.

Note that the measured antenna efficiencies of Antenna 1 and Antenna 2 have similar expressions, therefore, the statistical uncertainties should also be similar. For the sake of conciseness, we focus on η_1 here. To exhibit the analysis of the uncertainty clearly and intuitively, we denote $X = \langle |S_{11,s}|^2\rangle$ and $Y = e_b$. In this way, (1) can be rewritten as:

$$\eta_1 = \sqrt{\frac{C_{RC}}{Q_{\mathrm{TD}}}}\sqrt{\frac{X}{Y}}\ . \qquad (3)$$

It should be stressed that X and Y are random variables (RVs) following the distributions below [1], [19], [20]:

$$f(x) = \frac{N^N}{x_0^N \Gamma(N-1)} x^{N-1} \exp(-Nx/x_0)\ , \qquad (4)$$

$$f(y) = \frac{y_0^N}{y^{N+1}\Gamma(N)^3}\Bigg[{}_2F_1(\frac{3N}{2},\frac{3N}{2};\frac{1}{2};\frac{y_0^2}{4y^2})\Gamma(\frac{3N}{2})^2 - {}_2F_1(\frac{3N+1}{2},\frac{3N+1}{2};\frac{3}{2};\frac{y_0^2}{4y^2})\frac{y_0}{y}\Gamma(\frac{3N+1}{2})^2 \Bigg], \qquad (5)$$

where $x_0 = \langle |S_{11,s}|^2\rangle = 2Q_{\mathrm{TD}}/C_{RC}$ and $y_0 = 2$ denote x and y in an ideal RC, respectively. ${}_pF_q(a_1,...,a_p;b_1,...,b_q;x)$ is the generalized hypergeometric function [21], Γ is the

Gamma function. *N* represents the number of independent mechanical stirring samples. The standard deviations (STDs) of *X* and *Y* can be calculated using [19], [20]:

$$\mathrm{STD}(x) = \frac{x_0}{\sqrt{N}}, \tag{6}$$

$$\mathrm{STD}(y) = \frac{y_0}{N-1}\sqrt{N^2\frac{N-1}{N-2} - \frac{\Gamma(N+1/2)^4}{\Gamma(N)^4}}. \tag{7}$$

According to the law of propagation of uncertainty [22], the uncertainty of η_1, i.e., $u(\eta_1)$, can be estimated as:

$$u(\eta_1)=\sqrt{\left(\frac{\partial \eta_1}{\partial x}u(x)\right)^2 + \left(\frac{\partial \eta_1}{\partial y}u(y)\right)^2}. \tag{8}$$

Substituting (3), (6), and (7) into (8), we have:

$$\frac{u(\eta_1)}{\eta_1} = \sqrt{\frac{1}{4N} + \frac{1}{4(N-1)^2}\left(N^2\frac{N-1}{N-2} - \frac{\Gamma(N+1/2)^4}{\Gamma(N)^4}\right)}. \tag{9}$$

When *N* is large, we have:

$$\lim_{N\to\infty}\frac{\Gamma(N+t)}{\Gamma(N)N^t} = 1. \tag{10}$$

Further, Eq. (9) can be approximated as:

$$\lim_{N\to\infty} u_{\mathrm{rel}}(\eta_1) = \lim_{N\to\infty}\frac{u(\eta_1)}{\eta_1} = \frac{1}{\sqrt{2N}}. \tag{11}$$

It should be stressed that Eq. (9) is the analytical expression of the relative uncertainty, which is applicable for any value of *N*. By comparison, Eq. (11) is an approximation of the relative uncertainty, which is more concise yet only suitable for the cases of large *N*. As will be shown and discussed in Section III, the gap between Eqs. (9) and (11) diminishes rapidly as *N* increases, and becomes negligible when *N* is large.

III. SIMULATIONS

In order to verify the derived uncertainty model, Monte Carlo simulations are employed. For simplicity and without loss of generality, the true antenna efficiency is assumed to be 100% ($\eta_1 = 100\%$) in this section. For each number of independent samples *N* and each random variable, we randomly generated 1000 × *N* samples following the exponential distributions with different distribution parameters, i.e., $|S_{11,s}|^2, |S_{22,s}|^2 \sim Exp(C_{RC}/2Q)$ and $|S_{21,s}|^2 \sim Exp(C_{RC}/Q)$. Note that $Y = e_b$ can be obtained based on the generated samples by utilizing Eq. (2).

Figure 2 shows the simulated, analytical, and approximated relative STDs as functions of *N*. The STD from the Lindeberg-Levy central limit theory ($1/\sqrt{N}$) is also presented in the figure for comparison. The analytical relative STD does not exist when *N* is equal to 1 and 2. For a unified comparison of different STDs, all the STDs are plotted when $N \geq 3$.

It can be seen from Fig. 2 that both analytical and approximated relative STDs are in accordance with the simulated ones. It should be noted that the approximated relative STD is obtained under the assumption of large *N*. Surprisingly, the approximated relative STD outperforms the analytical one even when *N* is small. As *N* grows larger, the gaps between the simulated, analytical and approximated relative STDs decrease rapidly. Moreover, these three relative STDs become indistinguishable as *N* further increases. Therefore, the approximated one is preferred in practice for its concision. The same as the analytical and approximated relative STDs, $1/\sqrt{N}$ also provides an overestimation. However, discrepancies can still be observed when $N = 1000$. This indicates the factor of $1/\sqrt{2}$ cannot be omitted for a rigorous STD assessment of measured efficiencies using the two-antenna method.

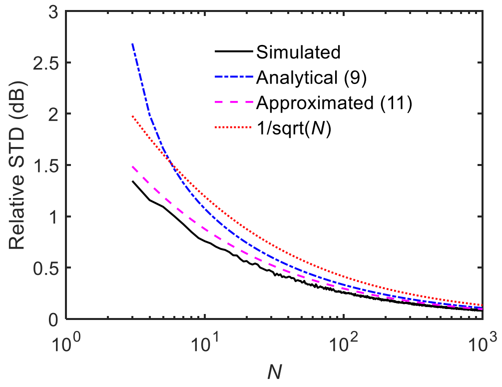

Fig. 2. Simulated, analytical and approximated STDs as functions of *N*. The curve of $1/\sqrt{N}$ is also presented as a reference.

IV. MEASUREMENTS AND RESULTS

Extensive measurements are also performed to verify the derived statistical model in an RC (as shown in Fig. 3). The inner size of the used RC is 1.50 × 1.44 × 0.92 m^3. The RC contains two mechanical stirrers (one vertical and one horizontal) and one platform. Two double-ridged horn antennas (Antennas 1 and 2) are adopted as antennas under test. Antenna 1 is mounted on a trestle with adjustable height and orientation, while Antenna 2 is located in the corner of the RC and oriented to the horizontal stirrer.

Key parameters for assessment of the relative uncertainty of antenna efficiency measured using the two-antenna method are shown in Table 1. Considering that the lowest usable frequency (LUF) of the RC is about 0.87 GHz and the operating frequency range of the two horn antennas is 0.8 GHz - 4.6 GHz, in order to have a better field uniformity and ensure the antennas perform well, the testing frequency range is selected as 2 GHz - 3 GHz (which is the center operating frequency range of the antennas). Another frequency range can be used. Yet the main purpose to experimentally validate the uncertainty model, while the specific frequency range is less important. The platform rotates with 36° per step. At each platform rotation state, two mechanical stirrers rotate with 72° per step simultaneously. It has been verified that these 50 samples are independent to each other [19]. At each stirring state, all the *S*-parameters are sampled and stored by the VNA with a frequency interval of 1 MHz. In order to characterize the statistics of the measured antenna efficiencies, the nine-case assessment method [23]-[24] is adopted here. Specifically, the trestle used to support Antenna 1 is adjusted to three heights, and at each height Antenna 1 is oriented to three directions. To ensure the independence of these nine measurements, the distance between any two adjacent heights is set to 15 cm (which is larger than half-wavelength at the lowest testing frequency) and the selected three orientations are orthogonal to each other.

Once the whole measurement procedure is completed, nine sets of antenna efficiencies can be determined using Eq. (1), and the empirical relative uncertainty can be further calculated. Note that $N = 50$ is known. Therefore, the analytical and approximated relative uncertainties can be directly calculated using Eqs. (9) and (11), respectively.

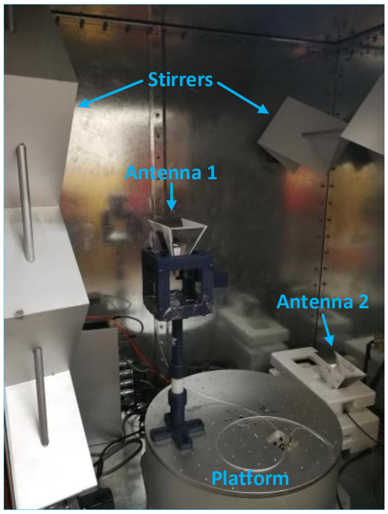

Fig. 3. Photograph of the experimental RC setup for antenna efficiency measurement using the two-antenna method.

Table 1: Key parameters for assessment of the relative uncertainty of antenna efficiency measured using the two-antenna method

Parameter		Value
Frequency range		2 GHz – 3 GHz
Number of frequency points		1001
IF bandwidth	Calibration	100 Hz
	Measurements	1 kHz
VNA output power level		-10 dBm
Stirrer and platform step size ($S \times P$)		72° × 36°
Number of stirring positions		5 × 10
Number of locations of Antenna 1		9

A. Analysis of measurement uncertainty

The empirical, analytical and approximated relative STDs are shown in Fig. 4. Noting that $N = 50$, the analytical and approximated relative STDs are very close to each other. Good agreements between the empirical, analytical and approximated relative STDs can be observed; and the approximated relative STD seems to provide a better estimation. By comparison, there exist obvious discrepancies between $1/\sqrt{N}$ and the empirical STD, which is in accordance with the theoretical analysis.

It should be stressed that both the analytical and approximated relative STDs provide good estimation of the relative STD. Therefore, it is more convenient and efficient to use the approximated STDs in practice. Moreover, the approximated STDs provide a better estimation regardless of *N*.

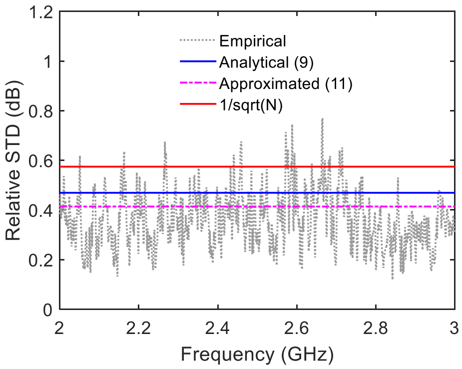

Fig. 4. Empirical, analytical and approximated relative STDs when $N = 50$. The curve of $1/\sqrt{N}$ is also presented as a reference.

B. Hybrid stirring

Multiple stirring techniques are commonly adopted to achieve a better uniformity of the EM field within the RC. Therefore, hybrid stirring is considered here to increase the usability of the statistical uncertainty model.

The coherence bandwidth (B_C) is defined as the frequency shift (Δf) when the magnitude of the complex autocorrelation function ($|\rho(\Delta f)|$) drops from 1 to 0.5 [23]. The complex autocorrelation function can be calculated using:

$$\rho_f(\Delta f) = \frac{\langle S_{21}^*(f) S_{21}(f+\Delta f)\rangle_N}{\langle |S_{21}(f)|^2\rangle_N}, \tag{12}$$

where * denotes the conjugation operator.

It is known that measurements performed at frequencies separated by more than one coherence bandwidth can be treated as independent. Thus, the number of independent frequency samples can be determined by [23]:

$$N_F = \frac{\mathrm{BW}}{\langle B_C \rangle}, \tag{13}$$

where BW is the bandwidth of frequency stirring, $\langle B_C \rangle$ denotes the coherence bandwidth averaged over BW. We have calculated $|\rho_f(\Delta f)|$ over the whole testing bandwidth, and found $\langle B_C \rangle \approx 2.5\ \text{MHz}$.

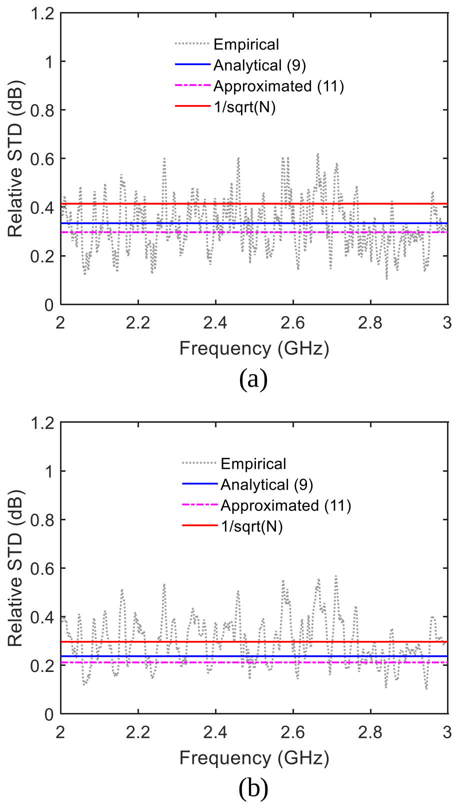

Fig. 5. Empirical and analytical relative STDs with: (a) 5 MHz and (b) 10 MHz frequency stirring when $N = 50$.

Taking N_F into consideration, the number of independent samples should be $N \times N_F$ (where N represents the number of independent mechanical stirring samples). In other words, the parameter N in the statistical uncertainty model should be modified as $N \times N_F$ when frequency stirring is utilized.

For hybrid stirring, frequency stirring with two different bandwidths, i.e., a 5 MHz frequency stirring ($N_F = 2$) and a 10 MHz frequency stirring ($N_F = 4$), are considered. Corresponding empirical and analytical relative STDs are shown in Fig. 5. As expected, all STDs decrease when the frequency stirring bandwidth increases from 5 MHz to 10 MHz. It can be seen that the analytical relative STDs are in accordance with the empirical ones for both frequency stirring situations. Moreover, in accordance with previous findings, $1/\sqrt{N}$ possesses relatively large estimation error. Nevertheless, the statistical model is applicable to not only single mechanical stirring, but also hybrid stirring.

C. Comparisons of three non-reference antenna methods

In order to exhibit a comprehensive and intuitively comparisons of three non-reference antenna methods, more simulations and measurements are performed. For the one- and three-antenna methods, the corresponding relative uncertainties can be easily derived based on the statistical models [19]. Figure 6 (a) shows the analytical relative STDs of three non-reference antenna methods when $N \in [1, 10^3]$. It can be seen that the one-antenna method possesses the lowest uncertainty regardless of N, while the other two methods provide comparable performance. Intuitively speaking, this is easy to understand. Suppose that we are measuring η_1 and all the prerequisites of corresponding methods are satisfied, the analytical uncertainty comes from: S_{11} for one-antenna method, S_{11}, S_{22} and S_{21} for two-antenna method, S_{21}, S_{21} and S_{32} for three-antenna method. Obviously, the one-antenna method is associated with only one random variable, while two- and three-antenna methods are associated with three random variables. However, it is worth stressing that the uncertainty may be different in practical measurements.

Figure 6 (b) shows η_1 measured using three non-reference antenna methods when $N = 50$, corresponding analytical values are also plotted for a convenient comparison. As can be seen, the empirical relative STDs of one- and three-antenna methods show good agreements with the corresponding analytical ones. Meanwhile, the empirical relative STD of two-antenna method is comparable with that of three-antenna method, which is in accordance with analytical analysis. However, the empirical STD of one-antenna method is far larger than the analytical one. This is mainly due to the inconsistence between the measured and assumed e_b [10], [19]. For two-antenna method, the uniformity of e_b may not be well in accordance with assumption, however, the uncertainty of e_b is already considered in the theoretical analysis. As a result, the empirical and analytical STDs show good agreement. Nevertheless, the uncertainty models of two- and three-antenna methods seem to be more stable than that of one-antenna method.

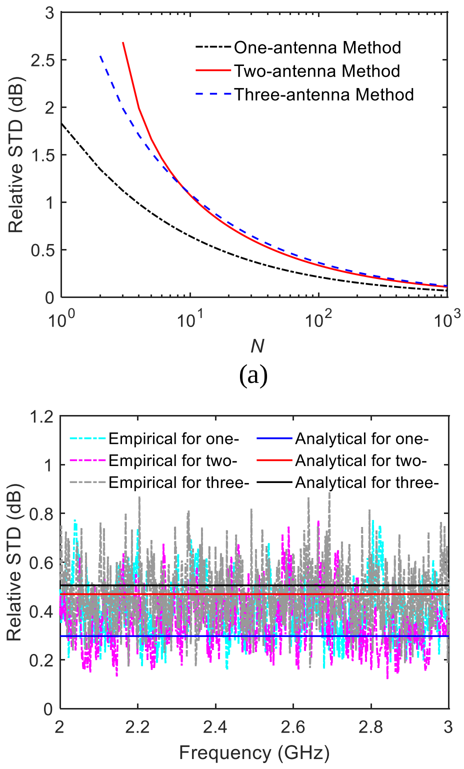

(a)

(b)

Fig. 6. Comparisons of relative STDs of one-, two-, and three-antenna methods: (a) Analytical relative STDs when $N \in [1,10^3]$, and (b) analytical and empirical STDs when $N = 50$.

V. CONCLUSIONS

In this paper, the statistical uncertainty model of the two-antenna method was proposed. Both Monte Carlo simulations and RC measurements were performed to verify the proposed statistical model. Good agreements between the analytical and empirical relative uncertainties were observed. Hybrid stirring was also investigated. Corresponding measurement results were in accordance with the theoretical analysis, indicating that the statistical model could also be applicable to analysis of measurement uncertainty when frequency stirring was adopted. Moreover, it was theoretically and experimentally verified that the approximated relative uncertainty was $1/\sqrt{2N}$ (instead of $1/\sqrt{N}$). In practical measurements, the approximated relative uncertainty is an efficient and convenient way to assess the measurement uncertainty.

ACKNOWLEDGMENT

This work was supported in part by the National Natural Science Foundation of China under Grant 61801366, the Natural Science Foundation of Shaanxi Province under Grant 2020JM-078.

REFERENCES

[1] D. A. Hill, *Electromagnetic Fields in Cavities: Deterministic and Statistical Theories*. Piscataway, NJ, USA, USA: Wiley, 2009.

[2] Q. Xu and Y. Huang, *Anechoic and Reverberation Chambers: Theory, Design and Measurements*. Wiley-IEEE, UK, 2019.

[3] J. C. West and C. F. Bunting, "Effects of frequency stirring on reverberation chamber testing: An analysis as a radiation problem," *IEEE Trans. Electromagn. Compat.*, vol. 61, no. 4, pp. 1345-1352, Aug. 2019.

[4] G. Andrieu and N. Ticaud, "Performance comparison and critical examination of the most popular stirring techniques in reverberation chambers using the 'well-stirred' condition method," *IEEE Trans. Electromagn. Compat.*, vol. 62, no. 1, pp. 3-15, Feb. 2020.

[5] V. Rajamani, C. F. Bunting, and J. C. West, "Stirred-mode operation of reverberation chambers for EMC testing," *IEEE Trans. Instrum. Meas.*, vol. 61, no. 10, pp. 2759-2764, Oct. 2012.

[6] K. A. Remley, C. J. Wang, D. F. Williams, J. J. aan den Toorn, and C. L. Holloway, "A significance test for reverberation-chamber measurement uncertainty in total radiated power of wireless devices," *IEEE Trans. Electromagn. Compat.*, vol. 58, no. 1, pp. 207-219, Feb. 2016.

[7] W. Xue, F. Li, X. Chen, S. Zhu, A. Zhang, and T. Svensson, "A unified approach for uncertainty analyses for total radiated power and total isotropic sensitivity measurements in reverberation chamber," *IEEE Trans. Instrum. Meas.*, vol. 70, pp. 1-12, Nov. 2020.

[8] M. Á. García-Fernández, J. D. Sánchez-Heredia, A. M. Martínez-González, D. A. Sánchez-Hernández, and J. F. Valenzuela-Valdés, "Advances in mode-stirred reverberation chambers for wireless communication performance evaluation," *IEEE Commun. Mag.*, vol. 49, no. 7, pp. 140-147, July 2011.

[9] X. Chen, W. Xue, H. Shi, J. Yi, and W. E. I. Sha, "Orbital angular momentum multiplexing in highly

reverberant environments,” *IEEE Microw. Wireless Compon. Lett.*, vol. 30, no. 1, pp. 112-115, Jan. 2020.

[10] C. L. Holloway, H. A. Shah, R. J. Pirkl, W. F. Young, D. A. Hill, and J. Ladbury, “Reverberation chamber techniques for determining the radiation and total efficiency of antennas,” *IEEE Trans. Antennas Propag.*, vol. 60, no. 4, pp. 1758-1770, Apr. 2012.

[11] D. Senic, D. F. Williams, K. A. Remley, C.-M. Wang, C. L. Holloway, Z. Yang, and K. F. Warnick, “Improved antenna efficiency measurement uncertainty in a reverberation chamber at millimeter-wave frequencies,” *IEEE Trans. Antennas Propag.*, vol. 65, no. 8, pp. 4209-4219, Aug. 2017.

[12] A. Gifuni, I. D. Flintoft, S. J. Bale, G. C. R. Melia, and A. C. Marvin, “A theory of alternative methods for measurements of absorption cross section and antenna radiation efficiency using nested and contiguous reverberation chambers,” *IEEE Trans. Electromagn. Compat.*, vol. 58, no. 3, pp. 678-685, June 2016.

[13] G. Le Fur, P. Besnier, and A. Sharaiha, “Time reversal efficiency measurement in reverberation chamber,” *IEEE Trans. Antennas Propag.*, vol. 60, no. 6, pp. 2921-2928, June 2012.

[14] A. Cozza and Abd el-Bassir Abou el-Aileh, “Accurate radiation-pattern measurements in a time-reversal electromagnetic chamber,” *IEEE Antennas Propag. Mag.*, vol. 52, no. 2, pp. 186-193, Apr. 2010.

[15] V. Fiumara, A. Fusco, V. Matta, and I. M. Pinto, “Free-space antenna field/pattern retrieval in reverberation environments,” *IEEE Antennas and Wireless Propag. Lett.*, vol. 4, pp. 329-332, Sep. 2005.

[16] Q. Xu, Y. Huang, L. Xing, C. Song, Z. Tian, S. S. Alja’afreh, and M. Stanley, “3-D antenna radiation pattern reconstruction in a reverberation chamber using spherical wave decomposition,” *IEEE Trans. Antennas Propag.*, vol. 65, no. 4, pp. 1728-1739, Apr. 2017.

[17] P.-S. Kildal and K. Rosengren, “Electromagnetic analysis of effective and apparent diversity gain of two parallel dipoles,” *IEEE Antennas and Wireless Propag. Lett.*, vol. 2, pp. 9-13, 2003.

[18] X. Chen, “On statistics of the measured antenna efficiency in a reverberation chamber,” *IEEE Trans. Antennas Propag.*, vol. 61, no. 11, pp. 5417-5424, Nov. 2013.

[19] W. Xue, X. Chen, M. Zhang, L. Zhao, A. Zhang, and Y. Huang, “Statistical analysis of antenna efficiency measurements with non-reference antenna methods in a reverberation chamber,” *IEEE Access*, vol. 8, pp. 113967-113980, June 2020.

[20] Q. Xu, L. Xing, Z. Tian, Y. Zhao, X. Chen, L. Shi, and Y. Huang, “Statistical distribution of the enhanced backscatter coefficient in reverberation chamber,” *IEEE Trans. Antennas Propag.*, vol. 66, no. 4, pp. 2161-2164, Apr. 2018.

[21] M. Abramowitz and I. A. Stegun, *Handbook of Mathematical Functions with Formulas, Graphs, and Mathematical Tables*. New York, NY, USA: Dover, 1972.

[22] B. N. Taylor and C. E. Kuyatt, “Guidelines for Evaluating and Expressing the Uncertainty of NIST Measurement Results,” Gaithersburg, MD, USA: National Institute of Standards and Technology, 1994.

[23] P.-S. Kildal, X. Chen, C. Orlenius, M. Franzen, and C. S. L. Patane, “Characterization of reverberation chambers for OTA measurements of wireless devices: Physical formulations of channel matrix and new uncertainty formula,” *IEEE Trans. Antennas Propag.*, vol. 60, no. 8, pp. 3875-3891, Aug. 2012.

[24] K. A. Remley, J. Dortmans, C. Weldon, R. D. Horansky, T. B. Meurs, C.-M. Wang, D. F. Williams, C. L. Holloway, and P. F. Wilson, “Configuring and verifying reverberation chambers for testing cellular wireless devices,” *IEEE Trans. Electromagn. Compat.*, vol. 58, no. 3, pp. 661-672, June 2016.

Compact Octa-band Bandpass Filter based on Controllable Transmission Zeros with Wide Upper Stopband

Qian Yang, Shuangyang Liu, Kai-Da Xu, and Anxue Zhang

School of Information and Communications Engineering
Xi'an Jiaotong University, Xi'an, Shaanxi 710049, China
yangqiandianxin@mail.xjtu.edu.cn, lsy6820@stu.xjtu.edu.cn, kaidaxu@ieee.org, anxuezhang@mail.xjtu.edu.cn

***Abstract* ─** A novel synthesis method is proposed to design multi-band bandpass filters (BPFs) using an L-C ladder prototype lowpass filter loaded with two symmetric shorted stubs. The transmission zeros (TZs) are produced by the shorted stubs, which are used to realize multiple passbands. By controlling the number of the open stubs loaded on the shorted stub, the number of TZs is exactly determined. Therefore, multi-band BPF is easy to be obtained by increasing the number of the open stubs. The TZs can be adjusted by optimizing the L-C values of the equivalent circuit of the proposed filter to tune the center frequencies of each passband independently. The proposed BPF also has wide upper stopband. For demonstration, an octa-band BPF is designed and manufactured. The measured results show good agreement with the simulated ones.

***Index Terms* ─** Bandpass filters, multi-band, octa-band, transmission zeros, wide upper stopband.

I. INTRODUCTION

With the rapid development of modern communication system, multi-band microwave bandpass filters (BPFs) have gained increasing attentions [1–14]. In order to obtain multiple passbands, multiple single-passband resonators are coupled in parallel with large size [1]. In [2–6], multi-mode resonators (MMRs) have been used to reduce the size. The MMRs use the configuration of stepped-impedance resonator (SIR) or short/open-circuited stubs loaded SIR. Therefore, when the BPF has more passbands, the MMRs have complex structures to excite multiple resonant modes. Another widely used method for designing multi-band BPFs is to synthesize transmission poles (TPs) in passband and transmission zeros (TZs) in stopband or introduce signal-interference to form multiple passbands [7-16]. A tri-notch-band is introduced into a ring-stub multimode resonator to realize multi-band BPF [7]. When the number of the passband grows, more layers of the vertically expendable low-temperature cofired ceramic structure are needed, which increases the fabrication complexity [8]. The tunable TZs in [9-14] can divide one passband into multiple passbands with center frequency and bandwidth adjusting easily. However, the coupling matrix between the resonators are complicated when the number of passband is increased. The in-series cascade of different reflective-type transversal filtering sections shaped by two in-parallel unequal length transmission line segments are proposed in [15], the structure has a large size when the number of passband increases.

Furthermore, in order to realize wide upper stopband performance, bandstop filters are usually cascaded with BPFs to suppress the spurious response, which are harmful to communication systems [16,17]. Meanwhile, open/shorted coupled lines and transversal signal-interaction concepts are usually adopted to improve the stopband performances [18,19]. However, the sizes are increased and the structures are complicated. Recently, the SIRs in [20,21] with different impedance ratios are presented with compact sizes.

This paper presents a novel synthesis method for designing multiple passbands BPFs by using controllable TZs. Following our early work [22], the theoretical analysis of the TZs and the transmission poles (TPs) is shown in this paper for designing BPF with more passbands. With more degrees of the middle L-C section, more TPs can be positioned in the passbands, which can realized wide passbands. Furthermore, the upper stopband have been also extended with more degrees of middle L-C section. Since the TZs can be independently controlled, the center frequencies (CFs) of each passband can also be independently controlled. However, the bandwidth of each passband cannot be tuned independently. The proposed method for designing multi-band BPF is simple and effective. Due to the filter structure loaded with shorted stubs, the proposed BPF has a wide upper stopband. For demonstration, an octa-band BPF has been designed and fabricated to verify the proposed concept.

II. SYNTHESIS ANALYZE

The proposed multi-band BPF network is shown in Fig. 1. The transmission network can be divided into three sub-networks, which is symmetrical. The middle

Submitted On: May 21, 2021
Accepted On: July 19, 2021

https://doi.org/10.47037/2021.ACES.J.360906

section is formed by a lowpass filter (LPF), the equivalent circuit of which is shown in Fig. 2. The middle section consists of five-order LPF. The shunt admittance section is composed of a short-circuited stub loaded with eight open stubs, which is shown in Fig. 3. The equivalent circuit of the shunt stub is shown in Fig. 4, where the loaded open stubs can be equivalent to capacitors and the separated short transmission lines with high characteristic impedance Z_1 can be equivalent to inductors.

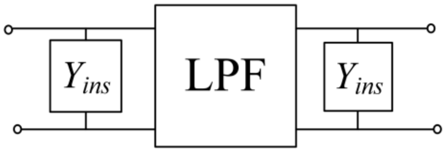

Fig. 1. The proposed multi-band BPF network.

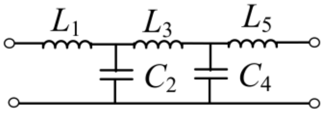

Fig. 2. The equivalent circuit of the middle LPF section.

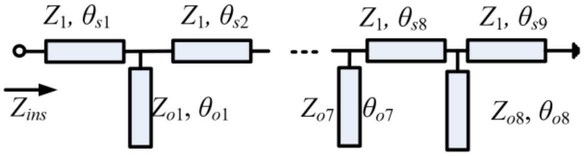

Fig. 3. The shunt admittance section composed by a short-circuited stub loaded with eight open stubs.

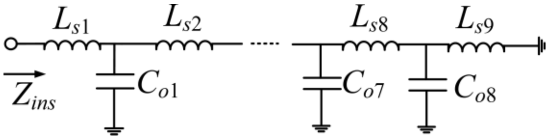

Fig. 4. The equivalent circuit of the parallel stub.

The shunt impedance Z_{ins} can be expressed by the lumped elements in Fig. 4 as follows:

$$Z_{ins}(s)=\frac{a_{17}s^{17}+a_{15}s^{15}+\cdots+a_5s^5+a_3s^3+a_1s}{b_{16}s^{16}+b_{14}s^{14}+\cdots+b_4s^4+b_2s^2+b_0}, \qquad (1)$$

where a_i and b_i (i = 0, 1, … , 16) are the constant coefficients, s = jω is the radius frequency variable. The coefficients of the numerator and denominator polynomials of equation (1) are all positive real numbers, which can be calculated by the positive L-C values in Fig. 4. The degree of the numerator is 17, which is the number of all the L-C elements. The number can be calculated by the number of the loaded open stubs n, $2n + 1 = 17$, where $n = 8$. Meanwhile, the numerator polynomial only has odd degree terms.

When the shunt impedance Z_{ins} equals to zero, it introduces short-circuiting effect between the input and output ports, which produces TZs in the frequency response. Therefore, the TZs can be determined by the parameters of the shunt stub. The number of the TZs are the same as that of the numerator degree. Since the numerator polynomial only has odd degree terms, one of the TZs is located at the zero frequency, which is also the direct-current (DC) frequency, and the other sixteen TZs are conjugated and positioned on the frequency axis. As a result, the shunt stub inserts 9 TZs into the LPF positive frequency response and realizes eight passband.

The TPs can be calculated by the approach in [22]. Due to the symmetry of the proposed filter structure, the LPF section parameters are also symmetrical, where $C_4 = C_2$ and $L_5 = L_1$. The TPs can be calculated by the transmission matrix cascaded by the three section in Fig. 1. The degree of the polynomial is the sum of the degree of the two shunt stubs and the degree of the LPF section, which is $2(2n+1) + 5 = 4n+7$. From the analysis in [22], the polynomial has one root at origin, two symmetric real roots, and the remaining $4n + 4$ roots are conjugate and symmetrical on the imaginary axis or in four quadrants. Therefore, the BPF has $2n + 2$ TPs at most.

Since the equations for the calculation of TZs and TPs are nonlinear, the optimization algorithm is adapted to calculate the L-C values for design octa-band BPF. Differential evolution algorithm is used in this paper. The optimization goal consists of the positions of TZs and the return losses of each passband, which are set to be larger than 10 dB for easy implementation. After obtaining the L-C values, the electrical length of the open stub θ_{oi} and the electrical length θ_{si} in Fig. 4 are calculated at the center frequency of the first and last passband $f_0 = (f_{01} + f_{08})/2$, where f_{01} and f_{08} are the CFs of the first and eighth passband [23]:

$$\theta_{si}=\arcsin\left(\frac{2\pi f_0 L_{oi}}{Z_1}\right), \qquad (2)$$

$$\theta_{oi}=\arctan\left[Z_{oi}2\pi f_0 C_{oi}-\frac{Z_{oi}}{Z_1}\tan\left(\frac{\theta_{si}}{2}\right)-\frac{Z_{oi}}{Z_1}\tan\left(\frac{\theta_{s,i+1}}{2}\right)\right]. \qquad (3)$$

The design guidelines can be described as follows.

1. Due to the specifications of the octa-band, the TZs are determined by the locations of the CFs and the bandwidths, which are positioned nearly at the center of the two adjacent CFs.

2. The values of all L-C elements are optimized by satisfying the return losses (RLs) in each passband.

3. After the equivalent circuit calculation, the physical parameters of the microstrip transmission lines are firstly determined by the equivalent L-C values, and finally optimized by the electromagnetic simulation software HFSS.

III. OCTA-BAND BPF DESIGN

An octa-band BPF is designed to demonstrate the design method. The CFs of the octa-passband are 0.6, 1.6, 2.6, 3.4, 4.0, 4.6, 5.0 and 5.9GHz, respectively. Therefore, the TZs are preset as 0, 0.98, 1.97, 2.81, 3.74, 4.46, 4.99, 5.45, and 7GHz. The optimized L-C values are: L_{S1} = 0.9981, L_{S2} = 3.2471, L_{S3} = 2.6099, L_{S4} = 3.3404, L_{S5} = 2.6263, L_{S6} = 2.6421, L_{S7} = 2.9019, L_{S8} = 2.9040, L_{S9} = 3.512, L_1 = 2.5879, L_3 = 3.8654 (unit in nH), C_{O1} =0.6963, C_{O2} = 1.0725, C_{O3} = 1.1104, C_{O4} = 1.1445, C_{O5} = 1.2021, C_{O6} = 1.1491, C_{O7} = 1.3274, C_{O8} = 1.3596, C_2 = 0.6755 (unit in pF). The TZs and TPs are drawn in Fig. 5. The radian frequency variable s is calculated in unit GHz with facility.

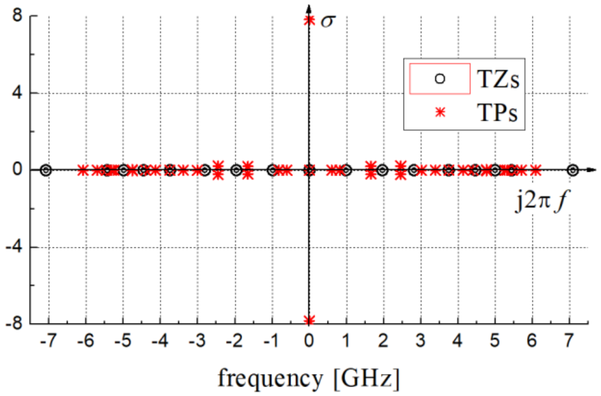

Fig. 5. The calculated TZs and TPs by the equivalent L-C circuit.

All TZs are symmetrical and double values. The $4n+7$ roots related to TPs are conjugate and symmetrical on the axis or in four quadrants, which are consistent with the theoretical analysis in Section II. Three of the roots are real numbers, one of which is at the origin. The remained $4n+4$ roots are distributed symmetrically beside the y axis. Therefore, each passband could have 2 TPs as shown in Fig. 5, and there are still 2 ($(4n+4)/2-2n = 2$, where $n = 8$) roots that can be located freely. One of the remained 2 roots in Fig. 5 is positioned in the eighth passband, while the other one coincides with the fourth TZ.

From Fig. 5, the roots related to TPs in the second and third passbands are two conjugate roots. The related S-parameters calculated by the optimized L-C values are shown in Fig. 6. Therefore, the second and third passbands do not have two TPs as shown in Fig. 6. The eighth passband has three TPs in Fig. 6 as described in Fig. 5. The frequency response in the negative region is not drawn, which is symmetrical to that of the positive region.

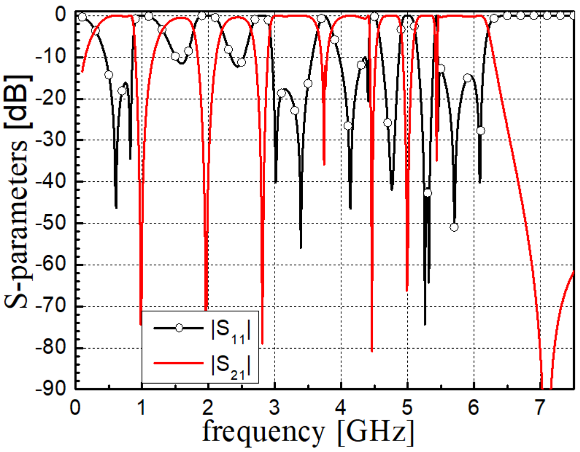

Fig. 6. The calculated S-parameters by optimized L-C values.

IV. EXPERIMENTAL RESULTS

The BPF is simulated and fabricated on a substrate with ε_r = 2.65, tanδ = 0.003, and h = 1 mm. Here we choose 117.8 Ω high-impedance line and 50 Ω low-impedance line, which have the line-width of 0.5 and 2.73 mm, respectively. All the lumped element values are represented by microstrip distributed elements using some equations in [23] at frequency $(f_{01} + f_{08})/2$, where f_{01} and f_{08} are the CFs of the first and eighth passbands, respectively. The configuration of the proposed BPF is shown in Fig. 7. The small part between the two ports is the lowpass filter section as shown in Fig. 1. The two symmetrical shorted stubs are connected to the input and output ports, respectively. The configuration is arranged as a circle to share the same grounded via hole. As shown in Fig. 7, the line width of the open stub which acts as a capacitor is tapered. The characteristic impedance is calculated by the waist width of the taper. Due to the discontinuity of the microstrip line and the minor coupling between the open stubs, the final dimension parameters are optimized by the full-wave electromagnetic simulation software HFSS. The circuit size is about $0.12\,\lambda_g \times 0.12\,\lambda_g$, where λ_g is the guided wavelength at f_{01}.

Figure 8 shows the simulated and measured S-parameters. The wideband response view and the photograph of the designed filter are shown in Fig. 9 and Fig. 10, respectively. The measured results are in good agreement with the simulated ones. The discrepancies between the simulated results and the measured results may be due to the ignorance of transmission line discontinuity and fabrication tolerances. The measured CFs, fractional bandwidths (FBWs), insertion losses (ILs), and out-band suppressions (OBSs) are listed in Table 1. As shown in Table 1, the proposed octa-band

BPF with simple circuit topology has advantages such as low IL, wide FBW, and wide upper stopband.

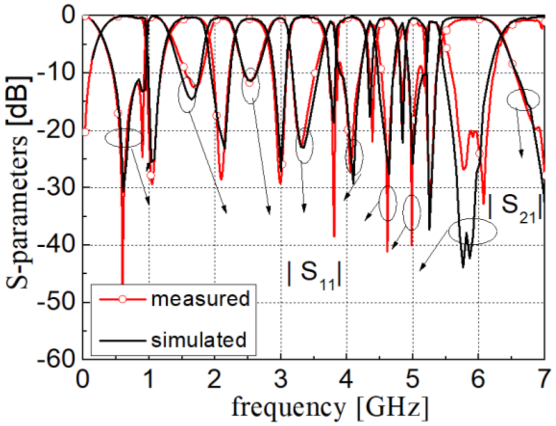

Fig. 8. The passband response view of the designed octa-band BPF.

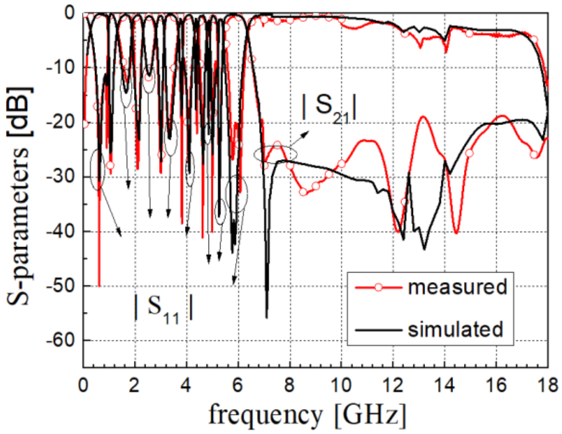

Fig. 9. The wideband response view of the fabricated filter.

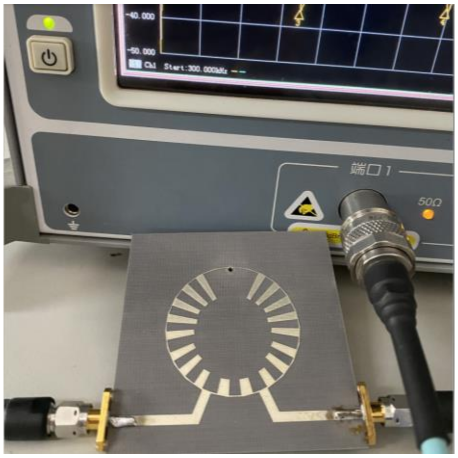

Fig. 10. The fabricated octa-band BPF photograph.

Table 1: Comparisons of proposed filter with related works

Ref.	CF (GHz)/ FBW (%)	IL (dB)	OBS	Size $(\lambda_g \times \lambda_g)$
[1]	0.8/2.3, 1.2/2.9, 1.4/3.3, 1.8/3.2, 2.2/2, 2.5/2	2.9, 2.3, 2.6, 2.2, 2.7, 2.6	--	0.76 × 0.06
[2]	0.63/29.7, 1.34/8.5, 2.03/2.7, 2.73/5.4, 3.44/6.25, 3.99/9	0.5, 1.3, 1.9, 1.4, 1.2, 1.1	$1.2\ f_{06}$, >10dB	0.013 × 0.055
[3]	0.63/28.5, 1.2/10, 1.8/13.6, 2.5/4.8, 3.46/4.2	0.4, 0.9, 1.1, 2, 2.55	$1.1\ f_{05}$, >10dB	0.12 × 0.18
[4]	0.7/10.2, 2/13.2, 3.2/11.3, 4.5/8.1, 5.8/8.2, 7/4.3	1.3, 0.6, 0.8, 1.1, 1.4, 2.2	$1.5\ f_{06}$, >15dB	0.16 × 0.09
This work	0.6/115.2, 1.6/37.5, 2.55/19.6, 3.4/14.4, 4.1/10.3, 4.6/6.7, 5/4.9, 5.9/14.4	0.1, 0.3, 0.6, 0.3, 0.4, 0.6, 0.5, 0.3	$3.1\ f_{08}$, >19dB	0.12 × 0.12

V. CONCLUSION

An octa-band BPF is designed by the method of independently controlling TZs. By optimizing the equivalent circuit lumped elements value, the center frequencies of the octa-passband can be controlled flexibly, making the filter obtain wide passband and wide upper stopband performances. With simple filter structure and good performance, the proposed method is attractive for designing more multi-passband BPFs to apply in modern high data-rate system.

ACKNOWLEDGMENT

This work was supported in part by the National Natural Science Foundation of China under Grant 61801367, and in part by the China Postdoctoral Science Foundation under Grant 2018M631162.

REFERENCES

[1] W.-H. Tu, and K.-W. Hsu, "Design of sext-band bandpass filter and sext-taplexer using semilumped resonators for system in a package," *IEEE Trans. Compon. Packag. Manuf. Technol.*, vol. 5, no. 2, pp. 265-273, Feb. 2015.

[2] J. Xu, W. Wu, and G Wei, "Compact multi-band bandpass filters with mixed electric and magnetic coupling using multiple-mode resonator," *IEEE Trans. Microw. Theory Tech.*, vol. 63, no. 12, pp. 3909-3919, Dec. 2015.

[3] C. Zhu, J. Xu, W. Kang, and W. Wu, "Compact QB-BPF based on single PMR," *Electron. Lett.*, vol. 52, no. 17, pp. 1463-1465, Aug. 2016.

[4] J. Ai, Y. Zhang, K.-D. Xu, Y. Guo, and Q.-H. Liu, "Compact sext-band bandpass filter based on single multimode resonator with high band-to-band isolations," *Electron. Lett.*, vol. 52, no. 9, pp. 729-731, Apr. 2016.

[5] P. Ma, B. Wei, J. Hong, Z. Xu, X. Guo, B. Cao, and L. Jiang, "A design method of multimode multiband bandpass filters," *IEEE Trans. Microw. Theory Tech.*, vol. 66, no. 6, pp. 2791-2799, June 2018.

[6] T. Firmansyah, M. Alaydrus, Y. Wahyu, E. T. Rahardjo, and G. Wibisono, "A highly independent multiband bandpass filter using a multi-coupled line stub-SIR with folding structure," *IEEE Access*, vol. 8, pp. 83009-83026, May 2020.

[7] Y. Li, W. Li, C. Liu, and Q. Ye, "A compact UWB band-pass filter with ultra-narrow tri-notch-band characteristic," *Applied Computational Electromagnetics Society* (*ACES) Journal*, vol. 29, no. 2, pp. 170-177, Feb. 2014.

[8] Y.-C. Lin, T.-S. Horng, and H.-H. Huang, "Synthesizing a multiband LTCC bandpass filter with specified transmission- and refection-zero frequencies," *IEEE Trans. Microw. Theory Tech.*, vol. 62, no. 12, pp. 3351-3361, Dec. 2014.

[9] D. Psychogiou, R. Gómez-García, and D. Peroulis, "Fully adaptive multiband bandstop filtering sections and their application to multifunctional components," *IEEE Trans. Microw. Theory Tech.*, vol. 64, no. 12, pp. 4405-4418, Dec. 2016.

[10] R. Gómez-García, A. C. Guyette, D. Psychogiou, E. J. Naglich, and D. Peroulis, "Quasi-elliptic multi-band filters with center frequency and bandwidth tunability," *IEEE Microw. Wireless Compon. Lett.*, vol. 26, no. 3, pp. 192-194, Mar. 2016.

[11] D. Psychogiou, R. Gómez-García, and D. Peroulis, "RF wide-band bandpss filter with dynamic in-band multi-interference suppression capability," *IEEE Trans. Circuits and Systems-II: Express Briefs*, vol. 65, no. 7, pp. 898-902, July 2018.

[12] R. Gómez-García, J.-M. Muñoz-Ferreras, and D. Peroulis, "High-order input-reflectionless bandpass/ bandstop filters and multiplexers," *IEEE Trans. Microw. Theory Tech.*, vol. 67, no. 9, pp. 3683-3695, Sep. 2019.

[13] D. J. Simpson, R. Gómez-García, and D. Psychogiou, "Single-/multi-band bandpass filters and duplexers with fully reconfigurable transfer-function characteristics," *IEEE Trans. Microw. Theory Tech.*, vol. 67, no. 5, pp. 1854-1869, May 2019.

[14] R. Gómez-García, L, Yang, and J.-M. Muñoz-Ferreras, "Low-refection signal-interference single- and multipassband filters with shunted lossy stubs," *IEEE Microw. Wireless Compon. Lett.*, vol. 30, no. 4, pp. 355-358, Apr. 2020.

[15] E. Musonda, R. A. Paradkar, I. C. Hunter, and R. Parry, "Synthesis of multiband filters by linear optimization," *IEEE Trans. Microw. Theory Tech.*, vol. 67, no. 12, pp. 4764-4772, Dec. 2019.

[16] C.-W. Tang and M.-G. Chen, "A microstrip ultra-wideband bandpass filter with cascaded broadband bandpass and bandstop filters," *IEEE Trans Microw. Theory Tech.*, vol. 55, no. 11, pp. 2412-2418, Nov. 2007.

[17] H. W. Wu, M. H. Weng, Y. K. Su, C. Y. Hung, and R. Y. Yang, "Spurious suppression of a dual-mode bandpass filter using simple C-shaped electro-magnetic bandgap cells," *Microw. Opt. Technol. Lett.*, vol. 48, no. 10, pp. 2090-2093, Oct. 2006.

[18] W. Feng, M. Hong, and W. Che, "Narrow-band bandpass filters with improved upper stopband using open/shorted coupled lines," *Applied Computational Electromagnetics Society* (*ACES) Journal*, vol. 31, no. 2, pp. 152-158, Feb. 2016.

[19] R. Yin, W. Feng, and W. Che, "High selectivity dual-band bandpass filters using dual-mode resonators," *Applied Computational Electromagnetics Society* (*ACES) Journal*, vol. 32, no. 9, pp. 800-805, Sep. 2017.

[20] S. Jun and K. Chang, "Second harmonic suppression bandpass filter using nonuniform open stubs," *Microw. Opt. Technol. Lett.*, vol. 55, no.7, pp. 1451-1453, July 2013.

[21] J. Marimuthu, A. M. Abbosh, and B. Henin, "Bandpass filter with wide stopband using loaded short-section of parallel-coupled lines," *Microw. Opt. Technol. Lett.*, vol. 57, no. 12, pp. 2824-2829, Dec. 2015.

[22] Q. Yang, Y.-C. Jiao, and Z. Zhang, "Dual-wideband BPF with wide upper stopband using shorted stepped-impedance stub-loaded lowpass filter," *Electon. Lett.*, vol. 52, no. 19, pp. 1615-1616, Sep. 2016.

[23] J.-S. Hong and M. J. Lancaster, *Microstrip Filters for RF/Microwave Applications*, Wiley, New York, NY, 2001.

A Low-Profile Hybrid-Fed Dual-Polarized Antenna with High Isolation and High Cross-Polar Discrimination

M. Ciydem [1] and E. A. Miran [2]

[1] Dept. of Electrical and Electronics Engineering, Faculty of Engineering
Gazi University, 06570 Maltepe, Ankara, Turkey
mehmetciydem@gazi.edu.tr

[2] Dept. of Electrical and Electronics Engineering, Middle East Technical University, 06520 Balgat, Ankara, Turkey
alpmiran@gmail.com

Abstract **─** This work presents a wideband hybrid-fed ±45º linear dual-polarized patch antenna design for sub-6 GHz 5G base stations. Two polarizations are created by a slot-coupling with rectangular H-slot (+45°) and a capacitive coupling with modified L-probe (–45°). Antenna exhibits wideband −10 dB impedance bandwidths of 40.7% and 35.6% for slot-fed and probe-fed ports, respectively. Due to the special design of suspended stacked patches with hybrid-fed excitations, high port isolation (< –47 dB) and high cross-polar discrimination (> 38 dB) are achieved. Symmetric and directional radiation patterns with stable gain are obtained in E and H planes for each polarization. Compared to its bandwidth, antenna is low-profile (10.6 mm) with front-to-back ratio greater than 22 dB. Simulations and experimental results are reported and discussed.

Index Terms **─** 5G base station, cross-polar discrimination, dual-polarization, hybrid feeds, isolation, low-profile, massive MIMO, sub-6 GHz, wideband patch antenna.

I. INTRODUCTION

Dual-polarization (±45° or Vertical/Horizontal (V/H)) is commonly employed in base station antennas since it helps to fight against multipath and increase in capacity by polarization diversity [1-2]. Moreover, today's base station antennas require wide impedance bandwidth (IBW), good matching level ($|S_{11}|$, $|S_{22}| < -15$ dB), high port isolation ($|S_{21}| < -20$ dB), high front to back ratio (FBR > 20 dB), and high cross-polar discrimination (XPD > 15 dB within ± 30° of boresight). Hence it is not easy to meet all these requirements simultaneously in the same design. With the advent of 5G technology, massive multiple-input multiple-output (mMIMO) has been one the key enabling technologies to reach the goals of 5G. High isolation and high XPD are more desirable in mMIMO array than in conventional (2G/3G/4G-LTE) base station antennas to make full use of it, especially for low envelope correlation coefficient (ECC) [3]. In space-limited applications such as mMIMO arrays with huge number of antenna elements, compactness and low-profile of the antenna are also preferable. Therefore, design of a dual-polarized antenna element with high isolation and high XPD satisfying all above requirements facilitates mMIMO array to reach desired performance since it is a building element of that array.

Crossed-dipoles [2,4,5] and patch antennas [5-14] are used in base stations in dual polarization configuration with a pair of feeds. Crossed-dipole antennas are good in terms of wide IBW, high isolation and high XPD. However, they have complex feeding structure with balun and high profile. Moreover, they are not easy to be integrated with planar circuit elements for mMIMO applications. Patch antennas can be preferred in mMIMO arrays owing to their compactness, low-profile, and lightweight. However, they have suffered from narrowband operation, and many efforts on different feeding techniques [5-14] have been developed to improve their performance.

In dual-polarized patch antennas, feeds excite the patch and creates desired fundamental modes and undesired higher order modes. Currents of flowing on the feeds-ground plane whose interactions with patch and with each other are the main factors determining the isolation and XPD. Hence, feeding structures and feed types play an important role in the design. A variety of techniques [3, 15-23] for high isolation and high XPD have been developed for patch antennas. For the same type of feeds (slot-slot, probe-probe), differential feeding [3,15,16], which utilizes 180° phase difference between feeds to suppress higher order modes, helps to improve isolation and XPD. However, differential feeding may bring complexity in feeding network and sometimes difficulty in obtaining wide IBW. Moreover, in slot-slot configuration, an additional reflector plate which increases antenna profile, may be required to reduce back

Submitted On: April 20, 2021
Accepted On: July 25, 2021

https://doi.org/10.47037/2021.ACES.J.360907

radiation of slots for high FBR. But the ground plane and reflector plate may form a waveguide and some modes may propagate inside this causing again deterioration of isolation and XPD. Then hybrid feeds (slot-probe) may be employed as a solution for high isolation and high XPD since probe feed (capacitively coupled) has almost no coupling current on the ground plane and hence coupling and cross polarization between slot-probe will be eliminated on the ground plane. Furthermore, the mechanism for tuning and radiation of hybrid-fed antenna will be totally different for slot-fed and probe-fed ports, and this property may be used as an advantage for high isolation and high XPD. On the other hand, this brings difficulties in achieving separate designs which satisfy all performance requirements for each feed (polarization) utilizing the same radiating patches of hybrid-fed antenna.

In literature, several dual-polarized hybrid-fed patch antenna designs [17-23] have been reported. Two hybrid-fed designs with slot-probe feeds are proposed in [17,18] achieving high isolation and high XPD but they operate in 2.2-2.6 GHz with 14% IBW. [19] presents a circular patch antenna with conical (omni) and broadside modes using hybrid feed network of H-slot and probe feeds. The goal of [19] is to have different characteristics (radiation pattern, gain, S-parameters) in each polarization and to utilize them as multifunction and diversity antennas. However, this is not the case for 5G mMIMO arrays which require similar characteristics and performance for both polarizations in order to achieve low ECC [3]. In [20], a hybrid-fed dual-polarized patch antenna has been introduced but it is very narrow band. Moreover, its isolation and XPD levels are not satisfactory. [21] implements hybrid-fed antenna with a pair of hook shaped probes with 180° phase difference for one polarization and magnetic-coupled metallic loop for the other polarization. Its performance is good in many aspects but does not cover sub-6 GHz 5G spectrum (3.3-3.8 GHz) completely. In [22], a balanced-probe feed and a slot feed is implemented for V/H polarizations for meteorological radar which requires high isolation and high XPD. Another novel hybrid-fed patch antenna with electric-coupled and magnetic coupled feeds has been reported in [23]. Recently, a meta-material based decoupling structure in X-band for high isolation has also been introduced in [24]. Performance summary and comparison of similar works are given in Table 1.

To the best of authors' knowledge, hybrid-fed patch antenna design for sub-6 GHz 5G applications has not been investigated sufficiently yet. Therefore, this study deals with design of a low profile, wideband, dual-polarized hybrid-fed patch antenna with high isolation and high XPD. Although it is intended to operate in 3.3-3.8 GHz, slot feed (port-1) and probe feed (port-2) exhibits much more wider IBW. Proposed antenna provides similar s-parameter performance, gain and broadside radiation patterns in principal planes for both polarizations. The antenna can also be assumed to be low-profile (10.6 mm) with its IBW and operating band when compared to similar works in Table 1.

Table 1: Comparison of related works (NG: Not Given)

Ref.	Antenna and Feed Type	IBW (GHz, %)	Matching $|S_{11}|$, $|S_{22}|$ (dB)	Isolation $|S_{21}|$ (dB)	FBR (dB)	XPD (dB)	Dimensions (mm)
[3]	Crossed dipole- differential feeding	3.23-5.27, 48%	<−10	< −55	>22	>35	90x90x19.5
[15]	Patch-differential feeding	1.84-2.73, 38.7%	<−10	<−40	>12	>24	105x105x19.6
[16]	Patch-differential feeding	3.16-3.74, 17.2%	<−10	<−38.5	>18	>33	80x80x5.8
[17]	Patch-hybrid fed (slot/probe coupled)	1.64-1.88, 13.6% 1.57-2.02, 25%	<−10	<−32	NG	>27	100x100x14.4
[18]	Patch-hybrid feeding (slot/probe coupled)	2.27-2.62, 14.2% 2.24-2.6, 14.5%	<−10	<−40	>12	>35	150x150x13.1
[19]	Patch-hybrid feeding (slot/probe coupled)	2.16-2.72, 23% 2.14-2.64, 20.5%	<−10	<−40	>12	>21	100x100x10.5
[20]	Patch-hybrid feeding (slot/probe coupled)	2.36-2.38, 0.94% 2.35-2.38, 1.33%	<−15	<−24	>15	>15	80x80x1.5
[21]	Patch-hybrid feeding (probe/magnetic coupled)	2.45-3.7, 40.7% 2.6-3.85, 38.7%	<−10	<−40	>20	>30	100x100x17
[22]	Patch-hybrid feeding (slot/probe coupled)	2.58-2.91, 12% 2.51-2.9, 14.4%	<−10	<−43	>25	>32	60x60x7.8
[23]	Patch-hybrid feeding (electric/magnetic coupled)	1.63-2.78, 52% 1.68-2.72, 47.3%	<−10	<–26.5	>16	>23	170x170x25.3
Pro.	Patch-hybrid feeding (slot/probe coupled)	2.95-4.46, 40.7% 3.2-4.59, 35.6%	<−10	<−47	>22	>38	110x110x10.6

II. ANTENNA DESIGN

A. Geometry and configuration

Figure 1 displays structure of the proposed antenna while Table 2 provides its physical parameters and dimensions. The antenna is comprised of a feedline substrate and two square patches (main and parasitic patch), all separated by air. Suspended stacked patches are adopted to have wide IBW. Dual-polarization (±45º) is implemented in hybrid configuration by a slot feed (port-1) and a probe feed (port-2) as shown in Figs. 1-3. Capacitive coupling is realized by a modified L-probe and slot coupling is carried out by a rectangular H-slot. Substrate for the feedline is FR4 ($\varepsilon_r = 4.4$, $\tan\delta = 0.02$, $h = 1.6$ mm). The patches are copper sheets of 0.25 mm thick whose lengths are denoted as L_{p1} and L_{p2}. They are suspended over the feedline substrate at heights of h_{p1} and h_{p2}. The bottom of the feedline substrate contains feeding network for slot feed (port-1) and a ground pad for port-2 while probe feed (port-2) resides on its topside together with the H-slot etched on the common ground. The ground pad and the common ground are connected by four conducting posts so that outer conductor of SMA connector touches the ground plane. Air gaps are realized using separators of appropriate heights. Finally, the feedline substrate and the patches are assembled by plastic screws. The feeding network of port-1 (+45°) is depicted in Fig. 2. It consists of two parts: (i) matching section and (ii) branch lines. The slot is excited by two parallel 100 Ω microstrip branches separated by a distance of L_d. L-shaped stubs are used to terminate the branches and compensate the reactive part of the input impedance of the patch. A T-junction connects the branches to the matching section which provides wideband matching between the patch and port-1. It includes a two-section binomial transformer. Length of the sections are approximately $\lambda_g/4$ (L_{t1}, L_{t2}) at the center frequency of the intended band, $f_c = 3.55$ GHz ($\lambda_c = 84.55$ mm, $\lambda_g = \lambda_c/\sqrt{\varepsilon_r} \approx 40.31$ mm) where λ_g is guided wavelength. As for port-2 (–45°), a 50 Ω coplanar feed line of length L_{mp} is connected to the modified L-probe whose topside is triangular as shown in Fig. 3.

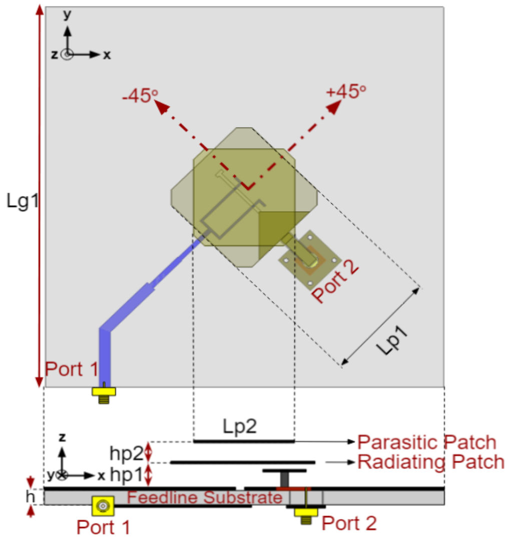

Fig. 1. Antenna configuration and geometry.

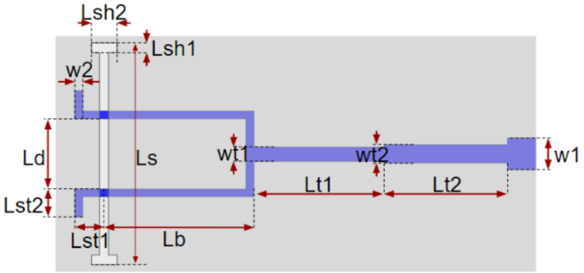

Fig. 2. Feedline and slot-coupled feed (port-1).

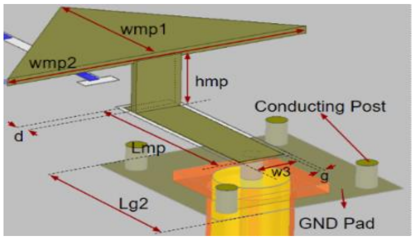

Fig. 3. Capacitively coupled probe feed (port-2).

Table 2: Physical dimensions of the proposed antenna

Description	Parameter	Dimensions (mm)
Ground plane (square) / ground pad (square)	L_{g1} / L_{g2}	110 / 12.4
Main patch (square) / parasitic patch (square)	L_{p1} / L_{p2}	32.5 / 28
Lower/upper air height	h_p /h_{p2}	5 / 4
Slot dimensions / vertical slot width	L_s, L_{sh1}, L_{sh2} / L_{sl2}	20.4, 0.9, 2.3 / 3.2
1st and 2nd binomial section length/width	L_{t1}, L_{t2}, w_{t1}, w_{t2}	11.78, 11.08, 1.32, 1.65
Branch lines separation / branch line length, width	L_d / L_b, w_2	6.53 / 15.48, 0.67
50 Ω line width / co-planar feedline width, length, gap	w_1 / w_3, L_{mp}, g	2.94 / 3, 10.75, 0.35
Probe height / probe offset / probe head	h_{mp} / d / w_{mp1}, w_{mp2}	3.75/ 1 / 10, 20

B. Working principles

Electromagnetic power is coupled to patches through slot and probe, and ±45° dual polarizations are created. Dimensions and placement of the patches at proper heights are of critical importance for good wideband matching, isolation, and FBR. Although the main patch has dominant effect in total design, parasitic one must also be considered in combination with it. The lower h_{p1} makes efficient coupling from slot to the patch easier, hence resulting in good FBR. However, this lower h_{p1} makes broadband operation difficult. On the other hand, the higher h_{p1} facilitates broadband operation but efficient coupling from slot to the patch becomes more difficult and hence resulting in poor FBR. After setting the design of slot feed (port-1) as explained above, the probe feed (port-2), which capacitively couples the energy to the patch, is designed with proper placement of the probe (L_{mp}, h_{mp}). The parasitic patch provides further tuning for each port simultaneously. Existence of the parasitic patch also modifies the current distribution on the main patch, and vectorial combination of currents flowing on the two patches has a total effect of improving the isolation and XPD. Although parasitic patch partially increases the overall antenna profile, it is necessary for design since desired technical performances cannot be obtained by only main patch. However, one can still keep the antenna low-profile.

Figure 4 plots current distributions on the patches, as the antenna is excited from port-1 and port-2 separately, at lower and higher frequency limits of 3.3-3.8 GHz band. When excited from port-1 (Figs. 4 (a)-(b)), currents are established symmetrically around −45° diagonal line on the patches. At 3.3 GHz, amplitude of currents on the main patch gradually increases towards radiating edges, whereas the currents on the parasitic patch are weaker and possess uniform distribution. At 3.8 GHz, stronger coupling is observed between two patches; thus, amplitude of the currents flowing on the parasitic patch increases. This phenomenon leads to resonant behavior around 3.8 GHz. Note that a small portion of the slot is beneath the modified L-shaped probe and this slightly disturbs the current distribution. However, it does not affect the symmetry of the radiation patterns in principal planes as shown later in Fig. 12. Similarly, when excited from port-2 (Figs. 4 (c)-(d)), currents are established symmetrically around +45° diagonal line on the patches. And the antenna again demonstrates its resonant behavior through the parasitic patch at 3.8 GHz. The symmetric characteristics of each polarization along ±45º diagonal line and different distributions of currents (high amplitudes of port-1 and low amplitudes of port-2) for each port reduces the coupling between ports and hence they provide high isolation and high XPD. Moreover, Fig. 5 illustrates simulations of electric field radiated by the slot and coupled to the main patch and the probe. It can be observed that most of the electric field is coupled to the main patch while it is very weak on the probe. This shows that interaction of feeds themselves are reduced by hybrid feeds and it also helps high isolation and high XPD.

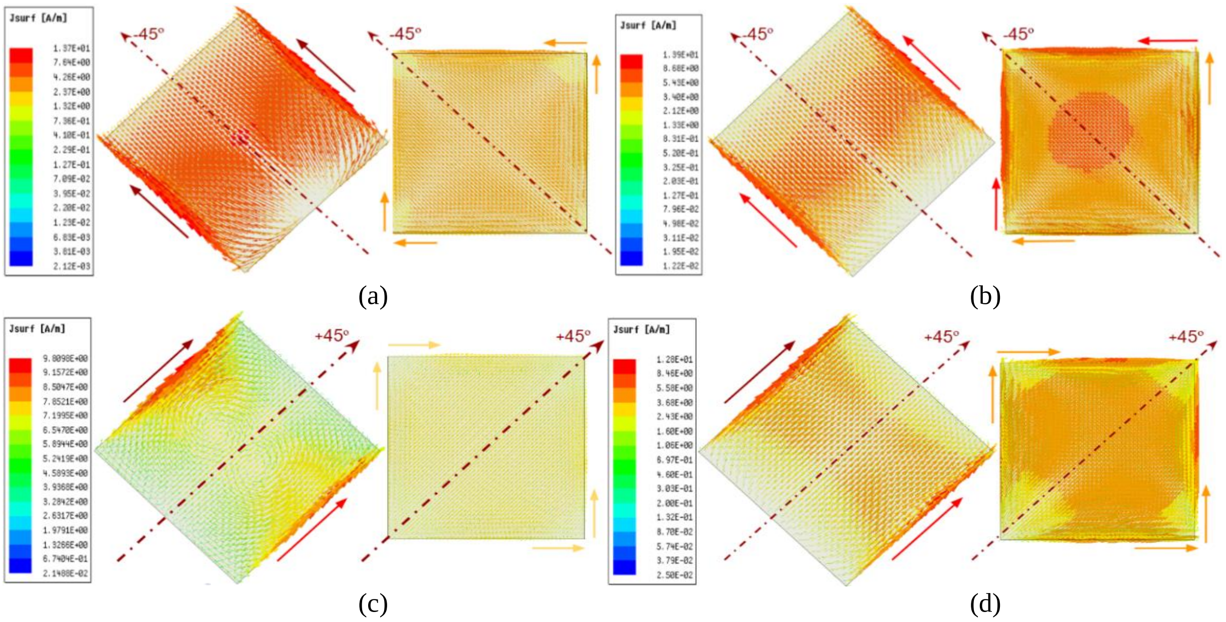

(a) (b)

(c) (d)

Fig. 4. Current distributions on the patches when the antenna is excited from port-1 at (a) 3.3 GHz and (b) 3.8 GHz; from port-2 at (c) 3.3 GHz and (d) 3.8 GHz.

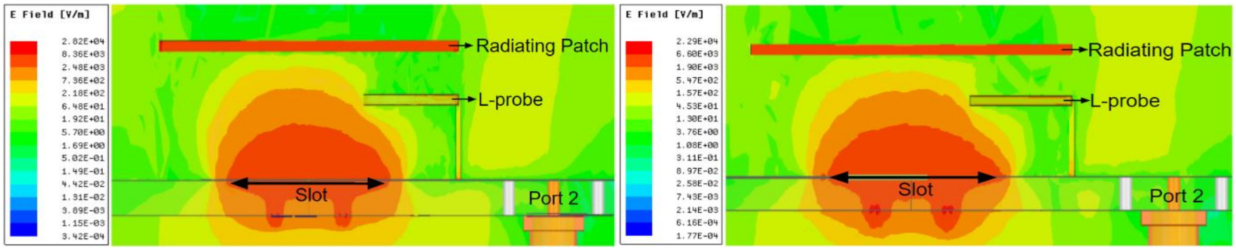

(a) (b)

Fig. 5. E-field distribution when the antenna is excited from port-1 (a) 3.3 GHz and (b) 3.8 GHz.

III. NUMERICAL STUDIES

The proposed antenna is modeled in Ansoft HFSS. A two-stage parametric calculation is carried out in order to obtain optimum electrical performance. In the first stage, slot feed (port-1) is optimized for wideband matching. Then in the second stage, probe feed (port-2) is tuned to give the best matching while checking the isolation performance between the ports. Parametric calculations have been done by sweeping one parameter at a time within a specified range, while keeping the rest unchanged.

A. Slot feed (Port-1)

Owing to simple structure, effect of only one parameter regarding slot feed is reported here. Despite the fact that many other physical aspects (e.g., slot length, stub length, etc.) are also analyzed, they either have minor effects on the antenna performance or none. Patch heights (h_{p1} and h_{p2}) significantly affect wideband matching at port-1. Figure 6 plots $|S_{11}|$ as a function of h_{p1} while it is swept within 4 mm – 6 mm range by 1 mm step. As it is shown, although the IBW is almost the same for all values, $h_{p1} = 5$ mm yields $|S_{11}| < -18$ dB along 3.3-3.8 GHz band, which is better than the others. After fixing h_{p1} at 5 mm, h_{p2} is swept from 3 mm to 5 mm by 1 mm step and their effects are depicted in Fig. 7. The antenna has its largest −15 dB IBW when $h_{p2} = 3$ mm and exhibits the best impedance matching level in 3.3-3.8 GHz band when $h_{p2} = 5$ mm. Here, we decide to select intermediate value of $h_{p2} = 4$ mm, since it results better matching than $h_{p2} = 3$ mm and still wide enough IBW although it is less than that of $h_{p2} = 5$ mm.

B. Probe feed (Port-2)

After the patch heights are fixed for port-1, tuning of the probe feed (port-2) is mainly realized by adjusting the height of the modified L-probe, h_{mp}. Figure 8 illustrates how h_{mp} affects wideband mathcing at port-2. As can be seen, the antenna attains the best impedance matching when $h_{mp} = 3.75$ mm, i.e., $|S_{22}| < -21$ dB in 3.3-3.8 GHz band and it has wide enough IBW.

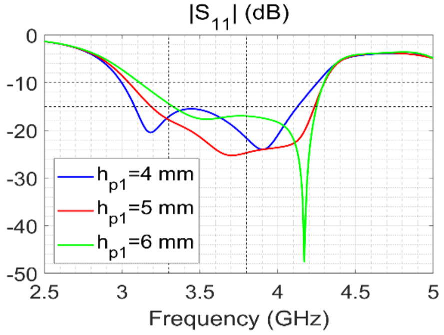

Fig. 6. $|S_{11}|$ as a function of h_{p1} (port-1).

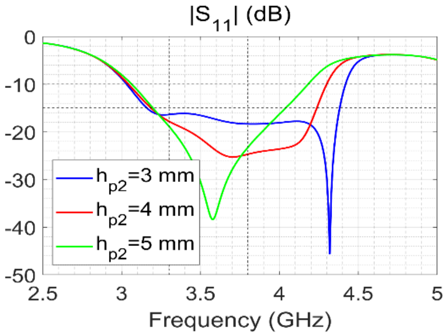

Fig. 7. $|S_{11}|$ as a function of h_{p2} (port-1).

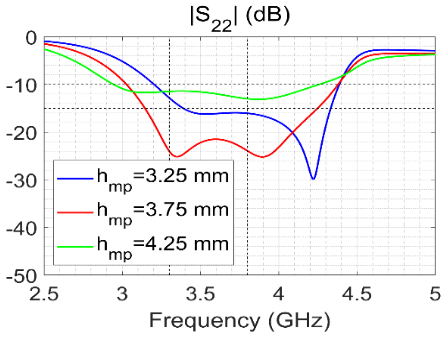

Fig. 8. $|S_{22}|$ as a function of h_{mp} (port-2).

C. Isolation

Finally, with the incorporation of the both feeds described and fixed above, the isolation performance between the ports ($|S_{21}|$) has been checked and obtained to be below −47 dB as shown in Fig. 9. However, it is less than –50 dB in the desired intended band (3.3-3.8 GHz).

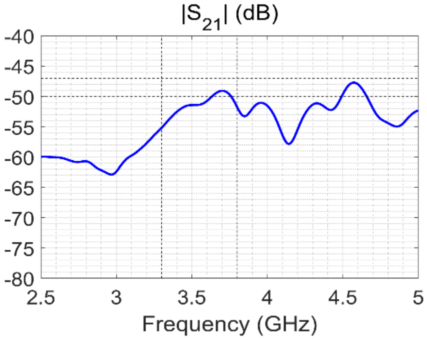

Fig. 9. Simulated port isolation of the antenna.

IV. MEASUREMENT RESULTS

The proposed antenna is prototyped (Fig. 10), in accordance with design descriptions given in Section 2 with FR4 (ε_r = 4.4, tanδ = 0.02) of height 1.6 mm. Galvanized metal sheets of 0.25 mm thickness are used for patches. The overall size of the antenna is 110 mm × 110 mm × 10.6 mm with profile being 10.6 mm.

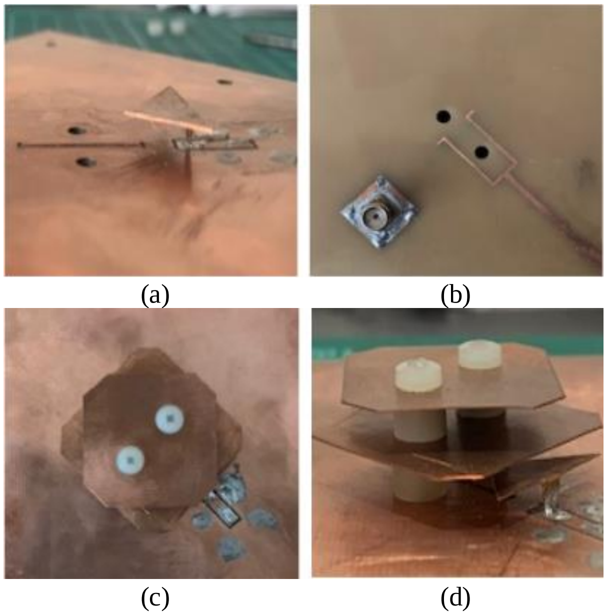

Fig. 10. Prototype antenna (a) slot-probe feeds, (b) feedline layer for slot and SMA connector for probe, (c) top view, and (d) side view.

To prove the proposed design, S-parameters ($|S_{11}|$, $|S_{22}|$, and $|S_{21}|$) and radiation patterns (co-pol and cross-pol) have been measured. S-parameters of the antenna are measured by HP-8720D vector network analyzer and results are given in Fig. 11 in parallel with simulations. The lower and higher limits of the intended operating band (3.3 GHz and 3.8 GHz) are indicated by vertical dashed lines. It must be noted that the discrepancies between them are mostly caused by imperfect assembly and soldering of the components, especially for the modified L-probe (port-2). As shown in Fig. 11, slot feed (port-1) exhibits 40.7% IBW for $|S_{11}| < -10$ dB whereas probe feed (port-2) exhibits 35.6% IBW for $|S_{22}| < -10$ dB. The isolation ($|S_{21}|$) between the ports is less than −47 dB. However, in the operating band (3.3-3.8 GHz), $|S_{11}|$ and $|S_{22}|$ are < –15 dB and $|S_{21}|$ is < –50 dB.

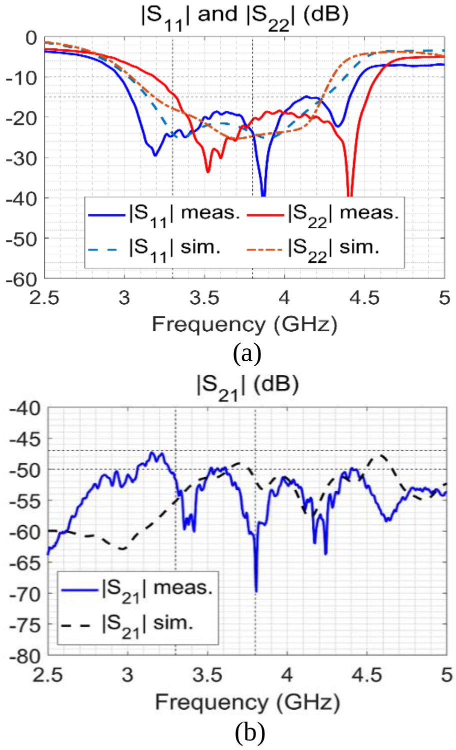

Fig. 11. S-parameters (a) $|S_{11}|$, $|S_{22}|$, and (b) $|S_{21}|$.

The normalized radiation patterns have been measured at 3.3 GHz and 3.8 GHz for both polarizations and plotted in Fig. 12 together with simulations. They are symmetric and directional in broadside. Half power beamwidths (HPBWs) are 50º-60º and 57º-62º for port-1 while they are 56º-64º and 59º-62º for port-2 in E and H planes, respectively. Gain of the antenna varies in 8.5-9.0 dBi for port-1 and in 8.0-8.6 dBi for port-2 as shown in Fig. 13. From radiation patterns, it can also be inferred that XPD levels are greater than 38 dB and 40.5 dB for port-1 and for port-2 respectively, which are measured withing ±30° of boresight. That means a very high XPD has been achieved between two polarizations. High isolation and high XPD performance are due to very low coupling between the feeds and the patches as explained in Section II-B. In addition, a good FBR is also obtained as 22 dB and 25 dB for port-1 and for port-2 respectively.

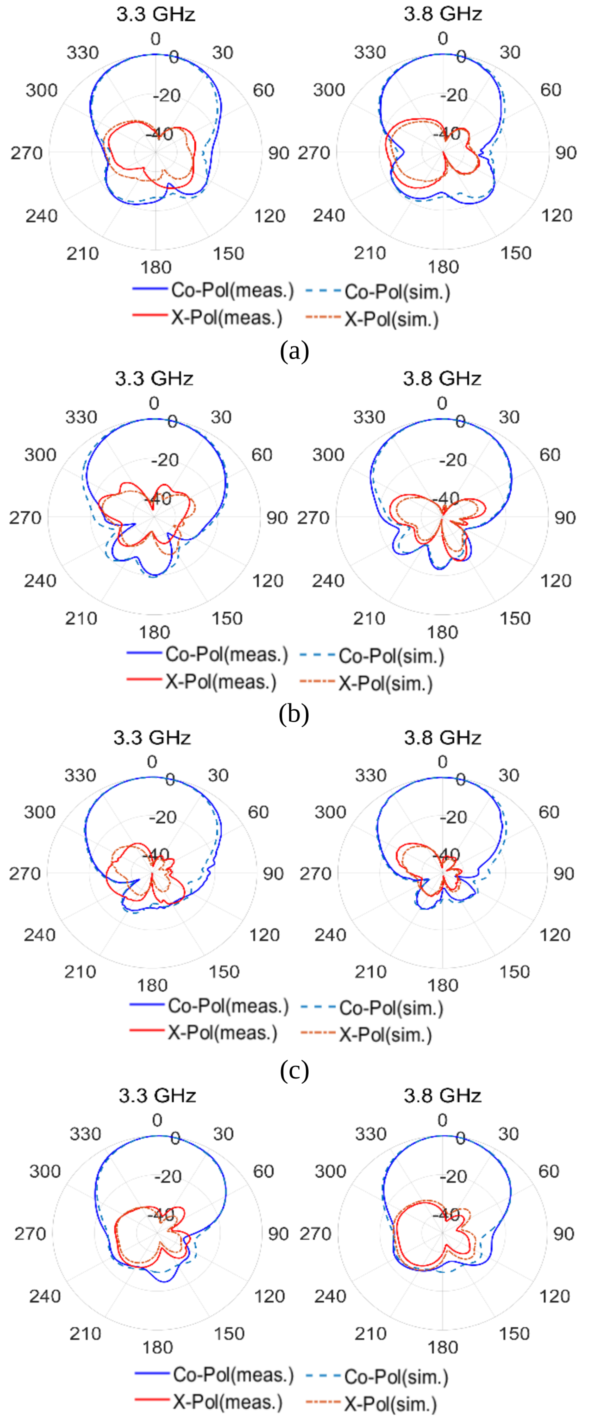

(a)

(b)

(c)

(d)

Fig. 12. Radiation patterns at 3.3 GHz and 3.8 GHz in (a) E-plane for port-1, (b) H-plane for port-1, (c) E-plane for port-2, and (d) H-plane for port-2.

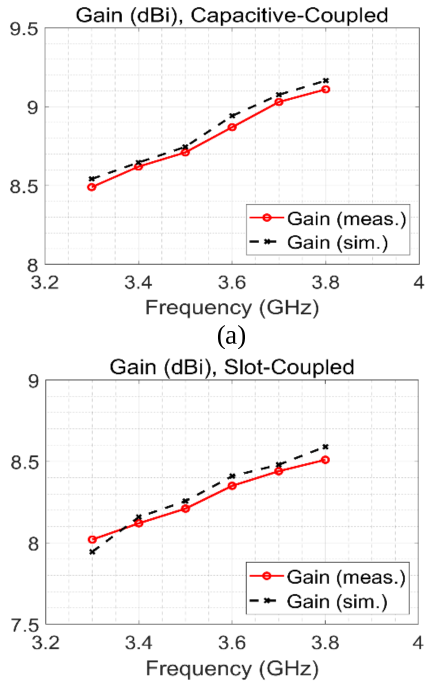

(a)

(b)

Fig. 13. Gain of the antenna (a) port-1 and (b) port-2.

V. CONCLUSION

In this study, a low-profile, wideband, hybrid-fed dual-polarized suspended stacked patch antenna with high isolation and high XPD has been introduced to be used in mMIMO arrays of sub-6 GHz 5G base stations (3.3-3.8 GHz). ±45º slant linear polarizations are established by using a slot-coupled feed and a capacitive-coupled probe feed. All performance specifications regarding wide IBW, good matching level, high isolation (< −47 dB), and high XPD (> 38 dB) have been obtained by a special design of stacked patches with hybrid feed excitations and making the coupling and interactions feeds and patches as low as possible. Measured patterns have symmetric, stable and broadside radiations with sufficient gains. Proposed antenna does not use any additional reflector plate to reduce back radiation. Hence, it is low-profile (10.6 mm) and has still good FBR (> 22 dB). In addition to desired high isolation and high XPD in 5G massive MIMO arrays, similar and stable characteristics (S-parameters, radiation patterns, gains) of each polarization port are necessary to have low ECC. Specifically, gain difference between each polarization port must be small (< 1 dB). In proposed design, this is achieved by gain difference of 0.5 dB, which is acceptable. Comparison of proposed work with similar ones in Table 1 also demonstrates superior and competitive features of the proposed antenna. As a result, it can be used as an antenna element in mMIMO array design in order to facilitate mMIMO array to reach its full performance.

ACKNOWLEDGMENT

This work is partially funded by The Scientific and Technological Research Council of Turkey (TUBITAK) under Grant No. 3180114.

REFERENCES

[1] P. K. Mishra, D. R. Jahagirda, and G. Kumar, "A review of broadband dual linearly polarized microstrip antenna designs with high isolation," *IEEE Antennas Propag. Mag.*, vol. 56, no. 6, pp. 238-251, Dec. 2014.

[2] Y. Luo, Q. X. Chu, and D. L. Wen, "A plus/minus 45-degree dual-polarized base-station antenna with enhanced cross-polarization discrimination via addition of four parasitic elements placed in a square contour," *IEEE Trans. Antennas Propag.*, vol. 64, no. 4, pp. 1514-1519, Apr. 2016.

[3] B. Feng, T. Luo, T. Zhou, and C.-Y.-D. Sim, "A dual-polarized antenna with low cross polarization, high gain, and isolation for the fifth-generation array multiple-input multiple-output communications," *Int. J. RF Microw. Comput. Aided Eng.*, May 2020, DOI: 10.1002/mmce.22278.

[4] X. T. Son, I. Park, and R. W. Ziolkowski, "Crossed dipoles antennas: A review," *IEEE Antennas Propag. Mag.*, vol. 15, no. 15, pp. 107-122, 2015.

[5] M. A. Jensen and J. W. Wallace, "A review of antennas and propagation for MIMO wireless communications," *IEEE Trans. Antennas Propag.*, vol. 52, no. 11, pp. 2810-2824, Nov. 2004.

[6] M. Li, X. Chen, A. Zhang, and K. A. Ahmed, "Dual-polarized broadband base station antenna backed with dielectric cavity for 5G communications," *IEEE Trans. Antennas Propag.*, vol. 18, no. 10, pp. 2051-2055, Oct. 2019.

[7] H.-W. Lai and K.-M. Luk, "Dual polarized patch antenna fed by meandering probes," *IEEE Trans. Antennas Propag.*, vol. 55, no. 9, pp. 2625-2627, Sept. 2007.

[8] F. Zhu, S. Gao, A. T. S. Ho, R. A. Abd-Alhameed, C. H. See, T. W. C. Brown, J. Li, and G. We, "Ultra-wideband dual-polarized patch antenna with four capacitively coupled feeds," *IEEE Trans. Antennas Propag.*, vol. 62, no. 5, pp. 2440-2449, May 2014.

[9] M. Ciydem and A. E. Miran, "Dual polarization wideband sub-6 GHz suspended patch antenna for 5G base stations," *IEEE Antennas Wirel. Propag. Lett.*, vol.19, no. 7, pp. 1142-1146, July 2020.

[10] M. Ciydem and S. Koc, "High isolation dual-polarized broadband antenna for base stations," *Microwave Opt. Technol. Lett.*, vol. 57, pp. 603-607, Jan. 2015.

[11] M. Barba, "A high-isolation, wideband and dual-linear polarization patch antenna," *IEEE Trans. Antennas Propag.*, vol. 56, no. 5, pp. 1472-1476, May 2008.

[12] A. A. Serra, P. Nepa, G. Manara, G. Tribellini, and S. Cioci, "A wideband dual-polarized stacked patch antenna," *IEEE Antennas Wirel. Propag. Lett.*, vol. 6, pp. 141-143, Apr. 2007.

[13] K.-L. Wong, H.-C. Tung, and T.-W. Chiou, "Broadband dual-polarized aperture-coupled patch antennas with modified H-shaped coupling slots," *IEEE Trans. Antennas Propag.*, vol. 50, no. 2, pp. 188-191, Aug. 2002.

[14] R. Caso, A. Serra, A. Buffi, M. R-Pino, P. Nepa, and G. Manara, "Dual-polarized slot-coupled patch antenna excited by a square ring slot," *IET Microw. Antennas Propag.*, vol. 5, no. 5, pp. 605-610, Apr. 2011.

[15] X. J. Lin, Z. M. Xie, and P. S. Zhang, "High isolation dual-polarized patch antenna with hybrid ring feeding," *Int. J. Antennas Propag.*, Article ID 6193102, 2017.

[16] L. H. Wen, S. Gao, Q. Luo, Q. Yang, W. Hu, and Y. Yin Y, "A low-cost differentially driven dual-polarized patch antenna by using open-loop resonators," *IEEE Trans. Antennas Propag.*, vol. 67, no. 4, pp. 2745-2750, Apr. 2019.

[17] K.-L. Wong and T.-W. Chiou, "Broadband dual-polarized patch antennas fed by capacitively coupled feed and slot-coupled feed," *IEEE Trans. Antennas Propag.*, vol. 50, no. 3, pp. 346-351, Mar. 2002.

[18] C. Sim, C. Chang, and J. Row, "Dual-feed dual-polarized patch antenna with low cross polarization and high isolation," *IEEE Trans. Antennas Propag.*, vol. 57, no. 10, pp. 3321-3324, Oct. 2009.

[19] K. Wei, Z. Zhang, W. Chen, and Z. Feng, "A novel hybrid-fed patch antenna with pattern diversity," *IEEE Antennas Wirel. Propag. Lett.*, vol. 9, pp. 562-565, 2010.

[20] T. An and W. Zhang, "A dual-polarized microstrip patch antenna using hybrid feed," *Electromagnetics*, vol. 30, pp. 256-268, 2010.

[21] J.-J. Xie, Y.-Z. Yin, J.-H. Wang, and X.-L. Liu, "Wideband dual-polarized electromagnetic fed patch antenna with high isolation and low cross-polarization," *IET Electron. Lett.*, vol. 49, no. 3, pp. 171-173, Jan. 2013.

[22] H. Saeidi-Manesh and G. Zhang, "High-isolation, low cross-polarization, dual-polarization, hybrid feed microstrip patch array antenna for MPAR application," *IEEE Trans. Antennas Propag.*, vol. 66, no. 5, pp. 2326-2332, May 2018.

[23] M. Xue, J. Liu, Z. Zhao, X. Yang, and Y. Yin, "Wideband dual-polarized hybrid fed patch antenna," *Int. J. RF Microw. Comput. Aided Eng.*, Mar. 2019, DOI: 10.1002/mmce.21711.

[24] J. Jiang, Y. Li, L. Zhao, and X. Liu, “Wideband MIMO directional antenna array with a simple meta-material decoupling structure for X-band applications,” *Appl. Comput. Electromagn. Soc. J*, vol. 35, no. 5, pp.556-566, May 2020.

Mehmet Ciydem was born in 1971 in Ankara, Turkey. He received his B.Sc., M.Sc. and Ph.D. degrees all in Electrical Engineering from Middle East Technical University (METU), Ankara, Turkey with high honors. After working in defense industry (Aselsan, Havelsan, TAI) for many years, he founded Engitek Ltd. company in 2009 where he is President. He is an Associate Professor of electromagnetic theory and communications lecturing occasionally in several universities (Bilkent Univ., Gazi Univ., Karatay Univ., Hacettepe Univ., and Army War Academy). His research interests are in the areas of electromagnetics, wave propagation, antennas, RF/ microwave engineering, radar and communication systems.

Emre A. Miran was born in Izmir, Turkey in 1990. He received the B.S. degree in Electrical and Electronics Engineering from Dokuz Eylul University, Izmir, Turkey, in 2012. He is currently pursuing the Ph.D. degree in Electrical and Electronics Engineering Department at Middle East Technical University (METU), Ankara, Turkey. He was Teaching/Research Assistant at Micro/mm-wave Research Laboratory between 2012-2017. Then, he joined Engitek Ltd. as a Senior RF/Antenna Design Engineer. His research interest mainly includes the fields of electromagnetics, antenna design, RF system design, and radar imaging.

Dictionary Learning and Waveform Design for Dense False Target Jamming Suppression

Tao Jiang [1], Leixin Yu [1], Jiangnan Xing [1], Yinfeng Xia [1,*], Zhe Du [2], Yingsong Li [1], Guoning Zhi [3], and Yanbo Zhao [3]

[1] College of Information and Communications Engineering
Harbin Engineering University, Harbin, 150001, China
*xiayinfeng@hrbeu.edu.cn

[2] Shanghai Electro-Mechanical Engineering Institute, Shanghai 201109, China

[3] Beijing Aerospace Measurement & Control Technology CO. LTD

Abstract **─** For linear frequency modulation (LFM) pulse radars, dense false targets generated by new system jamming seriously damage the performance of such radar systems. In order to avoid the influence of dense false target jamming, an anti-jamming strategy combining waveform design and sparse decomposition are proposed. Specifically, the radar system transmits a random pulse initial phase (RPIP) signal, and uses peak detection method to detect the deception jamming. The phase distribution of the RPIP signal is partially randomly perturbed for a jamming, and we use optimization algorithm to design a phase perturbed LFM (PPLFM) signal with good autocorrelation characteristics. Using the correlation function of the designed signal, the target sample set and the jamming sample set are constructed, and the target echo and the jamming signal are separated using designed dictionary learning method to achieve suppression of dense false target jamming and range side-lobes. The effectiveness of the proposed method is verified by numerical simulation, and the results proved that this proposed method maintains good anti-jamming performance under low signal-to-noise ratio (SNR).

Index Terms **─** Anti-jamming, dense false target jamming, dictionary learning, jamming detection, waveform design.

I. INTRODUCTION

In recent years, the development of radar electronic countermeasures (ECM) technology has made military radars face new challenges. In particular, the rapid development of digital radio frequency memory (DRFM) technology has further promoted the implementation of active deception jamming [1]. Among them, new system jamming such as chopping and interleaving (C&I) and smeared spectrum (SMSP) has the advantages of deception jamming that makes it difficult for LFM radar system to distinguish true or false targets, and saturate radar data processing severely destroys the radar's ability to detect and track targets [2-4].

In response to the influence of sliced jamming (C&I and SMSP), some electronic counter-countermeasures (ECCM) strategies are proposed. Among them, typical methods can be divided into two categories. The first category methods use pulse diversity technology. In [5], a jamming cancellation method based on temporal pulse diversity has been reported for suppressing slice jamming. The waveform design algorithm based on a priori information of electronic jamming in the radar environment knowledge base proposed by [6] achieves suppression of SMSP and C&I jamming. It is worth noting that when there is strong jamming in the radar echo, the higher range side-lobes of the orthogonal signal or quasi-orthogonal signal after matching filtering will still affect the radar's detection performance for real targets. The second category of method is anti-jamming signal processing algorithms. For example, some scholars have used compressed sensing theory and blind source separation technology to achieve the separation of target echo and jamming signals [7, 8]. Paper [9] proposes a countering SMSP jamming method based on jointing time-frequency distribution and compressed sensing. In [10], the authors studied distributed radar to suppress SMSP jamming, and proposed a framework based on joint blind source separation (JBSS). Since noise energy has a great impact on the source method, it makes the jamming suppression performance worse at lower SNR.

In view of the above problems, we consider waveform design to weaken the influence of side-lobes. Since the signal has good sparsity under the adaptive dictionary, we combined the dictionary learning method and sparse decomposition theory to achieve jamming

Submitted On: March 23, 2021
Accepted On: June 10, 2021

https://doi.org/10.47037/2021.ACES.J.360908

suppression. Because the agile radar system transmits multiple RPIP signals in a coherent processing interval (CPI), the jammer requires a certain processing time for the radar signal. According to the difference in the initial phase between the jamming signal and the radar emission signal, the proposed peak detection method uses a wavelet transform algorithm to estimate the phase difference of the pulse compression (PC) signal in two adjacent PRIs so as to achieve detection of radar deception jamming. When jamming is detected in the radar echo, the radar system starts to perform phase perturbation processing on the RPIP signal. Then, the integrated auto-correlation side-lobes energy (IASE) of the transmitted signal is minimized as the criterion for waveform design. We use genetic algorithm (GA) to design the parameters of the phase perturbed term and get a series of PPLFM waveforms with good autocorrelation characteristics. In addition, there are many studies on the identification and feature parameter extraction of C&I and SMSP jamming [11, 12]. We assume that the modulation parameters of electronic jamming are known to construct a mathematical model for the jamming signal. Next, the target sample set is constructed using the autocorrelation of the designed PPLFM signal, and the cross correlation between the designed PPLFM signal and the jamming model is used to construct the jamming sample set. Finally, the dictionary learning method proposed in our research work is used to suppress the jamming of dense false targets.

II. SIGNAL MODEL

The RPIP agile waveform is that the radar transmits M-pulse signal with different initial phases in a CPI, and the pulse signal transmitted in the m-th PRI is $S_m(t)$:

$$S_m(t) = e^{j\varphi_m} \cdot s_{LFM}(t) = \exp\left(j\pi\mu t^2 + j\varphi_m\right), \tag{1}$$

where $\mu = B/T$ is chirp rate, B is pulse bandwidth, T is pulse duration. φ_m is the initial phase of the radar signal, and it follows uniform distribution on $[-\pi, \pi]$.

Assuming that the amplitude and delay of the target echo remain unchanged within a CPI, then, the target echo can be modeled as:

$$T_m(t) = \sigma_T \cdot e^{j\varphi_m} \cdot s_{LFM}(t - \tau_T), \tag{2}$$

where σ_T and τ_T denote the amplitude and time-delay of the target echo, respectively.

The mathematical model of C&I jamming can be written as:

$$j_m^1(t) = \sum_{l=0}^{L-1} C_m^1\left(t - l\frac{T}{L \cdot n_{c\&i}}\right), \tag{3}$$

where L and $n_{c\&i}$ represent the sampling interval and the number of sub-pulse repetitions, respectively:

$$C_m^1(t) = S_m(t) \cdot \sum_{i=1}^{n_{c\&i}} rect\left(\frac{t - \tau_b - (i-1)T}{\tau_b}\right), \tag{4}$$

where $rect(t)$ is rectangular function, τ_b is the sub-pulse width.

The model expression forming the SMSP jamming is given as follows:

$$j_m^2(t) = \sum_{i=1}^{n_{smsp}} C_m^2\left(t - (i-1)\frac{T}{n_{smsp}}\right), \tag{5}$$

where n_{smsp} is the number of sub-pulse repetitions,

$$C_m^2(t) = \exp\left(j\pi n_{smsp}\mu t^2\right), \quad 0 \le t \le T/n_{smsp} . \tag{6}$$

Due to the radar transmission signal intercepted by the DRFM jammer is modulated as a jamming signal, it requires a certain processing time. As the agile radar with RPIP waveform is the active side, the jammer becomes the passive side. Then, the jamming signal for the m-th PRI received by the radar can be expressed as:

$$J_m(t) = \sigma_J \cdot e^{j\varphi_{m-I}}\, j_m^k(t - \tau_J), \quad k = 1, 2, \tag{7}$$

where I is the number of PRIs for the jamming signal lagging the transmitted signal.

Then, the radar echo signal received by the radar receiver in the m-th PRI is:

$$r_m(t) = T_m(t) + J_m(t) + N_m(t), \tag{8}$$

where $N_m(t)$ is white Gaussian noise.

Finally, the radar echo $r_m(t)$ is transmitted to a filter with a matching coefficient of $h_m(t) = S_m^*(-t)$. Then, the PC of the *m*-th radar echo signal after matching filter can be written as:

$$\begin{aligned} y_m(t) &= r_m(t) \otimes h_m(t) \\ &= \sigma_T R_{LFM}(t - \tau_T) + e^{j\phi_n} \cdot \sigma_J R_{LFM,J}(t - \tau_J) + W_m(t) \end{aligned}, \tag{9}$$

where $\phi_m = \varphi_m - \varphi_{m-I}$ is the phase residual, $W_m(t)$ is white Gaussian noise. $R_{LFM}(t)$ is the autocorrelation function of signal $s_{LFM}(t)$, $R_{LFM,J}(t)$ is the cross-correlation function between signal $s_{LFM}(t)$ and jamming $j_m^k(t)$.

III. JAMMING SUPPRESSION STRATEGY

The strategy proposed in this paper can both realize the detection of deception jamming and suppress the jamming. Figure 1 shows the workflow of the agile LFM radar against slice jamming. First, the radar transmits RPIP agile pulse signals and uses the peak detection method to determine whether there is jamming in the radar echo. If there is no jamming, the radar system directly detects the real target. If there is a jamming, the agile radar changes to transmit a quasi-RPIP (Q-RPIP) signal. Then, according to a certain process, the peak detection method is used to estimate the lagging I value, and the coding sequence of the phase perturbed term in the jamming signal is obtained. After that, the agile radar changes to transmit a PPLFM signal via optimized design. We perform autocorrelation processing on the optimized signal, and cross-correlation processing between the optimized signal and the jamming signal, and then, the target sample set and the jamming sample set are constructed in a range gate, respectively. Finally, the sample set of the two signals is used to separate the target and the jamming through the dictionary learning method so that the radar can detect the real target.

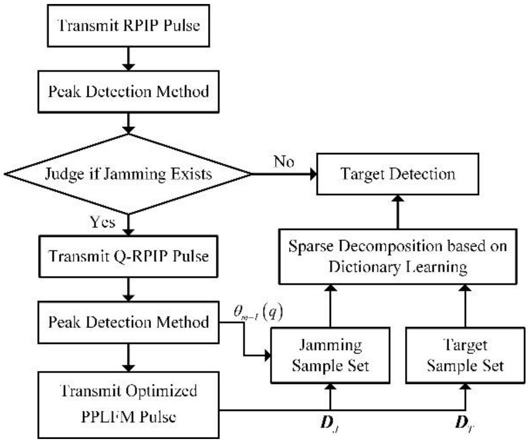

Fig. 1. Agile LFM radar against slice jamming workflow.

A. Detection of deception jamming

This section introduces the basic principle of the peak detection method to detect radar active deception jamming. The radar system transmits the RPIP agile waveform, and the received echo is processed by matched filtering to obtain pulse compression signals $y_m(t)$ and $y_{m+1}(t)$ in the two adjacent PRIs. As shown in Fig. 2, the red dotted line represents SMSP jamming, the blue solid line represents the target echo, and the black dotted line represents noise signal. It is understood from equation (9) that the jamming signal is affected by random initial phase changes, resulting in unequal initial phases of the jamming signals in two adjacent PRIs. In other words, the phase difference of the two jamming signals is non-zero, and the phase difference of the target echo is zero. Therefore, according to this difference characteristic, we intercept the segment of the PC signal with a large peak position and estimate the phase difference of the intercepted signal fragments. If the estimated phase difference is zero, the signal segment is the target signal. If the phase difference is not zero, it means that this signal segment is a jamming signal.

We use the wavelet transform algorithm to estimate the phase difference of the signals in the two adjacent PRIs. According to the definition of wavelet transform, the continuous wavelet transform of signal $s(t)$ is:

$$W_s(a,b)=\frac{1}{\sqrt{a}}\int_{-\infty}^{+\infty}s(t)\Psi^*(\frac{t-b}{a})dt\,, \tag{10}$$

where a is scale factor, b is displacement parameters, * represents conjugate, function $\Psi(t)$ is a basic wavelet. In this paper, Morlet wavelet is used as the continuous wavelet transform.

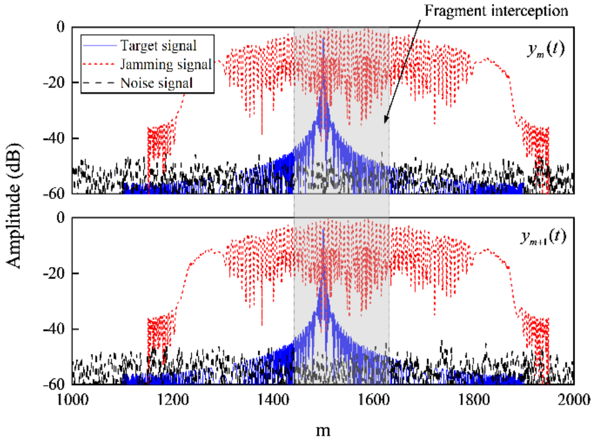

Fig. 2. Schematic diagram of peak detection method.

Intercepting the time series $y'_m(t)$ and $y'_{m+1}(t)$ of the PC signal in the range gate, and defining the cross wavelet transform is given by:

$$W_{y'_m,y'_{m+1}}=W_{y'_m}W^*_{y'_{m+1}}\,, \tag{11}$$

where $W_{y'_m}$ and $W_{y'_{m+1}}$ are wavelet transform for $y'_m(t)$ and $y'_{m+1}(t)$, respectively. The corresponding cross wavelet power is $\left|W_{y'_m,y'_{m+1}}\right|$. The estimated phase difference is:

$$\Phi_{y'_m,y'_{m+1}}(a,b)=\arg\left[W_{y'_m,y'_{m+1}}(a,b)\right], \tag{12}$$

where $\arg[\bullet]$ is used to calculate the complex angle with range of $[-\pi,\pi]$.

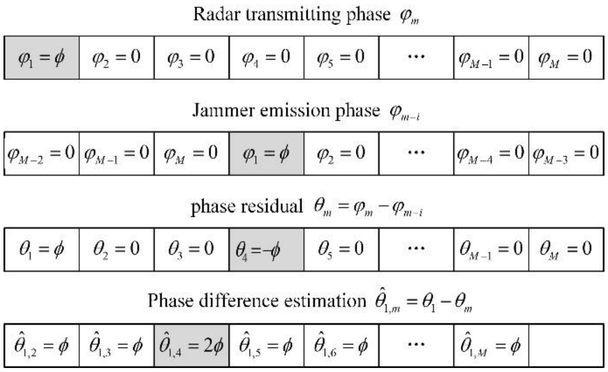

Radar transmitting phase φ_m

$\varphi_1=\phi$	$\varphi_2=0$	$\varphi_3=0$	$\varphi_4=0$	$\varphi_5=0$	$\cdots$	$\varphi_{M-1}=0$	$\varphi_M=0$

Jammer emission phase φ_{m-i}

$\varphi_{M-2}=0$	$\varphi_{M-1}=0$	$\varphi_M=0$	$\varphi_1=\phi$	$\varphi_2=0$	$\cdots$	$\varphi_{M-4}=0$	$\varphi_{M-3}=0$

phase residual $\theta_m=\varphi_m-\varphi_{m-i}$

$\theta_1=\phi$	$\theta_2=0$	$\theta_3=0$	$\theta_4=-\phi$	$\theta_5=0$	$\cdots$	$\theta_{M-1}=0$	$\theta_M=0$

Phase difference estimation $\hat{\theta}_{1,m}=\theta_1-\theta_m$

$\hat{\theta}_{1,2}=\phi$	$\hat{\theta}_{1,3}=\phi$	$\hat{\theta}_{1,4}=2\phi$	$\hat{\theta}_{1,5}=\phi$	$\hat{\theta}_{1,6}=\phi$	$\cdots$	$\hat{\theta}_{1,M}=\phi$	

Fig. 3. Schematic of estimated jamming at lagging *I*.

Next, the peak detection method is used to estimate the jamming lagging *I*. As shown in Fig. 3, the LFM pulse radar transmits the Q-RPIP waveform set. The initial phase of the first signal in the waveform set is set to $\varphi_1 = \phi$, while the initial phase of the other signals is $\varphi_m = 0$ $(m = 2, \cdots, M)$. Assuming that the jamming lagging *I* is 3, then the initial phase of the fourth pulse signal in the waveform set emitted by the jammer is $\varphi_4 = \phi$. Then, the phase residuals of the first pulse signal and the fourth pulse signal after pulse compression processing are $\theta_1 = \phi$ and $\theta_4 = -\phi$, respectively. Finally, the peak detection method is used to estimate the phase difference between the first PC signal peak and the subsequent *M*-1 PC signal peaks. The phase difference estimated in the third detection is $\hat{\theta}_{1,3} = 2\phi$, and the other phase differences are estimated to be $\hat{\theta}_{1,m} = \varphi (m \neq 3)$. In this way, it is determined that the number of PRIs for the jamming signal sent by the jammer lagging the transmitted signal is 3.

B. Optimized design of PPLFM waveform

The PPLFM signal constructed using partial random perturbance to the phase distribution of the RPIP signal to get:

$$\begin{aligned} P_m(t) &= S_m(t) \cdot p_m(t) \\ &= \exp\left(j\pi\mu t^2 + j\theta_m(t) + j\varphi_m \right) \end{aligned}, \tag{13}$$

where $p_m(t) = \exp\left(j\theta_m(t)\right)$ is the random phase perturbed term in the PPLFM signal.

Generally, random signals $\theta_m(t)$ can be expressed as:

$$\theta_m(t) = \sum_{q=1}^{Q} \theta_m(q) \cdot \left[U\left(t - qt_p\right) - U\left(t - (q-1)t_p\right) \right], \tag{14}$$

where the pulse signal in the time domain is divided into $Q = T/t_p$ sub-pulses, t_p is the width of each sub-pulse in the time domain. $U(t)$ is the step function, $\theta_m(q)$ is the phase coding sequence of the *m*-th waveform in the waveform set with $\theta_m(q) \in [-\pi, \pi]$.

In order to avoid high range side-lobes jamming, the IASE of the transmitted signal $P_m(t)$ is minimized as basic criterion for waveform design. The calculation of IASE for $P_m(t)$ is:

$$IASE_m = \int_{t \in \text{sidelobe}} \left| R_{P_m}(t) \right|^2 \mathrm{d}t, \tag{15}$$

where $R_{P_m}(t)$ is the autocorrelation function of the *m*-th transmitted signal $P_m(t)$.

According to the above-mentioned waveform design criteria, the waveform design problem model is constructed as follows:

$$\min_{\theta_m} \quad CF = IASE_m. \tag{16}$$

GA is used to solve the optimal solution of the above expressions to minimize the autocorrelation side-lobes energy. The obtained solution is used as the coding sequence of the phase perturbed term.

C. Dictionary learning method to separate target echo and jamming signal

Calculate the autocorrelation function $\bar{R}_{P_m}(t)$ of the optimized PPLFM signal, and construct the target sample set as:

$$\boldsymbol{D}_T = \left\{ D_T^n(t) = \bar{R}_{P_m}\left(t - \tau_n\right), \quad n = 1, 2, \cdots, N \right\}. \tag{17}$$

Then, according to the coding sequence $\theta_{m-I}(q)$ obtained by the peak detection method, the cross-correlation function $\bar{R}_{P_m,J}(t)$ between the jamming signal and the optimized signal is calculated, and the jamming sample set is created as:

$$\boldsymbol{D}_J = \left\{ D_J^n(t) = \bar{R}_{P_m,J}\left(t - \tau_n\right), \quad n = 1, 2, \cdots, N \right\}, \tag{18}$$

where *N* is the number of all possible echoes within the detection range of the radar range gate. According to the radar range gate width range $[d_{\min}, d_{\max}]$ and the minimum resolution distance *d*, the number of atoms in the dictionary is determined as $N = \left(d_{\max} - d_{\min}\right)/d$. Time-delay τ_{n} can be written as:

$$\tau_n = \frac{2\left(d_{\min} + n \cdot d\right)}{C}, \tag{19}$$

where *C* is the speed of light.

The atoms in the sample set (initial dictionary) $\boldsymbol{D}_T$ and $\boldsymbol{D}_J$ are converted into autocorrelation matrix diagonal vectors, and then normalized to construct new dictionaries $\boldsymbol{G}_T$ and $\boldsymbol{G}_J$, respectively. After that, we use the adaptive dictionary learning method to construct the approximate Q-KLT basis of the target and the jamming signal.

The specific steps to achieve the separation of the target echo and the jamming signal under the approximate Q-KLT basis are described below.

1. Calculate the autocorrelation matrix $\boldsymbol{R}_y$ of the PC signal $\boldsymbol{y}$ in the radar range gate and the diagonal vector $\boldsymbol{d}_y$.
2. We use OMP algorithm to iterate the input signal $\boldsymbol{d}_y$ and the joint dictionary $\boldsymbol{G}_{unit} = [\boldsymbol{G}_T, \boldsymbol{G}_J]$, and obtain two output results (Subset $\boldsymbol{G}_{I_{unit}}$ of union dictionary $\boldsymbol{G}_{unit}$, sparse projection vector $\gamma_{I_{unit}}$ of

signal $\boldsymbol{d}_y$ under dictionary $\boldsymbol{G}_{I_{unit}}$). The atoms in $\boldsymbol{G}_{unit}$ can be divided into two groups, one of which is from $\boldsymbol{G}_T$ denoted as $\bar{\boldsymbol{g}}_T^{k_1}, \bar{\boldsymbol{g}}_T^{k_2}, \cdots, \bar{\boldsymbol{g}}_T^{k_j}$, while the other is from $\boldsymbol{G}_J$ denoted as $\bar{\boldsymbol{g}}_J^{k_1}, \bar{\boldsymbol{g}}_J^{k_2}, \cdots, \bar{\boldsymbol{g}}_J^{k_i}$. The coefficient corresponding to $\bar{\boldsymbol{g}}_T^{k_1}, \bar{\boldsymbol{g}}_T^{k_2}, \cdots, \bar{\boldsymbol{g}}_T^{k_j}$ in $\gamma_{I_{unit}}$ is designated as $\gamma_{k_1}, \gamma_{k_2}, \cdots, \gamma_{k_j}$, , and the coefficients corresponding to $\bar{\boldsymbol{g}}_J^{k_1}, \bar{\boldsymbol{g}}_J^{k_2}, \cdots, \bar{\boldsymbol{g}}_J^{k_i}$ in $\gamma_{I_{unit}}$ are $\gamma_{k_{j+1}}, \gamma_{k_{j+2}}, \cdots, \gamma_{k_{j+i}}$.

(3) Select the atom corresponding to $\bar{\boldsymbol{g}}_T^{k_1}, \bar{\boldsymbol{g}}_T^{k_2}, \cdots, \bar{\boldsymbol{g}}_T^{k_j}$ from the dictionary $\boldsymbol{D}_T$ to generate the template $\boldsymbol{R}_T^{k_1}, \boldsymbol{R}_T^{k_2}, \cdots, \boldsymbol{R}_T^{k_j}$, and select the atom corresponding to $\bar{\boldsymbol{g}}_J^{k_1}, \bar{\boldsymbol{g}}_J^{k_2}, \cdots, \bar{\boldsymbol{g}}_J^{k_i}$ from the dictionary $\boldsymbol{D}_J$ to generate the template $\boldsymbol{R}_J^{k_1}, \boldsymbol{R}_J^{k_2}, \cdots, \boldsymbol{R}_J^{k_i}$.

(4) Calculate the approximate autocorrelation matrix of the target and jamming:

$$\widehat{\boldsymbol{R}}_T = \sum_{n=1}^{j} \gamma_{k_n} \boldsymbol{R}_T^{k_n} , \tag{20}$$

$$\widehat{\boldsymbol{R}}_J = \sum_{n=1}^{i} \gamma_{k_{j+n}} \boldsymbol{R}_J^{k_n} . \tag{21}$$

(5) Perform eigenvalue decomposition on $\widehat{\boldsymbol{R}}_T$ and $\widehat{\boldsymbol{R}}_J$ to find the approximate Q-KLT basis $\boldsymbol{U}_T^H$ and $\boldsymbol{U}_J^H$ of the target echo and jamming signal.

(6) The basis pursuit algorithm is used to solve the estimate $\boldsymbol{\Theta}_T$ of the sparse representation of the target echo under $\boldsymbol{U}_T^H$, and the estimate $\boldsymbol{\Theta}_J$ of the sparse representation of the jamming signal under $\boldsymbol{U}_J^H$.

(7) Reconstructed to separate target echo $\hat{\boldsymbol{Y}}_T = \boldsymbol{U}_T \boldsymbol{\Theta}_T$, and jamming signal $\hat{\boldsymbol{Y}}_J = \boldsymbol{U}_J \boldsymbol{\Theta}_J$.

IV. SIMULATION RESULTS AND ANALYSIS

A. The simulation results of detection of deception jamming

In this paper, the radar operating at X-band is considered, the time width of LFM signal is 10us, the bandwidth is 10 MHz, PRI=200 us, CPI=64. The number of C&I jamming and SMSP jamming sub-pulses is 20, and the number of repetitions is 5. We assume that the target echo time-delay is 125 us, and the jamming time-delay is 125.5 us. The jamming lag *I* is 10. The SNR is set to 10 dB and the jamming to signal ratio (JSR) is 30 dB.

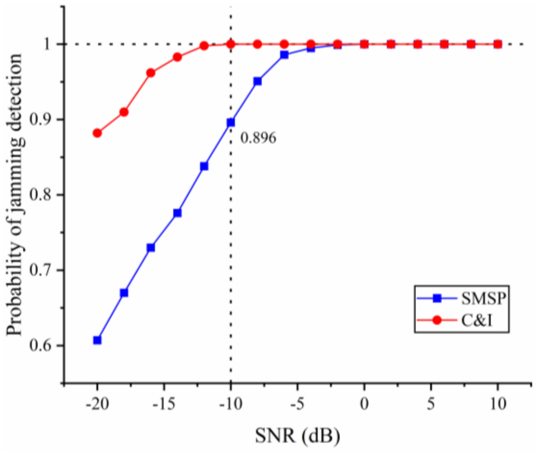

Fig. 4. Detection probability of jamming signal.

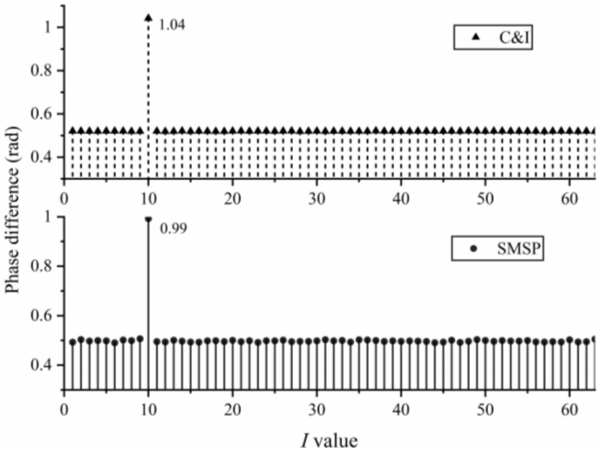

Fig. 5. Estimation of *I*.

In order to verify the performance of the peak detection method for slice-type interference detection, C&I and SMSP jamming signals are detected by employing the proposed peak detecting method. Figure 4 shows the results of detection probability of jamming signal. It can be seen that as the SNR decreases, the detection probabilities of both jamming signals show a downward trend. Under the same detection threshold, the peak detection method has a higher detection probability for C&I jamming. When SNR=-10 dB, the jamming detection probability remains around 0.9. The simulated results in Fig. 4 demonstrate the effectiveness of the proposed peak detection method for slice-type interference detection.

When the jamming signal is estimated, the number of the period of the signal transmitted by the radar is needed to be determined. Figure 5 is the simulation result of the peak detection method to estimate the lagging *I*. It can be seen that the corresponding phase difference at

I=10 is twice that of other elements, which shows that for the slice jamming, the peak detection method can effectively estimate the lagging *I*. The results also can be as the prior information for the anti-jamming method.

B. The simulation results of the optimized design of PPLFM waveform

According to the optimized design of the PPLM waveform, the simulated result is presented in Fig. 6. Figure 6 shows the relevant characteristics of the optimized PPLFM. The code length Q=100 of the phase perturbed term in the PPLFM signal. The GA parameters are set as follows: the maximum number of iterations is 600, the number of populations is 200, the crossover probability is 0.9, and the mutation probability is 0.1. It can be seen from the Fig. 6 that the auto-correlation (AC) and cross-correlation (CC) of the green dotted LFM signal are the same, and the peak of the auto-correlation side-lobe reaches -13.5 dB. The solid blue line represents the auto-correlation of the optimized PPLFM signal. The auto-correlation side-lobe peak reaches -22.18 dB, which is more conducive to the detection of real targets for radar under strong jamming and low SNR conditions.

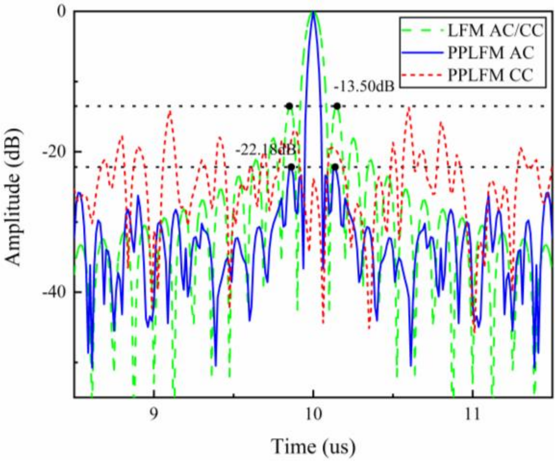

Fig. 6. Related characteristics of PPLFM signals.

C. The simulation results of the dictionary learning method to separate target echo and jamming signal

The effectiveness of the peak detection method is verified under both C&I and SMSP jamming signals in section A. The designed transmitted signal is also given in section B. In this section, the simulation results of the dictionary learning method to separate target echo and jamming signal will be presented.

Figure 7 depicts the results of sliced jamming suppression. The red dotted line represents the result of matched filtering processing of the fixed LFM signal transmitted by the radar. It can be seen that the dense false targets formed by these two sliced jamming completely overwhelm the real targets. In this paper, the agile radar transmits the optimized PPLFM signal, and the solid black line represents the target echo separated by the dictionary learning method. It can be seen that the proposed strategy effectively suppresses the sliced jamming.

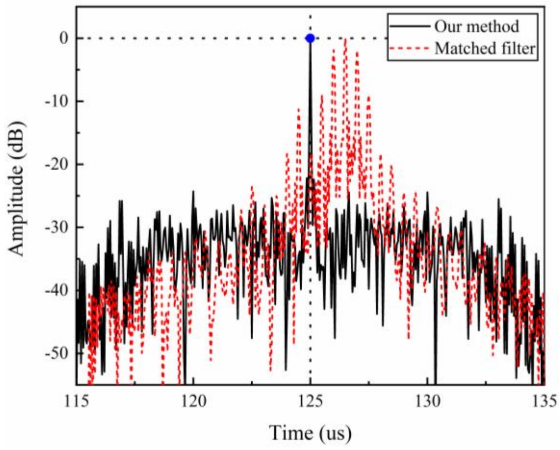

(a) C&I

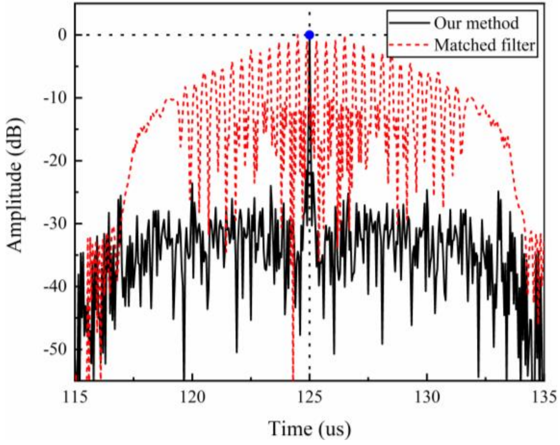

(b) SMSP

Fig. 7. Suppression results of sliced jamming.

In order to analyze the impact of different JSR and SNR on our strategy to separate signals, we use the gini coefficient to measure the sparsity of the projected vectors of the target and jamming signals under approximate Q-KLT basis. Among them, the gini sparse range is [0, 1], the larger the value, the stronger the sparsity. Figure 8 shows the results of 100 Monte Carlo simulations.

Figure 8 (a) shows that with the improvement of JSR, the sparseness of the target projection vector tends to be stable, and the gini coefficient remains around 0.75. It shows that the sparseness of the projection vector of the target signal under the approximate Q-KLT basis is not affected by the jamming intensity. The sparsity of the target projection vector in Fig. 8 (b) increases with the increasing of SNR, showing that SNR affects the sparsity of the target projection.

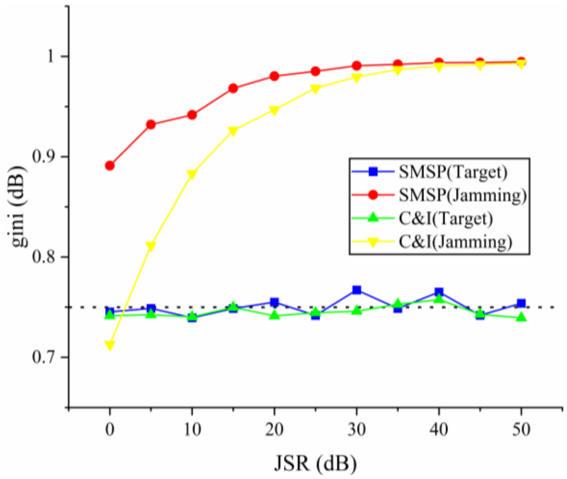

(a) JSR

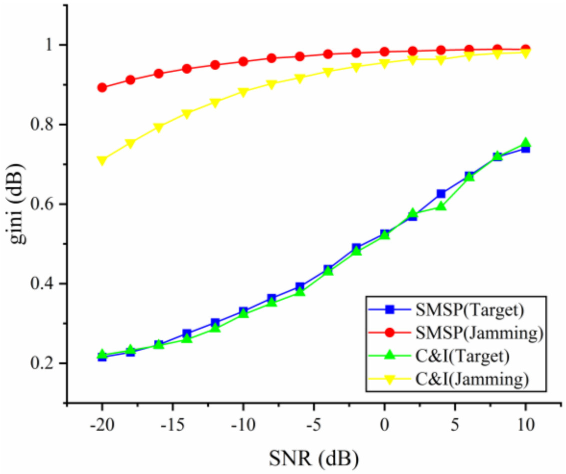

(b) SNR

Fig. 8. Gini coefficient versus JSR and SNR.

Next, we evaluate the impact of JSR and SNR on the peak side-lobes ratio (PSLR) after jamming suppression. Figure 9 shows the results of 100 Monte Carlo simulations. Figure 9 (a) shows that the PSLR after this strategy suppresses sliced jamming maintaining around 21.75 dB, which is similar to the gini coefficient of the target projection vector in Fig. 8 (a). Therefore, it is further verified that the PSLR of this strategy is not affected by the jamming intensity. Figure 9 (b) shows that the PSLR decreases as the SNR decreases, and the change trend is still the same as the target gini coefficient change in Fig. 8 (b). And when SNR=-10 dB, the PSLR after interference suppression reaches 18.31 dB, but it shows that the proposed strategy can maintain high anti-jamming performance under low SNR.

Finally, we compare the anti-jamming ability of the proposed strategy with the JBSS method in [10]. Taking SMSP jamming as an example, set JSR=20 dB. We carried out 100 independent trials for Monte-Carlo simulations under the same conditions of other parameters. Figure 10 shows the comparison results of PSLR after jamming suppression for the two methods. It can be seen that the PSLR of the proposed strategy after jamming suppression is better than the JBSS method, and the strategy still maintains good performance under low SNR. The PSLR of the JBSS method drops sharply with the SNR decreases. Since the principle of the JBSS method in [10] is based on the independence between the target and the jamming signal and the correlation between the target signals in different receivers, it will be affected by noise energy. Based on the good sparsity of the PC signals of target and jamming under their respective adaptive dictionaries, these signals can still be well separated under low SNR conditions.

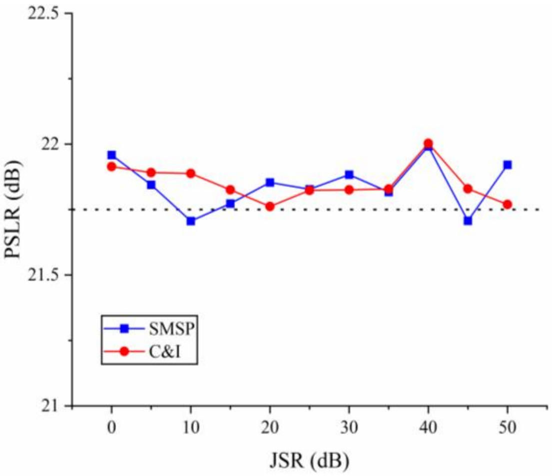

(a) JSR

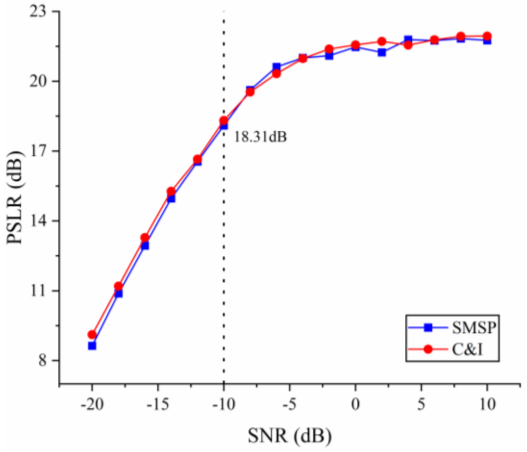

(b) SNR

Fig. 9. PSLR after the jamming suppression versus JSR and SNR.

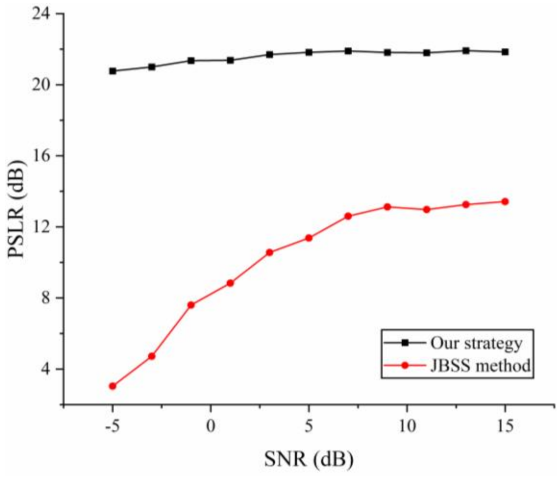

Fig. 10. Performance comparison of the two methods.

V. CONCLUSION

This paper studies the problem of agile LFM radar against dense false target jamming. According to the RPIP signal transmitted by the radar system, we use the peak detection method to detect deception jamming. Then, we construct the target sample set and the jamming sample set, and we implement the separation of the target echo and the jamming signal via the adaptive dictionary learning and the optimized PPLFM signal to achieve the range side-lobes suppression. Finally, simulation experiments are given, the results show that the proposed strategy can effectively detect the presence of jamming and suppress such slice jamming. In addition, the anti-jamming performance is not affected by the jamming intensity. Compared with the JBSS method, it can be concluded that the strategy can still maintain good anti-jamming performance under low SNR conditions. To further improve the performance of the radar, the matched filter can be considered by employing adaptive filter algorithms [13-22] in the future work.

ACKNOWLEDGMENTS

This work was supported by the Fundamental Research Funds for the Central Universities (3072021CF0804) and Funding of Key Laboratory of Advanced Marine Communication and Information Technology, MIIT, China (AMCIT2101-03).

REFERENCES

[1] Q. Shi, N. Tai, C. Wang, and N. Yuan, "On deception jamming for countering LFM radar based on periodic 0-phase modulation," *AEU-International Journal of Electronics and Communications*, vol. 83, pp. 245-252, Jan. 2018.

[2] K. Olivier, J. E. Cilliers, and M. D. Plessis, "Design and performance of wideband DRFM for radar test and evaluation," *Electronics Letters*, vol. 47, no. 14, pp. 824-825, July 2011.

[3] P. Lei, J. Wang, P. Guo, and D. Cai, "Automatic classification of radar targets with micro-motions using entropy segmentation and time-frequency features," *AEU-International Journal of Electronics and Communications*, vol. 65, no. 10, pp. 806-813, Oct. 2011.

[4] N. Tai, H. Han, C. Wang, X. Xu, R. Wu, and Y. Zeng, "An improved multiplication modulation deception jamming method for countering ISAR," *AEU-International Journal of Electronics and Communications*, vol. 110, article number: 152853, Oct. 2019.

[5] G. Lu, S. Liao, S. Luo, and B. Tang, "Cancellation of complicated DRFM range false targets via temporal pulse diversity," *Progress in Electromagnetics Research C*, vol. 16, pp. 69-84, Sept. 2010.

[6] S. Lu, G. Cui, X. Yu, L. Kong, and X. Yang, "Cognitive radar waveform design against signal-dependent modulated jamming," *Progress in Electromagnetics Research B*, vol. 80, pp. 59-77, Mar. 2018.

[7] Z. Liu, J. Sui, Z. Wei, and X. Li, "A sparse-driven anti-velocity deception jamming strategy based on pulse-doppler radar with random pulse initial phases," *Sensors (Basel)*, vol. 18, no. 4, Apr. 2018.

[8] B. Zhou, R. Li, W. Liu, Y. Wang, L. Dai, and Y. Shao, "A BSS-based space-time multi-channel algorithm for complex-jamming suppression," *Digital Signal Processing*, vol. 87, pp. 86-103, Apr. 2019.

[9] Y. Lu, M. Li, R. Cao, Z. Wang, and H. Chen, "Jointing time-frequency distribution and compressed sensing for countering smeared spectrum jamming," *Journal of Electronics and Information Technology*, vol. 38, no. 12, pp. 3275-3281, Dec. 2016.

[10] G. Cui and L. Kong, "Main lobe jamming suppression for distributed radar via joint blind source separation," *IET Radar, Sonar & Navigation*, vol. 13, no. 7, pp. 1189-1199, July 2019.

[11] Y. Li, X. Ying, and B. Tang, "SMSP jamming identification based on Matched Signal transform," *2011 International Conference on Computational Problem-Solving (ICCP)*, Chengdu, China, pp. 182-185, Oct. 21-23, 2011.

[12] A. Aubry, A. D. Maio, M. Piezzo, M. M. Naghsh, M. Soltanalian, and P. Stoica, "Cognitive radar waveform design for spectral coexistence in signal-dependent jamming," *2014 IEEE Radar Conference*, Cincinnati, OH, USA, pp. 0474-0478, May 19-23, 2014.

[13] Y. Li, Z. Jiang, W. Shi, X. Han, and B. Chen, "Blocked maximum correntropy criterion algorithm

for cluster-sparse system identifications," *IEEE Trans. Circuits Syst. II, Express Briefs*, vol. 66, no. 11, pp. 1915-1919, Nov. 2019.

[14] W. Shi, Y. Li, and Y. Wang, "Noise-free maximum correntropy criterion algorithm in non-Gaussian environment," *IEEE Trans. Circuits Syst. II Express Briefs*, vol. 67, no. 10, pp. 2224-2228, Oct. 2020.

[15] W. Shi, Y. Li, and B. Chen, "A separable maximum correntropy adaptive algorithm," *IEEE Trans. Circuits Syst. II, Express Briefs*, vol. 67, no. 11, pp. 2797-2801, Nov. 2020.

[16] Y. Li, Y. Wang, and T. Jiang, "Norm-adaption penalized least mean square/fourth algorithm for sparse channel estimation," *Signal Processing*, vol. 128, pp. 243-251, 2016.

[17] W. Shi, Y. Li, L. Zhao, and X. Liu, "Controllable sparse antenna array for adaptive beamforming," *IEEE Access*, vol. 7, pp. 6412-6423, 2019.

[18] X. Huang, Y. Li, Y. V. Zakharow, Y. Li, and B. Chen, "Affine-projection Lorentzian algorithm for vehicle hands-free echo cancellation," vol. 70, no. 3, pp. 2561-2575, 2021.

[19] T. Liang, Y. Li, W. Xue, Y. Li, and T. Jiang, "Performance and analysis of recursive constrained least Lncosh algorithm under impulsive noises," *IEEE Transactions on Circuits and Systems II: Express Briefs*, vol. 68, no. 7, pp. 2217-2221, 2021.

[20] T. Liang, Y. Li, Y. V. Zakhrow, W. Xue, and J. Qi, "Constrained least Lncosh adaptive filtering algorithm," *Signal Processing*, vol. 183, 2021.

[21] Y. Li and Y. Wang, "Sparse SM-NLMS algorithm based on correntropy criterion," vol. 52, no. 17, pp. 1461-1463, 2016.

[22] Y. Li, C. Zhang, and S. Wang, "Low-complexity non-uniform penalized affine projection algorithm for sparse system identification," *Circuits, Systems, and Signal Processing*, vol. 35, no. 5, pp. 1611-1624, 2016.

A New Mode Stirrer Design for the Reverberation Chamber

Jiazhi Tang [1], Furong Li [1], Junhao Zheng [1], Xiaoming Chen [1], Yingsong Li [2,3], and Juan Chen [4]

[1] School of Information and Communications Engineering
Xi’an Jiaotong University, Xi’an, 710049, China
furong.li@xjtu.edu.cn

[2] College of Information and Communication Engineering
Harbin Engineering University, Harbin, 150001, China

[3] Key Laboratory of Microwave Remote Sensing
National Space Science Center, Chinese Academy of Sciences, Beijing, 100190, China

[4] Shenzhen Research School
Xi'an Jiaotong University, Shenzhen, 518057, China

Abstract **─** In this paper, a mode stirrer composed of random positioned metal plates is proposed for reverberation chamber. The designing procedure of the mode stirrer is presented. The designed stirrer is compared with the common Z-shaped stirrer in both simulation and measurement. It is shown that in general the proposed stirrer outperforms the common Z-shaped stirrer with the same sweeping volume. Nevertheless, the measurement results show that the performance improvement of the designed stirrer becomes insignificant at higher frequencies with additional platform stirring. Albeit the difference, the stirring improvement of the designed stirrer is clearly demonstrated at low frequencies, which is more important due to the inherent low mode density at low frequency.

Index Terms **─** Independent sample number, measurement uncertainty, mode stirrer, reverberation chamber.

I. INTRODUCTION

The reverberation chamber is a shielded room with various stirring mechanisms for over-the-air (OTA) and electromagnetic compatibility (EMC) tests [1]. Whether the electromagnetic fields are statistically homogeneous and isotropic or not is of great importance to the reverberation chamber testing. Due to the stochastic nature of reverberation chamber measurements, measurement uncertainty analysis is of great importance for EMC/OTA tests in the reverberation chamber [2]-[7]. Experimental evaluation of the measurement uncertainty dictates many independent and repeated measurements. To avoid the time-consuming uncertainty characterization, one can resort to the equivalent number of independent samples N_{ind}, which is related to the standard deviation (uncertainty) σ as $\sigma = 1/\sqrt{N_{ind}}$ [6]. The advantage of using N_{ind} is that, instead of conducing many sets of independent measurements, one can estimate N_{ind} from one set of measurement [2],[6]. The measurement uncertainty and the field uniformity are equivalent for evaluating the stirring performance of the reverberation chamber. As a result, many studies use the number of independent samples (or a slightly different form of it) to evaluate the stirring performance in the reverberation chamber, e.g., [7]-[11]. Hence, we will use the same performance indicator in this work.

There are complicated factors affecting the electromagnetic field distribution in the reverberation chamber, including mode stirrer, turntable platform, and scatters on the metal walls. Many works are carried out to optimize these factors to reduce the measurement uncertainty, e.g., stirrer [12],[13], diffusors [14],[15], turntable platform [16] or source stirring [17],[18], metasurface for changing the cavity boundary condition [19]-[21].

In this work, we use a random optimization algorithm to optimize the mode stirrer. The optimized stirrer is fabricated and measured in a reverberation chamber. Superior performance to the conventional Z-shaped stirrer is observed by both simulation and measurement. This is especially true at low frequencies. However, it is shown from measurement result that with platform stirring, the superior performance of the designed stirrer vanish at higher frequencies. Explanation and verification are given. Nevertheless, since the inherent mode density of the reverberation chamber increases with frequency, it is more important to improve the

Submitted On: October 21, 2020
Accepted On: March 4, 2021

https://doi.org/10.47037/2021.ACES.J.360909

measurement uncertainty at the lowest usable frequency. Therefore, the designed stirrer proves to be useful for practical reverberation chamber measurements.

II. DESIGN OF STIRRER

There are in general two types of mode stirrers: rotating stirrer and translating stirrer. It was found that the rotating stirrer not only enjoys simpler motor structure but also has better stirring performance as compared with the translating stirrer, provided that the sweeping volume of the two types of mode stirrers are the same [15]. Therefore, this work focuses solely on the rotating stirrer.

The (rotating) stirrer in a reverberation chamber is usually composed of a central axis, several metal plates, and an electric motor. It can be seen in Fig. 1 (a) that the metal plates of Z-shape stirrer are stitched one by one with a uniform 120 degree flare angle (except at the top and bottom). Note that each metal plate shall be no less than one quarter of the wavelength at the lowest usable frequency [2].

For comparison fair in this work, we set the sweeping volume of all the stirrers to be 0.2 m × 0.2 m × 1.2 m. The initial state of the stirrer to be optimized is shown in Fig. 1 (b). There are in total 196 metal plates each with a size of 10 mm × 10 mm. Obviously, the stirrer shown in Fig. 1 (b) will be inefficient for mode stirring in a reverberation chamber due to its symmetry around the rotating axis. Hence, for optimal stirring performance, we should make it asymmetric and irregular.

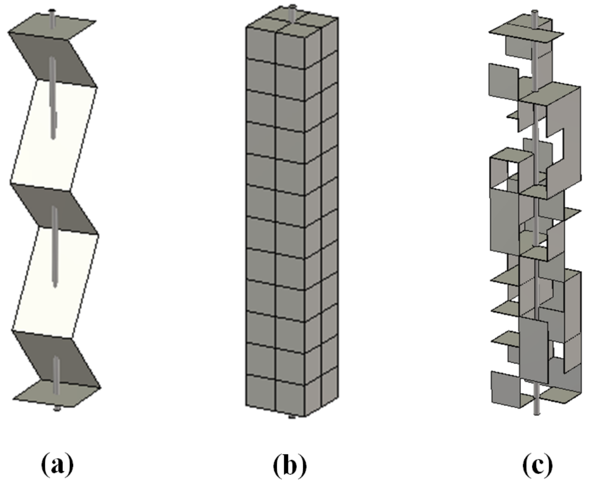

Fig. 1. Models of stirrers: (a) Z-shape stirrer, (b) initial state of the stirrer to be optimized, and (c) optimized stirrer.

By applying the genetic algorithm (GA) [12] to optimize the stirrer, the final design of the stirrer is depicted in Fig. 1 (c). Such an irregular design can be intuitively explained via Fig. 2, from which it can be seen that merely several metal plates can form different metal structures. Under different incident wave directions, different metal structures result in different wave reflections and diffractions. Therefore, the whole stirrer can be designed by using many such metal cavities with random positions. In order to simplify the design procedure, coding ideas are applied. According to the binary theory, the 196 metal plates are converted into a 196-bit code composed of 1 and 0 codes. When constructing the stirrer, 0 means that the corresponding position of the stirrer is empty, while 1 means that there is a corresponding metal plate at that position.

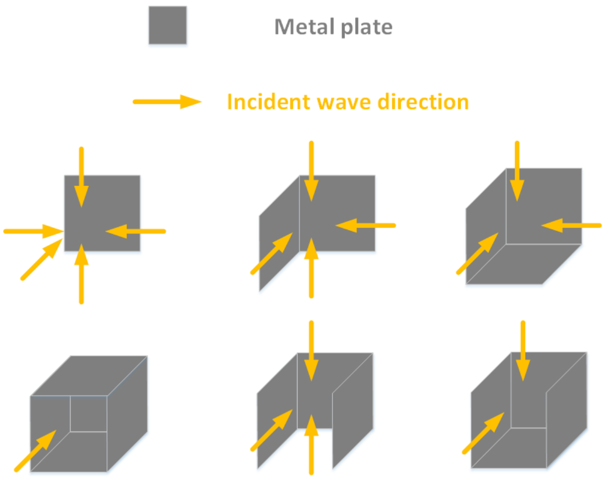

Fig. 2. Different metal plate structures with different incident wave directions.

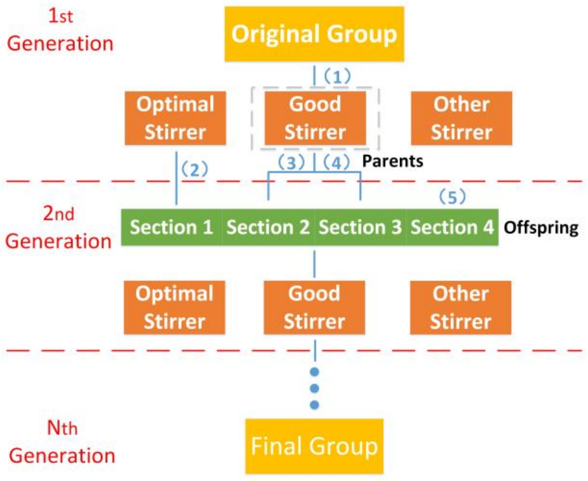

Fig. 3. Optimization process of stirrer through the genetic algorithm.

The optimization process is accomplished through co-simulations with Matlab and CST full wave simulation software, where the evaluation of each stirrer is carried through in CST and all the data processing as well as the optimization algorithm are conducted in Matlab. The whole procedure is depicted in Fig. 3, which mainly demonstrates how the first generation evolves into the second generation. Note that in the optimization algorithm the stirrer is regarded as the chromosome while the 196 metal plates are the genes. At the beginning of the procedure, 50 stirrers that are randomly generated constitute the original group (cf. orange color box) and there are 5 steps in its evolution into next generation (cf. green color boxes): 1) evaluate all members in the original group ranking from the best to the worst, where the optimal stirrer is the top one, the good stirrers are the 2nd-10th members in rank and the other stirrers are the rest; 2) the optimal stirrer is chosen directly as section 1 of the offspring; 3) two individuals from good stirrers are selected as parents according to probability (calculated from the rank) and provide their genes (half of each one's genes for crossover) to form one offspring. 19 new stirrers are constructed like this in section 2; 4) there are 20 new stirrers born in section 3 and every offspring get its genes as in step 3), whereas 5% of its genes are chosen to mutate (random gene locations); 5) 10 stirrers are randomly generated in section 4 to maintain the population diversity. Finally, in total 50 offspring from the four sections become the second generation. In fact, these steps are the so-called evaluation fitness, natural selection, mate selection, mutation and offspring generating in the GA. When repeating the 5 steps, the second, third and N_{th} generation with 50 stirrers can be acquired until the optimization is converged [12]. Next, the evaluation process will be illustrated in the following paragraph.

To evaluate the performance of the coded stirrer, a top view of schematic diagram is shown in Fig. 4. The stirrer (blue square) is located in the center and spherical uniform incident wave (grey dotted circle line) is generated impinging on it. Field probes are set surrounding the stirrer to observe the reflected wave. E and H field values recorded by the probes are used to calculate the average angle of the Poynting vector $\theta_{Ave\_poynting}$, which signifies a measure of the ability of changing the electromagnetic field distribution. Through the GA algorithm optimization in Fig. 3, the proposed stirrer can be obtained and the comparison of the mean angle of the Poynting vector has been exhibited in Table 1. As can be seen, the optimized stirrer (cf. Fig. 1 (c)) has the highest value, whereas the initial state of the stirrer (cf. Fig. 1 (b)) has the lowest value as expected. From Table 1, it can be inferred that the optimized stirrer has the best stirring performance. By applying this stirrer in a reverberation chamber, the electromagnetic field will be stirred more efficiently and its distribution can become more uniform from a statistical point of view.

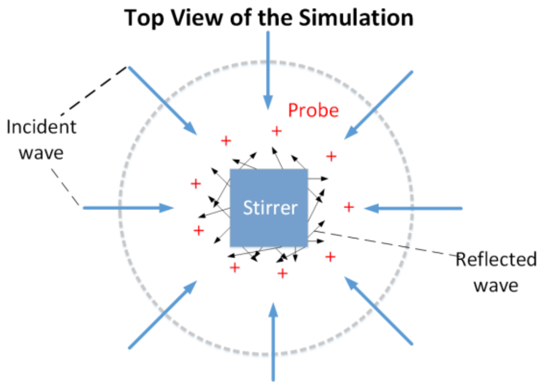

Fig. 4. Model to evaluate the stirrer.

Table 1: Average angle of the Poynting vector

Stirrer	$\theta_{Ave\_poynting}$
Z–shape	7.64
Original	5.25
Final	12.73

III. SIMULATIONS

The reverberation chamber used for simulation has a size of 1.44 m × 0.92 m × 1.5 m as shown in Fig. 5. The dimensions are chosen to be the same as the reverberation chamber in the Lab. In this model, the transmit antenna is a discone antenna (red color) placed in the corner, while the stirrer is located vertically around the z-axis. Furthermore, the working volume is set as 0.4 m × 0.52 m × 0.3 m with 8 field probes (black cross figure) at its 8 vertices to sample the electric field. (Each probe can sample three orthogonal rectangular components of the E field.) The testing frequency range is from 1 to 2 GHz. Given the chamber's dimensions, one can readily find out that the lowest usable frequency of the reverberation chamber is around 1 GHz [2].

The simulation is also carried out in the CST full wave simulation software. During the simulation, the proposed stirrer rotates stepwise around the vertical axis with an angular step of 6°. The 8 electric probes record the rectangular components of E field at each rotation angle of the stirrer. After 60 rotations, the sampled data of probes are collected and analyzed. To evaluate the stirrer’s stirring performance, the number of independent samples of test is calculated by the auto-correlation function (ACF) method [6]. According to the ACF method, the *n*-th auto-correlation coefficient is calculated by:

$$\rho_n = \frac{\sum_{i}^{N-1}\left(x_j - \langle x\rangle\right)\left(x_{j+n} - \langle x\rangle\right)}{(N-1)\sigma^2}, \tag{1}$$

where x is the recorded data, σ^2 is the variance of x:

$$r = \frac{1}{e}\left(1 - \frac{7.22}{N^{0.64}}\right), \tag{2}$$

where e is the base of the natural logarithm function (e≈2.7183) [2] and r is the threshold of the auto-correlation coefficient of the measured samples [7] and often equal to 0.37. The offset number $N_{\Delta,i}$ is determined from the ACF using the threshold. The number of independent samples of the data is then determined as:

$$N_{ind,i} = \frac{N}{N_{\Delta,i}}, \tag{3}$$

where i ranges from 1 to 24 (8 probe locations × 3 electric field rectangular components) and $N = 60$ is the whole rotation sample number. Finally, the averaged number of independent samples over all the probes N_{all} is calculated as:

$$N_{all} = \frac{\sum_{i}^{24} N_{ind,i}}{24}. \tag{4}$$

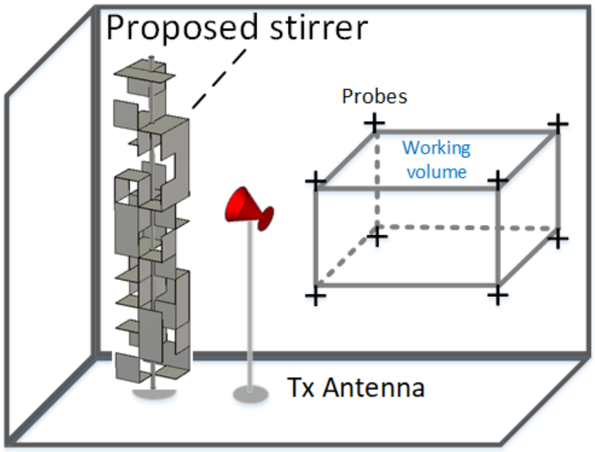

Fig. 5. Simulation model of stirrer in reverberation chamber.

The simulation procedure is repeated for the optimized stirrer and a common Z-shaped stirrer, respectively. For fair comparison, the sweeping volume of the two stirrers are set to be the same. Their stirring performances are compared in Fig. 6. The black line represents the number of independent samples corresponding to the Z-shaped stirrer, while the red color line stands for the number of independent samples corresponding to the optimized stirrer. Note that due to the stochastic nature of the reverberation chamber, both curves are fluctuated and a 50-MHz smoothing windows is applied to make them more readable [6]. Nevertheless, it is obvious that the value of the red line apparently larger than that of the black line over the entire frequency range. This implies that the optimized stirrer clearly outperforms the common Z-shaped stirrer.

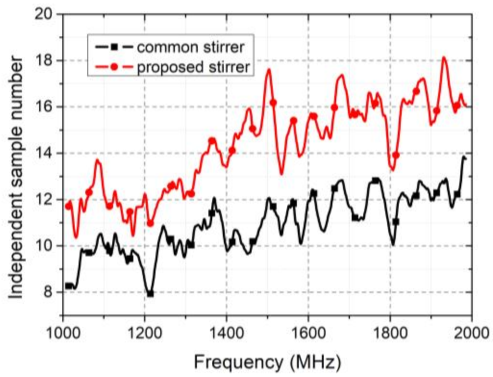

Fig. 6. Comparison of numbers of independent samples of simulated reverberation chamber with the two different stirrers.

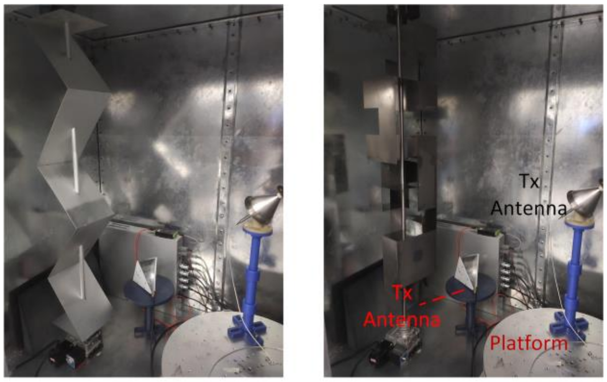

(a) (b)

Fig. 7. Measurement setup of reverberation chamber with: (a) Z-shaped stirrer and (b) optimized stirrer.

IV. MEASUREMENTS

The used reverberation chamber for actual measurements is located at the Xi'an Jiaotong University, Xi'an, China. The proposed stirrer is manufactured and installed in the reverberation chamber as shown in Fig. 7. The reverberation chamber is mainly equipped with a turntable platform, a transmit antenna, and a receive antenna. In the measuring process, the stirrer and turntable platform are controlled by a personal computer (PC). A vector network analyzer is used to collect the data from the two antennas. The sampling number of the test is 100 (10 stirrer rotation angles × 10 platform rotation angles).

Figure 8 shows the estimated numbers of independent samples (solid curves) with the Z-shaped stirrer and the optimized stirrer together. As can be seen, the number of independent samples of optimized stirrer is larger than that of the Z-shaped stirrer below 1.6 GHz. Above 1.6 GHz, the two stirrers have essentially the same stirring performance. The different trends between the measurement and simulation in Fig. 5 are attributed to several factors: 1) the boundary condition of the actual reverberation chamber is much more complicated than that of the simulated chamber; 2) the actual chamber is equipped with a turn-table platform that is missing in the simulation due to computational complexity; 3) it has been found experimentally that platform stirring is more effective than mode stirring [22]. The last factor is probably the dominant one, because once the distance between two consecutive positions of the antenna on the platform is larger than the coherence distance [10] (which is the case at higher frequencies), the stirring performance is dominated by the platform stirring and the stirrer performance improvement becomes insignificant. To verify the analysis, another simulation including the platform stirring condition is conduct and the results are also exhibited in Fig. 8 (dotted curves). It is noted that the two dotted lines above 1.55 GHz have smaller difference than that below 1.55 GHz, which is in accordance with the measurement curves. Hence the additional simulation results substantiate that the third factor is the main cause of the difference of solid lines between Fig. 6 and Fig. 8. Nevertheless, as mentioned before, for reverberation chamber measurements it is most challenging and important to improve the stirring performance around the lowest usable frequency. The stirring performance at higher frequencies are good anyway due to the inherent mode density of the reverberation chamber that increases with frequency. Thus, it is highly desirable to have such a stirrer (cf. Fig. 1 (c)) that can improve the stirring performance at lowest usable frequency.

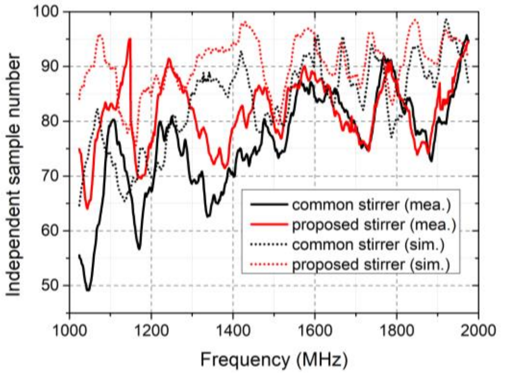

Fig. 8. Comparison of numbers of independent samples of measurements (solid curves) and simulations (dotted curve) of the two different stirrers with platform.

V. CONCLUSION

In this paper, an optimized stirrer was presented. Its superior performance was demonstrated by simulation as well as measurement. The differences between simulation and measurement was explained. It was shown that the optimized stirrer could improve the stirring performance of the reverberation chamber around the lowest usable frequency. At higher frequency, however, the stirring performance was dominated by the turntable platform. Nevertheless, as explained in the paper, it was of great importance to have such an optimized stirrer to improve the performance of the reverberation chamber at low frequencies, where the mode density was inherently low.

ACKNOWLEDGMENT

This work was supported in part by the National Natural Science Foundation of China under Grants 61801366 and the Natural Science Foundation of Shaanxi Province under Grant 2020JM-078, and by Technology Program of Shenzhen (grant number JCYJ20180508152233431).

REFERENCES

[1] X. Chen, J. Tang, T. Li, S. Zhu, Y. Ren, Z. Zhang, and A. Zhang, “Reverberation chambers for over-the-air tests: An overview of two decades of research,” *IEEE Access*, vol. 6, pp. 49129-49143, Aug. 2018.

[2] IEC 61000-4-21: Electromagnetic Compatibility (EMC), Part 4-21: Testing and Measurement Techniques - Reverberation Chamber Test Methods. *Int. Electrotech Comm*., Edition 2.0, 2011.

[3] A. Gifuni, I. D. Flintoft, S. J. Bale, G. C. R. Melia, and A. C. Marvin, “A theory of alternative methods for measurements of absorption cross section and antenna radiation efficiency using nested and contiguous reverberation chambers,” *IEEE Trans. Electromagn. Compat*., vol. 58, no. 3, pp. 678-685, June 2016.

[4] M. Barazzetta, D. Micheli, L. Bastianelli, R. Diamanti, M. Totta, P. Obino, R. Lattanzi, F. Moglie, and V. Mariani Primiani, “A comparison between different reception diversity schemes of a 4G-LTE base station in reverberation chamber: A deployment in a live cellular network,” *IEEE Trans. Electromagn. Compat.*, vol. 59, no. 6, pp. 2029-2037, Dec. 2017.

[5] K. A. Remley, R. J. Pirkl, C. Wang, D. Senić, A. C. Homer, M. V. North, M. G. Becker, R. D. Horansky, and C. L. Holloway, “Estimating and correcting the device-under-test transfer function in loaded reverberation chambers for over-the-air tests,” *IEEE Trans. Electromagn. Compat.*, vol. 59, no. 6, pp. 1724-1734, Dec. 2017.

[6] X. Chen, “Experimental investigation of the number of independent samples and the measurement uncertainty in a reverberation chamber,” *IEEE Trans. Electromagn. Compat.,* vol. 55, no. 5, pp. 816-824, Oct. 2013.

[7] N. Wellander, O. Lunden, and M. Bäckström, “Experimental investigation and methematical

modeling of design parameters for efficient stirrers in mode-stirred reverberation chambers," *Trans. Electromagn. Compat.*, vol. 49, no. 1, pp. 94-103, Feb. 2007.

[8] C. Lemoine, P. Besnier, and M. Drissi, "Estimating the effective sample size to select independent measurements in a reverberation chamber," *IEEE Trans. Electromagn. Compat.*, vol. 50, no. 2, pp. 227-236, May 2008.

[9] R. J. Pirkl, K. A. Remley, and C. S. L. Patané, "Reverberation chamber measurement correlation," *IEEE Trans. Electromagn. Compat.*, vol. 54, no. 3, pp. 533-544, June 2012.

[10] X. Chen, "On near-field and far-field correlations in reverberation chambers," *IEEE Microw. and Wireless Compon. Lett.*, vol. 29, no. 1, pp. 74-76, Jan. 2019.

[11] G. Gradoni, V. Mariani Primiani, and F. Moglie, "Reverberation chamber as a multivariate process: FDTD evaluation of correlation matrix and independent positions," *Progress in Electromagnetics Research*, vol. 133, pp. 217-234, Jan. 2013.

[12] J. Clegg, A. C. Marvin, J. F. Dawson, and S. J. Porter, "Optimization of stirrer designs in a reverberation chamber," *IEEE Trans. Electromagn. Compat.*, vol. 47, no. 4, pp. 824-832, Nov. 2005.

[13] Q. Xu and Y. Huang, *Anechoic and Reverberation Chambers: Theory, Design and Measurements*. Wiley-IEEE Press, 2018

[14] W. Petirsch and A. J. Schwab, "Investigation of the field uniformity of a mode-stirred chamber using diffusers based on acoustic theory," *IEEE Trans. Electromagn. Compat.*, vol. 41, no. 4, pp. 446-451, Nov. 1999.

[15] X. Chen, "Measurement uncertainty of RC and its reduction techniques for OTA tests: A review," *IET Microw., Antennas, Propag.*, vol. 13, no. 15, pp. 2598-2604, May 2019.

[16] X. Chen, "Scaling factor for turn-table platform stirring in reverberation chamber," *IEEE Antennas and Wireless Propagat. Lett.*, vol. 16, pp. 2799-2802, Aug. 2017.

[17] G. Cerri, V. Mariani Primiani, S. Pennesi, and P. Russo, "Source stirring mode for reverberation chambers," *IEEE Trans. Electromagn. Compat.*, vol. 47, no. 4, pp. 815-823, Nov. 2005.

[18] X. Chen, W. Xue, H. Shi, J. Yi, and W. E. I. Sha, "Orbital angular momentum multiplexing in highly reverberant environments," *IEEE Microw. and Wireless Compon. Lett.*, vol. 30, no. 1, pp. 112-115, Jan. 2020.

[19] L. Wanderlinder, D. Lemaire, I. Coccato, and D. Seetharamdoo, "Practical implementation of metamaterials in a reverberation chamber to reduce the LUF," *IEEE 5th Int. Symp. Electromag. Compat.*, Beijing, China, Oct. 2017.

[20] H. Sun, C. Gu, Z. Li, Q. Xu, J. Song, B. Xu, X. Dong, K. Wang, and F. Martín, "Enhancing the number of modes in metasurfaced reverberation chambers for field uniformity improvement," *Sensor*, vol. 18, pp. 1-10, Sep. 2018.

[21] J.-B. Gros and P. Hougne, "Tuning a regular cavity to wave chaos with metasurface-reconfigurable walls," *Phy. Review A*, vol. 101, 061801(R), June 2020.

[22] P.-S. Kildal, X. Chen, C. Orlenius, M. Franzén, C. and S. Lötbäck Patané, "Characterization of reverberation chambers for OTA measurements of wireless devices: physical formulations of channel matrix and new uncertainty formula," *IEEE Trans. Antennas Propagat.*, vol. 60, no. 8, pp. 3875-3891, Aug. 2012.

Jiazhi Tang is currently pursuing the Ph.D. degree in Xi'an Jiaotong University. His research interest is metasurface and reverberation chamber.

Furong Li is a Research Assistant at Xi'an Jiaotong University, Xi'an, China.

Junhao Zheng is currently pursuing the Ph.D. degree in Xi'an Jiaotong University. His research interest is OTA testing. He received the B.S. degree in Shandong University, Shandong, China, in 2017, and M.S. degree in Northwest Polytechnic University, Xi'an, China, in 2020.

Xiaoming Chen (M'16, SM'19) received the B.Sc. degree in Electrical Engineering from Northwestern Polytechnical University, Xi'an, China, in 2006, and M.Sc. and Ph.D. degrees in Electrical Engineering from Chalmers University of Technology, Gothenburg, Sweden, in 2007 and 2012, respectively. From 2013 to 2014, he was a Postdoctoral Researcher at the same University. From 2014 to 2017, he was with Qamcom Research & Technology AB, Gothenburg, Sweden, where he was involved in the EU H2020 5GPPP mmMAGIC project (on 5G millimeter-wave wireless access techniques). Since 2017, he has been a Professor at Xi'an Jiaotong University, Xi'an, China. His research areas include 5G multi-antenna techniques, over-the-air (OTA) testing, and reverberation chambers. He has coauthored one book, two book chapter, more than 80 journal papers on these topics. Chen serves as an Associate Editor (AE) for the journal of IEEE Antennas and Wireless Propagation Letters (AWPL). He was also a Guest Editor of a Special Cluster on "5G/6G enabling antenna systems and associated testing technologies" in AWPL and a Special Issue on "Metrology for 5G Technologies" in the journal of IET Microwaves, Antennas & Propagation. He received the URSI (International Union of Radio Science) Young Scientist Awards in 2017 and 2018, and the IEEE outstanding AE awards in 2018 and 2019.

Yingsong Li (M'14-SM'19) received his B.S. degree in Electrical and Information Engineering, and M.S. degree in Electromagnetic Field and Microwave Technology from Harbin Engineering University, 2006 and 2011, respectively. He received his Ph.D. degree from both Kochi University of Technology (KUT), Japan and Harbin Engineering University, China in 2014. He was a Visiting Scholar of University of California, Davis from March 2016 to March 2017, a visiting Professor of University of York, UK in 2018, a Visiting Professor of Far Eastern Federal University (FEFU) and KUT from 2018. He is a Postdoc of Key Laboratory of Microwave Remote Sensing, Chinese Academy of Sciences from 2016 to 2020. Now, he is a full professor of Harbin Engineering University from July 2014. He is a Fellow of Applied computational Electromagnetics Society (ACES Fellow), and he is also a senior member of Chinese Institute of Electronics (CIE) and a senior member of IEEE. He has authored and coauthored about 300 publications in various areas of electrical engineering, antennas and wireless communications. His current research interests include remote sensing, underwater communications, signal processing, radar, SAR imaging, metasurface designs and microwave antennas.

Li is an Area Editor of AEÜ-International Journal of Electronics and Communications, and he is an Associate Editor of IEEE Access and Applied Computational Electromagnetics Society Journal (ACES Journal). He is the TPC Co-Chair of the 2019-2020 IEEE International Workshop on Electromagnetics (iWEM 2019), 2019 IEEE 2nd International Conference on Electronic Information and Communication Technology (ICEICT 2019), 2019 International Applied Computational Electromagnetics Society (ACES) Symposium-China, 2019 Cross Strait Quad-regional Radio Science and Wireless Technology Conference (2019 CSQRWC), and iWEM 2020. He also serves as a Session Chair or Organizer for many international conferences, including the WCNC, AP-S, ACES etc. He acts as a Reviewer of numerous IEEE, IET, Elsevier and other international journals.

Juan Chen was born in Chongqing, China, in 1981. She received the Ph.D. degree in Electromagnetic Field and Microwave Techniques at the Xi'an Jiaotong University, Xi'an, China, in 2008. From April 2016 to March 2017, she was a Visiting Researcher in the Department of Electrical and Computer Engineering, Duke University, Durham, NC, under the financial support from the China Scholarship Council. She now serves as a Professor at Xi'an Jiaotong University.

Her research interests are the numerical electromagnetic methods, advanced antenna designs, and graphene theory and application.

Design of an Array-based Plane Wave Generator for Compact Field Antenna Testing

Fangyun Peng [1], **Xiaoming Chen** [1,2], **Furong Li** [1], **Xiaobo Liu** [1], **Jiaying Zhang** [3], **Ming Zhang** [1], **and Yingsong Li** [4,5]

[1] Faculty of Electronic and Information Engineering
Xian Jiaotong University, Xi’an, 710049, China
xiaoming.chen@mail.xjtu.edu.cn

[2] State Key Laboratory of Millimeter Waves
Southeast University, Nanjing, 211189, China

[3] EM-Testing, Shanghai, 200000, China

[4] College of Information and Communication Engineering
Harbin Engineering University, Harbin, 150001, China

[5] Key Laboratory of Microwave Remote Sensing
National Space Science Center, Chinese Academy of Sciences, Beijing, 100190, China

Abstract **─** A near-field planar array of wideband dual polarized antennas for plane-wave synthesis has been investigated. The paper presents a PWG with a concentric ring array of 84 Vivaldi antennas which can work at 0.6GHz-3GHz. The constraint least square (CLS) algorithm is used to optimize the weight coefficients of the array elements, which effectively reduce the influence of system uncertainty on quiet zone (QZ) ripple. To reduce the system cost and complexity, the array elements in each concentric ring form a sub-array and the elements of the same sub-array adopt a passive beam forming network. The simulation and initial test results of a circular QZ with a diameter of 600 mm are given. The results demonstrate the feasibility of our design.

Index Terms **─** Constrained Least Square (CLS), plane wave synthesis, wideband dual polarized.

I. INTRODUCTION

The fifth generation (5G) technology [1-2] has brought new challenges to radiated tests of radio frequency (RF) and antenna systems [3-22]. The integrated design of RF front-end and antenna makes the traditional conductive test no longer applicable, which puts forward new requirements for 5G testing. Various over-the-air (OTA) measurement methods have attracted great attentions in the development of wireless devices. Generally speaking, all wireless tests conducted in controllable environments, such as anechoic chamber (AC) [5, 6] or reverberation chamber (RC) [7], belong to OTA tests. Direct far-field testing dictates a long distance between the antenna under test and the measurement probe. This can impose challenging demand on the size of the AC, link budget, etc. To reduce the size of the AC (and, therefore, the system cost), various near field antenna measurement techniques have been proposed. The near field antenna measurement system collects the amplitude and phase of each point over a specific plane in the test zone and converts the near-field to the far-field through sophisticated transformation algorithms to obtain the far-field radiation characteristics of the antenna [8]. The compact antenna test range (CATR) relies on the parabolic reflector to convert spherical waves into plane waves. Good measurement performance can be achieved. However, the method is somehow limited by the construction cost and manufacture accuracy. In order to avoid the complicated near-to-far field transformation and reduce the cost, a promising solution is to synthesize plane waves in the near field using the plane wave generator (PWG) method [9-13].

The PWG can generate quasi-plane wave in short distance by optimizing the amplitude and phase of the weighting coefficient of each element, which has the advantages of high accuracy, small size and low maintenance cost. The synthesis procedures and design guidelines regarding size and shape of the PWG, as well as the number of radiating sources needed to synthesize the required plane waves were given in [14]. The

Submitted On: July 29, 2020
Accepted On: April 18, 2021

https://doi.org/10.47037/2021.ACES.J.360910

research focus of PWG designs is to calculate the proper weighting coefficients and to determine the positions of the array elements given the number of radiating sources and the distance between PWG and the antenna under test (AUT). The literature proposes some algorithms, such as least square method (LSM), singular value decomposition (SVD), Genetic Algorithm (GA), Particle Swarm Optimization (PSO), etc. [15-20] to solve the optimization problem. Most of the studies on PWG lack experimental validations until very recently [21-23]. The design and measured performance of a dual-polarized PWG are reported in [22, 23].

The LS method is widely used for plane wave synthesis, but it has the disadvantage of poor adaptability of the mean square error to measurement noise. In order to obtain a stable solution to the ill-conditioned LS problem, the weighting coefficients of the array elements are calculated using the constraint least square (CLS) algorithm based on Lagrange multiplier method, which effectively reduce the influence of system uncertainty on quiet zone (QZ) ripple. And a reference area larger than QZ is introduced to reduce the reflection effect caused by the uneven distribution of the field outside QZ.

We designed a plane wave generator with 84 broadband dual polarized Vivaldi antennas, which is divided into 6 sub-arrays to reduce the system cost. Compared with the previous works [24], the presented PWG design has much fewer antennas and RF chains (and, therefore, a much lower system cost), while providing reasonably good performance. It is a reciprocal structure that can test radiated performances of the RF transceiver link, such as EIRP (Effective Isotropic Radiated Power), EIS (Electrochemical Impedance Spectroscopy), and EVM (Error Vector Magnitude). The designed prototype is validated by experiments.

The structure of the paper is as follows. Section II describes the system model of the PWG and the optimization algorithms in the synthesis processes. A PWG prototype with 84 array elements is designed. In Section III, simulation results and experimental validations show that the PWG can generate a quiet zone (QZ) in the desired frequency band with satisfactory amplitude and phase errors. Section IV draws conclusions.

II. METHOD OF PLANE WAVE SYNTHESIS

A. System model

In this paper, a PWG with a plane array of N antennas and an AUT with a square array of M samples is considered. Assuming the distance between the PWG and AUT is D. As shown in Fig. 1, the field of the m-th sample on the AUT is:

$$E_m = \sum_{n=1}^{N} I_n \frac{e^{j(2\pi/\lambda)R_{mn}}}{4\pi R_{mn}}, \tag{1}$$

where I_n is the excitation current of the n-th antenna element in the PWG, λ is the wavelength and R_{mn} is the distance between the m-th sample and the center of the n-th antenna element. Its vector-matrix representation is given as follows:

$$\mathbf{E} = \mathbf{AI}, \tag{2}$$

where $\mathbf{I} = [I_1, I_2, \cdots I_N]^H$, $\mathbf{E} = [E_1, E_2, \cdots E_M]^H$ with the superscript H denoting conjugate transpose, and $\mathbf{A}$ is a $M \times N$ coefficient matrix given by:

$$\mathbf{A} = \begin{bmatrix} \frac{e^{-j(2\pi/\lambda)R_{11}}}{4\pi R_{11}} & \cdots & \frac{e^{-j(2\pi/\lambda)R_{1N}}}{4\pi R_{1N}} \\ \vdots & \ddots & \vdots \\ \frac{e^{-j(2\pi/\lambda)R_{M1}}}{4\pi R_{M1}} & \cdots & \frac{e^{-j(2\pi/\lambda)R_{MN}}}{4\pi R_{MN}} \end{bmatrix}. \tag{3}$$

The objective is to minimize the amplitude and phase error between the target field and the field sample. And the objective function can be written as

$$f = \min \| \mathbf{A}_{M\times N} \mathbf{I}_{N\times 1} - \mathbf{E}_{0_{M\times 1}} \|_2 , \tag{4}$$

where $\mathbf{E}_0$ is the field of an ideal plane wave and $\|\bullet\|_2$ denotes the Euclidean norm. By taking the derivative of the cost function and forcing it equal zero, the least square (LS) solution is obtained as follows:

$$\mathbf{I} = (\mathbf{A}^H \mathbf{A})^{-1} \mathbf{A}^H \mathbf{E_0} . \tag{5}$$

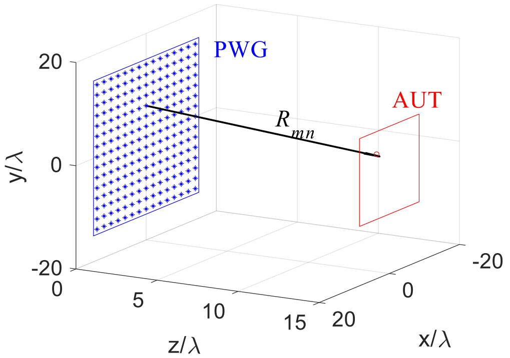

Fig. 1. Geometry of PWG and AUT.

B. The synthesis method

The LS method can find the optimal weighting coefficient of each array element by minimizing the square sum of the error. In order to synthesize a quasi-plane wave on antenna under test (AUT), we set M>>N. The LS problem is an ill-conditioned problem. Small disturbances in the coefficient matrix may cause huge disturbances in the solution, making the calculated LS solution meaningless. Especially in practical applications, the LS algorithm cannot fit well due to the uncertainty of the testing environment and the system accuracy. In order to obtain a stable solution to the ill-conditioned LS problem, we resort to the constrained least square (CLS) method.

The CLS can be expressed as:

$$\min \| \mathbf{AI}-\mathbf{E}_0 \|_2 \quad s.t.\ \mathbf{CI}=\mathbf{D}, \tag{6}$$

where $\mathbf{C}$ is a $P\times N$ matrix, and $\mathbf{D}$ is a $P\times1$-vector. $\| \mathbf{AI}-\mathbf{E}_0 \|_2$ is the objective function and $\mathbf{CI}=\mathbf{D}$ are the equality constraints. $\hat{\mathbf{I}}$ is a solution of CLS. If $\mathbf{C}\hat{\mathbf{I}}=\mathbf{D}$, $\|\mathbf{A}\hat{\mathbf{I}}-\mathbf{E}_0\|_2 \le \|\mathbf{AI}-\mathbf{E}_0\|_2$ holds for any $N\times1$ vector I that satisfies $\mathbf{CI}=\mathbf{D}$.

In this paper, we introduce a reference zone that is larger than the ideal QZ. $\mathbf{E}_0$ is the field of the plane wave of the ideal area, $\mathbf{D}$ is the field of the reference area, and $\mathbf{C}$ is the coefficient matrix of the PWG and the reference area. The amplitude, phase and size of the field outside the QZ and the weighting coefficient of each element on the PWG can be optimized using the global optimization algorithm.

C. Design of PWG

As shown in Fig. 2 (a), the PWG system is mainly composed of antenna array, beam forming network, polarization control turntable, test instruments, and multi-axis turntable. In this paper, a PWG with a concentric ring array of 84 probe elements is designed. The radial spacing between each ring of the PWG is 125 mm. The elements between two neighbouring rings are offset by certain degrees [see Fig. 2 (b)] to reduce to keep the mutual coupling in an acceptable level [24].

In order to improve the QZ size and accuracy, the basic idea of the PWG is to use multiple probe antennas, each of which is equipped with a phase shifter and an attenuator, to synthesize plane wave on the AUT area. However, the application of large-scale antenna arrays will increase construction and maintenance costs. A feasible solution is to divide the whole array into several sub-arrays and the elements in each sub-array share the same phase shifter and attenuator. In total, there are six concentric sub-arrays.

The elements in a concentric ring forms a sub-array and the radiating elements of the same sub-array adopt a passive beam forming network using approximately the same amplitude and phase excitation. As shown in Fig. 3, we use a multi-stage power divider network with power dividers of 1 to 2, 1 to 4, and 1 to 8 power dividers according to the number of each sub-array element.

In the near-field test, the probe has a great influence on the electrical performance of the test system. There are two methods to achieve dual polarized near-field measurement. One is to rotate a single-polarized probe mechanically and the other is to directly use a dual-polarized probe. Since the former increases the hardware complexity of the PWG and the measurement time, dual-polarized probe antennas are widely used. Preferably, the dual-polarized probe should have low cross-polarization, broadband characteristics and small size. The dual-polarized Vivaldi antenna is an ultra-wideband antenna that fulfills all the requirements [25]. Therefore, it is chosen as the radiating element of the PWG in this work.

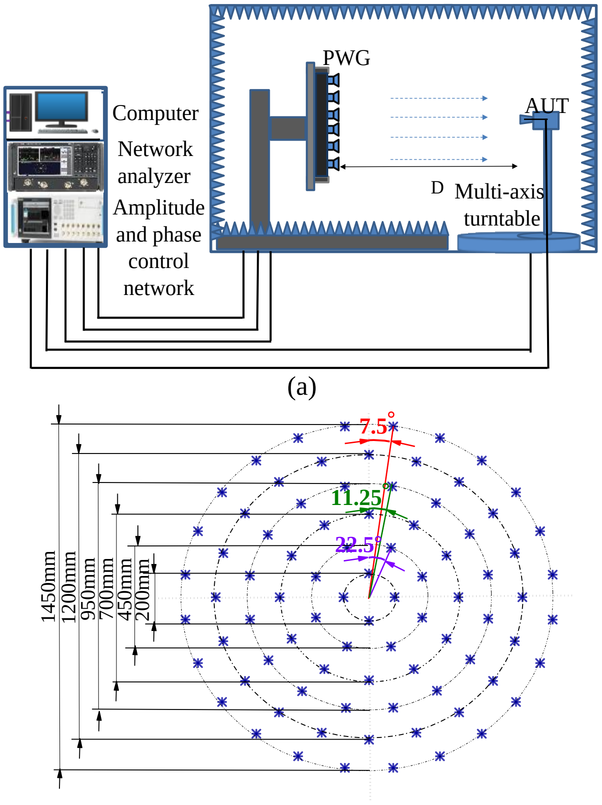

(a)

(b)

Fig. 2. (a) Structure diagram of the PWG testing system; (b) element positions (marked as asterisks) of the PWG.

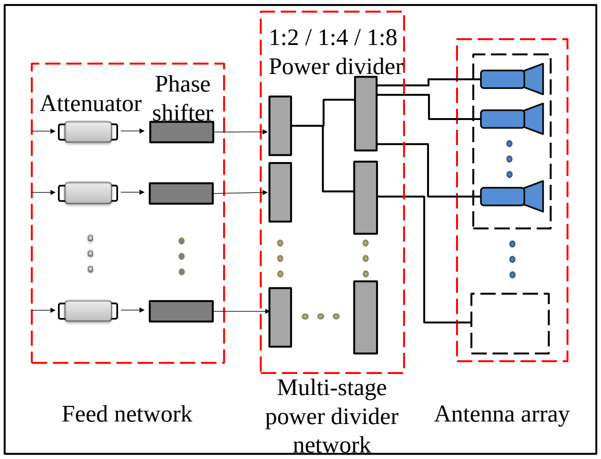

Fig. 3. The structure of the PWG.

III. SIMULATION AND MEASUREMENT RESULTS

A. Simulation

The designed PWG was simulated at 3 GHz. The circular QZ has a diameter of 600 mm. The inter-element spacing of the sampling grids in the QZ is 0.01 m. The distance between the AUT and the PWG is 1.8 m.

The reference area is a circular area with a diameter of 800 mm containing the QZ at its center. Figures 4 and 5 shows the simulation results of the PWG based on the LS and CLS methods (where the QZ is marked in a black circle). The amplitude and phase errors of the QZ generated by the CLS method are within ±0.8 dB and ±5º, respectively. Obviously, the plane waves synthesized by the CLS method are more consistent. Furthermore, compared with the LS method, it can effectively reduce the multipath scattering around the quiet zone. This indicates that the design meets the performance requirements well.

Considering the method of sub-array division, each concentric circle is used as a sub-array to match the excitation source with the same amplitude and phase. This is a trade-off between QZ performance and system complexity. The corresponding simulation results are shown in Fig. 6.

Figure 7 shows the maximum amplitude and phase errors of the QZ on the AUT with distances of 1.5m, 1.8m, 2.0m and 2.3m between the PWG and AUT. As can be seen, when the PWG works within the frequency range of 0.6 GHz-3 GHz, its maximum amplitude error is less than 1 dB and the maximum phase error is less than 2º as the distance of PWG and AUT is more than 2m.

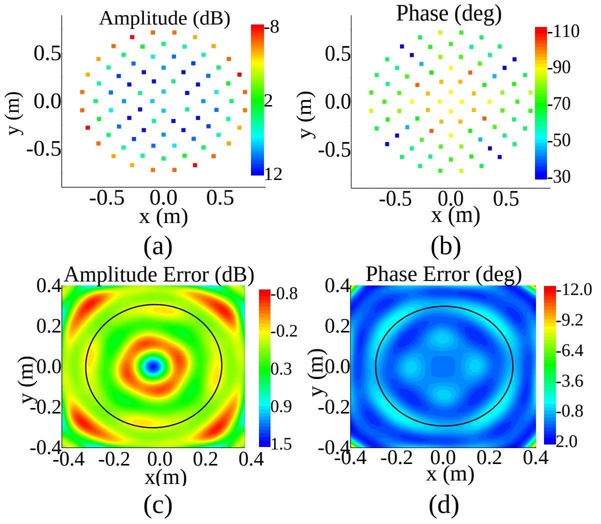

(a) (b)

(c) (d)

Fig. 4. Simulation results of the PWG based on the LS method at 3 GHz. The amplitude (a) and phase (b) of the excitations of the antenna elements in the PWG; the amplitude (c) and phase error (d) on the AUT.

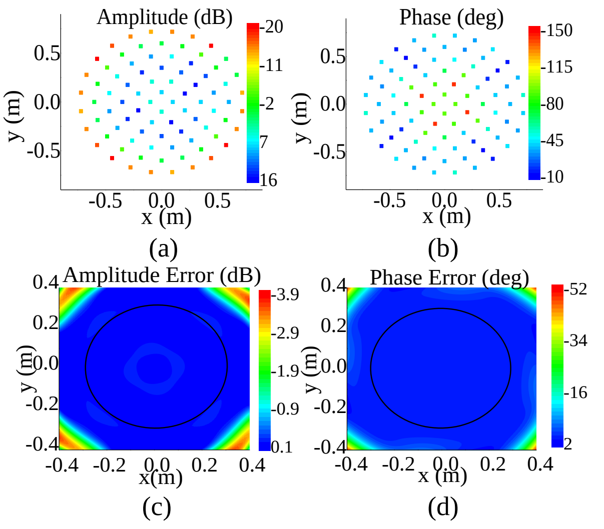

(a) (b)

(c) (d)

Fig. 5. Simulation results of the PWG based on the CLS method at 3 GHz. The amplitude (a) and phase (b) of the excitations of the antenna elements in the PWG; the amplitude (c) and phase error (d) on the AUT.

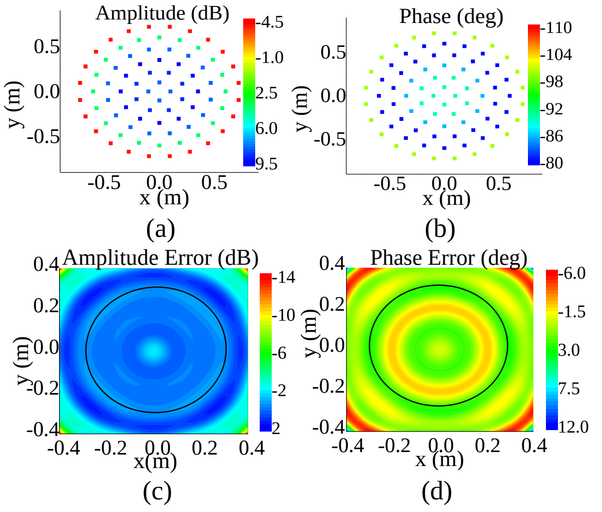

(a) (b)

(c) (d)

Fig. 6. Simulation results of the PWG based on the sub-array method at 3 GHz. The amplitude (a) and phase (b) of the excitations of the antenna elements in the PWG; the amplitude (c) and phase error (d) on the AUT.

B. Measurement

Figure 8 is the actual measurement setup of the PWG system. The mutual coupling between antennas is reduced by inserting absorbing materials between the antenna array elements. The vertical flatness of the QZ was measured using the scanning frame. Figures 9 and 10 present the amplitude and phase errors at the frequencies, 0.6 GHz, 1.5 GHz and 3 GHz with two different distances between the PWG and AUT of 1.8 m and 2.3 m. As can be seen, as the distance increases, the testing results have been significantly improved.

Note that due to the inconsistency of the radiation characteristics of the measurement error of the test probe, the multipath array elements, imperfect calibration of the amplitude and phase imbalance of the feeding network, reflections in the non-anechoic testing environment, etc., the measured results are not as good as the simulated ones. Nevertheless, as can be seen from Figs. 9 and 10, reasonable plane waves can be generated using the PWG at the near-field range.

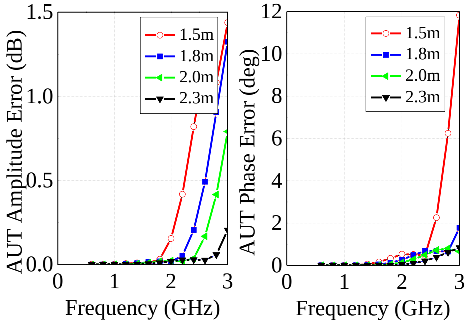

Fig. 7. Maximum amplitude (a) and phase errors (b) on the AUT as a function of frequency with a distance of 1.5 m, 1.8 m, 2.0 m and 2.3 m between the PWG and AUT, respectively.

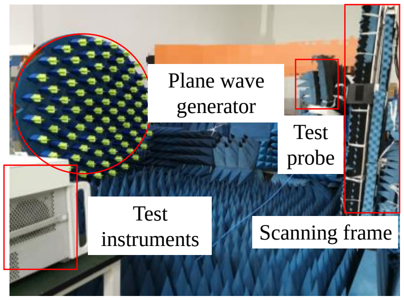

Fig. 8. Measurement setup of the PWG.

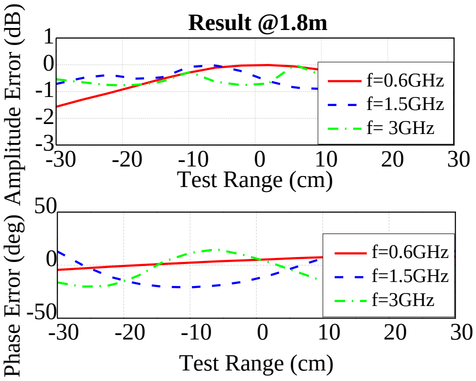

Fig. 9. Measurement results of the PWG at 0.6 GHz, 1.5 GHz and 3 GHz with a distance of 1.8 m between the PWG and AUT.

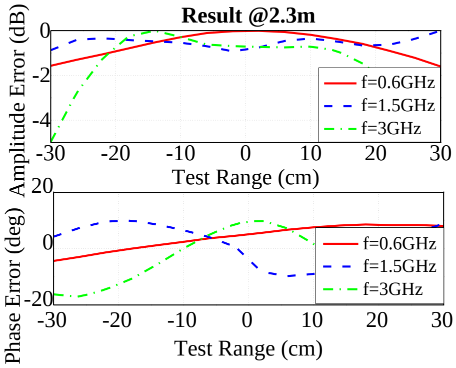

Fig. 10. Measurement results of PWG at 0.6GHz, 1.5GHz and 3GHz with a distance of 2.3m between PWG and AUT.

IV. CONCLUSION

The PWG is an effective OTA test method with the advantages of high accuracy, small size and low maintenance cost. In this paper, we designed a wideband dual-polarized PWG consisting of 84 Vivaldi antennas (divided into six concentric subarrays). In order to enhance the robustness of the system, CLS algorithm is proposed to optimize the weights of array elements. By tradeoff between QZ performance and system complexity, the design of sub-array is introduced to reduce the number of RF channels. The simulation and measurement results of the designed PWG are given in the frequency range of 0.6 GHz - 3 GHz. The test results of the amplitude and phase error in the QZ are in ±1 dB and ±10°, respectively. The unsatisfactory test environment may have a slight impact on the results.

ACKNOWLEDGMENT

This work is supported in part by the National Natural Science Foundation of China under Grants 61801366, 61901354 and by the State Key Laboratory of Millimeter Waves under Grant K201933 and Natural Science Foundation of Shaanxi Province under Grant 2020 JM-078.

REFERENCES

[1] R. He, B. Ai, G. Wang, Z. Zhong, C. Schneider, D. A. Dupleich, R. S. Thomae, M. Boban, J. Luo, and Y. Zhang, “Propagation channels of 5G millimeter wave vehicle-to-vehicle communications: Recent advances and future challenges,” *IEEE Vehicular Technology Magazine*, vol. 15, no. 1, pp. 16-26, Mar. 2020.

[2] G. We and Q. Feng, “Side-frame dual-band MIMO antennas for 5G smartphone applications,” *Applied Computational Electromagnetics Society (ACES) Journal*, vol. 35, no. 11, pp. 1314-1315, Nov. 2020.

[3] W. Fan, P. Kyösti, M. Romney, X. Chen, and G. F.

Pedersen, “Over-the-air radiated testing of millimeter-wave beam-steerable devices in a cost-effective measurement setup,” *IEEE Comm. Mag.*, vol. 56, no. 7, pp. 64-71, July 2018.

[4] X. Chen, W. Fan, P. Kyösti, L. Hentilä, and G. F. Pedersen, “Throughput modeling and validations for MIMO-OTA testing with arbitrary multipath,” *IEEE Antennas Wireless Propag. Lett.*, vol. 17, no. 4, pp. 637-640, Apr. 2018.

[5] Y. Ji, W. Fan, G. F. Pedersen, and X. Wu, “On channel emulation methods in multiprobe anechoic chamber setups for over-the-air testing,” *IEEE Trans. Veh. Technol.*, vol. 67, no. 8, pp. 6740-6751, Aug. 2018.

[6] R. Johnson, H. Ecker, and R. Moore, “Compact range techniques and measurements,” *IEEE Trans. Antennas Propag.*, vol. 17, no. 5, pp. 568-576, Sep. 1969.

[7] X. Chen, W. Xue, H. Shi, J. Yi, and W. Sha, “Orbital angular momentum multiplexing in highly reverberant environments,” *IEEE Microw. Wireless Compon. Lett.*, vol. 30, no. 1, pp. 112-115, Jan. 2020.

[8] M. A. Qureshi, C. H. Schmidt, and T. F. Eibert, “Efficient near-field far-field transformation for nonredundant sampling representation on arbitrary surfaces in near-field antenna measurements,” *IEEE Trans. Antennas Propag.*, vol. 61, no. 4, pp. 2025-576, Apr. 2013.

[9] X. H. Zhang, Z. H. Zhang, and Y. J. Ma, “5G antenna system OTA testing with plane wave generator in range-constrained anechoic chamber,” *Proc. 6th Asia–Pacific Conf. Antennas Propag.*, pp. 1-3, Oct. 2017.

[10] A. Khatun, V. M. Kolmonen, V. Hovinen, D. Parveg, M. Berg, K. Haneda, K. I. Nikoskinen, and E. T. Salonen, “Experimental verification of a plane-wave field synthesis technique for MIMO OTA antenna testing,” *IEEE Transactions on Antennas and Propagation*, vol. 64, no. 7, pp. 3141-3150, July 2016.

[11] R. Xie, X. Wang, R. Wang, T. Wang, D. Chen, T. Song, L. Kuang, and S. Zhu, “Synthesis of plane wave applied to 5G communication antenna measurement,”*2017 Progress in Electromagnetics Research Symposium-Spring (PIERS)*, pp. 195-198, Jan. 2017.

[12] R. Haupt, “Generating a plane wave with a linear array of line sources,” *IEEE Trans. Antennas Propag.*, vol. 51, no. 2, pp. 273-278, Feb. 2003.

[13] O. M. Bucci, C. Gennarelli, and C. Savarese, “Representation of electromagnetic fields over arbitrary surfaces by a finite and nonredundant number of samples,” *IEEE Trans. Antennas Propag.*, vol. 46, no. 3, pp. 351-359, Mar. 1998.

[14] O. M. Bucci, M. D. Migliore, G. Panariello, and D. Pinchera, “Plane-wave generators: Design guidelines, achievable performances and effective synthesis,” *IEEE Trans. Antennas Propag.*, vol. 61, no. 4, pp. 2005-2018, Apr. 2013.

[15] D. Yu, H. Zhang, and W. Liu, “Synthesis of a plane-wave via linear array with unequal interval,” *ISAPE2012*, pp. 827-829, Oct. 2012.

[16] D. A. Hill, “A numerical method for near-field array synthesis,” *IEEE Transactions on Electromagnetic Compatibility*, vol. EMC-27, no. 4, pp. 201-211, Nov. 1985.

[17] A. Capozzoli, C. Curcio, G. D'Elia, A. Liseno, and P. Vinetti, “A novel approach to the design of generalized plane-wave synthesizers,” *European Conference on Antennas and Propagation (EuCAP)*, Berlin, Germany pp. 3375-3379, Mar. 2009.

[18] A. Capozzoli, C. Curcio, and A. Liseno, “Singular value optimization in inverse electromagnetic scattering,” *IEEE Antennas and Wireless Propag. Lett.*, vol. 16, pp. 1094-1097, 2017.

[19] M. D'Urso, G. Prisco, and M. Cicolani, “Synthesis of plane-wave generators via nonredundant sparse arrays,” *IEEE Antennas and Wireless Propagation Letters*, vol.8, pp. 449-452, Mar. 2009.

[20] D. Yu, G. Xie, W. Zhai, and D. Fu, “The optimization of cosine window function using genetic algorithm and its application in plane wave synthesis,” *2011 4th IEEE International Symposium on Microwave, Antenna, Propagation and EMC Technologies for Wireless Communications*, Beijing, pp. 194-197, Nov. 2011.

[21] R&S Report. Report on R&S®PWC200 Plane Wave Converter for 5G massive MIMO base station testing, March, 2019. https://scdn.rohde-schwarz.com/ur/pws/dl_downloads/dl_common_library/dl_brochures_and_datasheets/pdf_1/PWC200_fly_en_5215-5971-32_v0200.pdf

[22] F. Scattone, D. Sekuljica, A. Giacomini, F. Saccardi, A. Scannavini, N. Gross, E. Kaverine, P. O. Iversen, and L. J. Foged, “Design of dual polarised wide band plane wave generator for direct far-field testing,” *European Conference on Antennas and Propagation (EuCAP)*, Kracow, Poland, pp. 1-4, Apr. 2019.

[23] Y. Zhang, Z. Wang, X, Sun, Z. Qiao, and J. Miao, “Design and implementation of a wideband dual polarized plane wave generator with tapered feeding nonuniform array,” *IEEE Antennas and Wireless Propag. Lett.*, vol. 19, no. 11, pp. 1988-1992, Nov. 2020.

[24] X. Chen, S. Zhang, and Q. Li, “A review of mutual coupling in MIMO systems,” *IEEE Access*, vol. 6, pp. 24706-24719, Apr. 2018.

[25] H. Lv, Q. Huang, J. Hou, and J. Liu, “Wideband dual-polarized Vivaldi antenna with gain enhancement,” *Applied Computational Electromagnetics*

Society (ACES) Journal, vol. 33, no. 9, pp. 990-996, Sep. 2020.

Fangyun Peng received the B.Sc. degree in Electrical Information Engineering from Southwest Jiaotong University, Chengdu, China, in 2018. She is currently pursuing the M.S. degree in Information Engineering from Xi'an Jiaotong University. Her research interests include OTA test.

Xiaoming Chen received the Ph.D. degree from the Chalmers University of Technology, Gothenburg, Sweden, in 2012. From 2012 to 2014, he was a Postdoctoral Researcher at the same University. From 2014 to 2017, he was with Qamcom Research & Technology AB, Gothenburg. Since 2017, he has been a Professor with Xi'an Jiaotong University, Xi'an. His research areas include 5G multi-antenna techniques, over-the-air (OTA) testing, and reverberation chambers. Prof. Chen serves as an Associate Editor (AE) for the journal of IEEE Antennas and Wireless Propagation Letters (AWPL).

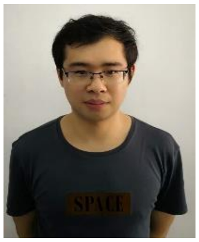

Furong Li is a Research Assistant at Xi’an Jiaotong University, Xi’an, China.

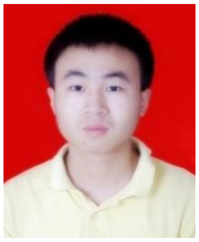

Xiaobo Liu received the Ph.D. degree in Electronic Science and Technology from Xi’an Jiaotong University, Xi’an, China, in 2018. Since 2020, he has been an Assistant Professor with Xi’an Jiaotong University. His research interests include electromagnetic and microwave theory, computational electromagnetics, antenna design, and microwave circuit.

Jiaying Zhang is the General Manager in Shanghai EM-Testing Co., LTD.

Ming Zhang received the Ph.D. degree from Xi'an Jiaotong University, Xi'an, China, in 2017, respectively. He is now an Associated Professor at Xi'an Jiaotong University.

Yingsong Li received his Ph.D. degree from both Kochi University of Technology (KUT), Japan and Harbin Engineering University, China in 2014. He is currently a Full Professor of Harbin Engineering University. His current research interests include remote sensing, underwater communications, signal processing, radar, SAR imaging, and microwave antennas. Li is an Area Editor of AEÜ-International Journal of Electronics and Communications, and he is an Associate Editor of IEEE Access and Applied Computational Electromagnetics Society Journal (ACES Journal).

A Compact Multi-Probe Reverberation Chamber for Over-the-Air Testing

Wenjun Qi, Feng Fang, Wenjun Xia, Yongjiu Zhao, Lei Xing, and Qian Xu*

College of Electronic and Information Engineering
Nanjing University of Aeronautics and Astronautics, Nanjing 211106, China
qiwenjun@nuaa.edu.cn, *emxu@foxmail.com

Abstract ─ In this paper, a compact multi-probe reverberation chamber (RC) is proposed for over-the-air (OTA) testing. 16 probe antennas are used to reduce the measurement time. Typical parameters of the RC, such as field uniformity (FU), quality factor (*Q* factor), and independent samples are given. Total radiated power (TRP) and pattern correlation measurements have been performed to validate the RC system.

Index Terms ─ Compact, multi-probe RC, OTA.

I. INTRODUCTION

Reverberation chamber (RC) is an electrically large shielded cavity, which utilizes the rotation of mechanical stirrers to create a statistically uniform, isotropic, and randomly polarized fields [1-2]. Initially, an RC was widely applied to electromagnetic compatibility (EMC) testing [3-4].

With the development of the fifth-generation (5G) wireless system and various discoveries of new statistical electromagnetics in recent years, researchers have introduced RC into over-the-air (OTA) wireless device testing gradually [5]. In contrast with multi-probe anechoic chamber (MPAC) [6] and radiated two-stage (RTS) [7], RCs are more cost-effective and has larger test area in some applications. Thus, well-developed standards have been proposed in industry for OTA testing, such as IEC 61000-4-21and CTIA [8, 9]. RC has been generally used to perform total radiated power (TRP), total isotropic sensitivity (TIS), pattern correlation, diversity gain, throughput measurements of a device under test (DUT), and other fields [10-13]. Typical simulation methods of an RC are Monte-Carlo method, time domain simulation, and frequency domain simulation [14-16].

In previous work, multi-probe systems are generally used to evaluate the performance of RC or anechoic chamber (AC) [17-20]. In this paper, a compact multi-probe RC for OTA testing is designed and fabricated to meet the needs of large scale and rapid measurement of wireless devices. Compared with conventional RCs equipped with limited receiving (Rx) antennas [8], multi-probe Rx antennas can measure more samples rapidly and enhance the testing efficiency. A vertical stirrer is also used to have a hybrid stirring.

Section II presents the parameters of the proposed RC. A brief introduction of measurement setup and results are shown in Section III. Finally, Section IV concludes this article.

II. DESIGN AND ANALYSIS

The design of the proposed RC is introduced in Fig. 1, with internal dimensions of 0.6 m×0.45 m ×0.46 m. 16 probe antennas are optimized to have a good isolation and are placed on the walls of the RC. A radio frequency (RF) switch is used to switch received power from different probes. In this section, typical figures of merit: field uniformity (FU), quality factor (*Q* factor), independent sample number of the multi-probe RC are investigated to characterize its performance.

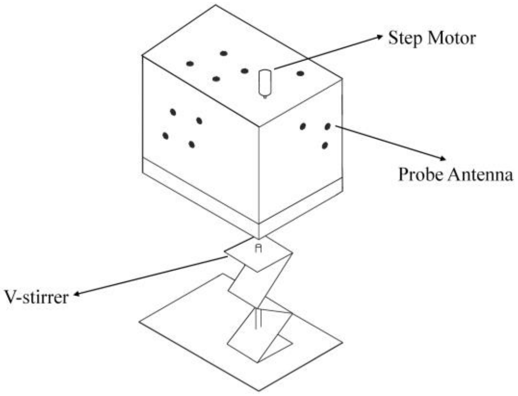

Fig. 1. The multi-probe RC, the inner dimensions are 0.6 m×0.45 m×0.46 m.

A. Field uniformity

The FU is a fundamental parameter of an RC, which characterizes the statistical uniformity of an RC. It is defined as the relative standard deviation of the maximum values obtained at the eight positions in RC [2]. When the standard deviation (dB) is lower than the field uniformity tolerance requirements given in [8], the field in RC can be regarded as statistically uniform. The

Submitted On: June 24, 2021
Accepted On: August 24, 2021

https://doi.org/10.47037/2021.ACES.J.360911

lowest usable frequency (LUF) is the lowest frequency, which occurs three to six times the first chamber resonance f_{1st}. The f_{1st} is 410MHz and the theoretical LUF is about 1.23 GHz~2.46 GHz. The possible mode is 72, which meets the requirements in the RC [8].

In this measurement, transmitting (Tx) antenna is placed at 5 different positions within the corner and the center of the working volume, as shown in Fig. 2. In Fig. 3, the FUs obtained from the mean received power (P_r) and the maximum P_r, are lower than the FU tolerance from 0.94 GHz to 14 GHz. Furthermore, the LUF is 0.94GHz, lower than the theoretical value, which means the multi-probe Rx antennas system enhances the stirring efficiency.

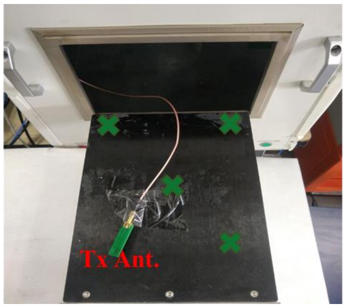

Fig. 2. FU measurement setup.

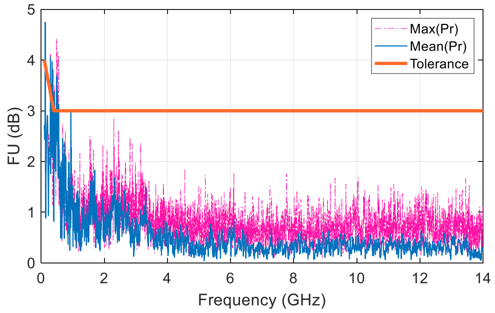

Fig. 3. The FU in the RC compared with the tolerance requirements.

B. Quality factor

Q factor represents the ability of a cavity to store energy, which is defined as the ratio of the dissipated power P_t to the stored power U:

$$Q = \frac{\omega U}{P_t}. \tag{1}$$

Here, we use the time domain (TD) method to calculate Q factor [2]. The chamber decay constant τ_{RC} is obtained from the trace of the received power in TD, thus Q factor can be calculated from:

$$Q = \omega \tau_{RC}, \tag{2}$$

where ω is the angular frequency. The coherence bandwidth Δf can be obtained as:

$$\Delta f = \frac{f}{Q}, \tag{3}$$

where f is the frequency of interest. The τ_{RC}, Q factor and Δf are demonstrated in Figs. 4 (a) and (b), which can be changed through different loading conditions. An appropriate value in RC is useful to realize a stable link for OTA testing.

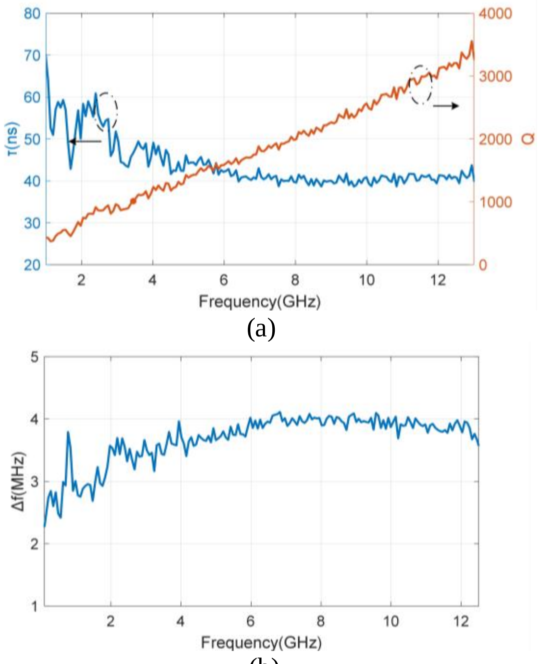

(a)

(b)

Fig. 4. Measured τ_{RC} , Q factor and Δf in the RC.

C. Correlation coefficient and independent sample number

To calculate the correlation coefficient among the probe antennas, we select two of 16 probes randomly, with a total of 120 combinations. The correlation coefficients from 1 GHz to 14 GHz are given in Fig. 5. When the frequency is larger than LUF, the R among typical groups is almost stable below 0.37, indicating that the probe antennas are mutually independent.

Then, the correlated angle and independent sample number for the V-stirrer are calculated. The correlation coefficient is to assess the performance of the stirrer, which is obtained as [8]:

$$\rho(\theta) = \frac{\frac{1}{n-1}\sum_{i}^{n}(x_i - u_x)(y_{\theta,i} - u_y)}{\sqrt{\frac{\sum_{i}^{n}(x_i - u_x)^2}{n-1}\frac{\sum_{i}^{n}(y_{\theta,i} - u_y)^2}{n-1}}}, \tag{4}$$

where n is the sample number over one rotation period, x_i is the received power at each stirrer position, $y_{\theta,i}$ is a shifted version of x_i by angle θ, u_x and u_y are averaged received powers. The correlated angle $\Delta\theta$ is decided by a threshold $e^{-1} \approx 0.37$. The independent sample number N_{Ind} is $360/\Delta\theta$. The results are shown in Fig. 6.

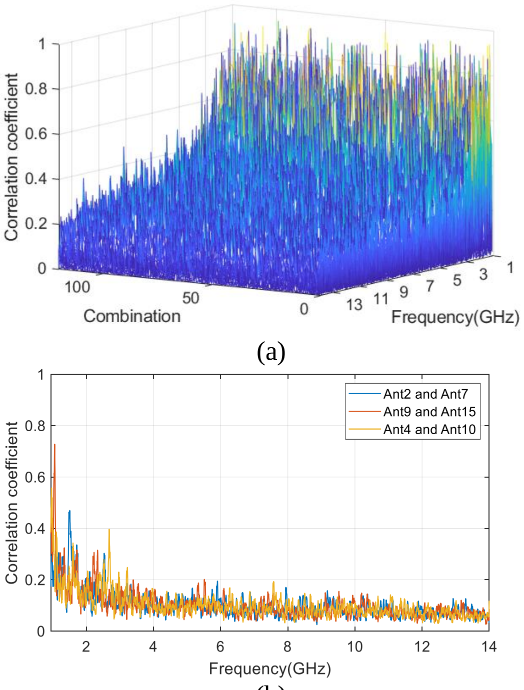

(a)

(b)

Fig. 5. The correlation coefficient between different probe antennas from 1 GHz to 14 GHz.

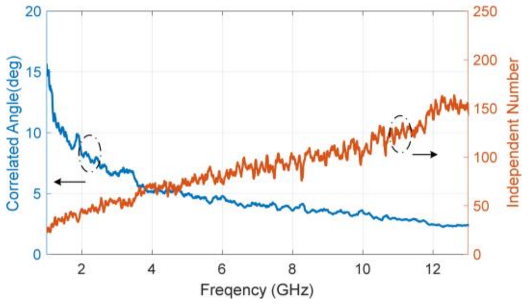

Fig. 6. Correlated angle and independent sample number.

D. *K*-Factor

The *K*-factor is the ratio between the direct power and the stirred power in RC [21]. When *K*=0, the channel is an ideal Rayleigh channel. To improve the accuracy of measurement, it is optimal to decrease the contribution of direct power. In this measurement, the *K*-factor is obtained from (5),

$$K = \frac{\left|\langle S_{21}\rangle\right|^2}{\left\langle\left|S_{21} - \langle S_{21}\rangle\right|^2\right\rangle}. \tag{5}$$

S parameters (16 × 180=2880) for different frequencies are measured between the Tx antenna and the Rx antenna. The measured *K*-factor is illustrated in Fig. 7, *K*-factors with typical probe 1, 7 and 9 are given, *K*-factor with hybrid stirring is also presented. Note that the mean value of the *K*-factor is lower than -20 dB using a hybrid stirring in the frequency range of (1 GHz -13 GHz), which means an equivalent high total scattering cross section is achieved (i.e., high stirring efficiency).

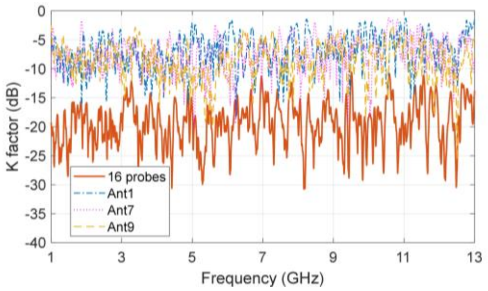

Fig. 7. Measured *K*-factors in the RC.

III. MEASUREMENTS AND RESULTS

A. Total radiated power

TRP is one of the performance indicators in OTA testing, which usually reflects the transmitted power of wireless devices. Here, we utilize multi-probe RC to realize fast and accurate measurements in 5G FR1 band.

As shown in Fig. 8, the test procedure of TRP is as follows:

1. Conduct the transfer function characterization procedure with the reference power [8].

2. Put the DUT (a WIFI device) into the RC. With the power meter and RF switch, measure and record 16 powers received by different probe antennas in each stirring sample.

3. TRP can be calculated from (6):

$$P_{\mathrm{TRP}} = \frac{1}{N}\frac{\sum_{n=1}^{N} P_n}{G_{\mathrm{ref}}\, e_{\mathrm{mismatch,meas}}\, \eta_{\mathrm{meas}}\, G_{\mathrm{cable}}}, \tag{6}$$

where N is the total sample number, P_n is the nth measured power, G_{ref} is the power transfer function, G_{cable} is the loss of the cable and $e_{\mathrm{mismatch,meas}}$ is the antenna mismatch factor.

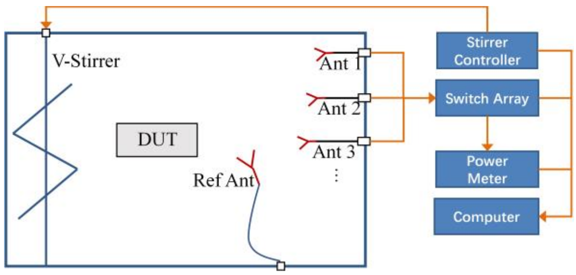

Fig. 8. Configuration of the multi-probe RC for TRP measurement.

We recorded 720 power values (8° one step and 45 stirrer positions) at 2.4 GHz and 5.18 GHz. When the V-stirrer rotates once, the RF switch turns to 16 probe antennas in sequence, therefore, 16 samples can be measured in one step. Multi-Probe could obtain 16 samples within 2.1 seconds, while conventional probe in RC needs 128 seconds. It only takes 5 minutes to get 720 samples. Thus, the method can effectively decrease the testing time and obtain much more samples rapidly and accurately in the same period.

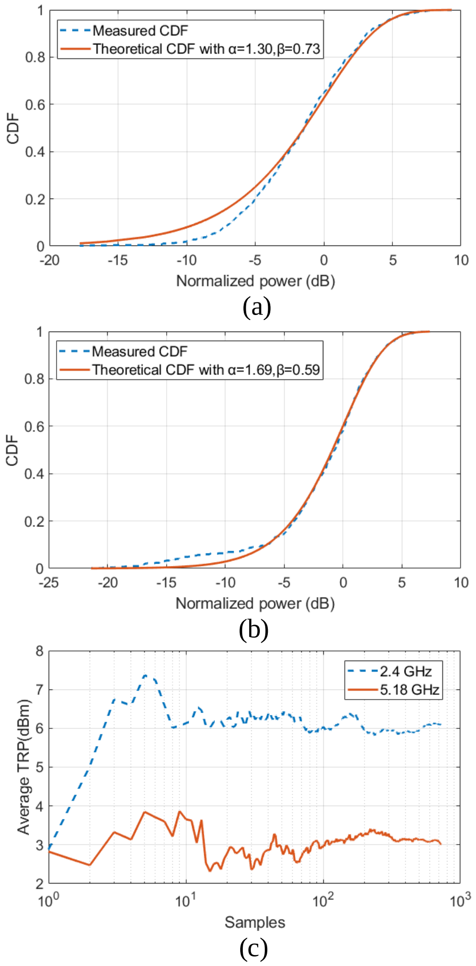

(a)

(b)

(c)

Fig. 9. (a) CDFs of the measured and theoretical normalized power samples at 2.4 GHz; (b) 5.18 GHz; (c) average TRP at 2.4 GHz, 6.03 dBm and 5.18 GHz, 3.00 dBm.

The bandwidth of signal transmitted from DUT is not much larger compared with the coherence bandwidth of the proposed RC shown in Fig. 4 (b) [22]. So that, the cumulative distribution function (CDF) of the measured normalized power *p(x)* is gamma distribution in (7):

$$p(x)=\frac{(1/\beta)^{\alpha}}{\Gamma(\alpha)}x^{\alpha-1}e^{-x/\beta}, \tag{7}$$

where $\alpha \approx \mathrm{BW}/\Delta f$, BW is the bandwidth of the signal, β is the mean value of measured power samples.

As shown in Figs. 9 (a)-(c), the measurement results agree well with the theoretical CDF at 2.4 GHz and 5.18 GHz. We also calculate average TRP of DUT in the above frequency. The theoretical lower limit of σ_{rTRP} is 4.21% at 2.4 GHz, 4.17% at 5.18 GHz.

B. Pattern correlation

The pattern correlation can be used to check the antenna status for a DUT with multiple antennas. Suppose we have a reference device (which we know the performance is good), by comparing the pattern correlations between the DUT antenna and the reference device (with the same port), we can identify the similarity between the radiation pattern of the DUT and the reference. If the pattern correlations deviate from reference values significantly, there should be something wrong for the antenna performance.

According to the conclusions given in [11], the angular correlation can be defined over the measured received power. Therefore, we can calculate the pattern correlation by the received powers of the multi-probe antennas. The testing setup of pattern correlation is similar to the measurement of TRP. The only distinction is that the pattern correlation measurement does not need a reference antenna. The procedure is executed using the following steps:

1. Place the reference device into the valid test volume of the chamber. Turn on the power meter, the measured radiated powers for all probe antennas and each mode-turn sample can be obtained, which is $P_{11}, P_{12}, \dots P_{1n}$($n$ represents mode-stirring numbers).

2. Replace the reference device with the DUT in the same position. Rotate the mode-stirring paddle as the same sequence determined by the standard-part procedure. The measured radiated powers $P_{21}, P_{22}, \dots P_{2n}$ can be received.

3. Calculate the value of radiated pattern correlation R by taking an average of all power samples and formula (8):

$$R=\frac{\frac{1}{n-1}\sum_{i}^{n}(P_{1i}-\langle P_1\rangle)(P_{2i}-\langle P_2\rangle)}{\sqrt{\frac{\sum_{i}^{n}(P_{1i}-\langle P_1\rangle)^2}{n-1}\frac{\sum_{i}^{n}(P_{2i}-\langle P_2\rangle)^2}{n-1}}}, \tag{8}$$

where P_n is the measured power for the n_{th} sample and N is the total number of mode-stirring samples, $\langle P_1\rangle$ and $\langle P_2\rangle$ are the average of the standard part and DUT total mode-stirring samples respectively. As shown in Fig. 10 (a), the pattern correlation coefficient R is close to 1, therefore DUT1 works well as expected. In (b), there should be something wrong of antenna 1 in DUT2.

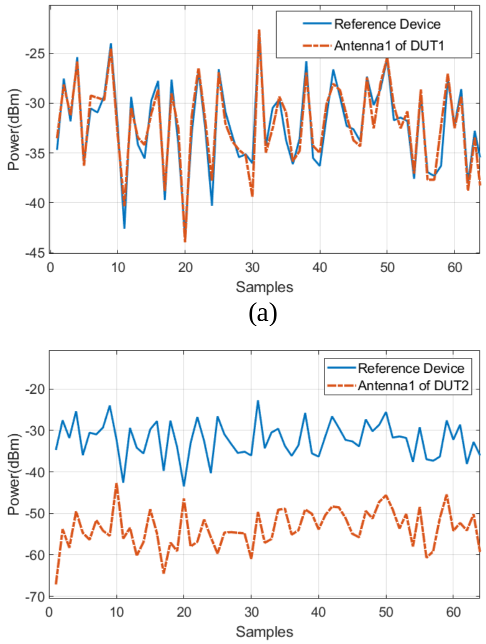

(a)

(b)

Fig. 10. Pattern correlation between different antennas: (a) R=0.9520; (b) R=0.1552.

IV. CONCLUSION

A compact multi-probe RC is manufactured in this paper. Typical figures of merit in the compact multi-probe RC are presented to assess the performance of RC. The FU satisfies the FU tolerance in [8] and the LUF is about 0.94 GHz. The correlation coefficient shows that 16 probe antennas are independent of each other.

We have shown that when the radiated spectrum is wider than the coherence bandwidth, the measured TRP has a Gamma distribution in the frequency band of 2.4 GHz and 5.18 GHz. The average TRP and σ_{rTRP} have been measured. The proposed system is very efficiency, in the TRP measurement, the measurement duration of 16 samples is about 2.1 seconds (with 0.13 s/sample). The pattern correlations between different antennas of the DUTs have also been measured.

ACKNOWLEDGMENT

This work was supported in part by the Fundamental Research Funds for the Central Universities (No. NS2021029), and in part by the National Natural Science Foundation of China under Grants 61701224 and 61601219.

REFERENCES

[1] D. A. Hill, *Electromagnetic Fields in Cavities: Deterministic and Statistical Theories*. Hoboken, NJ, USA, 2009.

[2] Q. Xu and Y. Huang, *Anechoic and Reverberation Chambers: Theory, Design and Measurements*. Wiley-IEEE, UK, 2019.

[3] P. Corona, G. Latmiral, E. Paolini, and L. Piccioli, "Use of a reverberating enclosure for measurements of radiated power in the microwave range," *IEEE Trans. Electromagn. Compat.*, vol. EMC-18, no. 2, pp. 54-59, May 1976.

[4] W. Li, C. Yue, and W. Yu, "Study on array source stirring reverberation chamber," *Applied Computational Electromagnetics Society Journal*, vol. 29, no. 12, pp. 1067-1076, Dec. 2014.

[5] X. Chen, J. Tang, T. Li, S. Zhu, Y. Ren, Z. Zhang, and A. Zhang, "Reverberation chambers for over-the-air tests: An overview of two decades of research," *IEEE Access*, vol. 6, pp. 49129-49143, Aug. 2018.

[6] W. Fan, X. C. B. de Lisbona, F. Sun, J. O. Nielsen, M. B. Knudsen, and G. F. Pedersen, "Emulating spatial characteristics of MIMO channels for OTA testing," *IEEE Trans. Antennas Propag.*, vol. 61, no. 8, pp. 4306-4314, Aug. 2013.

[7] W. Yu, Y. Qi, K. Liu, Y. Xu, and J. Fan, "Radiated two-stage method for LTE MIMO user equipment performance evaluation," *IEEE Trans. Electromagn. Compat.*, vol. 56, no. 6, pp. 1691-1696, Dec. 2014.

[8] IEC 61000-4-21, *Electromagnetic compatibility (EMC) – Part 4-21: Testing and measurement techniques – Reverberation chamber test methods*, IEC Standard, Ed 2.0, 2011-01.

[9] CTIA, *Test Plan for Wireless Large-Form-Factor Device Over-the-Air Performance*, ver. 1.2.1, Feb. 2019.

[10] H. G. Krauthauser, "On the measurement of total radiated power in uncalibrated reverberation chambers," *IEEE Trans. Electromagn. Compat.*, vol. 49, no. 2, pp. 270-279, June 2007.

[11] Q. Xu, L. Xing, D. Yan, Y. Zhao, and Y. Huang, "Experimental verification of stirrer angular correlation with different definitions in a reverberation chamber," *the 12th International Symposium on Antennas, Propag. and EM Theory (ISAPE 2018)*, Hangzhou, China, pp. 1-5, Feb. 2018.

[12] K. Karlsson, X. Chen, J. Carlsson, and A. Skarbratt, "On OTA test in the presence of doppler spreads in a reverberation chamber," *IEEE Antennas Wireless Propag. Lett*., vol. 12, pp. 886-889, July 2013.

[13] A. Sorrentino, G. Ferrara, and M. Migliaccio, "The reverberating chamber as a line-of-sight wireless channel emulator," *IEEE Trans. Antennas Propag.*, vol. 56, pp. 1825-1830, June 2008.

[14] Y. Cui, H. G. Wei, S. Wang, and L. Fan, "Efficient method of optimizing reverberation chamber using FDTD and genetic algorithm method," *Applied Computational Electromagnetics Society Journal*, vol. 28, no. 4, pp. 293-299, Apr. 2013.

[15] J. M. Ladbury, "Monte Carlo simulation of

reverberation chambers," *Gateway to the New Millennium. 18th Digital Avionics Systems Conference. Proceedings (Cat. No.99CH37033)*, pp. 10.C.1-10. C.1, Oct. 1999.

[16] S. Wang, Z. Wu, L. Du, G. Wei, and Y. Cui, "Study on the matrix pencil method with application to predict time-domain response of a reverberation chamber," *Applied Computational Electromagnetics Society Journal*, vol. 28, no. 9, pp. 763-771, Sep. 2013.

[17] D. Mandaris, R. Vogt-Ardatjew, E. Suthau, and F. Leferink, "Simultaneous multi-probe measurements for rapid evaluation of reverberation chambers," *2018 IEEE Intern. Symposium on Electromagn. Compat. and 2018 IEEE Asia-Pacific Symposium on Electromagn. Compat (EMC/APEMC)*, pp. 590-594, May 2018.

[18] D. Mandaris, R. Vogt-Ardatjew, M. Zaher Mahfouz, E. Suthau, and F. Leferink, "Time efficient reverberation chamber performance analysis using simultaneous multiprobe measurement technique," *Intern. Symposium on Electromagn. Compat. (EMC EUROPE)*, pp. 1-5, Aug. 2018.

[19] L. Anchidin, F. Bari, R. D. Tamas, L. Pometcu, and A. Sharaiha, "Near-field gain measurements: Single-probe distance averaging in a multipath site versus multi-probe field scanning inside an anechoic chamber," *2017 General Assembly and Scientific Symposium of the International Union of Radio Science (URSI GASS)*, pp. 1-3, Aug. 2017.

[20] J. Andersson and Z. Ying, "Analysis of different sampling methods in a reverberation chamber," *2006 First Eur. Conf. Antennas Propag. (EUCAP)*, pp. 1-5, Nov. 2006.

[21] C. L. Holloway, D. A. Hill, J. M. Ladbury, P. F. Wilson, G. Koepke, and J. Coder, "On the use of reverberation chambers to simulate a rician radio environment for the testing of wireless devices," *IEEE Trans. Antennas Propag.*, vol. 228, pp. 3167-3177, Nov. 2006.

[22] Q. Xu, W. Qi, C. Liu, L. Xing, D. Yan, Y. Zhao, T. Jia and Y. Huang, "Measuring the total radiated power of wideband signals in a reverberation chamber," *IEEE Antennas Wireless Propag. Lett.*, vol. 19, pp. 2260-2264, Oct. 2020.

A Broadband Dual-polarized Antenna for 2G/3G/4G/5G Base Station Applications

Ya-Li Chen [1], Yao-Zong Sui [1], Zhi-Qun Yang [2], Xiao-Yun Qu [2], and Wei-Hua Zong [1*]

[1] School of Electronics and Information
Qingdao University, Qingdao, 266000, China
*weihuazong@126.com

[2] Shandong Institute of Space Electronic Technology
Yantai, 264003, China

***Abstract* ─** This paper presents a novel broadband base station antenna element covering 2G/3G/4G/5G bands. The proposed antenna consists of a dual-dipole radiator and an open-box shaped reflector. The main radiating portion of each dipole arm is designed with a dual-hexagon shape to improve bandwidth. Four small hexagonal-shaped parasitic patches are adopted to further decrease the reflection coefficient. Dual polarization is excited by placing two dipoles orthogonally. The open-box shaped reflector derives from a planar metal plate with four inverted L-shaped edges which are arranged below the radiator to enhance the antenna gain and reduce the half power bandwidth (HPBW) in 3.3-3.8 GHz. The prototype has been fabricated and measured with bandwidth of 1.68-3.8 GHz, coupling below -20 dB, stable HPBW with 65°± 5° and average gain of 8.5 dBi. The values of the cross-polarization discrimination (XPD) are better than 20 dB at the boresight and 10 dB within ±60° directions. The proposed antenna has a small overall size of 145×145×35.6 mm^3.

***Index Terms* ─** 5G antenna, base station antenna, broadband antenna, dual-polarized antenna.

I. INTRODUCTION

The fifth-generation (5G) communication working at the FR1 band (0.45-6 GHz) has been commercially launched in many countries to provide high-speed data transmission and high-quality network link. There is an urgent need for base station antennas covering 5G FR1 band. The frequency bands of 2G/3G/4G are appealing to be included in the a 5G antenna covering 1.71-3.8 GHz frequency band [1] to save the space volume of a base station system. Dual polarization is also required for a base station antenna to increase channel capacity and decrease channel fading influence.

Plenty of researches on base station antenna have been performed over the last few years. To obtain dual polarization, adopting double orthogonal dipoles is an effective method [1-11]. Antenna with single patch can also achieve dual polarization by using orthogonal feeding lines [12] or slots [13-14].

To improve antenna bandwidth, a number of techniques have been proposed. In [3], a filter-based matching circuit is adopted to feed full-wavelength dipoles. In [4], parasitic patches are arranged on top of four-loop radiators for bandwidth enhancement. Wide bandwidth can be also achieved by designing dipole arm’s shape and improving coupling between adjacent arms [5-6]. In [7], double annular disks and gradient strips are adopted for the bandwidth enhancement. In [15], a stepped-impedance feeding structure combining with a T-shaped patch is used to excite multiple resonances. Microstrip balun is adopted in [16] to improve bandwidth. It is still challenging to design a broadband base station antenna covering 2G/3G/4G/5G bands with dual polarization and stable half power bandwidth (HPBW).

In this paper, a planar base station antenna covering 2G/3G/4G/5G bands of 1.71-3.8GH is proposed. The radiator consists of a pair of double-hexagon dipoles and four small hexagonal parasitic patches printed on double layers of the substrate orthogonally to achieve wide bandwidth and dual polarization. Four inverted L-shaped edges are added to a planar reflector enhance the antenna gain and reduce the HPBW.

II. ANTENNA CONFIGURATION

The configuration of the dual-polarized antenna is illustrated in Fig. 1. The proposed antenna consists of a radiator and a reflector. The radiator includes four main patches with double-hexagon shape (MP$_{11}$, MP$_{12}$, MP$_{21}$ and MP$_{22}$) and four small parasitic patches (PP$_1$, PP$_2$, PP$_3$ and PP$_4$). The main patches of MP$_{11}$ and MP$_{12}$ form a planar dipole with +45° polarization, and MP$_{21}$ and MP$_{22}$ form another one with -45° polarization. Each main patch consists of a larger hexagonal patch embedded with a smaller one. The larger hexagonal patch is etched with a polygonal slot to avoid overlapping with the inner

Submitted On: July 8, 2021
Accepted On: September 9, 2021

https://doi.org/10.47037/2021.ACES.J.360912

smaller one. As shown in Fig. 1, MP_{21}, PP_1, PP_2 and PP_3 are printed on the top layer of a FR-4 dielectric substrate, and MP_{11}, MP_{12}, MP_{22} and PP_4 are printed on its bottom layer. The FR-4 substrate has a relative permittivity of 4.4 and a dielectric loss tangent of 0.02.

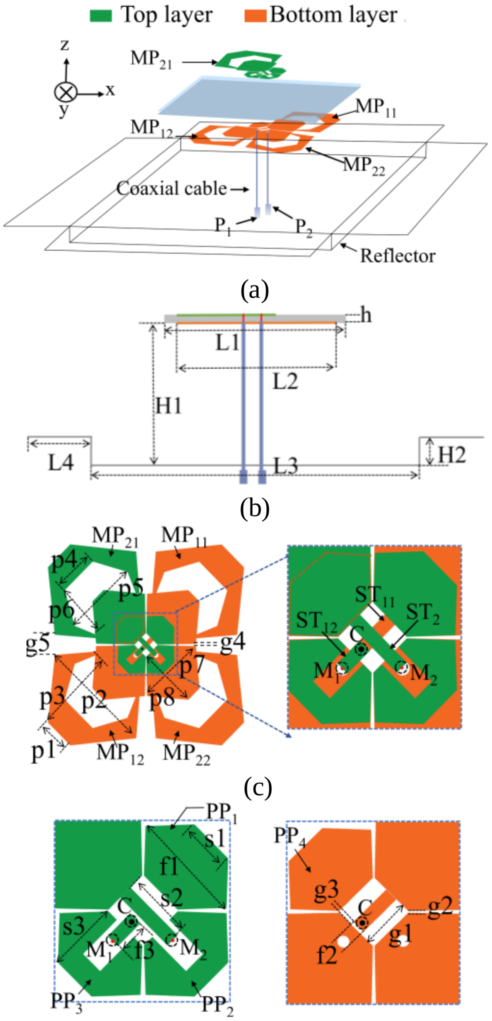

(a)

(b)

(c)

(d)

Fig. 1 Configuration of the proposed antenna: (a) 3-D view, (b) front view, (c) double layers of the radiator, and (d) the center portion of each layer in detail.

The two planar dipoles are fed at M_1 and M_2 points through three feeding strips of ST_{11}, ST_{12} and ST_2. To avoid the overlap among the feeding strips, ST_{12} and ST_2 are printed on the top layer, and ST_{11} is printed on the bottom layer. MP_{11} and MP_{12} are both on the bottom layer and fed at M_1 through ST_{12} and ST_{11}. ST_{12} starts at point M_1 on the top layer, and connects to ST_{11} at point C via a metalized hole, then ST_{11} connects to MP_{11} on the bottom layer. MP_{21} and MP_{22} are on different layers and fed at M_2 through ST_2. Coaxial cables are adopted to transform electrical signals. The inner conductors of the two coaxial cables are soldered with the end of ST_{12} and ST_2 at M_1 and M_2 points on the top layer, respectively. The outer conductors are soldered with MP_{12} and MP_{22} on the bottom layer, respectively.

Four inverted L-shaped edges are added to a planar reflector to enhance the gain and satisfy the HPBW requirement at the frequency band of 3.3-3.8 GHz. All of the details will be discussed in Section III. The proposed antenna was simulated and optimized by HFSS 15.0. Table 1 lists the optimized geometric dimension.

Table 1: Dimensions of the proposed antenna

Par.	Value (mm)	Par.	Value (mm)	Par.	Value (mm)
L1	55	f3	2.7	p1	8
L2	49.5	g1	4.2	p2	29
L3	95	g2	0.3	p3	19.7
L4	25	g3	0.5	p4	10
h	0.6	g4	0.7	p5	18.8
H1	35	g5	5	p6	12.7
H2	10	s1	4	p7	17.4
f1	5.6	s2	17.4	p8	15
f2	1.2	s3	6		

III. ANTENNA ANALYSIS

A. Radiation element analysis

The evolution of the radiator is depicted in Fig. 2 and their reflection coefficients are shown in Fig. 3. Ant. I is a dual-dipole antenna with hexagonal shaped patches. As shown in Fig. 3, Ant. I has better reflection coefficient at lower band but worse at frequencies above 3.2 GHz. The antenna bandwidth can be improved by optimizing the gap between each arm of the two dipoles [5-6]. Different from the published method, a smaller hexagonal patch is embedded into each larger hexagonal patch to get a tapered gap between each dipole arm. Each larger hexagon patch is etched with a polygonal slot to avoid overlapping with the smaller hexagonal patch which results in Ant. II. A new resonance is excited for Ant. II which results in improved -10 dB bandwidth of 1.59-4.34 GHz. However, the reflection coefficient is near -10 dB at 3.3-3.7 GHz. Considering fabrication errors, it might exceed -10 dB at these frequencies. Based on Ant. II, the proposed antenna is obtained by adding of a parasitic patch on the opposite layer of each main patch. As shown Fig. 3, the third resonance shifts to the lower frequency and the reflection coefficient decreases much in the 1.7-3.8 GHz band. The proposed antenna has a wide -10 dB bandwidth of 1.64-4.2 GHz, and -15 dB band of 1.71-4 GHz.

Current distributions of the proposed antenna and Ant. II at 3.6 GHz are plotted in Fig. 4 to illustrate the working mechanism of the parasitic patches. As shown in the figure, the parasitic patches induce more current distributing on the boundary of the main patches which improve the impedance matching.

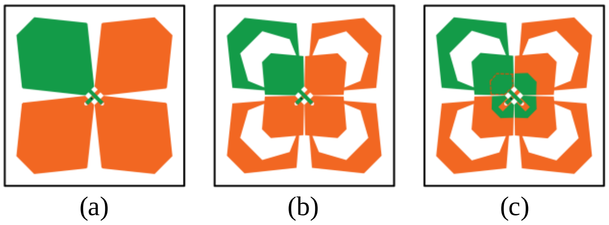
(a) (b) (c)

Fig. 2. Evolution of the radiator: (a) Ant. I, (b) Ant. II, and (c) the proposed antenna.

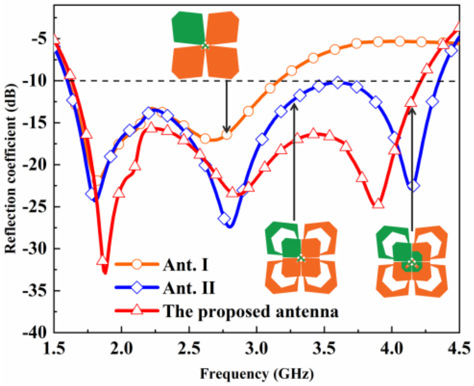

Fig. 3. Reflection coefficient of three antennas.

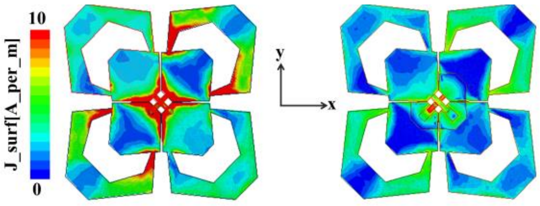

(a) (b)

Fig. 4. Current distributions at 3.6 GHz: (a) Ant. II and (b) the proposed antenna.

The gap size between two adjacent arms has a strong effect on the reflection coefficient. The influence of g2 and g4 is illustrated in Fig. 5 and Fig. 6, respectively. As shown in Fig. 5, changing of g2 has much influence on reflection coefficient at 3.3-3.8 GHz. At these frequencies, the reflection coefficient reduces dramatically with the decrease of g2. Considering fabrication error, g2 cannot be too small. As shown in Fig. 6, in the frequency range of 3-4 GHz, the reflection coefficient becomes larger with the increase of g4, and smaller in the frequency range of 2-2.7 GHz. The optimized bandwidth is obtained with g2=0.5 mm and g4=5 mm.

B. Reflector analysis

In a mobile communication system, the base station antenna is required with a 65±5° HPBW to cover 120° sector. It is challenging to design a reflector keeping stable patterns in the whole band of 1.71-3.8 GHz. The antenna with a planar reflector proposed in [6] has a 65°± 5° HPBW at 1.7-2.7 GHz and 95° at 3.4-3.6 GHz. The open-box shaped reflector proposed in this paper provides satisfied HPBW at 1.7-3.8 GHz.

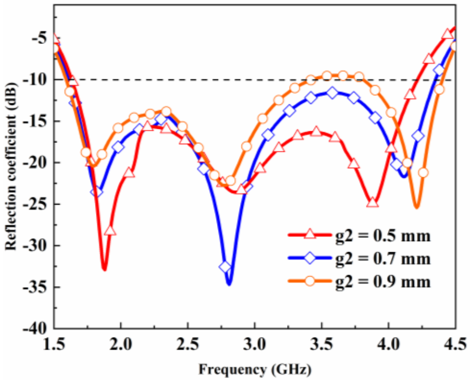

Fig. 5. Reflection coefficient versus g2.

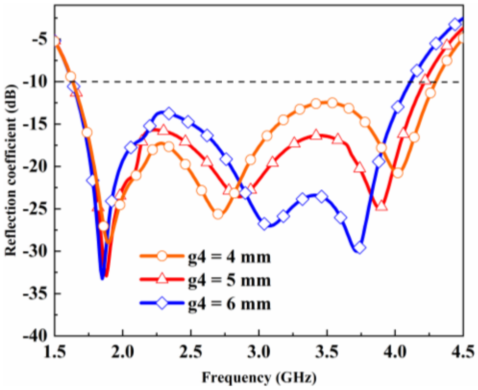

Fig. 6. Reflection coefficient versus g4.

The distance between the radiator and the reflector is crucial to a base station antenna's radiation pattern. It also affects the reflection coefficient. A planar reflector is arranged under the radiator with the distance of H1 to study the influence of the distance. Figure 7 and Fig. 8 show the influence of H1 on radiation pattern. As shown in the figures, narrower HPBW and higher gain are obtained with the decrease of H1 at frequencies above 2.3 GHz. Figure 9 shows (the) reflection coefficient with different H1. As shown in the figure, the reflection coefficient at lower band becomes worse with the decrease of H1 owing to the inductive current on the ground plane. The distance between an antenna radiator and a planar reflector is often adopted as a quarter wavelength to balance the radiation pattern and the bandwidth. Therefore, H1=35 mm is suitable for lower frequencies around 2.1 GHz, and H1=25 mm is suitable for the upper band around 3 GHz. The proposed open-box shaped reflector meets the lower frequencies' requirement with the bottom planar reflector at 35 mm under the radiator, and the four inverted-L shaped metal edges increasing 10 mm height meet the upper frequencies. Figure 10 gives comparison of HPBW and realized gain of the proposed radiator with a planar reflector, a box-shaped reflector, and the proposed open-box shaped reflector. As shown in the figure, with adding of four edges between the radiator and reflector, the HPBW decreases and the gain increases. The proposed reflector provides 65°±5° HPBW and higher than 8 dBi gain in 1.71-3.8 GHz.

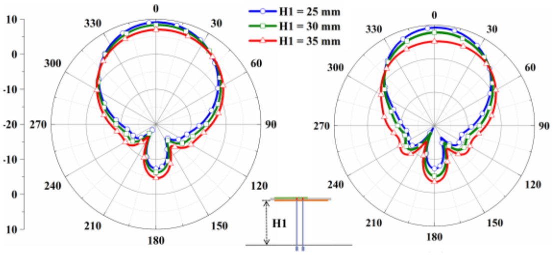

(a) 3.3 GHz (b) 3.8 GHz

Fig. 7. Radiation pattern of the proposed radiator with a planar reflector with different H1.

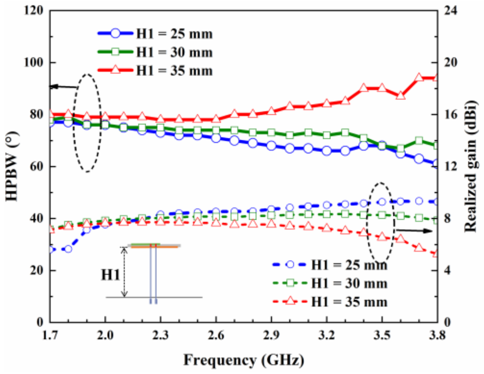

Fig. 8. HPBW and realized gain of the proposed radiator with a planar reflector varying with different H1.

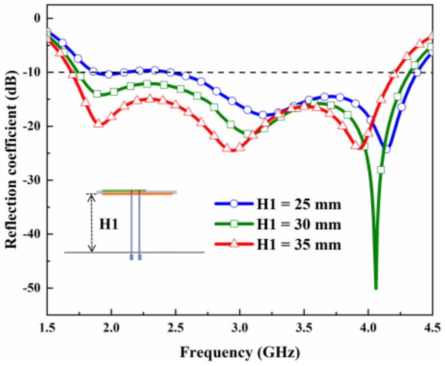

Fig. 9. Reflection coefficient of the proposed radiator with a planar reflector varying with H1.

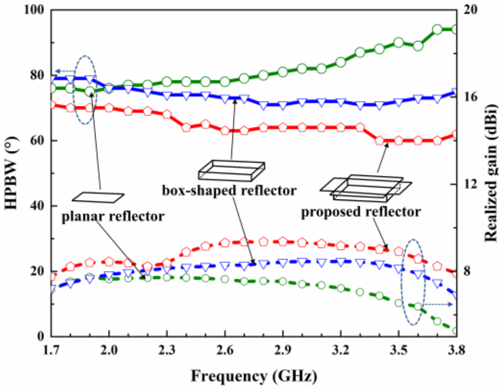

Fig. 10. HPBW and realized gain of three reflectors.

C. Current distribution

Current distributions on the radiator at 1.8, 2.5 and 3.5 GHz are shown in Fig. 11. As shown in the figure, when P_1 is excited, the current mainly distributes on the +45° polarization dipole and points to +45° direction. There are also currents distributing on the cross dipole which are induced by coupling. The path of coupling currents forms closed loops resulting in weak radiation. Therefore, +45° polarization is obtained. When P_2 is excited, -45° polarization is achieved. Although current distributions differ much at different frequencies, it can be seen that strong currents distribute at the gap edges between two adjacent arms at any frequency. It means that the gap size is crucial for impedance matching.

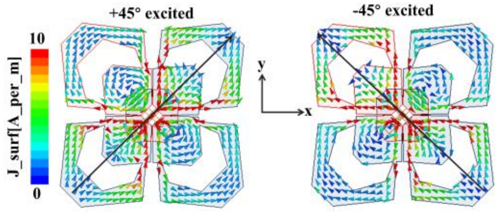

(a) 1.8 GHz

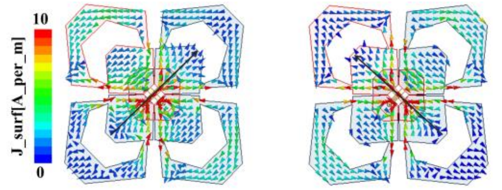

(b) 2.5 GHz

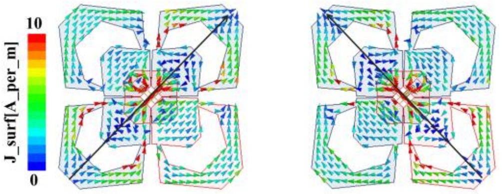

(c) 3.5 GHz

Fig. 11. Current distributions on the radiator.

IV. RESULTS AND DISCUSSION

The prototype of the proposed antenna has been fabricated and measured. Figure 12 shows photographs of the fabricated antenna. The comparison of the simulated and measured S-parameters is shown in Fig. 13 and Fig. 14. There is an obvious discrepancy between simulation and measurement. The simulated -10 dB bandwidth is 1.62-4.21 GHz, and -15 dB bandwidth is 1.71-4 GHz. The measured reflection coefficient is higher than -11 dB with -10dB bandwidth of 1.68-3.8 GHz. The simulated coupling is lower than -26 dB in 1.5-4.4 GHz. The measured coupling is higher than simulation in 16.-3.2 GHz, and lower than -20dB in the whole band. The discrepancy between simulation and measurement might come from fabrication errors, coaxial cable losses and soldering point losses.

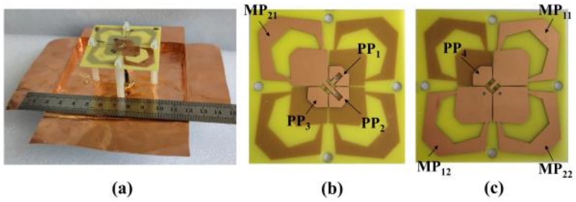

Fig. 12. Photographs of the fabricated antenna: (a) the whole antenna, (b) top layer of the radiator, and (c) bottom layer of the radiator.

Due to geometric symmetry of the proposed antenna, only the +45° polarization results are shown in Fig. 15 and Fig. 16. Figure 15 displays gain and total efficiency. It can be observed that the average simulated gain is 8.8 dBi agreeing with the measured one of 8.5 dBi. The simulated efficiency is a bit lower than the simulation with values higher than 80% in the whole band. Figure 16 presents radiation patterns of the horizontal plane (i.e., xOz) at 1.78, 2.18, 2.48, 2.68, 3.48 and 3.68 GHz. Both the simulated and measured results show that the proposed antenna has a stable HPBW around 65°± 5° at the whole operational band. The values of the cross-polarization discrimination (XPD) are better than 20 dB at the boresight and 10 dB within ±60° directions.

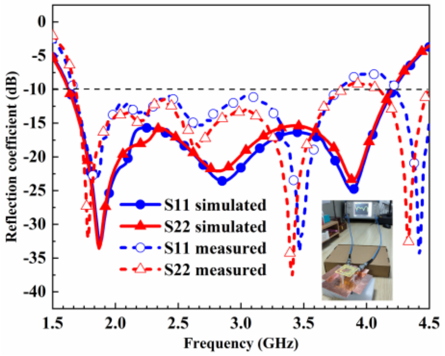

Fig. 13. Simulated and measured reflection coefficients.

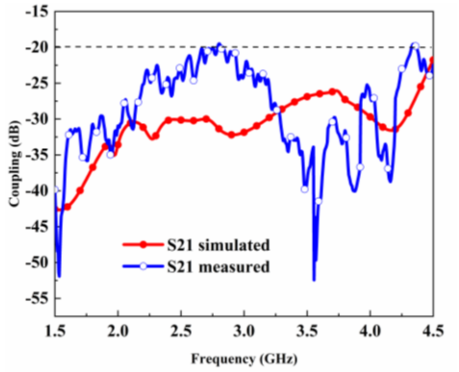

Fig. 14. Simulated and measured coupling.

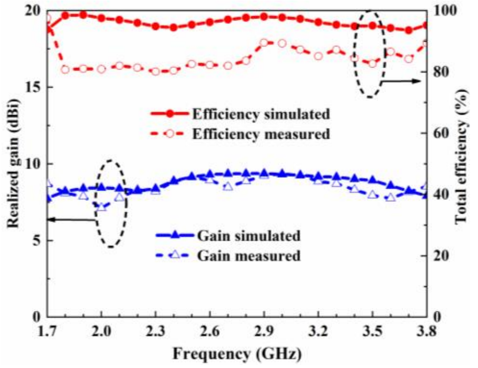

Fig. 15. Gain and total efficiency with +45° excited.

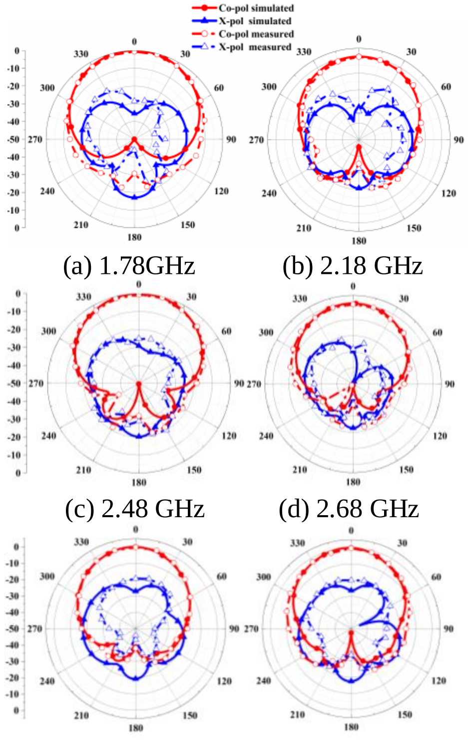

(a) 1.78GHz (b) 2.18 GHz

(c) 2.48 GHz (d) 2.68 GHz

(e) 3.48 GHz (f) 3.68 GHz

Fig. 16. Radiation patterns with +45° excited.

Table 2 shows the comparison of the proposed antenna with published papers. The proposed antenna has wider bandwidth than [2], [4], [12], better HPBW and higher gain than [6].

Table 2: Comparison of the proposed antenna with published literatures

Ref.	Size (mm^3)/ Size (λ_L^3)	VSWR	BW (GHz)	Coup. (dB)	Gain (dBi)	HPBW
[3]	160×160×41.8/ 0.87×0.87×0.23	2	1.63-3.71	-28	/	58°-64°
[4]	130×130×25.5/ 0.96×0.96×0.19	1.5	2.21-3.63	-30	8.3	60°-71°
[6]	145×145×36/ 0.81×0.81×0.2	1.5	1.68-3.7	-28	*8.6 **6.5	*61°-71° **95°
[12]	75×75×13.1/ 0.7×0.7×0.11	2	2.78-4.4	-28	8.95	56°-65°
Pro.	145×145×35.6/ 0.81×0.81×0.2	2	1.68-3.8	-20	8.5	60°-70°

* is at 1.7-2.7 GHz, **is at 3.4-3.6 GHz.

λ_L is the free space wavelength at the lowest operational frequency.

V. CONCLUSION

A dual-polarized base station antenna has been presented in this paper. By adjusting the gap between two dipoles' arms, the proposed antenna has achieved a broad bandwidth of 1.68-3.8 GHz with coupling below -20 dB. The overall volume of the proposed antenna is $145\times145\times35.6\ \text{mm}^3$. It has an average gain of 8.5 dBi, stable HPBW around 65°± 5° in the horizontal plane and XPD better than 10 dB in the whole -10 dB band. The proposed antenna is a promising and economical candidate of 2G/3G/4G/5G communication systems.

ACKNOWLEDGMENT

This work was supported by the Natural Science Foundation of Shandong Province, China (No. ZR2020MF023).

REFERENCES

[1] Q. Wu, P. Y. Liang, and X. M. Chen. "A broadband ±45° dual-polarized multiple-input multiple-output antenna for 5G base stations with extra decoupling elements," *Journal of Communications and Information Networks*, vol. 3, no. 1, pp. 31-37, Mar. 2018.

[2] S. X. Ta, D. M. Nguyen, K. K. Nguyen, C. D. Ngoc, and N. N. Trong, "Wideband differentially fed dual-polarized antenna for existing and sub-6 GHz 5G communications," *IEEE Antennas and Wireless Propagation Letters*, vol. 19, no. 12, pp. 2033-2037, Dec. 2020.

[3] C. Ding, H. Sun, H. Zhu, and Y. Jay Guo, "Achieving wider bandwidth with full-wavelength dipoles for 5G base stations," *IEEE Transactions on Antennas and Propagation*, vol. 68, no. 2, pp. 1119-1127, Feb. 2020.

[4] B. Wang, C. C. Zhu, C. Y. Liao, W. Luo, B. Yin, and P. Wang, "Broadband dual-polarized dipole antenna for LTE/5G base station applications," *Electromagnetics*, vol. 40, no. 1, pp. 13-22, Nov. 2019.

[5] D. Zheng and Q. Chu, "A wideband dual-polarized antenna with two independently controllable resonant modes and its array for base-station applications," *IEEE Antennas and Wireless Propagation Letters*, vol. 16, pp. 2014-2017, July 2017.

[6] Y. Zhang, Y. Zhang, D. Li, K. Liu, and Y. Fan, "Ultra-wideband dual-polarized antenna with three resonant modes for 2G/3G/4G/5G communication systems," *IEEE Access*, vol. 7, pp. 43214-43221, Apr. 2019.

[7] Z. Li, J. Han, Y. Mu, X. Gao, and L. Li, "Dual-band dual-polarized base station antenna with a notch band for 2/3/4/5G communication systems," *IEEE Antennas and Wireless Propagation Letters*, vol. 19, no. 12, pp. 2462-2466, Dec. 2020.

[8] B. Feng, L. Li, K. L. Chung, and Y. Li, "Wideband widebeam dual circularly polarized magnetoelectric dipole antenna/array with meta-columns loading for 5G and beyond," *IEEE Transactions on Antennas and Propagation*, vol. 69, no. 1, pp. 219-228, Jan. 2021.

[9] B. S. Qiu, S. Y. Luo, and Y. S. Li, "A broadband dual-polarized antenna for Sub-6 GHz base station application," *2020 IEEE 3rd International Conference on Electronic Information and Communication Technology (ICEICT)*, pp. 273-275, Nov. 2020.

[10] H. Zhai, J. Zhang, Y. Zang, Q. Gao, and C. Liang, "An LTE base-station magnetoelectric dipole antenna with anti-interference characteristics and its MIMO system application," *IEEE Antennas and Wireless Propagation Letters*, vol. 14, pp. 906-909, Apr. 2015.

[11] P. Chen, L. H. Wang, and T. Y. Ding, "A dual-polarized sakura-shaped base station antenna for 5G communications," *Applied Computational Electromagnetics Society Journal*, vol. 35, no. 5, pp. 567-571, May 2020.

[12] M. Ciydem and E. A. Miran, "Dual-polarization wideband sub-6 GHz suspended patch antenna for 5G base station," *IEEE Antennas and Wireless Propagation Letters*, vol. 19, no. 7, pp. 1142-1146, July 2020.

[13] R. Lian, Z. Wang, Y. Yin, J. Wu, and X. Song, "Design of a low-profile dual-polarized stepped slot antenna array for base station," *IEEE Antennas and Wireless Propagation Letters*, vol. 15, pp. 362-365, Feb. 2016.

[14] Y. Liu, S. Wang, X. Wang, and Y. Jia, "A differentially fed dual-polarized slot antenna with high isolation and low profile for base station application," *IEEE Antennas and Wireless Propagation Letters*, vol. 18, no. 2, pp. 303-307, Feb.

2019.

[15] Q. Hua, Y. Huang, S. Y. Song, M. O. Akinsolu, B. Liu, T. Y. Jia, Q. Xu, and A. Alieldin, "A novel compact quadruple-band indoor base station antenna for 2G/3G/4G/5G systems," *IEEE Access*, vol. 7, pp. 151350-151358. Oct. 2019.

[16] G. Gopal and A. Thangakalai, "Cross dipole antenna for 4G and sub-6 GHz 5G base station applications," *Applied Computational Electromagnetics Society Journal*, vol. 35, no. 1, pp. 16-22, Jan. 2020.

Ya-Li Chen was born in Neijiang, Sichuan, China, in 1997. She received the B.S. degree in Information Engineering from Hangzhou Dianzi University, Hangzhou, China, in 2019. She is currently pursuing the M.S. degree in Signal and Information Processing in Qingdao University, Qingdao, China. Her current research interest is in base station antennas.

Yao-Zong Sui was born in Shouguang, Shandong Province, China in 1996. In 2018, he graduated from the Electronic Information of Qingdao University. In 2020, He entered Qingdao University to pursue a master's degree in Signal and Information Processing. At present, the research direction is antenna design.

Zhi-Qun Yang received the Ph.D. degree in Communication and Information System from Nanjing University of Technology, Nanjing, Jiangsu Province, China, in 2003. He is with Shandong Institute of Space Electronic Technology, China Aerospace Science and Technology Corporation, Yantai, China, as a Senior Engineer. His research interest is signal processing and communication.

Xiao-Yun Qu was born in Yantai City, Shandong Province, China, in 1974. She received the B.S. in Applied Mathematics from Yantai University, in 1996, M.S. degree in Electromagnetic Fields and Microwave Technology from Nanjing Electronics Research Center, Nanjing, Jiangsu Province, China, in 1990. She is with Shandong Institute of Space Electronic Technology, Yantai, China, as a Senior Engineer. Her research interest is antenna design.

Wei-Hua Zong was born in Penglai City, Shandong Province, China, in 1975. She received the B.S. in Applied Mathematics from Yantai University, in 1997, M.S. degree in Electromagnetic Fields and Microwave Technology from Nanjing Electronics Research Center, Nanjing, Jiangsu Province, China, in 2000, and the Ph.D. degree in Electromagnetic Fields and microwave Technology from Xidian University, Xian, Shanxi Province, China, in 2004. In 2004, she joined Qingdao University, Qingdao, Shandong Province, China as a Lecturer. Since 2005, she has been an Associate Professor in Qingdao University. From February 2010 to August, she was a Visiting Scholar Assistant with Electrical and Computation Engineering Department, National University of Singapore. Her research interests include antenna design and electromagnetic material measurement.

A Dual Band AMC Backed Antenna for WLAN, WiMAX and 5G Wireless Applications

Junuthula Ashish and Amara Prakasa Rao

Department of Electronics and Communication Engineering
National Institute of Technology, Warangal, Telangana, India
jashrdy@gmail.com, aprao@nitw.ac.in

Abstract ─ This paper presents a multiband low profile antenna aimed for its application in existing WLAN, WiMAX and sub-6 GHz fifth generation (5G) frequency bands. The design incorporates a simple planar monopole antenna with slots etched on it to be able to operate in two frequency bands with (S11< -10 dB) ranging from 2.38 - 2.7 GHz and 3.28 - 5.8 GHz with percentage impedance bandwidths of 16 and 56. The peak gains of the antenna within the bands were observed to be 2.1 and 4.3 dBi respectively. In order to further enhance the Gain and improve the radiation characteristics of the antenna, a dual band artificial magnetic conductor (AMC) surface is designed and employed as a reflector at the ground side of the main radiator. The antenna and AMC 4x4 array prototypes are fabricated and its performance is measured. It is observed that there is an enhancement in the gain of 5 dB in the first band and 2.8 dB in the second band of operation.

Index Terms ─ AMC, WiMAX, WLAN.

I. INTRODUCTION

With ever-growing wireless communication systems there is a need for the subsequent increase in the growth of the antenna technology that is being employed in these systems. The requirement for a simple design yet well performing antenna is the need of the hour. 5G wireless communications are being initiated all around the world and the necessity emerges for the design of an antenna covering these 5G bands and the already existing wireless frequency bands. 5G spectrum being divided into three bands low frequency band (below 1GHz), mid frequency band (sub-6 GHz) and high frequency band (mm Wave) with the mid-band offering good data rates with decent coverage.

Multiband antennas are most desirable because they are flexible, and their role becomes even more important in this switching phase as they should be able to operate at both the existing WLAN and WiMAX bands as well as the upcoming technology. The frequency band between 3-5 GHz being promoted for the sub-6 GHz mid-band communications, the N77/N78/N79 bands are being operated in this range and a wider bandwidth covering the entire range is of the interest. Microstrip antennas has become a popular choice amongst the different available antennas because they are low profile, inexpensive and easy to integrate within the IC's. Several multi-band antennas are reported in the literature with slots on the radiating surface, especially the microstrip antenna with a U-shaped slot has proved to be a good wideband solution [1].

Several 5G antennas have come through in the recent times covering the sub-6GHz band. A planar antenna [2] with strips on either side of the substrate is proposed, but the gain is not stable over the entire frequency range. A multi-slotted antenna [3] with a partial ground plane was introduced for 3.15-5.55 GHz frequency with a maximum gain of 2.69 dBi in the band. The wideband folded wall antenna with an increased gain [4] was proposed with a bandwidth of 58%. An AMC based multi band antenna [5-6] with unidirectional radiation patterns and increased gain has been discussed. A dual band AMC reflector-based antenna [7] was designed (for 5G communications with relatively narrow (19.2% and 13.8%) bandwidths. Several other antennas aimed at sub-6 GHz, 5G applications were presented [8-9].

In this paper, a dual band U-slot monopole antenna has been designed to operate at 2.38 – 2.7 GHz and 3.28 – 5.8 GHz bands covering the already existing 2.4 and 5 GHz WLAN, 2.5, 3.5 and 5.5 GHz WiMAX and the sub-6 GHz, 5G bands which include N77 band with frequency ranging from 3.3-4.2 GHz, N78 band ranging from 3.3-3.8 GHz and N79 band ranging from 4.4-5 GHz. Moreover, an AMC unit cell is designed with zero reflection phase at two frequencies, 2.5 and 5.5 GHz and is periodically repeated to form a metasurface and is used as a reflector on the ground side of the radiating antenna to enhance its gain and radiation characteristic performance. The antenna can be used alone or including the AMC reflector for unidirectional radiation and enhanced gain.

Submitted On: May 28, 2021
Accepted On: September 2, 2021

https://doi.org/10.47037/2021.ACES.J.360913

II. ANTENNA DESIGN

A. Configuration of the proposed antenna

Figure 1 shows the configuration of the proposed dual band antenna with AMC reflector. The radiator is a microstrip circular patch antenna with a U-shaped slot and a rectangular slot incorporated on it, a symmetrical AMC reflector surface of the size 64 x 64 x 1.6 mm^3 is employed at a distance of H = 14mm on the ground side of the antenna. A Styrofoam layer with a permittivity value of 1.1, is used to separate the two structures.

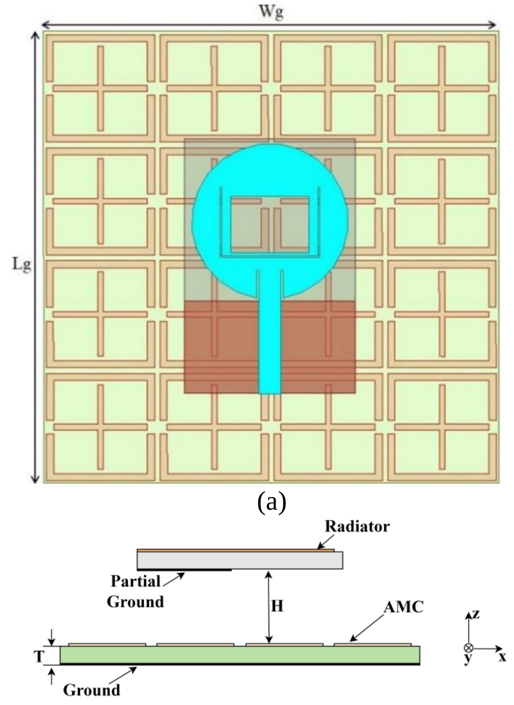

(a)

(b)

Fig. 1. Configuration of the proposed dual band AMC backed antenna: (a) top view and (b) side view.

B. Radiator design

The geometry of the main radiator is shown in the Fig. 2. It is printed on a 1.6 mm thick rectangular FR-4 substrate having a relative permittivity of 4.4 and a loss tangent value of 0.02. The size of the antenna is of the order of $0.3\lambda_0$ x $0.2\lambda_0$ x $0.01\lambda_0$ (where λ_0 is wavelength corresponding to the centre frequency of the first band). It is a microstrip fed antenna with inset feed for better impedance matching. A partial ground plane is being employed on the other side of the substrate in order to achieve a wider bandwidth. A U-shaped slot is introduced at an optimized position on the patch to enhance the bandwidth and lower the cross-polarization levels. Further an additional rectangular slot is also introduced to achieve proper impedance matching levels in the second band of operation. The dimensions of the designed antenna are stated in the Table 1. The simulations were carried out on the Ansys HFSS tool.

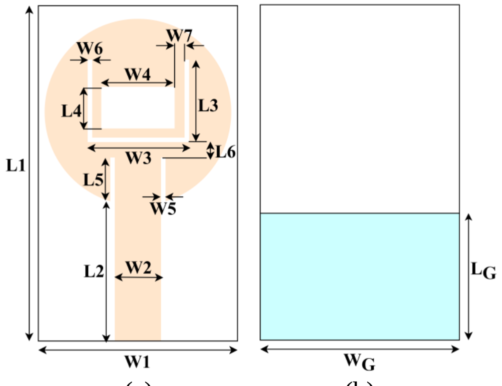

(a) (b)

Fig. 2. Design of the radiator: (a) top view and (b) bottom view.

Table 1: Optimized dimensions of the proposed antenna

Parameters	Value (mm)	Parameters	Value (mm)
H	14	*T*	1.6
Lg	64	*Wg*	64
L1	36	*W1*	24
L2	13.55	*W2*	3.059
L3	10	*W3*	14
L4	8	*W4*	11
L5	3.9	*W5*	0.3
L6	1.8	*W6*	0.2
L_G	13	*W7*	1.3
La1	16	W_G	24
La2	15.2	*Wa1*	16
La3	2	*Wa2*	15.2
La4	0.6	*Wa3*	0.8
La5	0.8	*Wa4*	0.8

The evolutionary steps involved in the design of the radiating patch are shown in the Fig. 3 (a). The S11 response of all the antennas is shown in the Fig. 3 (b). A conventional circular patch antenna is initially designed for, which a wide band resonance is achieved from 2.9 GHz to 5.9 GHz. Then a U-shaped slot is etched on the patch, which introduces a notch at the frequency band between 2.73-3.23 GHz. Hence, the antenna now works as a dual band antenna with operating frequencies ranging from 2.49–2.73 GHz and 3.23–5.73 GHz. Further with the introduction of an additional rectangular slot the impedance matching and the bandwidth of the antenna are enhanced. Finally the design of the antenna is simple making use of a low cost FR-4 substrate, operating in two bands with good impedance bandwidths covering the entire sub-6 GHz 5G frequency bands besides the existing 2.4/5 GHz WLAN, 2.5/3.5/5.5 GHz WiMAX bands.

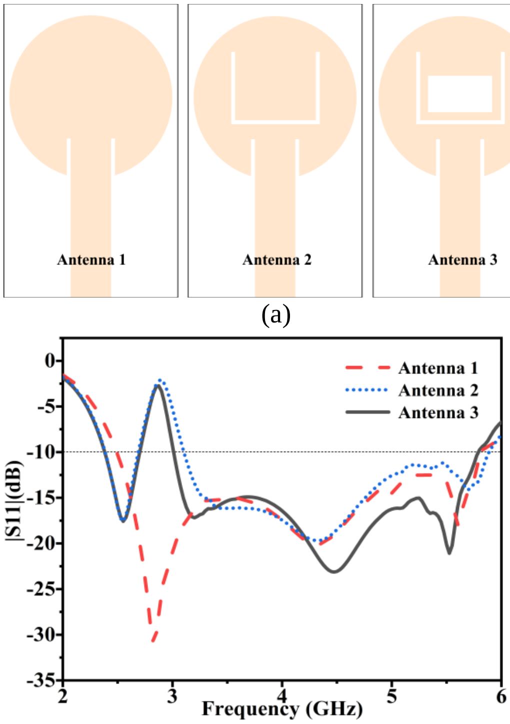

(a)

(b)

Fig. 3. (a) Evolutionary steps in the design of the radiator, and (b) reflection coefficients of radiating elements.

C. AMC design

The design geometry of the artificial magnetic conductor unit cell incorporates a square outline with slots at the centre on the opposite sides and an additional cross shaped patch at the centre as shown in the Fig. 4 (a). A low cost FR-4 substrate is employed with relative permittivity of 4.4 and a loss tangent value of 0.02. A metal ground is present at the bottom surface of the unit cell. The unit cell is simulated using the master-slave boundary set up. The reflection phase plot of this dual band AMC is as shown in the Fig. 4 (b). Initially a single band AMC with the reflection phase and of zero at 2.5 GHz is designed with no central cross shaped patch and with the introduction of the cross, a dual band AMC is realized with the other zero reflection phase occurring at 5.5 GHz. The reflection magnitude plot is shown in the Fig. 4 (c) and the values about 0.78 and 0.71 and is high enough to realize the gain enhancement of the antenna. The dimensions of the AMC unit cell are evaluated in accordance with the operating frequency range of the antenna and are listed in the Table 2.

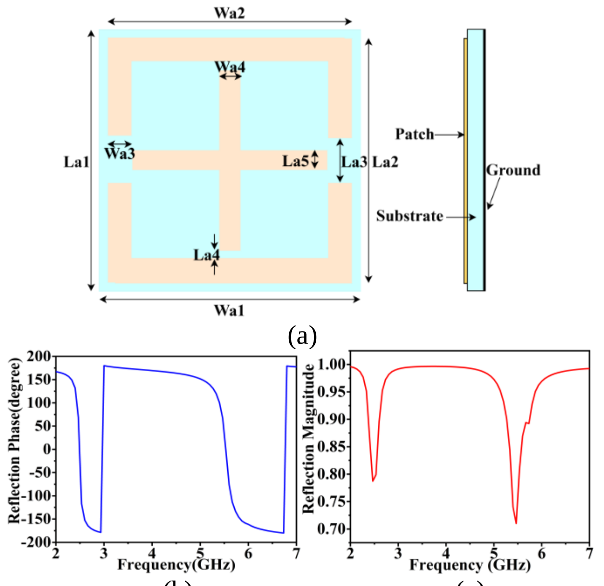

(a)

(b) (c)

Fig. 4. (a) Geometry of the proposed dual band AMC unit cell, (b) reflection phase of the AMC unit cell, and (c) reflection magnitude of the AMC unit cell.

D. Antenna loaded with AMC reflector

The designed dual band AMC unit cell is periodically repeated in x and y directions to form a 4 x 4 array metal surface and is placed at the groundside of the antenna separated by Styrofoam. The effect of the AMC surface on the S11 curve is depicted in the Fig. 5 (a). The performance of the antenna is influenced by the extent of separation between the antenna and the AMC surface. The radiations from the radiating antenna get reflected from the AMC surface with zero phase reversal to aid the radiations unidirectionally and hence increasing the gain of the antenna. A significant increase in the gain is observed in the first band and a reasonable increase in the second band of operation as shown in the Fig. 5 (b).

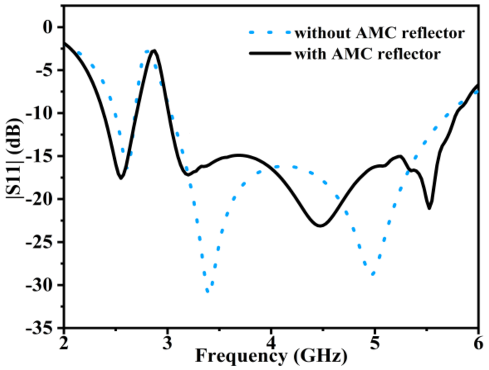

(a)

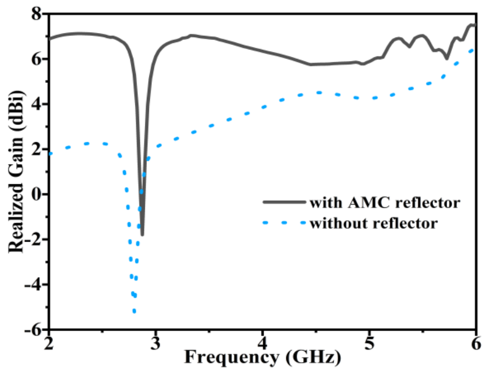

(b)

Fig. 5. (a) Simulated S11 of the antenna with and without AMC reflector, and (b) simulated gains with and without AMC reflector

The performance of the antenna in terms of the band selection and bandwidth depends on the dimensions of the slots. A parametric analysis based on the variation of these dimensions is as shown in the Fig. 6. The optimal values of these dimensions for which the choice of frequency bands is covered, is considered in the design.

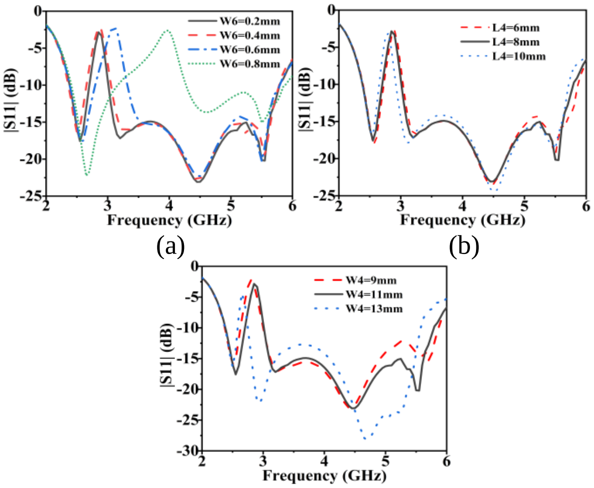

(a) (b)

(c)

Fig. 6. Simulated S11 of the antenna for different (a) W6, (b) L4, and (c) W4.

III. RESULTS AND DISCUSSION

The simulated design of the dual band operating antenna and the AMC surface are fabricated and is as shown in the Fig. 7 (a) and is of the size $0.53\lambda_0$ x $0.53\lambda_0$ x $0.14\lambda_0$. The measured and simulated S11 of the antenna and the AMC surface are shown in the Fig. 7 (b). The slight variation in the measured results from the simulated is due to the losses incurred during the fabrication process. A quarter wavelength separation should be maintained between the antenna and the AMC reflector in order to have a significant effect on the performance of the antenna, but, the low profile nature of the design will get affected. So, a trade-off between the performance and size of the antenna needs to be considered. It can be observed from the Fig. 8, that as the separation decreases, though the gain of the antenna increases, there is deterioration in the S11 performance of the antenna. So, an optimal separation (H=14mm) is chosen in order to preserve both the performances. The antenna is suited for 2.4/5 GHz WLAN applications, 2.5/3.5/5.5 GHz WiMAX applications and with the second band being wideband is able to cover the entire sub-6 GHz, 5G bands (3.3-3.8 GHz, 3.3-4.2 GHz and 4.4–5 GHz).

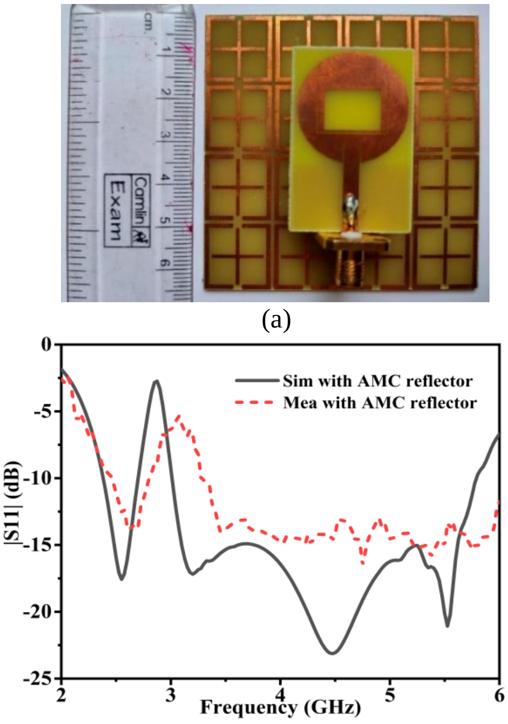

(a)

(b)

Fig. 7. (a) Fabricated prototype and the, and (b) simulated and measured S11, of the antenna with AMC.

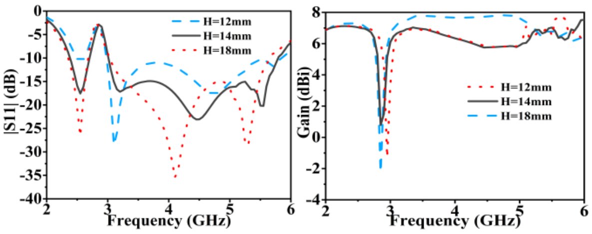

(a) (b)

Fig. 8. Simulated (a) S11 and (b) gain, for different H.

Table 2: Comparison of the dual band proposed antenna to the existing

References	Size	With AMC Reflector	Operating Range (GHz)	Gain (dBi)	Radiation Efficiency
[2]	135 x 80 x 0.8	No	0.7 – 0.9 1.6 – 5.5	-1.3 – 4.7	(41 – 88)%
[3]	20 x 30 x 1.5	No	3.15 – 5.55	1.8 – 2.7	(68.4 – 79.6)%
[4]	63 x 51.2 x 4.5	No	2.84 – 5.15	4.4 – 6.2	64%
[5]	104 x 104 x 11	Yes	2.36 – 2.76 5.12 – 5.62	7.2 7.3	65%
[7]	63 x 63 x 7	Yes	3.14 – 3.83 4.40 – 5.02	8.2	90%
[8]	105 x 105 x 25	Yes	2.5 – 2.7 3.3 – 3.6	8.4	N/A
Proposed	36 x 24 x 1.6	No	2.48 – 2.73 3.15 – 5.8	2.1 4.3	>90% >80%
Proposed (with AMC)	64 x 64 x 17.2	Yes	2.38 – 2.7 3.28 – 5.8	7.1 7.1	>90% >80%

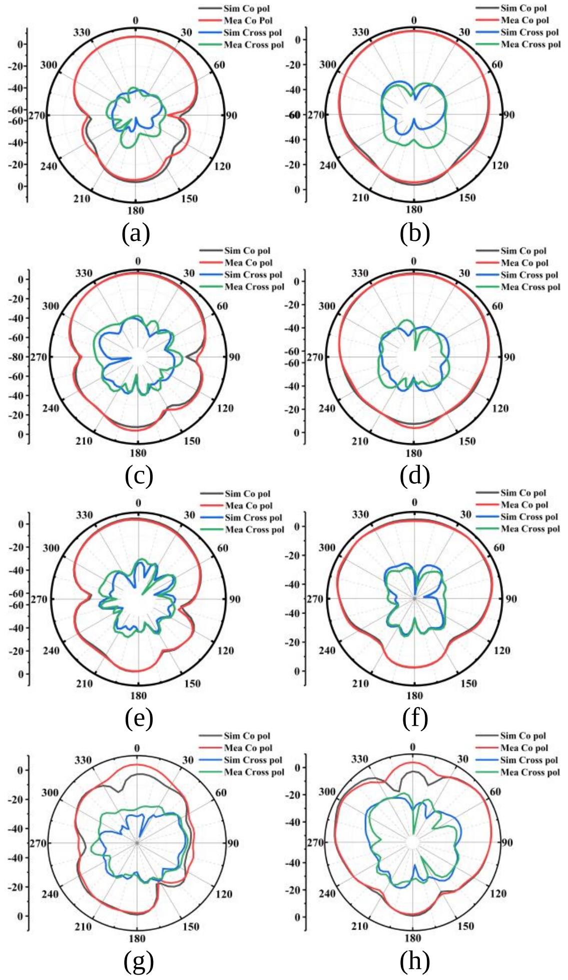

Fig. 9. Simulated and measured radiation patterns of the antenna in the plane: (a) XZ at 2.55 GHz, (b) YZ at 2.55 GHz, (c) XZ at 3.6 GHZ, (d) YZ at 3.6 GHz, (e) XZ at 4.7 GHz, (f) YZ at 4.7 GHz, (g) XZ at 5.5 GHz, and (h) YZ at 5.5 GHz.

The measured and simulated radiation patterns of the antenna loaded with the AMC reflector at frequencies 2.55 GHz, 3.6 GHz, 4.7 GHz and 5.5GHz are shown in the Fig. 9. The measured and simulated patterns were observed to be agreeing well with each other. The inconsistency in the cross polarization plots is due to losses that were incurred during the fabrication and measurement process. The antenna exhibits unidirectional patterns because of the reflections from the AMC surface. The radiation patterns at 5.5 GHz diverge because the antenna is operating in its second mode.The gains of the antenna along with the simulated radiation efficiency are shown in the Fig. 10.

It can be ascertained from the Fig. 10, that the radiation efficiency is above 90% for the entire first band and the sub-6 GHz 5G operating bands. The measured and simulated gains are about 6.7 dBi and 7.1 dBi in the first band and almost agree with each other for the entire range in the second band.

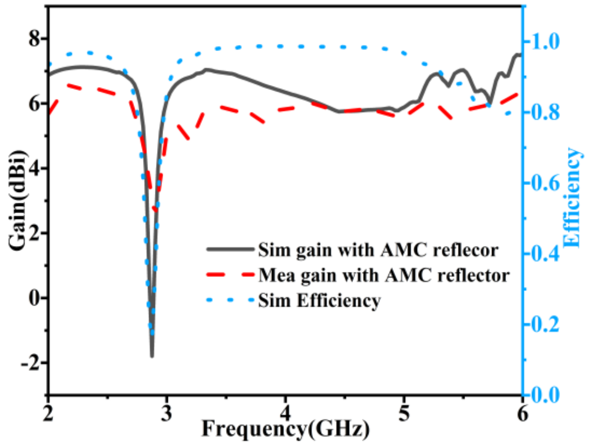

Fig. 10. Simulated and measured gain, simulated efficiency of the proposed antenna.

IV. CONCLUSION

This paper presents a low profile dual band antenna configuration designed for 2.4/5 GHz WLAN, 2.5/3.5/5.5 GHz WiMAX and sub-6 GHz 5G bands. The antenna is fabricated and the measured results are in agreement with the simulated. The size of the antenna without AMC reflector is of the order of $0.3\lambda_0$ x $0.2\lambda_0$ x $0.01\lambda_0$ and with AMC, it is of the order $0.53\lambda_0$ x $0.53\lambda_0$ x $0.14\lambda_0$ (where λ_0 is the free space wavelength corresponding to the centre frequency of the first band) with impedance bandwidths of 9.8% (2.48–2.73 GHz) and 56% (3.28 – 5.8 GHz). The gains of the antenna within the bands was observed to be 2.1 and 4.2 dBi respectively. In order to enhance the gain and radiation of the antenna a dual band AMC reflector which was designed at 2.5 GHz and 5.5 GHz was employed. A significant improvement in the gain of 5 dBi in the first band and 2.8 dBi in the second band was observed. Therefore, the antenna can be used alone for WLAN, WiMAX and 5G applications or with the AMC reflector for high gain base station applications.

REFERENCES

[1] S. Bhardwaj and Y. Rahmat-Samii, "A comparative study of c-shaped, e-shaped, and u-slotted patch antennas," *Microwave and Optical Technology Letters*, vol. 54, no. 7, pp. 1746-1757, July 2012.

[2] Z. An and M. He, "A simple planar antenna for sub-6 GHz applications in 5G mobile terminals," *Applied Computational Electromagnetics Society Journal*, vol. 35, no. 1, pp. 10-15, Jan. 2020.

[3] R. Azim, AKM. M. H. Meaze, A. Affandi, Md. M. Alam, R. Aktar, Md. S. Mia, T. Alam, Md. Samsuzzaman, and Md. T. Islam, "A multi-slotted antenna for LTE/5G sub-6 GHz wireless communication applications," *International Journal of Microwave and Wireless Technologies*, vol. 13, no. 5, pp. 486-496, June 2021.

[4] W. An, Y. Li, H. Fu, J. Ma, W. Chen, and B. Feng, "Low-profile and wideband microstrip antenna with stable gain for 5G wireless applications," *IEEE Antennas and Wireless Propagation Letters*, vol. 17, no. 4, pp. 621-624, Apr. 2018.

[5] H. Zhai, K. Zhang, S. Yang, and D. Feng, "A low-profile dual-band dual-polarized antenna with an AMC surface for WLAN applications," *IEEE Antennas and Wireless Propagation Letters*, vol. 16, pp. 2692-2695, Aug. 2017.

[6] E. W. Coetzee, J. W. Odendaal, and J. Joubert, "A quad-band antenna with AMC reflector for WLAN and WiMAX applications," *Applied Computational Electromagnetics Society Journal*, vol. 33, no. 10, pp. 1123-1128, Oct. 2018.

[7] Q. Liu, H. Liu, W. He, and S. He, "A low-profile dual-band dual-polarized antenna with an AMC reflector for 5G communications," *IEEE Access*, vol. 8, pp. 24072-24080, Jan. 2020.

[8] G. Jin, C. Deng, J. Yang, Y. Xu, and S. Liao, "A new differentially-fed frequency reconfigurable antenna for WLAN and sub-6GHz 5G applications," *IEEE Access*, vol. 7, pp. 56539-56546, Feb. 2019.

[9] Y. Liu, S. Wang, N. Li, J. Wang, and J. Zhao, "A compact dual-band dual-polarized antenna with filtering structures for sub-6 GHz base station applications," *IEEE Antennas and Wireless Propagation Letters*, vol. 17, no. 10, pp. 1764-1768, Oct. 2018.

Junuthula Ashish received his master's degree from National Institute of Technology, Warangal, India in 2017. He is currently with Electronics and Communication Department, working towards his Ph.D. at National Institute of Technology, Warangal, India. His research interests include multiband Antennas, metamaterial antennas and reconfigurable antennas.

Amara Prakasa Rao obtained his bachelor's degree in ECE from Nagarjuna University, A.P., India, and a master's degree from PEC-Pondicherry, India, with Electronics and Communication Engineering as specialization in 1994 and 1998, respectively. His doctoral degree is National Institute of Technology Warangal, India, in the year 2018. He has more than 20 years of experience in teaching at various organizations. Currently, he is with the Department of Electronics and Communication Engineering as an Associate Professor at National Institute of Technology, Warangal, India. About 20 papers are at his credit in international and national journals and conferences. His areas of interest include signal processing, smart antenna systems, and optimization techniques.

Single-cut Far-Field Antenna Radiation Pattern Reconstruction Accuracy Analysis in Compact Anechoic Chamber Setup

Ole K. Jensen, Yilin Ji, Fengchun Zhang, and Wei Fan[*]

Department of Electronic Systems, Aalborg University, Aalborg, 9000, Denmark
okj@es.aau.dk, yilin@es.aau.dk, fz@es.aau.dk, *wfa@es.aau.dk

Abstract **─** In production testing, it is of importance to measure the key radiation parameters of an antenna under test (AUT), e.g., main beam peak and direction, sidelobes, and null depth and direction in a cost-effective setup with a short measurement time. As a result, practical measurement setups are often compact and equipped with only a few probes (or probe locations). However, these system limitations would introduce errors for antenna testing. This problem has become even more pronounced for 5G radios due to utilization of large-scale antenna configurations and high frequency bands. Spherical near-field measurements are nowadays an accurate and mature technique for characterizing AUTs, which however, necessitates a full spherical acquisition, leading to a long measurement time. Single-cut near-to-far-field transformation is a promising strategy since most of the key AUT parameters are available in the single-cut pattern and it requires much reduced measurement time. In this work, a simple and flexible scheme is proposed to evaluate errors introduced by limitations in practical setups for single-cut far-field (FF) antenna radiation pattern reconstruction, where the near-field data can be easily generated and modified according to the limitations introduced in practical multi-probe anechoic chamber setups, e.g., measurement distance, truncation range, and sampling interval. The reconstructed FF pattern is obtained using a commercial near-field to far-field transformation tool, SNIFT. The proposed scheme is numerically validated via comparing the reference FF pattern of a 4×8 uniform planar array composed of ideal Hertzian dipoles and reconstructed FF pattern. With the proposed scheme, the impact of practical system limitations on single-cut reconstruction accuracy can be easily analyzed.

Index Terms **─** Antenna pattern measurement, near-field far-field transformation, near field measurement, over-the-air testing, and single-cut antenna pattern.

I. INTRODUCTION

The ever-increasing demand for high data-rate, reliable and ubiquitous wireless communication has motivated research towards the fifth generation (5G) communication system and beyond [1-3]. This has been made possible, thanks to key radio frequency (RF) and antenna technologies, e.g., millimeter-wave and sub-THz frequency, large system bandwidth, large-scale antenna configuration, and integrated and low-cost RF front-end design. It is essential that we should measure large-scale antenna arrays (e.g., massive multiple-input multiple-output (MIMO) base stations) in a fast, accurate, and cost-effective manner. This has become more important and urgent due to the massive installation of large-scale antenna systems in cellular, satellite and military applications. The far-field antenna radiation pattern is one of the most important metrics to evaluate the radiated performance of the antenna system. However, it is getting more expensive and time-consuming, as the antenna under test (AUT) is getting larger and more complicated. Furthermore, over-the-air (OTA) testing is seen inevitable for future highly integrated antenna systems [4-9].

The antenna pattern measurement methods may be grouped into two categories including near-field (NF) and far-field (FF) ranges. Classical NF measurement techniques are based on the NF measurement of antennas, and the antenna FF is subsequently calculated through the near-field to far-field transformation. The amplitude and phase response of the AUT are sampled at a regular sampling grid with a well-designed measurement probe. Though highly accurate and mature in the industry, this method, however, requires both accurate amplitude and phase measurement of the AUT over a large sampling surface (i.e., full scan), and it also necessitates high-accuracy positioners [10]. The measurement time also becomes prohibitive when the electrical size of the AUT becomes large. Different FF methods have been extensively employed in the industry, e.g., direct-far-field (DFF), compact antenna test range (CATR) and plane wave generator (PWG) [11, 12]. The basic principle of DFF is that a plane wave at the antenna can be directly approximated if the measurement range is no smaller than the Fraunhofer FF distance. However, the requirement of measurement range might lead to large (and therefore expensive) anechoic chambers and link budget (i.e., small dynamic range) problems [13],

Submitted On: May 19, 2021
Accepted On: June 21, 2021

https://doi.org/10.47037/2021.ACES.J.360914

especially for large-scale AUTs. The CATR generates a plane wave using transformation with a parabolic reflector in a much shorter distance than the DFF method. The PWG can also enable over-the-air (OTA) testing directly in the far field at a reduced distance, by exciting the PWG array elements with suitably optimized complex coefficients. The CATR and PWG offer a good dynamic range due to reduced measurement range. However, the setup cost is rather expensive for massive deployment. In [14, 15], a mid-field (MF) method is proposed and validated to achieve OTA RF measurement, including AUT FF antenna patterns, transmit and receive performance metrics. The method presents some unique advantages. For example, it can significantly reduce the measurement distance; it only requires simple transformation from MF to FF results and it does not need phase measurement. However, it still requires some knowledge of the AUT (i.e., a grey-box solution) and measurement samples on two different radiated NF test distances to reconstruct the far-field results. A review of some recent advances in antenna measurements can be found in [16].

In practice, it is important and sometimes sufficient to rapidly determine several key antenna radiation parameters of the AUT, including antenna pattern peak power and direction, null depth and direction, and sidelobe level and direction, rather than to measure the full 3D radiation pattern. Single-cut FF patterns (e.g., in the E-plane or H-plane) are therefore of interest in practice since these key parameters are available in the single-cut pattern [17]. Furthermore, single-cut far field patterns can significantly reduce the NF measurement time. Much effort has been made to investigate the possibility of obtaining single-cut FF patterns from NF measurement data [17-21]. In this work, the objective is to investigate whether we can accurately reconstruct the single-cut FF pattern of the AUT in a cost-effective anechoic chamber setup equipped only with a few probe antennas. It is of importance to understand how limitations in practical setups would affect the reconstruction accuracy of the single-cut FF antenna array radiation pattern. More specifically, we are interested in how the single-cut FF pattern reconstruction accuracy is affected by practical systems:

- Compact measurement setup. A large measurement setup will take large floor-space, which can be very expensive, especially when many measurement facilities are required for massive production testing. For production testing purposes, the measurement range is often limited, e.g., up to 1 m.
- Short measurement time. Measurement time is one of the key performance indicators in antenna measurement, due to the massive amount of AUTs to be tested and many RF parameters to be examined for a single AUT. In production testing, only a few measurement probe antennas might be available to reduce the measurement time. For single-cut measurements, this means that the measured accuracy might suffer from truncation error (introduced by a limited angular range covered by the probe antennas) and under-sampling error (introduced by the large sample spacing due to limited number of probe antennas).
- “Black-box” approach. In many cases, we might lack knowledge of the AUT design. Therefore, it is desirable that the testing method can be applied for any DUT, without knowledge of the DUT. This aspect is inherently covered by the spherical near field antenna measurement since the AUT is treated as black-box design.

The paper is organized as follows. We describe our strategy to reconstruct the single-cut FF antenna array pattern in Section II. After that, we numerically investigate how limitations in practical setups would affect the reconstruction accuracy of the single-cut FF antenna array radiation pattern. Section IV discusses the future work and concludes the paper.

II. METHOD

A. AUT configuration

Without loss of generality, a 4×8 UPA composed of ideal z-oriented Hertzian dipoles with an element spacing of 0.65λ at 3.5 GHz (i.e., 56 mm) is utilized as the AUT. The Hertzian dipole is selected for the array element since it is the simplest radiation source [22]. The array configuration is selected to mimic a realistic 5G base station antenna array configuration. The size of the UPA is $5.2\lambda \times 2.6\lambda$ at 3.5 GHz (i.e., 446 mm × 223 mm) including the antenna element size, and the array element excitations can be individually controlled for the AUT, to synthesize various antenna array radiation patterns. In the simulation, the mutual coupling among array elements is not considered for the sake of simplicity, though it is important for BS antenna performance [23]. To avoid a completely symmetric AUT radiation pattern (therefore potentially over-simplifying the research problem), 28 antenna elements (marked in grey) are excited with phase 0° while the rest 4 antenna elements (marked in black) are excited with phase -90°, as indicated in Fig. 1. Uniform amplitude excitations are allocated for all antenna elements in the AUT. Note that other array configurations and element excitations can be set as well following the same procedure.

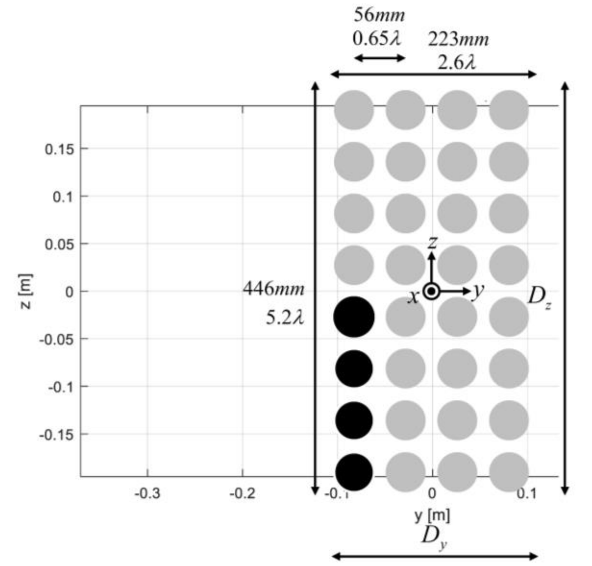

Fig. 1. An illustration of the AUT configuration and element excitations.

B. Problem statement

Following the standard spherical near field theory [24], the required number of spherical wave modes to fully reconstruct the AUT FF antenna pattern can be calculated according to the array geometry ($D_y = 2.6\lambda$, $D_z = 5.2\lambda$) as

$$N \approx \pi \frac{D_z}{\lambda} + \xi \approx 16 + \xi, \tag{1}$$

$$M \approx \pi \frac{D_y}{\lambda} + \xi \approx 8 + \xi, \tag{2}$$

where ξ is the margin [24, 25]. The maximum permissible sampling increments using standard spherical near field theory in θ and ϕ should satisfy, $\Delta_\theta < \frac{\pi}{N}$ and $\Delta_\phi < \frac{\pi}{M}$, respectively. Therefore, the number of spherical wave modes required is at minimum $M \cdot N = (8+\xi)(16+\xi) = 128 + 24\xi + \xi^2$. Using the standard spherical near field theory, we can obtain the full 3D FF pattern of the AUT, yet a large number of samples is required. As explained, for many applications, it is important to rapidly obtain the AUT FF pattern key parameters, including, e.g., array pattern peak power and direction, side-lobe power and direction, and null depth and direction, which are included the AUT single-cut FF antenna pattern within a certain angular region (e.g., $\pm 50°$ around the main beam peak).

In this work, we aim to reconstruct the single-cut FF pattern in a cost-effective measurement setup, where the number of probe antennas is limited to around 10 and the measurement range is limited to 1 m. A diagram of the setup is shown in Fig. 2. Note that the maximum size for an AUT with far-field distance of 1m is $D = 207$ mm at 3.5 GHz. Therefore, the far-field criterion is not fulfilled for the considered AUT and measurement range. To reduce the setup cost and measurement time, it is of importance to understand the impact of measurement range, number of probe antennas (i.e., finite samples) and truncation error (i.e., finite angular region covered by the probe antennas) on the accuracy of the reconstructed single-cut FF pattern. These aspects are considered in this work.

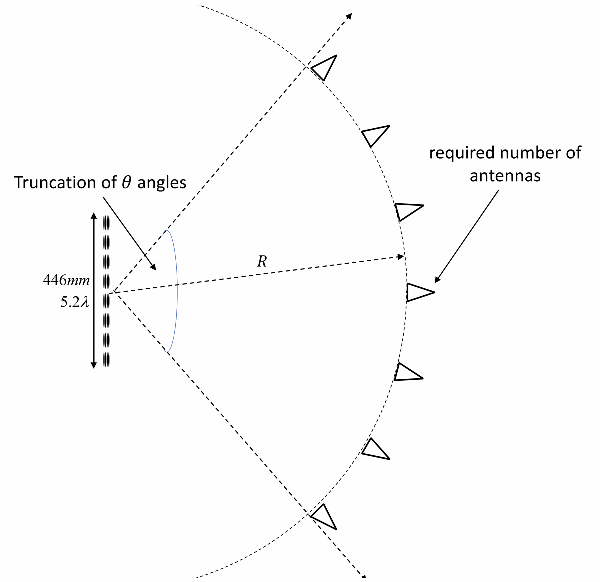

Fig. 2. Diagram of the multi-probe setup and a DUT.

In this article, two methods to obtain the AUT FF patterns are employed. With the first method, the NF and FF field pattern of the AUT composed of the 32 Hertzian dipoles with known excitation can be directly calculated according to the well-defined field radiation characteristics of Hertzian dipoles [22]. The other method to obtain the FF pattern is to use the spherical near-field to far-field transformation method. In our work, SNIFT developed by TICRA is utilized for this purpose [26]. The input NF data of SINFT is directly calculated from the known AUT (using the field pattern of the AUT), while the FF data is directly available at the SNIFT output. Ideal probe antennas (i.e., RF transparent probe antennas with isotropic antenna patterns) are assumed for the sake of simplicity, though it is not a limitation of SNIFT.

The calculated NF gain pattern at $R = 0.5$ m in Matlab is shown in Fig. 3, as an example. Using the NF data recorded at $R = 0.5$ m as input data, the FF pattern can be obtained using SNIFT, as shown in Fig. 3. The single-cut NF patterns (i.e., with $\phi = 0°$) at $R = 0.5$ m and FF distance are compared in Fig. 3. The FF pattern is not completely symmetric due to the non-symmetric AUT element excitation, as explained. The main beam and nulls in the NF pattern are not as obvious as in the FF pattern due to the small measurement distance, as expected. Therefore, there is a need for near-field to far-field transformation techniques to reconstruct the FF results based on NF data.

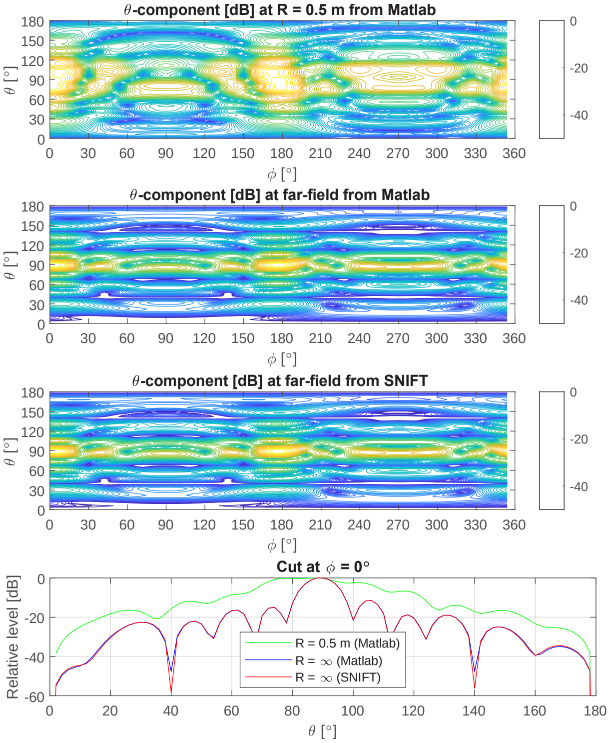

Fig. 3. Calculated NF pattern ($R = 0.5$ m) of the AUT in Matlab and FF pattern using SNIFT (input NF data at $R = 0.5$ m).

To validate whether our NF and FF calculations of the AUT based on radiated field of the Hertzian dipoles are correct, we can calculate the FF AUT pattern in Matlab and compare it with the FF pattern obtained from SNIFT, as shown in Fig. 3. The single-cut FF patterns using the two methods are also shown in Fig. 3. An excellent match is achieved within a range of 45 dB, which demonstrates the validity of our NF and FF calculations based on radiated field of the Hertzian dipoles.

C. Proposed strategy

To measure the ideal single-cut FF pattern, the measurement distance R should satisfy the far-field assumption while we have a sufficient number of samples, e.g., with 1° step to capture all details in the FF pattern. This, however, is not feasible for many measurement scenarios. As explained, it is desirable that we should reconstruct the single-cut FF pattern of the AUT in a fast and cost-effective manner. As for a practical multi-probe anechoic chamber setup, this implies a small measurement distance and a low number of probe antennas. In this work, we aim to reconstruct the single-cut FF pattern of the AUT based on single-cut NF data in a practical setup. A framework to investigate the single-cut FF pattern reconstruction accuracy is proposed in this work, as illustrated in Fig. 4 and explained below.

1) The AUT is composed of ideal Hertzian dipoles, and therefore the AUT characteristics can be fully determined once the array configuration and array element excitations are set.
2) The reference FF pattern can be directly calculated in Matlab according to the field distribution of Hertzian dipoles.
3) The NF of the AUT at a distance R can also be directly calculated following the field distribution of in Hertzian dipoles in Matlab. The NF single-cut pattern (i.e., with $\phi = 0°$) can be modified according to the compact anechoic chamber configurations:
    a) Single-cut operation. To obtain the single-cut FF pattern of the AUT based on NF data, the following procedure is used. The NF pattern at $\phi = 0°$ is selected and copied to all other ϕ-values. Then the reconstructed NF data is used as the input data to obtain the FF pattern of the AUT using SNIFT. An example is shown in Fig. 5, where the NF AUT pattern at $R = 0.5$ m and the reconstructed NF data is shown. Then the reconstructed NF data is used as the input data to obtain the FF pattern of the AUT using SNIFT, as shown in Fig. 5. The reconstructed single-cut FF pattern (i.e., with $\phi = 0°$) is compared with the target calculated single-cut FF pattern in Fig. 5. A good match can be achieved, while small deviations in the sidelobes and null depths exist. This is introduced by the single-cut operation of the NF data with a small measurement range.
    b) Single-cut operation with truncation of θ range. The NF data can be truncated in θ, e.g., 30° to 150° to demonstrate the impact of truncation error introduced by a limited angle covered by the probe antennas. The NF data outside the truncation range is simply set to 0. Note that θ truncation is not seen at the output (FF) of SNIFT, while only the input data (NF) is truncated.
    c) Single-cut operation with increased sampling intervals. The sampling interval will have to be updated according to the number of available probe antennas in the measurement system. The NF data (input) is re-

sampled according to the sampling interval. The FF data (output) can be interpolated to make the pattern curve smoother.

4) The modified NF data at distance R can be obtained via copying the NF pattern at $\phi = 0°$ to all other ϕ-values.
5) We can then obtain the reconstructed FF pattern of the modified NF pattern from SNIFT.
6) In the end, we can extract the single-cut FF pattern from the reference and reconstructed results and compare.

With the proposed framework, we can flexibly modify the NF data introduced by limitations in practical systems, i.e., measurement distance R, truncation of θ range, and sampling intervals, and investigate the inaccuracies introduced by these limitations.

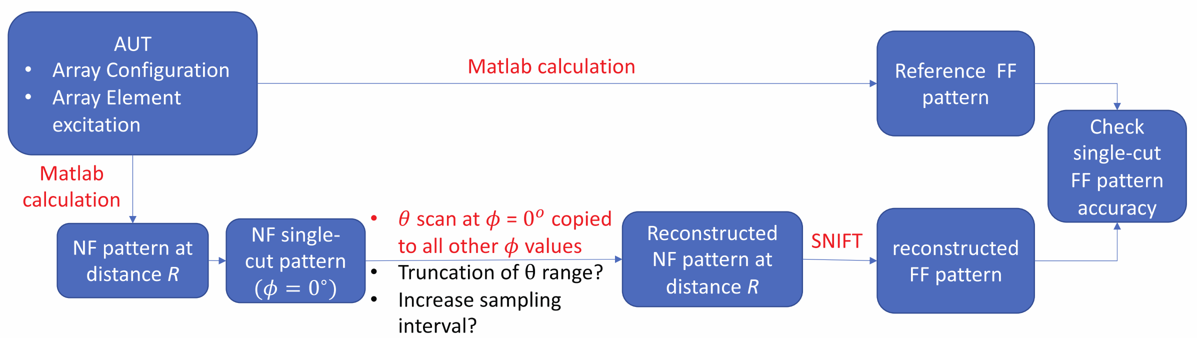

Fig. 4. The proposed simulation framework to investigate the single-cut FF pattern reconstruction accuracy.

III. SIMULATION RESULTS

A. Measurement distance R

The calculated FF pattern using Matlab and the FF pattern obtained from SNIFT (input data: calculated NF data at $R = 1$ m) are shown in Fig. 6. The two single-cut FF patterns (with $\phi = 0°$) are shown in Fig. 6 (bottom). As we can see, a better agreement is achieved, compared to the results in Fig. 5 (with NF data at $R = 0.5$ m). The improved accuracy is introduced by a larger measurement range, as expected. Generally speaking, a larger measurement distance would lead to less error in the single-cut FF pattern. It can be observed that the single-cut operation of the NF data will introduce negligible errors with $R = 1$ m for the considered AUT. Therefore, in the simulation below, $R = 1$ m is considered unless otherwise stated.

B. Truncation error

The next step is to investigate the impact of θ-range truncation on the single-cut FF pattern accuracy. For a practical system, we aim to determine the antenna pattern key parameters using the minimal required number of probe antennas. The key parameters, including main peak power and direction, first null depth and direction, and first side-lobe level and direction, are concentrated around $\theta = 90°$. Therefore, θ-range truncation might not affect the reconstruction accuracy of these key parameters. On the other hand, a large θ-range truncation with the same number of probe antennas (i.e., more concentrated probe configurations) also means a smaller sampling interval, which is beneficial to the pattern reconstruction accuracy.

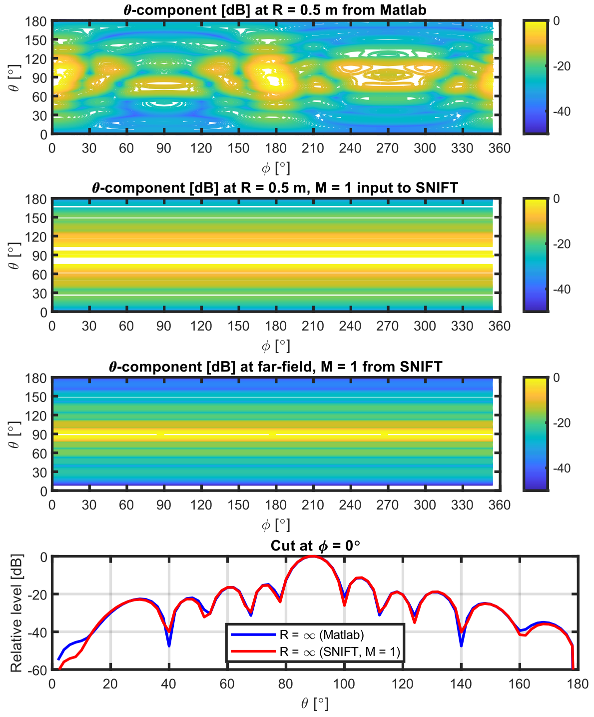

Fig. 5. Reconstructed FF AUT pattern in SNIFT (input NF data: modified AUT pattern at $R = 0.5$ m and pattern at $\phi = 0°$ is selected and copied to all other ϕ-values) (top) and comparison with target single-cut FF pattern (bottom).

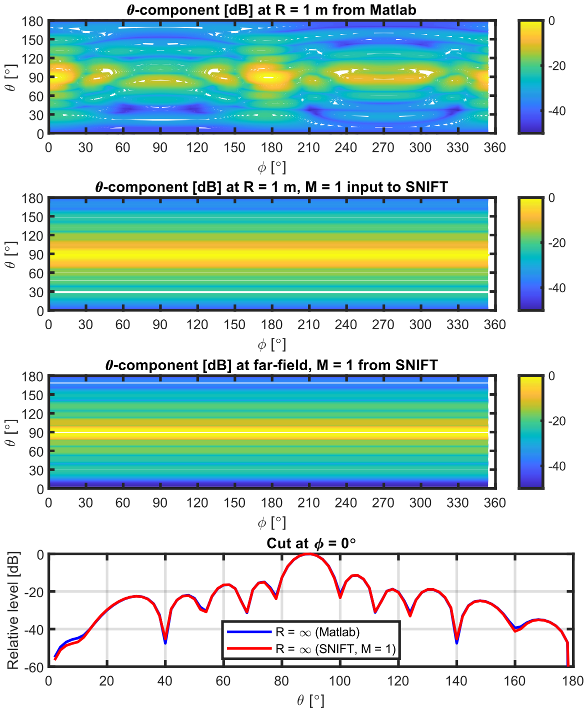

Fig. 6. Reconstructed FF AUT pattern in SNIFT (input NF data: modified AUT pattern at $R = 1$ m and pattern at $\phi = 0°$ is selected and copied to all other ϕ-values) (top) and comparison with target single-cut FF pattern (bottom).

The reconstructed single-cut FF patterns with θ truncation ranges $[0°, 180°]$ (i.e., no θ truncation), $[30°, 150°]$, $[45°, 135°]$, and $[60°, 120°]$ are shown and compared with the reference single-cut FF pattern in Fig. 7. As we can see, smaller θ-range truncations (i.e., θ truncation range $[30°, 150°]$ and $[45°, 135°]$) do not deteriorate the pattern reconstruction accuracy for the main lobe, the first null and the first side-lobe. However, a large all θ-range truncation (i.e., θ truncation range $[60°, 120°]$) leads to large deviations in the first null and also the side-lobe level as well. Therefore, the θ truncation range should be properly set in practical measurement systems to balance the measurement error and measurement time.

C. Number of probe antennas

The number of probe antennas is limited in practical measurement systems, due to cost and measurement time considerations. Therefore, it is important to understand the impact of the sampling interval on the single-cut FF radiation pattern reconstruction accuracy.

Following the standard spherical near field theory, the theoretical limit of the sampling interval is:

$$\Delta_\theta < \frac{180°}{\pi\frac{D_z}{\lambda}+\xi}. \tag{3}$$

That is, Δ_θ should be smaller than 12.6° without margin in principle to avoid errors introduced by under-sampling.

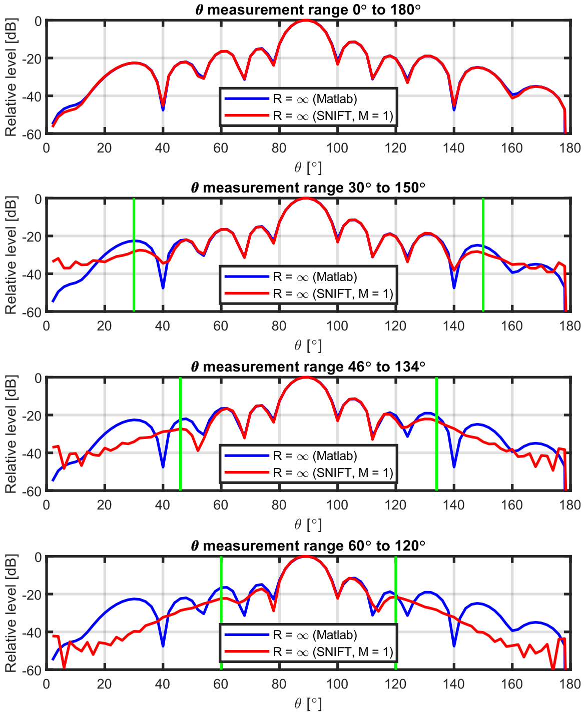

Fig. 7. Reconstructed single-cut FF patterns with θ truncation range $[0°, 180°]$, $[30°, 150°]$, $[45°, 135°]$ and $[60°, 120°]$.

The calculated FF pattern using Matlab (with sampling interval $\Delta_\theta = 5°$) is shown in Fig. 8. The FF pattern obtained from SNIFT using the modified NF data according to measurement setup (θ-scan at $\phi = 0°$, $\Delta_\theta = 5°$, θ truncation to $[30°, 150°]$, and measurement distance $R = 1$ m) is shown in Fig. 8. The single-cut FF patterns are compared in Fig. 8, where a good agreement can be observed. This is expected, since the sampling interval satisfies the theoretical limit. The truncation operation introduces some deviation for the angular region outside of the truncation region, as explained. This measurement system configuration would result in around 25 probe positions.

To be consistent with the simulation results shown so far (i.e., with $\Delta_\theta = 1°$), the output FF pattern from SNIFT (i.e., with $\Delta_\theta = 5°$) can also be interpolated, as shown in Fig. 8. Note that interpolation can be used to smooth the curve, while the reconstruction accuracy cannot be improved.

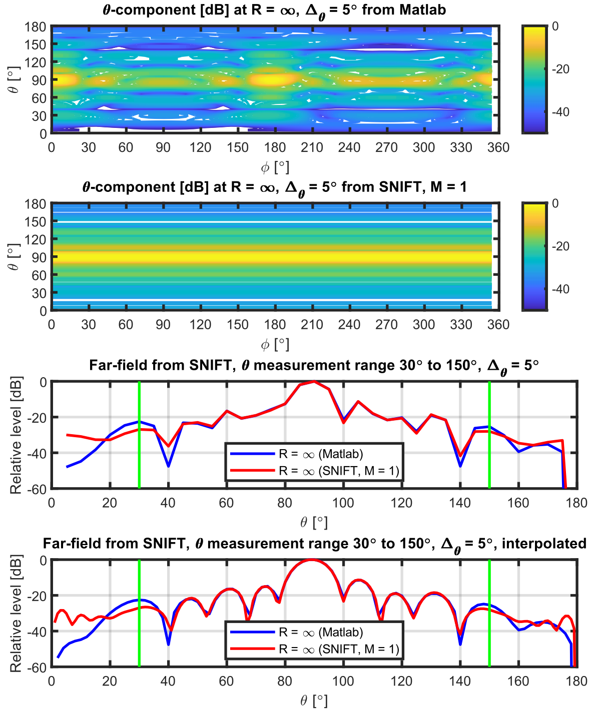

Fig. 8. The reference single-cut FF pattern and the interpolated reconstructed single-cut FF pattern with $\Delta_\theta = 5°$.

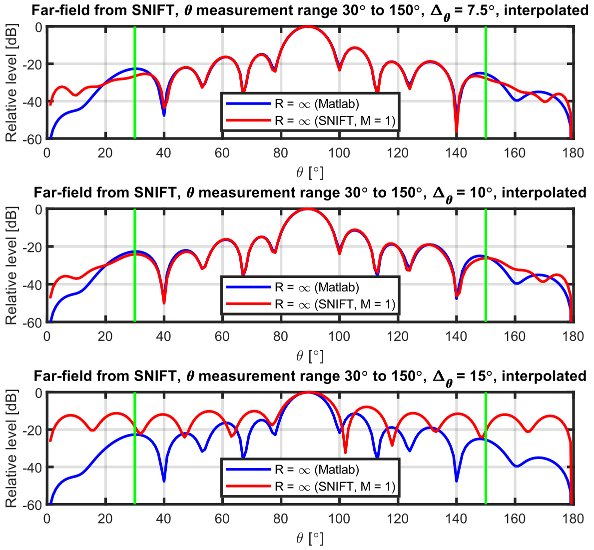

Fig. 9. Reconstructed FF single-cut pattern with sampling intervals $\Delta_\theta = 7.5°$, $\Delta_\theta = 10°$, and $\Delta_\theta = 15°$, respectively.

In Fig. 9, the θ truncation range is kept at $[30°, 150°]$ and interpolation is applied. Sampling intervals $\Delta_\theta = 7.5°$, $\Delta_\theta = 10°$, and $\Delta_\theta = 15°$ are set, respectively. As we can observe, if the theoretical limit is satisfied (i.e., $\Delta_\theta < 12.6°$), no errors will be introduced due to sampling. However, if the theoretical limit is violated (e.g., $\Delta_\theta = 15°$), large deviations in the main lobe, side-lobes and nulls can be observed. Therefore, for single-cut FF antenna pattern reconstruction, it is important that the sampling criteria satisfies the theoretical limit.

IV. CONCLUSION AND FUTURE WORK

In this work, the focus is on how limitations introduced in practical antenna measurement setups, e.g., measurement range, truncation error, sampling intervals would affect the single-cut far-field pattern reconstruction accuracy of the AUT. To address this problem, a simple and flexible scheme is proposed, where the near-field data can be generated and modified according to practical setup constraints. In this way, we can easily check how the reconstruction accuracy is affected by different settings. A 4 × 8 UPA composed of z-oriented ideal Hertzian dipoles with element spacing 0.65λ at 3.5 GHz (i.e., 56 mm) is utilized as the AUT. Extensive numerical simulations have been performed to demonstrate the impact of measurement range, truncation error and sampling interval on the reconstruction accuracy. We have shown in numerical simulations that we can accurately reconstruct the single-cut far-field pattern of the considered AUT with $R = 1$ m, a truncation range of $[30°, 150°]$, and a sampling interval of 10°.

There is some logic extension of the current work. The numerical simulations in the work are based on a UPA with ideal z-oriented Hertzian dipoles. It is of interest to investigate how well the proposed scheme works with more realistic antenna arrays (e.g., CST simulated or real array). The analysis is based on one specific case of AUT element excitations as explained in the AUT configuration section. We can also repeat the procedure to check more AUT excitations, to see whether the considered scenario is typical. For truncation error analysis, the data outside the truncation range is directly set to 0. We can also investigate whether we can improve the reconstruction accuracy by applying a window-function with the truncation. Furthermore, probe pattern correction should be considered for real measurements, which is not considered in our current work. It is also logic to investigate how the well proposed scheme works for planar scanning measurements.

ACKNOWLEDGMENT

The authors would like to thank for financial support from Huawei Technologies and InnoExplorer Project Funded by Innovation Fund Denmark (No. 20199122-00089A). Corresponding author is Dr. Wei Fan.

REFERENCES

[1] C. Huang, R. Wang, P. Tang, R. He, B. Ai, Z. Zhong, C. Oestges, and A. F. Molisch, “Geometry-

cluster-based stochastic MIMO model for vehicle-to-vehicle communications in street canyon scenarios," *IEEE Transactions on Wireless Communications*, vol. 20, no. 2, pp. 755-770, 2021.

[2] K. Guan, B. Peng, D. He, J. M. Eckhardt, S. Rey, B. Ai, Z. Zhong, and T. Kürner, "Channel characterization for intra-wagon communication at 60 and 300 GHz bands," *IEEE Transactions on Vehicular Technology*, vol. 68, no. 6, pp. 5193-5207, 2019.

[3] B. Peng, K. Guan, A. Kuter, S. Rey, M. Patzold, and T. Kuerner, "Channel modeling and system concepts for future terahertz communications: Getting ready for advances beyond 5G," *IEEE Vehicular Technology Magazine*, vol. 15, no. 2, pp. 136-143, 2020.

[4] W. Fan, P. Kyosti, M. Rumney, X. Chen, and G. F. Pedersen, "Over-the-air radiated testing of millimeter-wave beam-steerable devices in a cost-effective measurement setup," *IEEE Communications Magazine*, vol. 56, no. 7, pp. 64-71, 2018.

[5] X. Chen, M. Zhang, S. Zhu, and A. Zhang, "Empirical study of angular–temporal spectra in a reverberation chamber," *IEEE Transactions on Antennas and Propagation*, vol. 66, no. 11, pp. 6452-6456, 2018.

[6] W. Xue, F. Li, and X. Chen, "Effects of signal bandwidth on total isotropic sensitivity measurements in reverberation chamber," *IEEE Transactions on Instrumentation and Measurement*, vol. 70, pp. 1-8, 2021.

[7] X. Chen, W. Fan, L. Hentilä, P. Kyösti, and G. F. Pedersen, "Throughput modeling and validations for MIMO-OTA testing with arbitrary multipath," *IEEE Antennas and Wireless Propagation Letters*, vol. 17, no. 4, pp. 637-640, 2018.

[8] P. Kyösti, W. Fan, and J. Kyröläinen, "Assessing measurement distances for OTA testing of massive MIMO base station at 28 GHz," in *2017 11th European Conference on Antennas and Propagation (EUCAP)*, pp. 3679-3683, 2017.

[9] Y. Ji, W. Fan, G. F. Pedersen, and X. Wu, "On channel emulation methods in multiprobe anechoic chamber setups for over-the-air testing," *IEEE Transactions on Vehicular Technology*, vol. 67, no. 8, pp. 6740-6751, 2018.

[10] F. D'Agostino, F. Ferrara, C. Gennarelli, R. Guerriero, and M. Migliozzi, "Probe position errors corrected near-field-far-field transformation with spherical scanning," *Applied Computational Electromagnetics Society Journal*, vol. 31, no. 2, 2016.

[11] Z. Qiao, Z. Wang, W. Fan, X. Zhang, S. Gao, and J. Miao, "Low scattering plane wave generator design using a novel non-coplanar structure for near-field over-the-air testing," *IEEE Access*, vol. 8, pp. 211 348-211 357, 2020

[12] Y. Zhang, Z. Wang, X. Sun, Z. Qiao, W. Fan, and J. Miao, "Design and implementation of a wideband dual-polarized plane wave generator with tapered feeding nonuniform array," *IEEE Antennas and Wireless Propagation Letters*, vol. 19, no. 11, pp. 1988-1992, 2020.

[13] X. Chen, "Measurement uncertainty of antenna efficiency in a reverberation chamber," *IEEE Transactions on Electromagnetic Compatibility*, vol. 55, no. 6, pp. 1331-1334, 2013.

[14] H. Kong, Z. Wen, Y. Jing, and M. Yau, "Midfield over-the-air test: A new OTA RF performance test method for 5G massive MIMO devices," *IEEE Transactions on Microwave Theory and Techniques*, vol. 67, no. 7, pp. 2873-2883, 2019.

[15] H. Kong, Y. Jing, Z. Wen, and L. Cao, "Mid-field OTA RF test method: new developments and performance comparison with the compact antenna test range (CATR)," in *2020 14th European Conference on Antennas and Propagation (EuCAP)*, pp. 1-5, 2020.

[16] M. Sierra-Castañer, "Review of recent advances and future challenges in antenna measurement," *Applied Computational Electromagnetics Society Journal*, vol. 33, no. 1, 2018.

[17] R. Cornelius, T. Salmerón-Ruiz, F. Saccardi, L. Foged, D. Heberling, and M. Sierra-Castañer, "A comparison of different methods for fast single-cut near-to-far-field transformation [euraap corner]," *IEEE Antennas and Propagation Magazine*, vol. 56, no. 2, pp. 252-261, 2014.

[18] S. Omi, T. Uno, and T. Arima, "Single-cut near-field far-field transformation technique employing two-dimensional plane-wave expansion," *IEEE Antennas and Wireless Propagation Letters*, vol. 17, no. 8, pp. 1538-1541, 2018.

[19] X. Li, G. Wei, L. Yang, and B. Liao, "Fast determination of single-cut far-field pattern of base station antenna at a quasi-far-field distance," *IEEE Transactions on Antennas and Propagation*, vol. 68, no. 5, pp. 3989-3996, 2020.

[20] Y. Sugimoto, H. Arai, T. Maruyama, M. Nasuno, M. Hirose, and S. Kurokawa, "Fast far-field estimation method by compact single-cut near-field measurements for electrically long antenna array," *IEEE Transactions on Antennas and Propagation*, vol. 66, no. 11, pp. 5859-5868, 2018.

[21] F. Rodríguez Varela, B. G. Iragüen, and M. Sierra-Castañer, "Undersampled spherical near-field antenna measurements with error estimation," *IEEE Transactions on Antennas and Propagation*, vol. 68, no. 8, pp. 6364-6371, 2020.

[22] C. A. Balanis, *Modern Antenna Handbook*. John Wiley & Sons, 2011.

[23] X. Chen, S. Zhang, and Q. Li, "A review of mutual

coupling in MIMO systems," *IEEE Access*, vol. 6, pp. 24 706-24 719, 2018.

[24] J. E. Hansen, "Spherical near-field antenna measurements," *Peter Peregrinus Ltd. (IEE Electromagnetic Waves Series 26), IET*, vol. 26, 1988.

[25] F. Jensen and A. Frandsen, "On the number of modes in spherical wave expansions," *Proc. 26th AMTA*, vol. 2, no. 1, pp. 489-494, 2004.

[26] F. Jensen, "SNIFT-computer program for spherical near-field far-field technique, volume 2," *NASA STI/Recon Technical Report N*, vol. 77, p. 23328, 1976.

Accurate Far-Field Measurement of Wide-Angle Scanning Phased Array Antennas

Hongjun Tang [1] **and Xianbao Zheng** [2]

[1] Southwest China Institute of Electronic Technology, Chengdu, 610036, China
a_thj@163.com

[2] Nanjing Coral Electronic Equipment Co. Ltd, Nanjing, 210018, China
281591383@qq.co

Abstract **─** This paper presents a new approach to the accurate determination of the far-field (FF) pattern of wide-angle scanning phased array antennas (PAAs) that uses planar near-field (NF) technology. When PAAs are engaged in wide-angle scanning, a finite scanning plane and inaccurate probe compensation can lead to truncation errors. The proposed approach reduces these by rotating the PAA to make its main beam perpendicular to the scanning plane. To verify the effectiveness of the approach, both theoretical calculations and actual measurements were undertaken. The simulated and measured results prove that the proposed method is more accurate than traditional NF technology for a large PAA scanning angle, such as ψ_0=50° and Δ_0=50° (in simulation; 54° when measured).

Index Terms **─** Antenna measurement, planar near-field technology, wide-angle scanning phased array antenna.

I. INTRODUCTION

The effective measurement of antenna technologies [1-4] has always been a key issue. Phased array antennas (PAAs) are antennas that can be electrically controlled to change the direction and shape of the beam. In addition to fifth generation (5G) millimeter-wave mobile terminals [5], PAAs are often required in modern radar applications to provide scanning with spatial coverage over a broader angular range. A prominent concern in the design of PAAs has been to enlarge their scanning angle, so measuring their wide-angle scanning performance has become an important topic of research [6]. Wide-angle scanning PAA measurement technologies are usually applied to either far-field (FF) measurements or near-field (NF) measurements [7-9]. However, individual FF measurements tend to deliver very limited information. NF approaches are therefore commonly used for antenna radiation and RCS measurements. Existing planar NF measurements are also best suited to measuring antennas with pencil-beam characteristics. However, finite scanning surface truncation errors often affect the accuracy of planar NF measurements. For antennas that do not scan the beam and antennas that do not have a large scan angle, there usually needs to be a cutoff at the edge of the planar NF scanning plane, below -40 dB, to minimize the truncation error. When the beam of an antenna under test (AUT) is scanned, a large truncation angle is often required to meet the -40 dB cutoff. Unfortunately, large truncation angles are not always possible during actual measurement processes. Furthermore, when the scanning angle of an AUT is large, there can also be inaccuracies in the calculation of the probe compensation.

Various efforts have been made to try and reduce the truncation errors. The most commonly-used method is to select the most appropriate window function. This will have a smooth taper at the edges of the scan plane [10]. However, this method reduces the extent of the reliable region. An equivalent electric current or magnetic current can be introduced to determine the FF pattern [11], but this method requires certain kinds of a priori information, such as the geometry and position of the antenna. It is also extremely time-consuming for electrically large antennas. Some previously proposed techniques [e.g., 12] have suggested enlarging the reliable angular region, but they increase the complexity of the scanning system by demanding additional measurements of the shape. Recently, band-limited signal extrapolation algorithms have been applied to radiation [13] and RCS measurements [14] in the NF region, so as to reduce the truncation errors. However, these approaches cannot be directly applied to the measurement of wide-angle scanning antennas because most of the energy remains outside the NF scanning plane of the AUT and cannot be ignored.

In this paper, we present a novel method for accurately measuring wide-angle scanning PAAs. Prior to the planar NF measurement, the AUT is rotated by a specific angle so that the main beam is perpendicular to the scanning plane. During NF scanning on the test plane, it is then relatively easy to obtain lower near-field

Submitted On: April 22, 2021
Accepted On: August 11, 2021

https://doi.org/10.47037/2021.ACES.J.360915

truncation levels. After the mathematical transformation introduced in this paper, it is possible to achieve accurate PAA FF measurements.

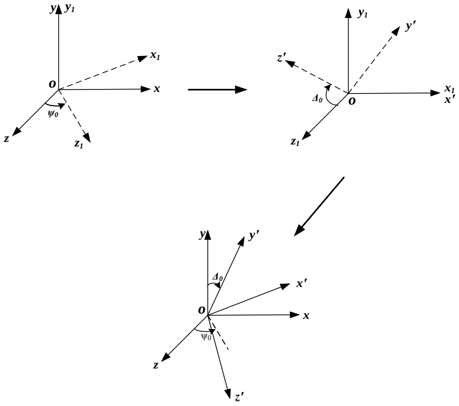

Fig. 1. The relationship between o-xyz and o-x′y′z′.

II. THEORETICAL BACKGROUND

A. Coordinate system transformation

Figure 1 illustrates the relationship between an original coordinate system, *o-xyz*, and a translated coordinate system, *o-x'y'z'*. Assuming that the rotation angles are ψ_0 and Δ_0 in the original coordinate system, we can get the *o-x'y'z'* coordinate system after two rotations. This relationship can be written as:

$$\begin{bmatrix}\hat{x}'\\ \hat{y}'\\ \hat{z}'\end{bmatrix} = T\begin{bmatrix}\hat{x}\\ \hat{y}\\ \hat{z}\end{bmatrix} = \begin{bmatrix}t_{11} & t_{12} & t_{13}\\ t_{21} & t_{22} & t_{23}\\ t_{31} & t_{32} & t_{33}\end{bmatrix}\begin{bmatrix}\hat{x}\\ \hat{y}\\ \hat{z}\end{bmatrix}, \qquad (1a)$$

$$\begin{bmatrix}\hat{x}\\ \hat{y}\\ \hat{z}\end{bmatrix} = \begin{bmatrix}t_{11} & t_{21} & t_{31}\\ t_{12} & t_{22} & t_{32}\\ t_{13} & t_{23} & t_{33}\end{bmatrix}\begin{bmatrix}\hat{x}'\\ \hat{y}'\\ \hat{z}'\end{bmatrix}, \qquad (1b)$$

where

$$t_{11} = cos\,\psi_0\,, t_{12} = 0, t_{13} = -sin\,\psi_0,$$
$$t_{21} = -\,sin\,\Delta_0\,sin\,\psi_0, t_{22} = cos\Delta_0, t_{23} - sin\,\Delta_0\,cos\,\psi_0$$
$$t_{31} = cos\Delta_0\,sin\,\psi_0, t_{32} = sin\,\Delta_0, t_{33} = cos\Delta_0\,cos\,\psi_0. \quad (2)$$

Assuming that the coordinates of the vector, $\vec{r}$, in the two coordinate systems are (x, y, z) and (x', y', z'), it can be represented as follows:

$$\vec{r} = [x \quad y \quad z]\begin{bmatrix}\hat{x}\\ \hat{y}\\ \hat{z}\end{bmatrix} = [x' \quad y' \quad z']\begin{bmatrix}\hat{x}'\\ \hat{y}'\\ \hat{z}'\end{bmatrix} =$$
$$[x' \quad y' \quad z']\begin{bmatrix}t_{11} & t_{12} & t_{13}\\ t_{21} & t_{22} & t_{23}\\ t_{31} & t_{32} & t_{33}\end{bmatrix}\begin{bmatrix}\hat{x}\\ \hat{y}\\ \hat{z}\end{bmatrix}. \qquad (3)$$

The relationship between (x, y, z) and (x', y', z') will then be:

$$\begin{bmatrix}x\\ y\\ z\end{bmatrix} = \begin{bmatrix}t_{11} & t_{21} & t_{31}\\ t_{12} & t_{22} & t_{32}\\ t_{13} & t_{23} & t_{33}\end{bmatrix}\begin{bmatrix}x'\\ y'\\ z'\end{bmatrix} = \begin{bmatrix}t_{11}x' + t_{21}y' + t_{31}z'\\ t_{12}x' + t_{22}y' + t_{32}z'\\ t_{13}x' + t_{23}y' + t_{33}z'\end{bmatrix}. \quad (4)$$

Similarly, we can obtain:

$$\begin{bmatrix}x'\\ y'\\ z'\end{bmatrix} = \begin{bmatrix}t_{11} & t_{12} & t_{13}\\ t_{21} & t_{22} & t_{23}\\ t_{31} & t_{32} & t_{33}\end{bmatrix}\begin{bmatrix}x\\ y\\ z\end{bmatrix} = \begin{bmatrix}t_{11}x + t_{12}y + t_{13}z\\ t_{21}x + t_{22}y + t_{23}z\\ t_{31}x + t_{32}y + t_{33}z\end{bmatrix}. \quad (5)$$

Vectors in any direction in space (ψ, Δ) will correspond to the $o - xyz$ coordinate system and (ψ', Δ') will correspond to the $o - x'y'z'$ coordinate system. Any unit vector, $\hat{r}$, can be represented as follows in the two coordinate systems:

$$\hat{r} = [cos\Delta sin\psi \quad sin\Delta \quad cos\Delta cos\psi]\begin{bmatrix}\hat{x}\\ \hat{y}\\ \hat{z}\end{bmatrix}$$
$$\hat{r} = [cos\Delta' sin\psi' \quad sin\Delta' \quad cos\Delta' cos\psi']\begin{bmatrix}\hat{x}'\\ \hat{y}'\\ \hat{z}'\end{bmatrix}$$
$$= [cos\Delta' sin\psi' \quad sin\Delta' \quad cos\Delta' cos\psi']T\begin{bmatrix}\hat{x}\\ \hat{y}\\ \hat{z}\end{bmatrix}. \qquad (6)$$

So, the transformation relationship between (ψ', Δ') and (ψ, Δ) will be:

$$\Delta = arcsin\,(t_{22}sin\Delta' + t_{32}cos\Delta' cos\psi')$$
$$\psi = angle((t_{13}cos\Delta' sin\psi' + t_{23}sin\Delta' t_{33}cos\Delta' cos\psi')$$
$$+j(t_{11}cos\Delta' sin\psi' + t_{21}sin\Delta' + \; t_{31}cos\Delta' cos\psi')). \quad (7)$$

Similarly, the transformation relationship between (ψ, Δ) and (ψ', Δ') will be:

$$\Delta' = arcsin\,(t_{21}cos\Delta sin\psi + t_{22}sin\Delta + t_{23}cos\Delta cos\psi)$$
$$\psi' = angle((t_{31}cos\Delta sin\psi + t_{32}sin\Delta + t_{33}cos\Delta cos\psi)$$
$$+j(t_{11}cos\Delta sin\psi + t_{13}cos\Delta cos\psi)). \qquad (8)$$

The relationship between $\left(\hat{\psi}, \hat{\Delta}\right)$ and $(\hat{x}, \hat{y}, \hat{z})$ is thus:

$$\begin{bmatrix}\hat{\psi}\\ \hat{\Delta}\end{bmatrix} = \begin{bmatrix}cos\psi & 0 & -sin\psi\\ -sin\Delta sin\psi & cos\Delta & -sin\Delta cos\psi\end{bmatrix}\begin{bmatrix}\hat{x}\\ \hat{y}\\ \hat{z}\end{bmatrix}, \qquad (9)$$

Similarly,

$$\begin{bmatrix}\hat{\psi}'\\ \hat{\Delta}'\end{bmatrix} = \begin{bmatrix}cos\psi' & 0 & -sin\psi'\\ -sin\Delta' sin\psi' & cos\Delta' & -sin\Delta' cos\psi'\end{bmatrix}\begin{bmatrix}\hat{x}'\\ \hat{y}'\\ \hat{z}'\end{bmatrix}, \quad (10)$$

The dot matrix between $(\hat{\psi}, \hat{\Delta})$ and $(\hat{\psi}', \widehat{\Delta'})$ can be expressed as:

$$\hat{\psi}\cdot\hat{\psi}' = cos\psi'(\mathrm{t}_{11}cos\psi - \mathrm{t}_{13}sin\psi)sin\psi'\,(\mathrm{t}_{31}cos\psi -$$
$$\mathrm{t}_{33}sin\psi), \qquad (11a)$$

$$\hat{\psi}\cdot\hat{\Delta}' = cos\Delta'(\mathrm{t}_{21}cos\psi - \mathrm{t}_{23}sin\psi) - sin\Delta' cos\psi'$$
$$(\mathrm{t}_{31}cos\psi - \mathrm{t}_{33}sin\psi) - sin\Delta' sin\psi'(\mathrm{t}_{11}cos - \mathrm{t}_{13}sin\psi),$$
$$(11b)$$

$$\hat{\Delta}\cdot\hat{\psi}' = sin\psi'(\mathrm{t}_{31}sin\Delta sin\psi - \mathrm{t}_{32}cos\Delta +$$
$$\mathrm{t}_{33}sin\Delta cos\psi) - cos\psi' sin\Delta(\mathrm{t}_{11}sin\psi + \mathrm{t}_{13}cos\psi), \quad (11c)$$

$$\hat{\Delta}\cdot\hat{\Delta}' = sin\Delta' cos\psi'(t_{31}sin\Delta sin\psi - t_{32}cos\Delta +$$
$$t_{33}sin\Delta cos\psi) \; - \; cos\Delta'(t_{21}sin\Delta sin\psi - t_{22}cos\Delta +$$
$$t_{23}sin\Delta cos\psi) \; + sin\Delta' sin\psi' sin\Delta(t_{11}sin\psi + t_{13}cos\psi).$$
$$(11d)$$

B. Pattern transformation

If a PAA is measured in an $o - x'y'z'$ coordinate system, then it must be transformed to an $o - xyz$ coordinate system to obtain its characteristics. The corresponding pattern in the two coordinate systems can be expressed by $\left(\hat{\psi}, \hat{\Delta}\right)$ and $\left(\hat{\psi}', \hat{\Delta}'\right)$, respectively:

$$\vec{F} = F_{\psi'}(\psi', \Delta')\hat{\psi}' + F_{\Delta'}(\psi', \Delta')\hat{\Delta}', \qquad (12a)$$
$$\vec{F} = F_{\psi}(\psi, \Delta)\hat{\psi} + F_{\Delta}(\psi, \Delta)\hat{\Delta}. \qquad (12b)$$

From this, the transformation relationship between the

$o-x'y'z'$ coordinate system's pattern and the $o-xyz$ coordinate system's pattern can be obtained:

$$F_{\psi}(\psi,\varDelta)=F_{\psi'}(\psi',\varDelta')\left(\hat{\psi}'\cdot\hat{\psi}\right)+F_{\varDelta'}(\psi',\varDelta')\left(\hat{\varDelta}'\cdot\hat{\psi}\right), \tag{13a}$$

$$F_{\Delta}(\psi,\varDelta)=F_{\psi'}(\psi',\varDelta')\left(\hat{\psi}'\cdot\hat{\Delta}\right)+F_{\varDelta'}(\psi',\varDelta')\left(\hat{\varDelta}'\cdot\hat{\Delta}\right). \tag{13b}$$

In Eqs. (13a) and (13b), $F_{\psi'}\left(\psi',\varDelta'\right)$ and $F_{\varDelta'}\left(\psi',\varDelta'\right)$ can be obtained through measurement, then, by substituting Eqs. (11a-11d) into Eqs. (13a) and (13b), the FF of the PAA can be acquired.

III. SIMULATED AND MEASURED RESULTS

A. Calculated results

In order to assess the effectiveness of the proposed approach, a measurement model was first established. Fig. 2 shows a schematic diagram of the model. The AUT here consisted of $N_x\times N_y$ electric dipole elements. The element intervals were d_x and d_y, respectively, and the amplitude had a -25dB sidelobe Taylor distribution in the direction of the azimuth and a -35dB sidelobe Taylor distribution in the direction of the elevation. The distance between the scan plane and the AUT was d. The reliable angles were θ_x and θ_y, respectively, and the sampling intervals were $\varDelta_x$ and $\varDelta_y$. The details of the parameters are presented in Table 1.

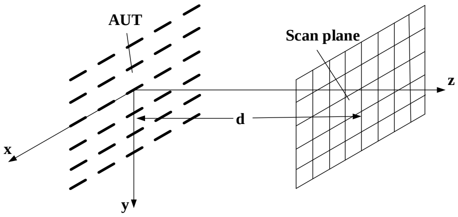

Fig. 2. Schematic diagram of the model.

Table 1: Detailed parameters

Parameter	Value	Parameter	Value
N_x	20	θ_x	60°
N_y	20	θ_y	60°
d_x	0.6λ	$\varDelta x$	0.4λ
d_y	0.6λ	θy	0.4λ
d	5λ	Antenna Size	12λ×12λ
		Scan Plane Size	29.3×29.3λ

It was assumed that the antenna beam scanning angle was ψ_0=50° and $\varDelta_0$=50°, with truncation angles of 60° and 85°, respectively. A comparison of these two cases relating to a normal NF-FF transformation and the theoretical results is shown in Fig. 3. The results show that when the PAA was in a wide-angle scanning mode, the difference between the calculated FF pattern and the theoretical FF pattern decreased as the truncation angle increased. When the truncation angle was 85°, there was an obvious difference between the calculated result and the theoretical result. However, this truncation angle is impossible to realize in actual practice. When the antenna aperture was rotated by ψ=50° and $\varDelta$=50°, which was the same as the scanning angle of the PAA, the main beam was orthogonal to the scanning plane. Here, a 60° truncation angle was assumed. As can be seen in Fig. 3 (a), the traditional 60° truncated angle NF-FF was noticeably different from the theoretical FF. Figure 3 (b) shows that they were in good agreement when the truncated angle increased to 85°. However, as can be seen in Fig. 3 (c), the results relating to the proposed method were consistent with the theoretical results when the truncated angle was just 60°. Figure 4 also shows that the calculated results using the proposed method were in good agreement with the theoretical results. This proves the validity and accuracy of the proposed method.

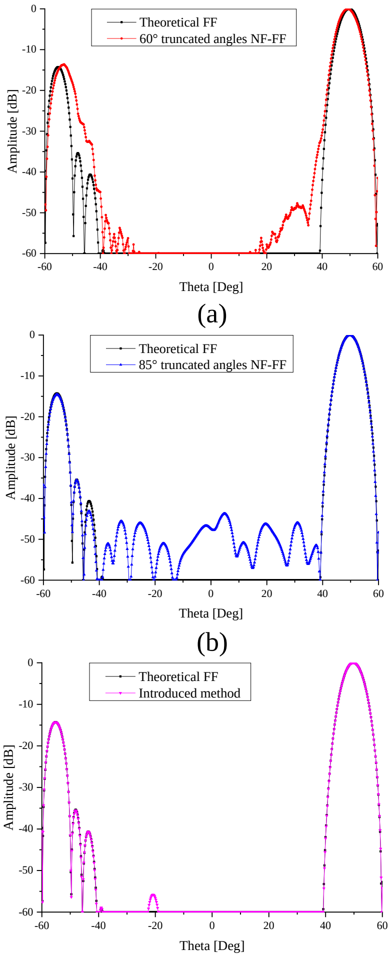

(a)

(b)

(c)

Fig. 3. Comparison between the theoretical results and calculated results for the elevation plane when ψ_0=50°. (a) Comparison between the theoretical FF and a 60° truncated angle NF-FF. (b) Comparison between the theoretical FF and an 85° truncated angle NF-FF. (c) Comparison between the theoretical FF and the proposed method.

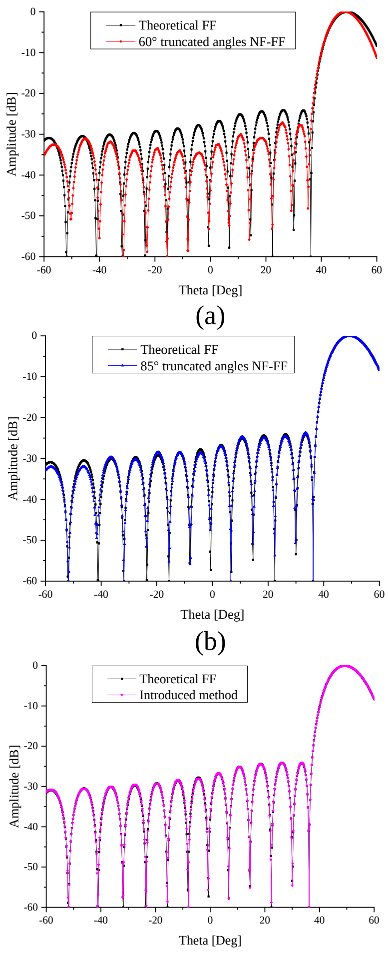

(a)

(b)

(c)

Fig. 4. Comparison between the theoretical results and calculated results for the elevation plane when Δ_0=50°. (a) Comparison between the theoretical FF and a 60° truncated angle NF-FF. (b) Comparison between the theoretical FF and an 85° truncated angle NF-FF. (c) Comparison between the theoretical FF and the proposed method.

B. Measured results

The proposed method was also used to measure a helix antenna array at 2.2 GHz. This was composed of 2×8 helix antenna elements spaced 85mm apart, with a uniform distribution. It was fed by a one-to-sixteen power divider. The size of the antenna array was 900mm×230mm×110mm, as shown in Fig. 5 (a). Beam scanning at 54° was realized by changing the cable length between the power divider and the radiation element (Fig. 5 (b)). The antenna was rotated so that the main beam was perpendicular to the scanning surface for another planar NF measurement, as shown in Fig. 5 (c). The positional accuracy of the scanning system was 0.05mm and its RMS value was 0.1mm. The 54° scanning angle results shown in Fig. 6 again confirm the effectiveness of the proposed algorithm.

The simulation-based and measured results together serve to confirm that the proposed method is more accurate than using traditional NF technology when the scanning angle of a PAA is large.

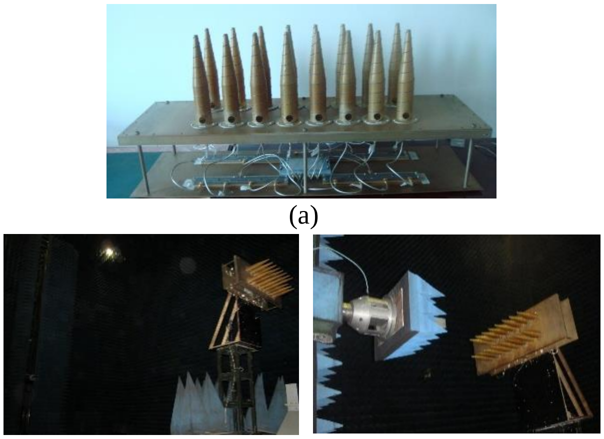

(a)

(b) (c)

Fig. 5. The antenna and measurement process: (a) the antenna, (b) conducting the FF measurement, and (c) conducting the NF measurement.

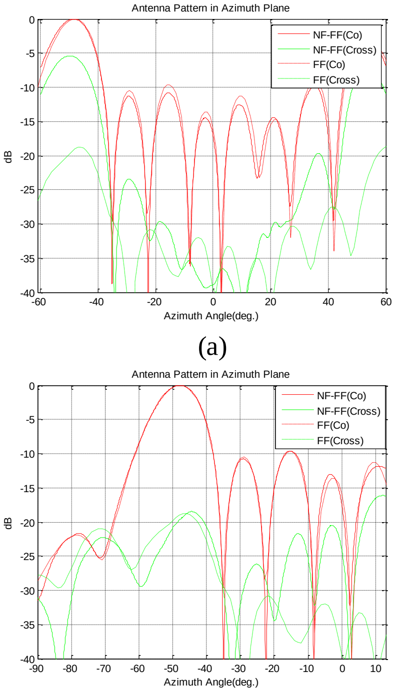

(a)

(b)

Fig. 6 Comparison of the NF-FF results and FF results for a 54° scanning angle: (a) using the traditional NF-FF method, and (b) using the proposed method.

IV. CONCLUSION

This paper has presented both theoretical analysis and the real application of an approach that can accurately determine the FF pattern of PAAs based on planar NF technology. Using this approach, it is only necessary to rotate the PAAs, so that the main beam is perpendicular to the scanning plane. The results from both simulations and physical measurements have established the validity of the proposed algorithm. The approach presented in this paper is especially suitable for wide-angle scanning PAAs.

REFERENCES

[1] X. Li, G. M. Wei, L. Yang, and B. Liao, "Fast determination of single-cut far-field pattern of base station antenna at a quasi-far-field distance," *IEEE Trans. Antennas Propag.*, vol. 68, no. 5, pp. 3989-3996, May 2020.

[2] X. Chen, W. Xue, H. Shi, J. Yi, and W. E. I. Sha, "Orbital angular momentum multiplexing in highly reverberant environments," *IEEE Microwave and Wireless Components Letters*, vol. 30, no. 1, pp. 112-115, Jan. 2020.

[3] X. Li, Y. T. Zhang, G. M. Wei, L. Yang, and B. Liao, "Reduction of truncation errors in planar near-field antenna measurements using improved Gerchberg-Papoulis algorithm," *IEEE Trans. Antennas Propag.*, vol. 69, no. 9, pp. 5972-5974, Sep. 2020.

[4] F. Faraz, X. Chen, Q. Li, J. Tang, and X. Zhang, "Mutual coupling reduction of dual polarized low profile MIMO antenna using decoupling resonators," *Applied Computational Electromagnetics Society Journal*, vol. 35, no. 1, pp. 38-43, 2020.

[5] S. Zhang, X. Chen, I. Syrytsin, and G. F. Pedersen, "A planar switchable 3-D-coverage phased array antenna and its user effects for 28-GHz mobile terminal applications," *IEEE Transactions on Antennas and Propagation*, vol. 65, no. 12, pp. 6413-6421, Dec. 2017.

[6] D. Yu, L. Yang, D. M. Fu, and Q. Z. Liu, "Analysis and simulation of system phase errors in planar near-field measurements on ultra-low sidelobe antennas," in *Proc. IEEE ICUWB2010*, pp. 20-23, Sept. 2010.

[7] J. R. Perez and J. Basterrechea, "Particle swarms applied to array synthesis and planar near-field antenna measurements," *Microwave and Optical Technology Letters*, vol. 50, pp. 544-548, Dec. 2007.

[8] X. Chen, "On near-field and far-field correlations in reverberation chambers," *IEEE Microwave and Wireless Components Letters*, vol. 29, no. 1, pp. 74-76, Jan. 2019.

[9] J. R. Perez and J. Basterrechea, "Particle-swarm optimization and finite-difference time-domain (PSO/FDTD) algorithm for multiband and wide-band patch antenna design," *Microwave and Optical Technology Letters*, vol. 44, pp. 398-403, Dec. 2005.

[10] E. B. Joy and C. A. Rose, "Windows 96 for planar near-field measurements," in *Proc. AMTA*, Seattle, WA, pp. 80-85, Oct. 1996.

[11] P. Petre and T. K. Sarkar, "Planar near-field to far-field transformation using an equivalent magnetic current approach," *IEEE Trans. Antennas Propag.*, vol. 40, no. 11, pp. 1348-1356, Nov. 1992.

[12] O. M. Bucci and M. D. Migliore, "A new method for avoiding the truncation error in near-field antennas measurements," *IEEE Trans. Antennas Propag.*, vol. 54, no. 10, pp. 2940-2952, Oct. 2006.

[13] E. Martini, O. Breinbjerg, and S. Maci, "Reduction of truncation errors in planar near-field aperture antenna measurements using the Gerchberg-Papoulis algorithm," *IEEE Trans. Antennas Propag.*, vol. 56, no. 11, pp. 3485-3493, Nov. 2008.

[14] K. T. Kim, "Truncation-error reduction in 2D cylindrical/spherical Near-field scanning," *IEEE Trans. Antennas Propag.*, vol. 58, no. 6, pp. 2153-2158, June 2010.

Hongjun Tang received the M.Sc. degree in Signal and Information Processing from the Institute of Telecommunications Science and Technology, in 2009.

At present, he is engaged in research work in Southwest Institute of electronic technology.

His research interests include array antenna, beam control, and array signal processing.

Xianbao Zheng graduated from China Academy of ordnance Sciences, holds a master's degree in Weapon System and Application Engineering. His main research interests include electronic countermeasure system design and interference simulation analysis.

A Low-Profile Dual-Polarized Antenna with High Isolation and High Front-to-Back Ratio for 5G Base Stations

M. Ciydem

Department of Electrical and Electronics Engineering
Faculty of Engineering, Gazi University, Ankara, 06570, Turkey
mehmetciydem@gazi.edu.tr

Abstract **─** A dual-polarized, broadband, slot-coupled patch antenna design is presented for sub-6 GHz 5G base stations. Proposed antenna is made up of two suspended stacked patches above feedline layer and is excited by crossed elliptic-H slots for ±45º slant, linear dual polarized operation. Prototyped antenna has an impedance bandwidth of 22.1% (3.14 - 3.92 GHz) for $|S_{11}|$, $|S_{22}| < -15$ dB and port isolation $|S_{21}|$ is also obtained to be < -28 dB in this band. Antenna exhibits directional radiation patterns with half power beamwidths of 57º - 65º and 60º - 64º in elevation and azimuth planes, respectively with varying gain of 8.6 - 9.1 dBi. Proposed antenna is also low profile (11.1 mm) with high front-to-back ratio (> 27 dB) without reflector. Design details, numerical studies, and measurement results are presented.

Index Terms **─** Dual-polarized, broadband antenna, isolation, front-to-back ratio, sub-6 GHz 5G base stations.

I. INTRODUCTION

Continuous increasing demands in data rates, bandwidth (BW) and quality of services (QoS) in cellular communication put challenging requirements for base station antennas such as being dual-polarization, low profile, broadband impedance matching ($|S_{11}|$, $|S_{22}| < -15$ dB), high port isolation ($|S_{21}| < -20$ dB), and high front-to-back ratio (FBR > 20 dB). 5G is a promising technology with massive multiple input multiple output (mMIMO) antenna arrays, which is one of the key enabling technologies of 5G, to meet the demands of celullar industry. N78 band (3.30-3.80 GHz) is assigned for sub-6 GHz 5G applications. Making full use of mMIMO requires further performance improvements such as isolation $|S_{21}| < -25$ dB and FBR > 25 dB. Design of single element antenna with high isolation and high front-to-back ratio helps mMIMO array to reach these performance levels easily. Moreover mMIMO arrays are bulky structures with huge number of antenna elements. Outdoor physical installation requirements necessitates mMIMO array to be compact and low profile. Therefore it is still a challenging problem to design dual-polarized, broadband antenna element with high isolation, high FBR and low profile in a simple configuration.

Patch antennas are widely used in dual-polarized base station antennas because of their compactness, low profile, and ease of manufacturing [1]. Despite their narrowband nature at the beginning, different feeding techniques have been developed to make them broadband. Probe feeding and slot coupling are common methods for exciting the patches. Together with such feeding mechanism, stacked patch antennas (SPAs) can also be employed for broadband operation. Several variations of probe feeding (L, T, F, meandering, and hook shapes, symmetric or anti-symmetric feeds) for dual-polarized patch antennas are introduced in [2-8]. Other common type of feeding is slot coupling in single or multilayer configurations. Dual-polarization feature of patch is accomplished by either crossed slots centered on common ground or two separate slots in orthogonal placement [9-14]. Crossed-slot geometry is more common because of its single layer feeding, making the antenna low profile and compact. In [9], a dual-polarized SPA is designed by utilizing a plus-like shaped slot. A four layer microstrip patch antenna is presented in [10] where the feeding lines for each polarization are mounted on separate layers and slots are etched on these layers accordingly. In [11], two modified-H slots are used to create dual-polarization on the patch. [12-13] reports square shaped ring slot structure feeding a patch and Jerusalem crossed radiator, respectively. In [14], a broadband multilayer SPA containing a quasi-crossed-shaped slot is presented. Furher different designs of slot coupled antennas can be found in [15-16].

Slot-coupled patch antennas may be simple, low profile however their FBR performance is poor because of undesirable back radiation of the slots. Hence additional reflector plane or cavity backed structure, which increases antenna profile, is generally employed to make FBR higher. Isolation between ports is also another problem in SPA design due to the mutual coupling of currents flowing in the slot plane. Additional reflector plane to improve the FBR may form a waveguide

Submitted On: April 17, 2021
Accepted On: July 6, 2021

https://doi.org/10.47037/2021.ACES.J.360916

with the ground plane causing flow of unwanted higher order currents and poor isolation. In order to improve the isolation, electromagnetic band-gap (EBG) and meta-material based superstrates have been proposed [17, 18].

In this paper, design of a simple, dual-polarized, slot-coupled SPA with easy fabrication is presented for sub-6 GHz 5G base stations to operate in 3.30-3.80 GHz band. Different than other works, elliptic-H slots are employed for exciting the patches. Design of stacked patches (dimensions and placement) are made in such way that that proposed SPA exhibits 22.1% (3.14-3.92 GHz) impedance BW for $|S_{11}|$, $|S_{22}| < -15$ dB, with a gain of 8.6-9.1 dBi. Broadside, directional radiation patterns have been obtained with half power beamwidths (HPBWs) of 57°- 65° and 60°- 64° in elevation and azimuth planes, respectively. Moreover, in addition to these performances, other prominent features of the proposed antenna can be counted as its high FBR (> 27 dB) and high isolation ($|S_{21}| < -28$) with low profile (11.1 mm). And they have been achieved without use of any additional reflector, cavity backed structure and EBG or meta-material based surface in the design.

This paper is organized as follows. Section II describes geometry, configuration and physical dimensions of proposed SPA with working principles. Section III deals with numerical studies including parametric studies and performance optimizations. Section IV presents measurement results while Section V discusses the study and concludes the work with detailed comparison of previous related ones showing the superior performance of proposed antenna.

II. ANTENNA DESIGN

A. Geometry and configuration

Geometry and configuration of SPA is illustrated in Fig. 1 while its physical dimensions are given in Table 1. SPA comprises two suspended stacked patches (main one and parasitic one) and a feedline layer, all separated by air. Heights of the main and parasitic patches are denoted by h_{s1} and h_{s2}, respectively. Patches are 0.25 mm thick metal squares whose sides are L_{s1} and L_{s2}. The feedline layer consists of a feed network at its bottom side and a common ground at its upper side. Elliptic-H slots are etched on this ground side. Feed network is composed of two parts: matching section and 100 Ω branch lines. Matching section provides broadband matching between input impedance of SPA and 50 Ω SMA port. It includes a two-section binomial transformer and an additional rectangular stub of size 3.1×4.0 mm^2. Transformer sections are approximately quarter wavelength (L_{t1}, L_{t2}) at the center frequency, f_c = 3.55 GHz (λ_c = 84.5 mm). Coupling to the slots is realized by two 100 Ω microstrip branch lines which are connected to the matching section by a T-junction. Branch lines are separated by a distance L_d and terminated by L-shaped stubs in order to compensate the reactive component of the input impedance of SPA and preclude the overlap. Line crossing between inner branches is inevitable and hence a small air bridge is introduced here to avoid intersection. Feedline layer is implemented on FR4 substrate (ε_r = 4.4, $\tan\delta$ = 0.02) of 1.6 mm thickness.

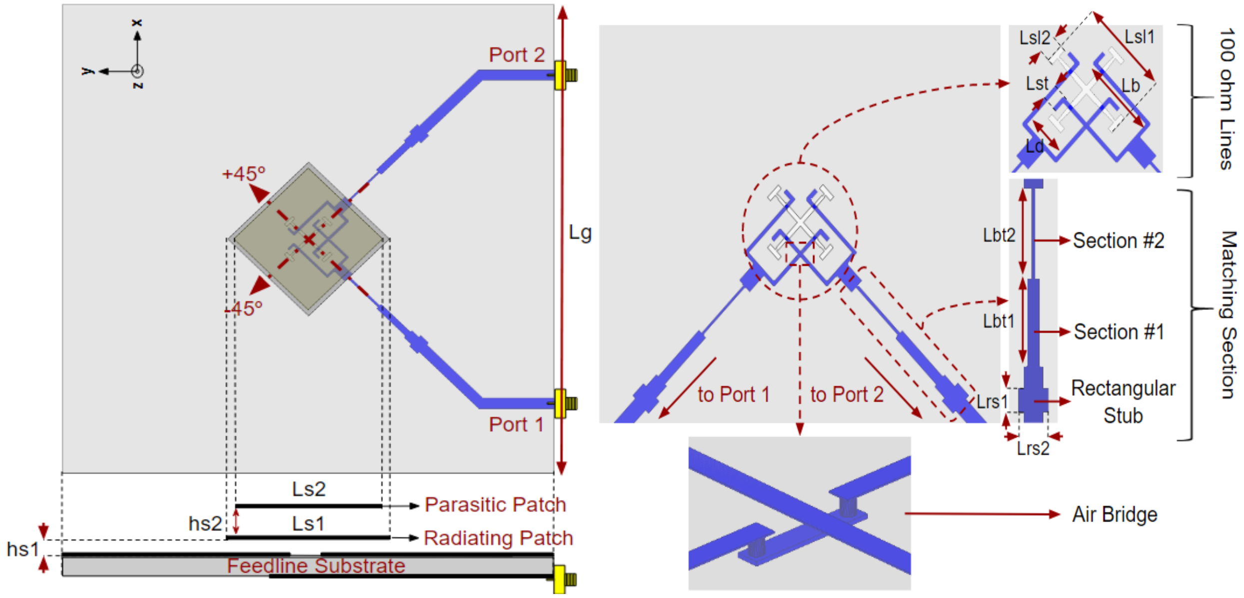

(a) (b)

Fig. 1. Antenna geometry and configuration (a) top view and cross-section, and (b) elliptic-H slots, feedlines and binomial transformer.

Table 1: Physical dimensions of the proposed antenna

Description	**Parameter**	**Dimensions (mm)**
Ground plane	L_g	110
Main patch	L_{s1}	32.5
Parasitic patch	L_{s2}	30
Lower/Upper air height	h_{s1}, h_{s2}	2, 7
Slot major axis length	L_{sl1}	16.5
Vertical slot width	L_{sl2}	3.2
Stub Length	L_{st}	2.35
1st binomial section length	L_{bt1}	11.55
2nd binomial section length	L_{bt2}	11.82
Branch lines separation	L_d	6.91
Rectangular stub length/width	L_{rs1}, L_{rs2}	3.1, 4
FR4 height	h	1.6
Overall SPA height	2+7+1.6+2x0.25 = 11.1	

B. Working principles

Electromagnetic power is coupled to patches through elliptic-H slots and ±45° dual polarizations are created. Dimensions and placement of patches at proper heights are of critical importance for good broadband matching, isolation and FBR. Although main patch (L_{s1}, h_{s1}) has dominant effect in total design, parasitic one (L_{s2}, h_{s2}) must also be considered in combination with it to reach desired performance. The lower h_{s1} makes efficient coupling from slots to SPA easier, hence resulting in good FBR. However, this lower h_{s1} makes broadband operation difficult. The higher h_{s1} facilitates broadband operation but efficient coupling from slots to SPA becomes more difficult and hence resulting in poor FBR. The existence of parasitic patch may be questioned because it increases the overall antenna profile. However, as shown in the next section, desired technical performances cannot be obtained by a single patch and hence parasitic one is also required. The basic idea of the design is to place main patch at the lowest possible height (h_{s1}) to have good FBR, and at the same with the proper combination of both patches (h_{s1}, h_{s2}), to reach desired impedance BW, matching level, isolation, and to keep overall SPA still profile low. Proper placement of the second patch (parasitic patch) with the main patch modifies the current distribution on the main patch. And vectorial combination of currents flowing on the two patches has a total effect of improving the isolation.

In this work, different than conventional rectangular-H slots, central sections of the slots are designed in elliptic form. As addressed in [19], elliptic slot is a simple technique for broadband efficient coupling between microstrip transitions and employed here as coupled-feeding mechanism. Axial ratio (A_x) of the ellipse, specifically length of its major axis, controls the level of the coupling. Tapered line nature of slots due to elliptic shape provides further separation between slots around the center where most coupling occurs and improves the isolation. Furthermore, elliptic shape of slots also provides better impedance matching and efficient power transfer from slots to the patches. This yields less return power and less flowing currents in the slot plane resulting in less backward radiation (high FBR) and less mutual coupling currents (high isolation).

Figure 2 plots surface current distributions on the main and parasitic patches at 3.30 GHz and 3.80 GHz when SPA is excited at port 1. Current amplitude on the main patch gradually increases towards edges at 3.30 GHz in symmetry with +45º diagonal line while the currents are weaker on the parasitic one. At 3.80 GHz, stronger coupling occurs between two patches and current amplitude on the parasitic patch increases while it remains almost same with little decrease on the main patch. This means that resonant behaviour around 3.80 GHz is mostly governed by the parasitic patch.

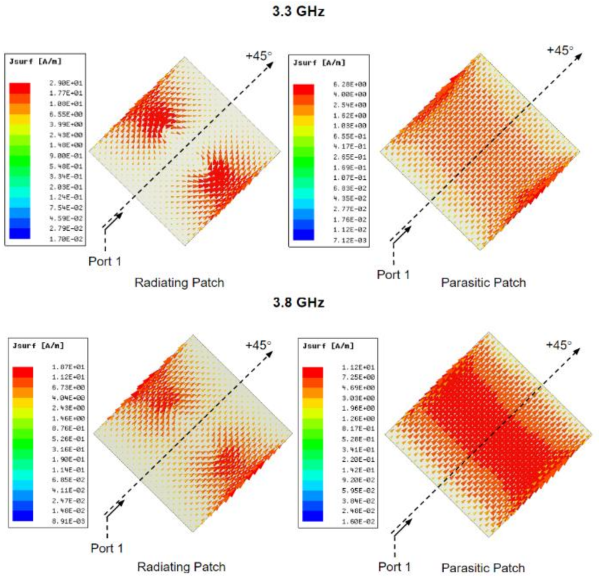

Fig. 2. Surface currents on the main and parasitic patches.

III. NUMERICAL STUDIES

A. Parametric analyses

Proposed SPA is modeled and simulated in Ansoft HFSS. Its electrical performances are numerically analyzed in terms of impedance matching ($|S_{11}|$) and port isolation ($|S_{21}|$) with parametric studies. Each parametric study is carried out by sweeping one parameter within a range while the rest is kept fixed. Since SPA ports are built in symmetric configuration, only $|S_{11}|$ results at port 1 are reported. Upper and lower boundaries of the desired band of operation (3.30-3.80 GHz) are shown with vertical black dashed lines in the figures.

|S$_{11}$| and |S$_{21}$| characteristics of SPA as a function of main patch height (h_{s1}) are given in Fig. 3. In this analysis, h_{s1} is swept in 1-3 mm range by 1 mm steps. Proposed SPA reaches its best matching level and largest impedance BW when h_{s1} is set to 2 mm. In addition, typical port isolation is obtained to be |S$_{21}$| < –26 dB at this value of h_{s1}.

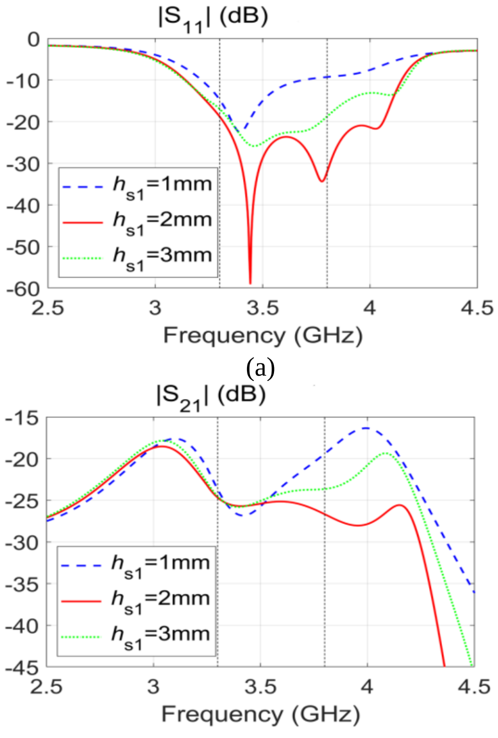

(a)

(b)

Fig. 3. Effect of the main patch height on (a) |S$_{11}$| and (b) |S$_{21}$|.

The same procedure is also carried out for the parasitic patch height (h_{s2}) and the best performance is achieved when h_{s2} = 7 mm as shown in Fig. 4. With these values (h_{s1} = 2 mm, h_{s2} = 7 mm), effect of parasitic patch can be seen better in Fig. 5 (a) showing that desired matching level and impedance BW cannot be achieved by a single patch. Figure 5 (b) plots the simulations of radiation pattern of SPA in azimuth plane (θ = 90°, $-180° < \phi < 180°$) by changing h_{s1} with fixed h_{s2} = 7 mm. It is observed that FBR gets better at lower h_{s1} values. As a result, the basic idea of this design to place main patch at the lowest possible height to have good FBR and utilize parasitic one to reach desired matching level, impedance BW and isolation is consistent. Moreover, Fig. 5 (b) shows that higher FBR can be attained without using any reflector by only positioning the main patch at lower heights.

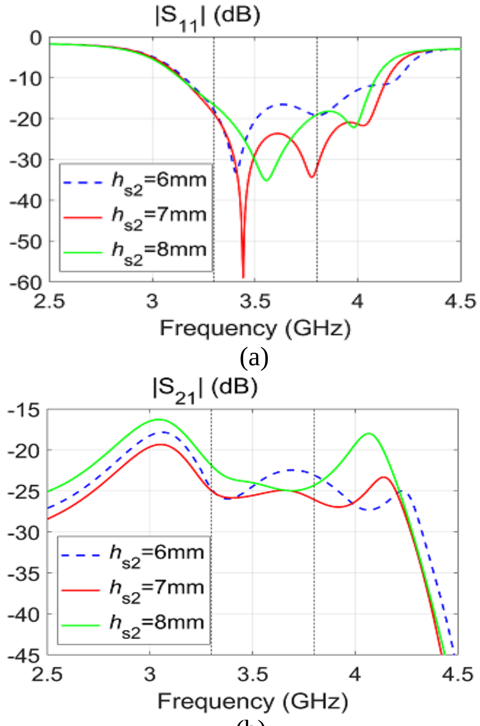

(a)

(b)

Fig. 4. Effect of the parasitic patch height on (a) |S$_{11}$| and (b) |S$_{21}$|.

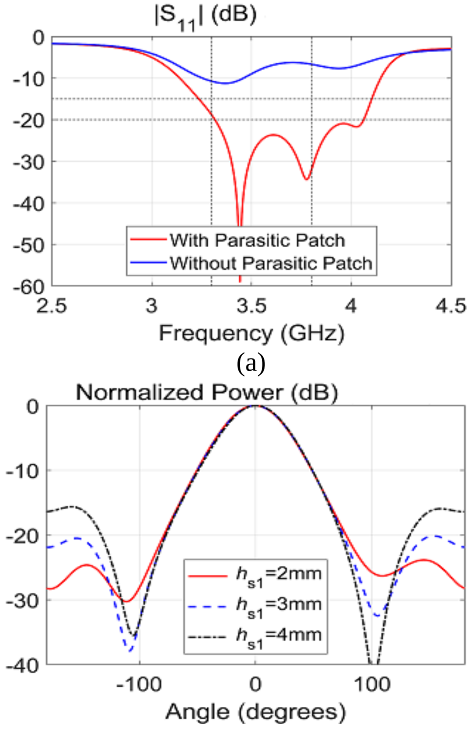

(a)

(b)

Fig. 5. |S$_{11}$| and FBR graphs (a) effect of the parasitic patch on |S$_{11}$|, and (b) effect of h_{s1} on FBR.

Figure 6 illustrates $|S_{11}|$ and $|S_{21}|$ performance of SPA regarding axial ratio (A_x) of the elliptic-H slots. This analysis is carried out as A_x is increased from 14.5 to 18.5 with increment of 1. When A_x = 16.5, antenna has two resonance points at 3.39 GHz and 3.74 GHz and 20% impedance BW for $|S_{11}| < -15$ dB. Port isolation does not vary much with respect to A_x in desired band. $|S_{21}|$ is typicallly < –26 dB.

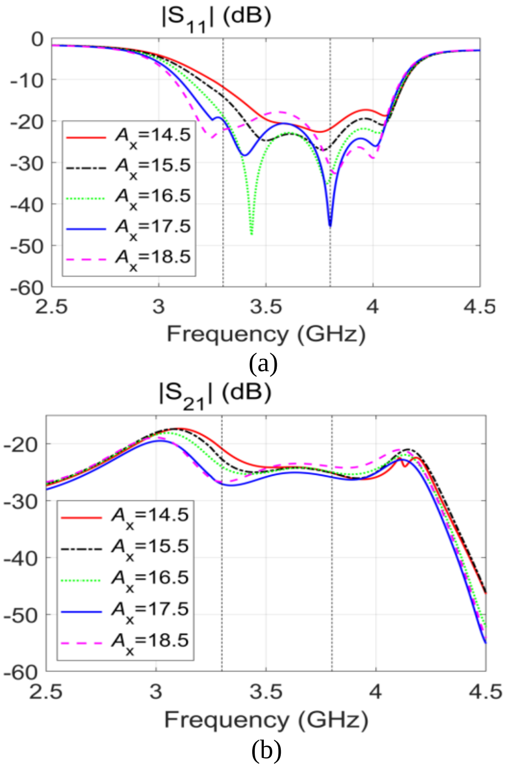

(a)

(b)

Fig. 6. Effect of A_x of elliptic slot on (a) $|S_{11}|$ and (b) $|S_{21}|$.

B. Effect of elliptic H-slots

Effect of the elliptic-H slots on the SPA performance is evaluated by comparing it with rectangular-H slots having the same length (L_s = 15.98 mm) and area ($A_s \approx$ 11.186 mm^2). Results are illustrated in Fig. 7 and Fig. 8. Elliptic-H slots improve matching level appreciably in the desired band. Port isolation is also improved by elliptic-H slots approximately 2.5 dB with respect to rectangular-H slots. For better understanding, comparison of the port isolation mechanism is also demonstrated with the currents flowing on the slot plane of feed line layer at 3.55 GHz. As shown in Fig. 8, the current distribution on the elliptic-H slots, aspecially around the center where most mutual coupling occurs between ports, are weaker than that of the rectangular-H slots. This weaker flowing current results in improvement in the port isolation.

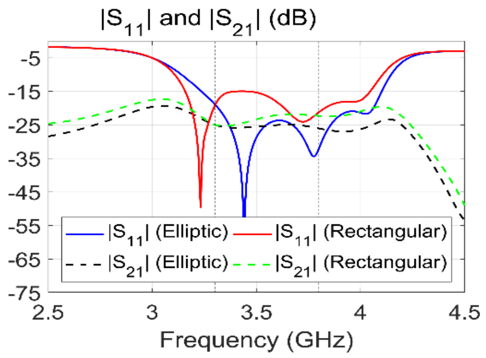

Fig. 7. Comparison of elliptic-H and rectangular-H slots.

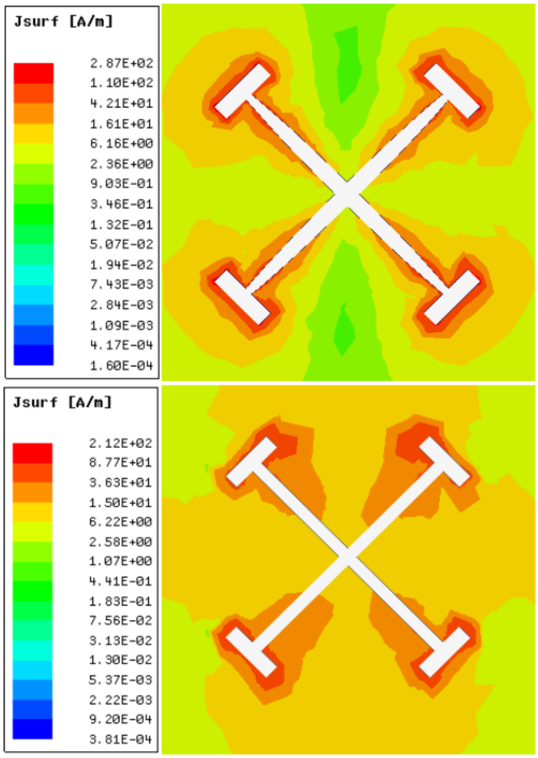

Fig. 8. Current distributions on the slot plane with elliptic-H and rectangular-H slots.

IV. MEASUREMENT RESULTS

Proposed SPA is prototyped in accordance with design descriptions given in Section II and is shown in Fig. 9. Air layers are formed by using plastic separators with appropriate heights. Overall size of the prototype SPA is 110 × 110 × 11.1 mm^3. Numerical results of Section III are experimentally verified by the measurements of S-parameters ($|S_{11}|$, $|S_{22}|$, and $|S_{21}|$) and radiation patterns (co-pol, cross-pol). S-parameters are measured by HP 8720D vector network analyzer and radiation pattern measurements are performed in an anechoic chamber.

Measurements are taken when the SPA is excited at port 1 (+45° polarization) while the other port is terminated by broadband 50 Ω load. Again due to the symmetric configuration of ports, results of port 2 (−45° polarization) are not included.


(a) (b) (c)

Fig. 9. Prototyped SPA (a) feed network, (b) elliptic-H slots, and (c) top view (not in scale).

Figure 10 plots measured and simulated S-parameters of SPA. It can be seen that measured results are consistent with the simulations. SPA exhibits 22.1% impedance BW for $|S_{11}|$, $|S_{22}| < -15$ dB along 3.14-3.92 GHz. Slight discrepancy between $|S_{11}|$ and $|S_{22}|$ is caused by the air bridge. The measured $|S_{21}|$ is < -28 dB in desired band of 3.30-3.80 GHz.

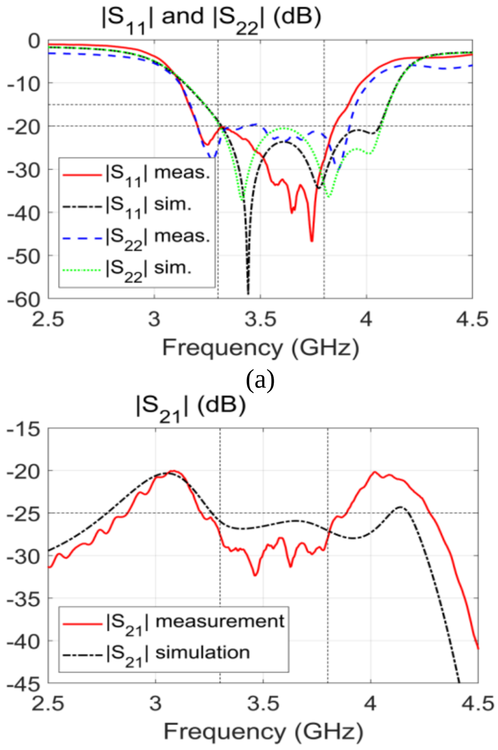

(a)

(b)

Fig. 10. Measured and simulated S-parameters (a) $|S_{11}|$, $|S_{22}|$, and (b) $|S_{21}|$.

Normalized co/cross-pol radiation patterns in elevation and azimuth planes are measured at 3.30 GHz, 3.55 GHz, 3.80 GHz frequencies within the operating band. Both simulations and measurement results, which are consistent with each other, are plotted in Fig. 11. SPA exhibits stable, symmetric and directional radiation patterns in both planes. Measured HPBWs are 65°, 62° and 57° in elevation plane and 64°, 62° and 60° in azimuth plane at the corresponding frequencies, respectively. Gain of the SPA in the operating band varies between 8.6-9.1 dBi and given in Fig. 12. High FBR, one of the design goals, is achieved to be > 27 dB. From Fig. 11, it is observed that cross-polar discrimination (XPD) level, which is another important performance criterion of base station antenna and not targeted in this study, is also very good. That is, XPD level at boresight is > 25 dB.

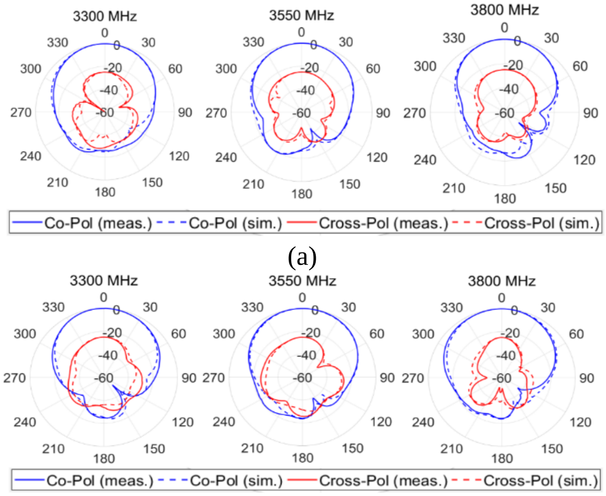

(a)

(b)

Fig. 11. Measured and simulated co-/cross-pol patterns in (a) elevation plane and (b) azimuth plane.

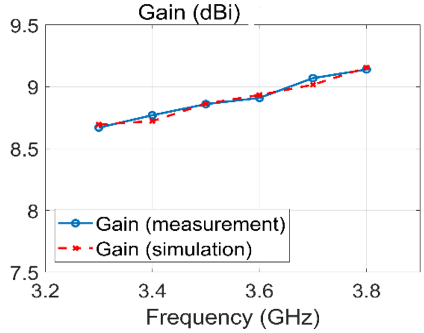

Fig. 12. Measured and simulated gain of the SPA.

V. CONCLUSION

In this paper, compact, dual-polarized, broadband, slot-coupled SPA with ease of fabrication is designed and investigated for Sub-6 GHz 5G base station applications. Proposed SPA is made up of main patch and parasitic patch layers above feedline layer and is excited by crossed elliptic-H slots creating ±45° dual slant polarizations. To summarize, proposed SPA exhibits 22.1% (3.14-3.92 GHz) impedance BW for $|S_{11}|$, $|S_{22}| < -15$ dB, port isolation $|S_{21}| < -28$ dB and FBR > 27 dB. It has HPBWs of 57°-65° and 60°-64° in elevation and azimuth planes, respectively with varying gain of 8.6-9.1 dBi.

Simulated and measured radiation patterns show that proposed SPA is low profile with high isolation and high FBR. In this design, placement of the main patch at a reasonably low height, then use of parasitic patch in combination with it and use of elliptic-H slots, all together provides the solution and helps to reach design goals for impedance BW, matching level, isolation and FBR with no reflector plane, cavity-backed structure, EBG or meta-material based surface. Moreover, overall height of the proposed antenna is still low profile (11.1 mm) as it can be verified among similar works in Table 2. Table 2 lists the performances of proposed work and some similar existing ones designed to operate in the same band (3.30-3.80 GHz) as a base station antenna. To make full comparison, note that [3-5] are patch antennas with probe feeding while [12-16] are patch antennas with slot coupling. As can be seen from Table 2, proposed SPA outperforms all of the slot coupled antennas [12-16] and competes with the probe-fed antennas [3-4] by satisfying all the desired performance parameters of base station antennas. Considering the numerical and experimental results, proposed SPA can be a good candidate to be used in and to facilitate the mMIMO array design for 5G applications.

ACKNOWLEDGMENT

The authors would like to acknowledge the support of The Scientific and Technological Research Council of Turkey (TUBITAK) under Grant No. 3180114.

Table 2: Comparison of proposed antenna with the related previous works

Work	BW (GHz, %)	$\|S_{11}\|$, $\|S_{22}\|$ (dB)	$\|S_{21}\|$ (dB)	FBR (dB)	Height (mm)	Reflector
[3]	3.15-4.55, 37%	< –10 dB	< –38	> 12.5	12.7	N/A
[4]	2.86-4.12, 36%	< –15 dB	< –30	> 28	13.4	N/A
[5]	3.13-4.16, 28.3%	< –15 dB	< –23	> 10	29.2	N/A
[12]	3.30-3.80, 14%	< –10 dB	< –20	> 30	37.2	W
[13]	3.33-3.83, 14%	< –10 dB	< –23	> 25	34	W
[14]	3.23-3.80, 17%	< –10 dB	< –50	> 10	10.5	W/O
[15]	3.25-3.80, 15.6%	< –15 dB	< –25	> 18	12.2	W
[16]	3.30-3.60, 8.9%	< –15 dB	< –25	> 16	18.8	W
This work	3.10-3.99, 25.1%, 3.14-3.92, 22.1%	< –10 dB < –15 dB	< –28	> 27	11.1	W/O

W: With reflector, W/O: Without reflector, N/A: Not applicable.

REFERENCES

[1] P. K. Mishra, D. R. Jahagirda, and G. Kumar, “A review of broadband dual linearly polarized microstrip antenna designs with high isolation,” *IEEE Antennas Propag. Mag.*, vol. 56, no. 6, pp. 238-251, Dec. 2014.

[2] H-W. Lai and K-M. Luk, “Dual polarized patch antenna fed by meandering probes,” *IEEE Trans. Antennas Propag.*, vol. 55, no. 9, pp. 2625-2627, Sept. 2007.

[3] K. S. Ryu and A. A. Kishk, “Wideband dual-polarized microstrip patch excited by hook shaped probes,” *IEEE Trans. Antennas Propag.*, vol. 56, no. 12, pp. 3645-3649, Dec. 2008.

[4] M. Ciydem and A. E. Miran, “Dual polarization wideband sub-6 GHz suspended patch antenna for 5G base stations,” *IEEE Antennas Wirel. Propag. Lett.*, vol.19, no. 7, pp. 1142-1146, July 2020.

[5] P. Chen, L. Whang, and T. Ding, “A broadband dual-polarized antenna with CRR-EBG structure for 5G applications,” *Applied Computational Electromagnetics Society Journal*, vol. 35, no. 21, pp. 1507-1512, Dec. 2020.

[6] J.-J. Xie, Y.-Z. Yin, J.-H. Wang, and X.-L. Liu, “Wideband dual-polarized electromagnetic fed patch antenna with high isolation and low cross-polarization,” *IET Electron. Lett.*, vol. 49, no. 3, pp. 171-173, Jan. 2013.

[7] Y. Jin and Z. Du, “Broadband dual-polarized F-probe fed stacked patch antenna for base stations,” *IEEE Antennas Wirel. Propag. Lett.*, vol. 14, pp. 1121-1124, Jan. 2015.

[8] K. M. Mak, H. W. Lai, and K. M. Luk, “A 5G wideband patch antenna with antisymmetric

L-shaped probe feeds," *IEEE Trans. Antennas Propag.*, vol. 66, no. 2, pp. 957-961, Feb. 2018.

[9] M. Barba, "A high-isolation, wideband and dual-linear polarization patch antenna," *IEEE Trans. Antennas Propag.*, vol. 56, no. 5, pp. 1472-1476, May 2008.

[10] A. A. Serra, P. Nepa, G. Manara, G. Tribellini, and S. Cioci, "A wideband dual-polarized stacked patch antenna," *IEEE Antennas Wirel. Propag. Lett.*, vol. 6, pp. 141-143, Apr. 2007.

[11] K.-L. Wong, H.-C. Tung, and T.-W. Chiou, "Broadband dual-polarized aperture-coupled patch antennas with modified H-shaped coupling slots," *IEEE Trans. Antennas Propag.*, vol. 50, no. 2, pp. 188-191, Aug. 2002.

[12] R. Caso, A. Serra, A. Buffi, M. R-Pino, P. Nepa, and G. Manara, "Dual-polarized slot-coupled patch antenna excited by a square ring slot," *IET Microw. Antennas Propag.*, vol. 5, no. 5, pp. 605-610, Apr. 2011.

[13] C. Hua, R. Li, Y. Wang, and Y. Lu, "Dual-polarized filtering antenna with printed Jerusalem-cross radiator," *IEEE Access*, vol. 6, pp. 9000-9005, Feb. 2018.

[14] J. Lu, Z. Kuai, X. Zhu, and N. Zhang, "A high-isolation dual-polarization microstrip patch antenna with quasi-cross-shaped coupling slot," *IEEE Trans. Antennas Propag.*, vol. 59, no. 7, pp. 2713-2717, 2011.

[15] A. Alieldin, Y. Huang, M. Stanley, S. D. Joseph, and D. Lei, "A 5G MIMO antenna for broadcast and traffic communication topologies based on pseudo inverse synthesis," *IEEE Access*, vol. 6, pp. 65935-65945, Oct. 2018.

[16] H. Huang, X. Li, and Y. Liu, "5G MIMO antenna based on vector synthetic mechanism," *IEEE Antennas Wirel. Propag. Lett.*, vol. 17, no. 16, pp. 1052-1055, June 2018.

[17] J. Jiang, Y. Li, L. Zhao, and X. Liu, "Wideband MIMO directional antenna array with a simple meta-material decoupling structure for X-band applications," *Applied Computational Electromagnetics Society Journal*, vol. 35, no. 5, pp. 556-566, May 2020.

[18] F. Liu, J. Guo, L. Zhao, G-L. Huang, Y. Li, and Y. Yin, "Dual-band metasurface-based decoupling method for two closely packed dual-band antennas," *IEEE Trans. Antennas Propag.*, vol. 68, no. 1, pp. 552-557, Jan. 2020.

[19] A. M. Abbosh, "Ultra-wideband vertical microstrip - microstrip transition," *IET Microw. Antennas Propag.*, vol. 1, no. 5, pp. 968-972, Oct. 2007.

Mehmet Ciydem was born in 1971 in Ankara, Turkey. He received his B.Sc., M.Sc. and Ph.D. degrees all in Electrical Engineering from Middle East Technical University (METU), Ankara, Turkey with high honors. After working in defense industry (Aselsan, Havelsan, TAI) for many years, he founded Engitek Ltd. company in 2009, where he is President. He is an Associate Professor of Electromagnetic Theory and Communications lecturing occasionally in several universities (Bilkent Univ., Gazi Univ., Karatay Univ., Hacettepe Univ., and Army War Academy). His research interests are in the areas of electromagnetics, wave propagation, antennas, RF/ microwave engineering, radar and communication systems.

A Novel Multidirectional Strain Sensor Realized by a 3D Microstrip-Line Fed Near-Circular Patch Antenna

Lingling Wang [1], Kwok L. Chung [1,2*], Song Gao [1], Mingliang Ma [1], Jianlin Luo [1], and Yingsong Li [3]

[1] Civionics Research Laboratory, School of Civil Engineering
Qingdao University of Technology, Qingdao, 266033, China

[2] School of Computer Science and Engineering
Huizhou University, Guangdong, 516007, China
*klchung@hzu.edu.cn

[3] College of Information and Communication Engineering,
Harbin Engineering University, Harbin, 15001, China

Abstract **─** In this paper, we propose a newly developed impedance method to gauge the variations of multi-directional strain using a near-circular-patch based sensor. A novel three-dimensional (3D) feeding mechanism realized by a 90-deg bended microstrip line is devised for allowing strain detection along any direction in the azimuth plane of a metallic surface. The simulated results, verified by experimental results, demonstrate that there is a linear relationship between normalized impedance and multi-directional strain with high sensitivities of about 100 ppm/με. The relationship between sensitivity and sensor orientation is derived as a cosine function, which is a useful feature for estimating principal strain direction.

Index Terms **─** 3D feeding mechanism, multidirectional strain monitoring, near-circular-patch, strain sensor.

I. INTRODUCTION

The aging of steel structures, such as high-speed train, bridge, railways and airplanes has become a social problem. Recently, engineering accidents are of great concern. On Aug. 14, 2018, the Morandi Bridge of Italy collapsed sending vehicles and tons of rubble to the ground 150 feet below and 43 people were killed. In structural health monitoring (SHM), accurate assessment of deterioration demands efficient sensing techniques [1-3]. Strain sensors are used extensively in applications including construction engineering, bridge fabrication and railroading project. Resistive strain gauge is known as one of the most common strain sensors; its low cost and easy installation are the most prominent advantages. Nevertheless, it suffers from low sensitivity of 2, cable installation and low immunity to environmental conditions such as temperature and humidity variations. Besides, one resistive strain gauge can only detect strain occurring in one direction which is known beforehand. For strain detection of unknown direction(s), multiple gauges have to be combined in the form of rosettes. Thus, a sensor of single sensing element that can detect unknown directional strain beforehand is highly anticipated.

Recently, there has been a rapid development of antenna technologies, which are gradually used for sensors [4-5]. Patch antenna-based sensors are a passive and cost-effective method for locally monitoring defects immediately. To apply antennas as sensors for strain and crack detecting in SHM [6], linear-polarization (LP) patch antennas with different shapes and sizes have been proposed [7-10]. Relationships between resonant frequency and length/size of patch were used. Good performance of the LP patch antenna sensor has been proved, but the sensitivities are unfortunately found to be limited to 1 ppm/με and the sizes are not small enough [11-13]. The unidirectional sensing and low sensitivity are the main disadvantages of LP patch antenna-based sensors. A comparative study into the directional sensitivity of two coaxial probe-fed LP-patch sensors and circular-polarization (CP) patch was firstly conducted by authors [14]. Mathematical derivation and experiment validation of CP patch-based strain sensor with size of 80 mm×80 mm was first elaborated in [15]. Moreover, with the rapid development of 5G sub-6-GHz base-stations [16], their application scenarios will greatly expand, which also brings some special requirements to sensor performance. Linearity and sensitivity are two important parameters of strain sensors. In some instruments, small strain monitoring is required that demands for high sensitivity in order to obtain better

Submitted On: March 31, 2021
Accepted On: August 11, 2021

https://doi.org/10.47037/2021.ACES.J.360917

resolution. For the sake of achieving precise detection of subtle strains, high linearity and high sensitivity are simultaneously required. This is a key research challenge that has not been sufficiently reported to date.

A high-sensitive antenna-based strain sensor called the proximity-fed circularly polarized (PFCP) patch has been initiated by the authors in [17]. High dielectric-constant substrate was used as the substrate for sensor-size reduction. Instead of the resonant-frequency-shift approach, wherein the shifts of resonant frequency represented the strain variations, the new approach of "phase-area" method using CP-patch-based sensor was investigated for strain monitoring. The simulation evidence has shown a liner correlation between normalized phase area change and micro-strain. High linearity for multi-directional strain was validated with favorable values of goodness-of-fit. However, alike the other wired sensors, for instance, the LP-patch based sensors [9-10], PFCP-patch sensor [17] also faced placement difficulty due to the Sub-Miniature-A (SMA) connector. Namely, the SMA connector needs to be installed perpendicular to the cross section of the metallic surface which limits the freedom of sensor's placement. In [9], a LP-patch sensor was installed for monitoring the strain on the central structural surface, a coaxial-feed patch antenna sensor was bonded at the center of a metallic plate through a hole on the metallic plate. The coaxial-feed patch antenna sensor has smaller overall size, but requires an "artificial hole" in the monitored structure. This method is impractical in real-world application. For all types of rectangular patch-based strain sensors presented in [14], [15] and [17], discrepancies were found in the two sensitivities under 0° and 90° direction. The perturbation segment, viz., the difference between the length and width of the rectangle patch is found to be the source of this discrepancies. To solve this problem, a near-circular patch is purposely used for eliminating the discrepancies.

In this study, our motivation is erected for building an antenna sensor with freedom placement for unknown strain detection. A near-circular-patch-based strain sensor with a novel feeding mechanism is designed that provides a way to solve the placement problem. The proposed strain sensor can be attached on any azimuth position of the monitored surface regardless of strain direction, wherein the variation of input impedance was used as the measurand for strain sensing. Moreover, strain direction can be determined based on the polarity and magnitude of the obtained sensitivity.

II. FEASIBILITY VERIFICATION OF 3D MICROSTRIP LINE FEED

Although the PFCP proof-of-concept prototype using "phase-area" method achieves good performances of high sensing sensitivity and linearity. Due to the fact that the SMA connector needs to be installed perpendicular to the cross section of monitored metallic surface, the installation location of sensor is limited. In order to solve the deficiency of the PFCP antenna sensor, a modified 3D feeding mechanism realized by a 90°-bended microstrip line is designed. This type of 3D fed near-circular-patch-based strain sensor provides a way to detect the strain in any direction of the structure surface.

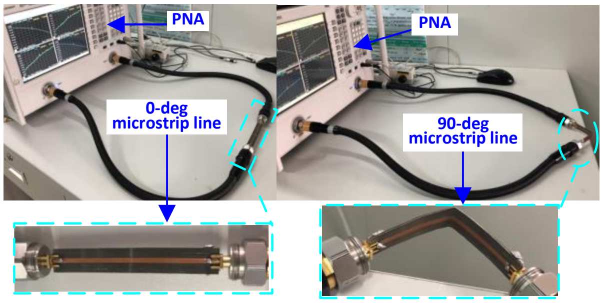

Fig. 1. Performance comparison of two 50-Ω microstrip lines: straight one versus 90°-bended one.

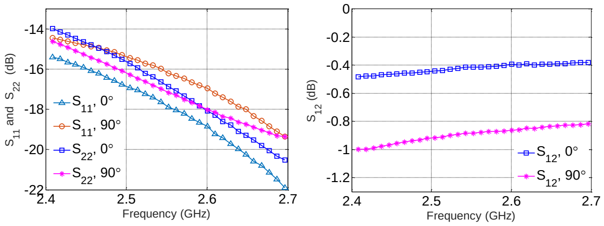

(a) (b)

Fig. 2. Comparison of S-parameters.

In order to verify the feasibility for applying the 3D feeding structure to patch-based strain sensor, two 50-Ω microstrip lines in length of 85 mm were fabricated. One is the straight microstrip line whereas the other is a 90° *L*-shaped microstrip line, which is expected to be used as the 3D feeding mechanism. As shown in Fig. 1, scattering parameters of two-port 50-Ohm microstrip lines were measured by a Keysight Performance Network Analyzer (PNA, N5222A) after calibration. Fig. 2 shows the comparison of S-parameters between 0-deg and 90-deg microstrip lines. The comparison result proves that the shape of microstrip line does not affect the impedance matching performance of it, which is promising for 3D microstrip line fed near-circular-patch-based strain sensors used to be attached to any position on the monitored surface along any direction.

III. STRAIN SENSOR USING NEAR-CIRCULAR PATCH

A. Multiphysics simulation of strain sensor

Figure 3 shows the geometry of the near-circular-patch with 90-deg bended microstrip line. RT/Duroid 5880 dielectric laminate (ε_r=2.2±0.02) with a thickness of 0.787 mm was chosen as the substrate for the near-circular patch having a major (*v*-) and minor (*u*-) length of *a* and *b*, respectively, backed by a square ground-plane of 60 mm×60 mm. A 90-deg bended microstrip line was deliberated to excite the patch so that the SMA connector can be connected along the *w*-axis.

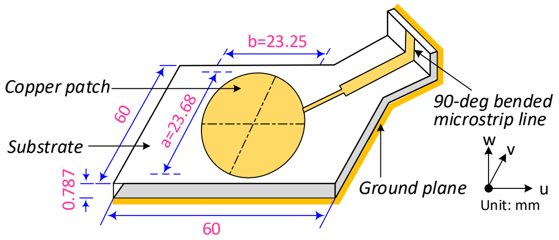

Fig. 3. Geometry of the 3D-line fed near-circular-patch-based strain sensor.

Finite-element-method based COMSOL Multiphysics has been adopted for not only designing antenna sensor but also predicting strain sensing performance. Figure 4 shows the domains including the perfectly matched layer (PML), an air sphere, a metallic surface and a 3D microstrip line fed near-circular-patch-based strain sensor. The PML is used for setting termination boundaries to simulate the simulation domain from an open structure to a finite domain. The near-circular-patch-based strain sensor consists of an upper copper patch and a dielectric substrate used for separating the copper patch from monitored metallic surface. The whole antenna sensor and the monitored metallic structure is placed inside an air sphere. The radiation patch is idealized as the perfect electric conductor (PEC).

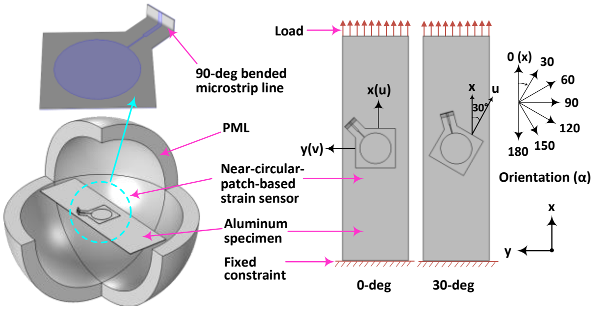

Fig. 4. COMSOL model of the 3D Tx-line fed near-circular-patch-based strain sensor.

The near-circular-patch-based strain sensor with 3D feeding mechanism bonded on the monitored aluminium specimen shown in Fig. 4 was built using the "mechanical-electromagnetic" double physical field coupling in COMSOL. In the mechanical simulation, only the patch-based strain sensor and aluminium specimen are involved. Firstly, the mechanical simulation was conducted at different strain levels from -1400 με to 1400 με at an increment of 350 με applied at the two ends of the aluminium specimen along *x*-axis. Strain is applied along *x*-axis, while the sensor orientation α is defined as the sensor angle with respect to *x*-axis (Fig. 4). Seven orientations of near-circular-patch-based strain sensor (0°, 30°, 60°, 90°, 120°, 150°, and 180°) were undertaken, in which two sensor orientations of 0° and 30° are illustrated as examples in Fig. 4. After the mechanical simulation at each strain level, the newly deformed configuration and meshing of the strain sensor was directly used for the next investigation via electromagnetic (EM) simulation. This convenience was achieved by coupling moving meshes with mechanical and EM field. For the EM simulation, a frequency domain solver is used to achieve the antenna responses at various orientations.

B. Simulated results for directional strain sensing

For the PFCP-patch strain sensor using the "phase-area" method achieved good performance of sensitivity and linearity when compared to the resistive strain gauge and LP patch-based strain sensors [17]. Nevertheless, the "phase-area" method is limited in identifying the strain direction when strain direction is unknown. Hence, a new method using the variation of degenerative mode's input impedance was proposed for identifying the strain direction. Figure 5 shows the variations of input impedance at orientations 0°, 30°, 60° and 90°. Based on the cavity-model theory, the copper patch and the ground plane form a resonant cavity. The patch antenna generates simultaneously two fundamental modes: TM_{01} and TM_{10} due to the perturbation of ellipticity (b/a=0.9818). Unlike the "phase-area" method, impedance curves under each strain level were bimodal wave curves. More interestingly, the maxima of TM_{01} shifts in frequency when sensor orientated at 0° and 30°, while a consistent shift of TM_{01} was observed when sensor orientation is at 60° and 90° placement. This phenomenon allows the determination of strain direction. Another observation is that there is a minimum between two modes and it changes obviously with strain variation. For sensor at 0° and 90° orientation, the minima of impedance curves vary obviously with strain variation. For sensor at 30° and 60° orientation, the minima of impedance curves vary slightly with strain variation.

After extracting the minima from impedance curves at each strain level, linear regression is performed between normalized minimum impedance ($Z_{\text{nor}} = \frac{\Delta|Z|}{|Z_0|}$) and strain to obtain the strain sensitivity (Fig. 6). As seen, fitting curves have good linearity between Z_{nor} and microstrain in multi-directional as verified by R-square (R^2) (all>0.95). Linear models of between simulated Z_{nor} and multi-directional strain verified with the experimental results are shown in Table 1. Very high strain sensitivities denoted by K (in unit of ppm/με) were achieved as indicated by the slopes of the regression lines. Sensitivities of 101.5, 56.11, -46.18, -100.5, -62.15, 40.63 and 98.88 ppm/με are achieved when sensor is placed in 0°, 30°, 60°, 90°, 120°, 150° and 180° orientation, respectively. The overall sensitivities are symmetrically distributed with the sensitivity of 90°.

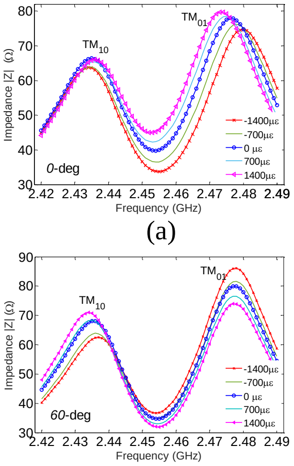

(a) (b)

(c) (d)

Fig. 5. Simulated input impedance with different sensor orientations: (a) 0°, (b) 30°, (c) 60°, and (d) 90°.

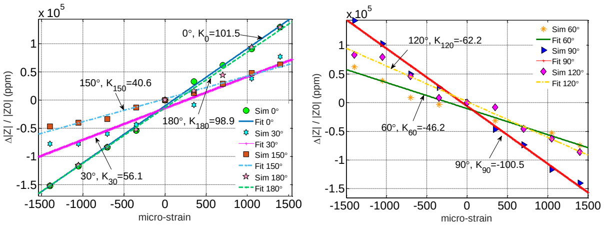

(a) (b)

Fig. 6. Simulated multidirectional strain sensing sensitivities: (a) 0°, 30°, 150° and 180°; (b) 60°, 90°, and 120°.

IV. EXPERIMENTAL VERIFICATION

To validate the multi-directional strain sensing of 3D microstrip line fed patch-based strain sensor, a cantilever beam made by aluminum was designed as shown in Fig. 7, where the sensor orientation of 30° is illustrated as an example. We can see that without the limitation of SMA connector, antenna-based strain sensor can be attached to virtually any position on the monitored surface along any direction. Due to the symmetry of sensitivity distribution, we undertook only the sensor at 0°, 30°, 60° and 90° orientation. The antenna sensor was connected to the aluminum surface by using superglue. One side of the cantilever was fixed to the work bench using C-clamp while the other side was loaded progressively using the load-weights with the increment of 100 g used for simulating different strain levels. Upon every load progress, the impedance of the patch sensor was measured using the PNA. Meanwhile, three metal foil strain gauges were attached onto the back of aluminum beam across the centerline of patch sensor to avoid interference from the metal strain gauges. Strain acquisition system (CF3820, Cheng Fu Electronics, China) was used for strain collection.

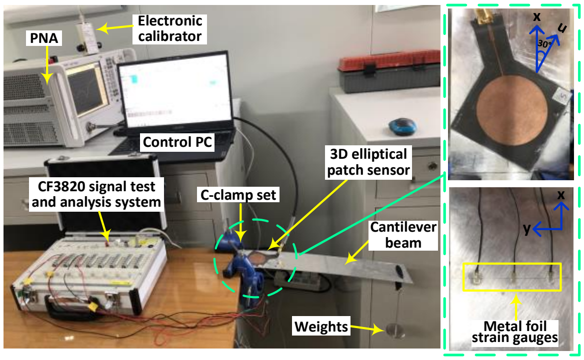

Fig. 7. Experimental set up of simultaneous measurement of multidirectional strain and input impedance.

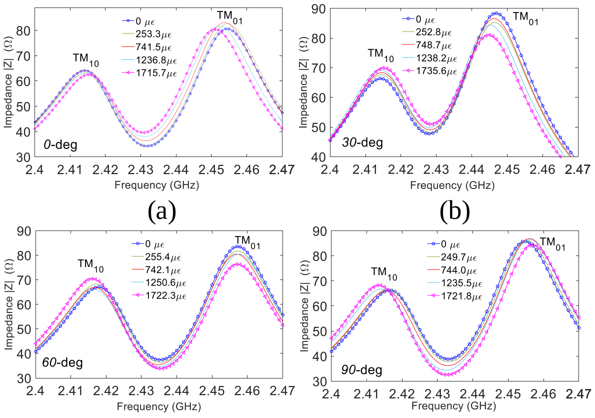

(a) (b)

(c) (d)

Fig. 8. Measured input impedance on strain arisen at sensor orientations of 0°, 30°, 60° and 90°.

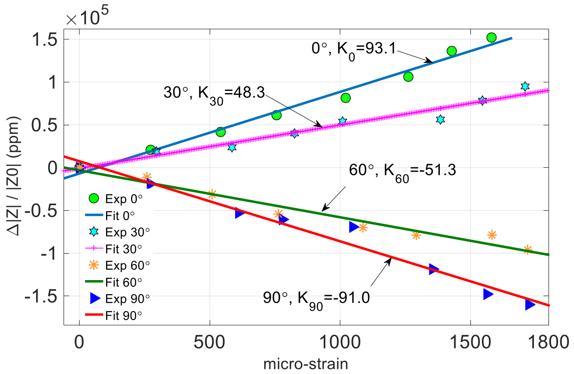

Fig. 9. Measured strain sensitivity at various sensor orientations.

The experimented impedance responses to multi-directional strain are shown in Fig. 8. As agreed with simulated results described in III-B, the TM_{01} shifts when sensor orientation is *0*-deg. We took this idea and reversed it: when the TM_{01} of impedance curves shifts, the strain can be inferred occur along the *0*-deg direction. Linear models between experimented Z_{nor} and multi-directional strain shown in Fig. 9 indicate that strain sensitivities of 93.05, 48.33, -51.25 and -91.03 ppm/με obtained by experiment also shows high sensitivities and good linearity verified by R^2 (all>0.96).

Experimented linear models compared with simulated ones are shown in Table. 1. Slight discrepancies were observed between experimented and simulated results, which may be attributed to the ideal boundary conditions or nominal values of material property parameters in simulation.

Table 1: Simulated linear models compared with measured ones

α (°)	**Simulated Models**	**Experimental Models**
0	Z_{nor}=101.5ε-9944	Z_{nor}=93.05ε-7007
30	Z_{nor}=56.11ε-13754	Z_{nor}=48.33ε-4199
60	Z_{nor}=-46.18ε-10400	Z_{nor}=-51.25ε-10640
90	Z_{nor}=-100.5ε-6021	Z_{nor}=-91.03ε-2346
120	Z_{nor}=-62.15ε+165	/
150	Z_{nor}=40.63ε+2296	/
180	Z_{nor}=98.88ε-13354	/

The fitting curve of relationship between sensitivity data and sensor orientation α (in unit of degree) is shown in Fig. 10. It can be clearly drawn from Fig. 10 that sensitivity data is almost symmetric with the sensor orientation of 90°, which is promising for multi-directional strain sensing of metallic structure. The relationship between sensitivity K and sensor orientation α can be expressed in a cosine function:

$$K(\alpha)=C_1\cos(C_2\alpha), \tag{1}$$

where C_1 is equal to 99.4 which represents the upper and lower bounds of the cosine function are ±99.4 ppm/με, C_2 is obtained by regression as 0.03409, which indicates the period T of cosine function is $T=\frac{2\pi}{0.03409}\cong 184^{\circ}$.

The coefficient C_1 of 99.4 indicates a maximum sensitivity of 99.4 ppm/με at 0° orientation whereas a minimum sensitivity of -99.4 ppm/με at orientation 90°. These are consistent with the maximum sensitivity of 93.05 ppm/με and minimum sensitivity of -91.03 ppm/με obtained from the measurement (Fig. 9). The coefficient C_2 represents the period of 184° which can be verified by the function displayed in Fig. 10. That's to say, strain orientation can be inferred by the magnitude and polarity of sensitivity using cosine function. When strain occurs in an unknown direction, the input impedance curve shifts and Z_{nor} can be obtained. Then, sensitivity calculated by linear model between Z_{nor} and multi-directional strain is substituted into (1) to obtain the sensor orientation (i.e., the direction of strain arisen). Unfortunately, sensitivity of around "0" ppm/με is inferred by orientation of 45° and 135° as observed from Fig. 10. Other strain measurand(s) and methods have to be used in order to obtain the strain sensitivities occurred at 45° and 135° orientation. These will be the objectives in future studies.

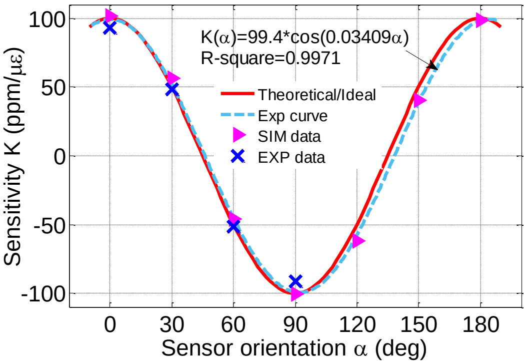

Fig. 10. Variation of sensitivity as a function of sensor orientation, α.

V. CONCLUSION

In this paper, we propose a near-circular-patch-based strain sensor with a novel 3D feeding mechanism for multidirectional strain sensing of metallic structures. The 3D feeding is realized by a 90-deg bended microstrip line, which allows the sensor to be placed in any position on the structure surface when the strain direction is not known beforehand. High sensitivity of about 100 ppm/με and linearity have been achieved simultaneously for multi-directional strain sensing. The relationship between strain sensitivity and sensor orientation is derived as a cosine function, where the strain direction can be estimated based the polarity and magnitude of the strain sensitivity. Symmetric sensitivity magnitude is obtained with respect to the 90° orientation attributed to the cosine function. Therefore, a single sensing element of the proposed strain sensor can detect unknown directional strain which is very viable yet cost-saving in practical application.

ACKNOWLEDGMENT

This work was supported by the National Natural Science Foundation of China (Grant No. 51978353).

REFERENCES

[1] B. S. Cook, A. Shamim, and M. Tentzeris, "Passive low-cost inkjet-printed smart skin sensor for structural health monitoring," *IET Microw., Antennas & Prop.*, vol. 6, pp. 1536-1541, Nov. 2012.

[2] H. Cao, S. K. Thakar, M. L. Oseng, C. M. Nguyen, C. Jebali, A. B. Kouki, and J. C. Chiao, "Development and characterization of a novel interdigitated capacitive strain sensor for structural health monitoring," *IEEE Sensors Journal*, vol. 15, pp. 6542-6548, Nov. 2015.

[3] T. T. Thai, H. Aubert, P. Pons, G. Dejean, M. M. Tentzeris, and R. Plana, "Novel design of a highly sensitive RF strain transducer for passive and remote sensing in two dimension," *IEEE Microwave Theory and Techniques*, vol. 61, pp. 1385-1396, Feb. 2013.

[4] A. All, S. I. Jafri, A. Habib, Y. Amin, and H. Tenhunen, "RFID humidity sensor tag for low-cost applications," *Applied Computational Electromagnetics Society Journal*, vol. 32, pp. 1083-1088, Dec. 2017.

[5] A. Darvazehban and T. Rezaee, "Ultra-wideband microstrip antenna for body centric communications," *Applied Computational Electromagnetics Society Journal*, vol. 33, pp. 355-358, Mar. 2018.

[6] P. Lopato and M. Herbko, "A circular microstrip antenna sensor for direction sensitive strain evaluation," *Sensors*, vol. 18, pp. 310-320, Jan. 2018.

[7] A. Daliri, A. Galehdar, W. S. T. Rowe, K. Ghorbani, and S. John, "Utilising microstrip patch antenna strain sensors for structural health monitoring," *Journal of Intelligent Material Systems and Structures*, vol 23, pp. 169-181, Jan. 2011.

[8] P. Lopato and M. Herbko, "A circular microstrip antenna sensor for direction sensitive strain evaluation," *Sensors*, vol. 18, pp. 310-320, Jan. 2018.

[9] S. C. Wang and M. S. Tong, "Mechanical deformation detection of building structures using microstrip patch antennas as sensors," *IEEE Sensors Journal*, vol. 18, pp. 8676-8684, Aug. 2018.

[10] M. Herbko and P. Lopato, "Microstrip patch strain sensor miniaturization using Sierpinski curve fractal geometry," *Sensors*, vol. 19, pp. 3989-4001, Sep. 2019.

[11] L. Chen, T. Geng, G. C. Wan, L. Y. Tang, and M. T. Tong, "Sensitivity modeling of a strain-sensing antenna," *Prog. Electromagn. Res. C*, vol. 75, pp. 87-97, June 2017.

[12] X. H. Yi, C. H. Cho, J. Copper, Y. Wang, M. M. Tentzeris, and R. T. Leon, "Passive wireless antenna sensor for strain and crack sensing—Electromagnetic modeling, simulation, and testing," *Smart Mater. Struct.*, vol. 22, pp. 085009-085026, July 2013.

[13] X. H. Yi, T. Wu, Y. Wang, and M. M. Tentzeris, "Sensitivity modeling of an RFID-based strain-sensing antenna with dielectric constant change," *IEEE Sens. J.*, vol. 15, no. 11, pp. 6147-6155, Nov. 2015.

[14] K. L. Chung, L. L. Wang, J. L. Luo, Y. S. Li, and Y. S. Li, "Comparative study on directional sensitivity of patch-antenna-based strain sensors," *Int. J. RF Microw. Comput.-Aid. Eng.*, vol. 30, pp. 22398-22407, Nov. 2020.

[15] L. L. Wang, K. L. Chung, W. Zong, and B. Feng, "A highly sensitive microwave patch sensor for multidirectional strain sensing based on near orthogonal modes," *IEEE Access.*, vol. 9, pp. 24669-24681, Feb. 2021.

[16] P. Chen, L. H. Wang, and Z. H. Ma, "Reconfigurable planar monopole antenna for fifth-generation mobile communication system," *Applied Computational Electromagnetics Society Journal*, vol. 36, pp. 67-74, Jan. 2021.

[17] L. L. Wang, K. L. Chung, and J. L. Luo, "CP-patch-based strain sensor with high sensitivity for structural health monitoring," *2020 IEEE 3rd International Conference on Electronic Information and Communication Technology*, Nov. 2020.

Lingling Wang was born in Qingdao, China, on January, 1993. She received the B.E. degree in Civil Engineering from Qingdao University of Technology, China, in 2015, where she is currently pursuing the Ph.D. degree in Civil Engineering. Her research interests include circularly polarized antenna, antenna-based sensor and structural health monitoring. She was a recipient of the Outstanding Graduate Award of Shandong Province from the Qingdao University, in 2015. She received the "National Encouragement Scholarship" and "National Scholarship" in 2014 and 2018, respectively.

Kwok L. Chung (Senior Member, IEEE) is a Research Professor and a Supervisor of Ph.D. students with Qingdao University of Technology (QUT). He was a Director of Civionics Research Laboratory where he led a cross-disciplinary research team at QUT. Chung is now with Huizhou University. His current research interests include passive wireless sensors, cement-based materials design and characterization, microwave antennas, and metasurface. He is the Founding Chair of the IEEE Qingdao AP/MTT/COM joint chapter (CN10879) under Beijing Section. He has been an Associate Editor of IEEE ACCESS and an Associate Editor of Elsevier Alexandria Engineering Journal since

2016 and 2020, respectively. He serves as a Reviewer for the numerous IEEE, IET, Elsevier, and other international journals.

Song Gao received the M.E. degree from University of Stellenbosch South Africa in 2005 and the Ph.D. degree from Qingdao University of Technology (QUT) in 2013. He is now an Associate Professor in the School of Civil Engineering, QUT, where he is also the Head of Engineering Materials Laboratory. His main research interests are high performance fiber reinforced cementations composite and high-performance building materials using recycled building waste.

Mingliang Ma received the B.S. degree from Ludong University in 2007, and received Ph.D. degree in Materials Science from Northwestern Polytechnical University in 2014. In late 2014, he joined the Qingdao University of Technology and now is an Associate Professor. His main research areas include design of multi-functional electromagnetic absorption materials, and disaster prevention mitigation and protection engineering.

Jianlin Luo received the M.S. degree in Structural Engineering in 2005, and Ph.D. degree in Engineering Mechanics in 2009 from Harbin Institute of Technology. In December 2009, he joined the School of Civil Engineering, Qingdao University of Technology, Qingdao (QUT), China as a Lecturer. He has been an Associate Professor at QUT since 2012. He was a Visiting Scholar in Monash University, Melbourne, Australia during 2015-2016 and a Visiting Fellow in Western Sydney University, Sydney, Australia during 2018-2019. Luo has authored and coauthored about 60 journal papers and held 20 invention patents. His current research interests include smart materials and structural health monitoring, advanced construction materials and applications in infrastructure.

Yingsong Li received his Ph.D. degree from both Kochi University of Technology (KUT), Japan and Harbin Engineering University, China in 2014. He is a Full Professor of Harbin Engineering University from July 2014. He is a senior member of Chinese Institute of Electronics (CIE) and a senior member of IEEE. He is an Associate Editor of IEEE Access and Applied Computational Electromagnetics Society Journal.

Li also serves as a reviewer for more than 20 journals. His current research interests include remote sensing, underwater communications, signal processing, radar, SAR imaging, compressed sensing and antennas.

Design and Analysis of High Gain Dual-polarized Dipole Antenna Based on Partially Reflective Metasurface

Chenqi Li [1]┼, Zhongsen Sun [1]┼, Zhejun Jin [1], Tian Liu [1], Leonid F. Chernjgor [1,2], and Yu Zheng [1,*]

[1] College of Electronic Information, Qingdao University, Qingdao, 266071, China

[2] Department of Space Radiophysics, V.N. Karazin Kharkiv National University, Kharkiv, 61022, Ukraine
┼ These authors contributed equally to this work, *zhengyu@qdu.edu.cn

Abstract **─** A partially reflective metasurface (PRMS) structure is proposed for dual-polarized dipole antenna with a high gain and wide broadband. Stable radiation patterns are realized by using quadrilateral bottom reflector. The phase bandwidth of PRMS structure reflection presented in this paper matches well with the antenna operating bandwidth. The gain of the dual-polarized antenna is improved to 10.2dBi at 1.8GHz by adjusting the size and height of PRMS structure. Meanwhile, the bandwidth is expanded (61.2%). Measured result demonstrates that the antenna has a stable beamwidth which is desirable in base station applications. Furthermore, the designed antenna can be used for communication in complex environment because of its excellent performance.

Index Terms **─** Dual-polarize, high gain, partially reflective metasurface (PRMS), quadrilateral bottom reflector.

I. INTRODUCTION

Recently, with the increasing complexity of the electromagnetic application, high-gain antennas are widely used in base station backhaul and direction-finding systems to compensate the communication link loss. In addition, the dual-polarized property is also necessary for base station antenna to obtain minute interference and extensive channel capacity. Designing an antenna with high gain and dual-polarized property will play a significant role in the many wireless system.

The base station antenna types are primarily divided into patch class, dipole class and gap class [1]. The patch antenna and slot antenna is simple to manufacture, but the bandwidth is difficult to expand. With the benefits of high isolation and stable radiation pattern, the dipole antenna is the widely used form. For example, a novel double-polarized dipole antenna unit which working frequency band is 1.7 GHz to 2.7GHz is proposed and high relativity gain (8.5dBi) is obtained [7]. However, the proposed antenna size (200×130 mm) limits its use as a base station cell. Using the differentially fed form, dual-polarized slot antenna realized high isolation and wide impedance bandwidths (19.3%). Nevertheless, the antenna structure is complex has a complicated structure, and the performance is hard to improve. Therefore, it is a meaningful challenge to increase the antenna gain and bandwidth with reduced antenna size.

Many research has proved that the new materials, such as frequency selective surface structures (FSSs), find wide applications in various antennas, radars (RCS reduction), and electromagnetic wave absorbers due to their many extraordinary properties [8-11]. The metamaterial structure can manipulate and control the surface distribution of electromagnetic waves by changing the geometry and alignment of the FSS to make the antenna obtain fine performance. Metamaterial structure is used as a partially reflective surface (PRS) which achieves an effect similar to a focusing lens. By selecting an artificial electromagnetic material to constitute a Fabry-Perot resonant antenna, a high gain and highly directional antenna was proposed in [12,13]. Moreover, thin subsurface is used in [14,15], which is improve the performance of circularized array antenna. In [16,17], the metamaterial reflective surface plays an important role for both single-feed circularly polarized antenna and microstrip patch antenna. As a result, the antennas obtain high gain and wide bandwidth. A partial reflector is also designed in [18] to make the antenna achieve dynamic control of beam width, which benefits from stable radiation pattern and high directivity. Therefore, the PRS, which has a compact structure, has been widely used to improve antenna performance. However, owing to the narrow reflection phase bandgap of metamaterial structure, it is difficult to integrate the antenna unit cell with the PRS while designing a high-gain base station antenna. Adding air dielectric layer maybe is an efficiency way to broaden the phase bandwidth of PRS structure [22].

In the present paper, we introduce the dual-polarized

Submitted On: March 24, 2021
Accepted On: July 6, 2021

https://doi.org/10.47037/2021.ACES.J.360918

dipole antenna with good performance that uses a metasurface structure with periodic arrays consisting of FSS and PRS for enchaining the gain and bandwidth. Also, an LC equivalent circuit model is used to demonstrate the feasibility of a partially reflective metasurface structure (PRMS). The measured results are in good agreement with the simulation results. By adjusting metasurface structure, the bandwidth is increased by 15.8%. Meanwhile, the maximum gain is increased by 4.9dBi at 2.8GHz. Moreover, the plane reflector is also modified.

II. DESIGN AND CONFIGUATION OF ANTENNA AND PRMS

A. Design of antenna and bottom reflector

A dual-polarized dipole antenna feed by two baluns is chosen as the primary antenna [2], as shown in Fig. 1. The size of two crossed-dipoles is *Wa* to realize the operating frequency band. When one pair of dipoles works, the other pair acts as a parasitic unit to widen the antenna impedance bandwidth. Moreover, the antenna uses a rectangular ring radiator with two short-circuiting branches in the ring to change the current distribution on the surface of the antenna, which is conducive to the isolation degree between the two antenna ports. The total height of the antenna is H to meet the distance between the reflector plate and the bottom of the radiator is 1/4 wavelength, which is beneficial to obtain the optimal unidirectional radiation performance of the antenna. What’s more, the antenna is fed by probe coupling, as shown in Fig. 1 (c). The vertical part of the probe adds insulating dielectric and the horizontal part of the feed bar adopts the bending structure. There is a height difference between two feed bars, which also ensures to get the port high isolation characteristics.

In order to improve the performance of the antenna, we changed the plane reflector to a curved reflector (quadrilateral reflector). The reflector can make the backward radiated electromagnetic wave superimposed with the primary radiated electromagnetic wave after reflection to improve the antenna's directivity and gain.

The distance between the radiation and the reflector affects the directivity of the antenna. If the distance is too small, the pattern presents a single lobe, and the -3dB beamwidth is very narrow. However, if the distance is too large, the pattern presents multiple lobes, and the directivity of the antenna decreases. When the distance is between 0.3~0.75λ, the radiation resistance can be maximized, as the result, the antenna will obtain an optimal performance.

The length of the quadrilateral bottom reflector designed in this paper is *Wr2*, the length of the top side is Wr1, and the bending angle is 130°. The reflector is made of the same material as the antenna, and the thickness is 0.5 mm. Finally, this paper ultimately devised a quadrilateral bottom reflector which has a size of 150×150mm, showed in Fig. 1 (a). The specific design dimensions of the antenna are given in Table 1.

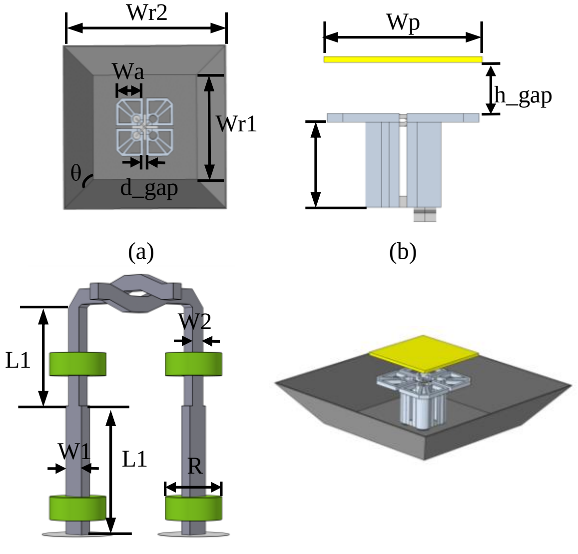

(a) (b)

(c) (d)

Fig. 1. Different configuration of the antenna. (a) With a quadrilateral reflector (top view). (b) With a PRMS structure (side view). (c) Structure of L-shaped probe. (d) With a quadrilateral reflector and PRMS structure.

Table 1: Geometric parameters of the antenna

Parameters	Value (mm)	Parameters	Value (mm)
Wa	23	L1	12
Wr1	100	L2	14
Wr2	150	D	7.5
W1	3	d_gap	2.7
W2	2	h_gap	18
Wp	56	h	33

B. Principle of PRMS structure

Nevertheless, the enhancement of antenna performance through the bottom reflector optimization is restricted. And the reflector can adversely affect impedance bandwidth. So, we used a partially reflective metasurface (PRMS) structure further.

Based on the principle of antenna energy radiation, the electromagnetic waves radiated from the feeder travel different distances to reach various positions on the partially reflective surface. Thus, the partially reflecting waves reflected multiple times have different reflection phases when they finally pass through the PRMS structure. Many studies have demonstrated that the reasonable phase compensation of the partially reflective surface can effectively broaden the gain bandwidth [21]. The phase bandwidth of the positive reflection should match the working frequency band of the antenna as much as possible. Increasing the relative dielectric constant of the dielectric plate is a way to obtain a wider phase bandwidth, but increasing the thickness is directly equivalent to increasing the cost. Another method is to add an air gap between the ground plate and the dielectric plate of FSS [20],[22]. The substrate's energy bound is reduced because the low dielectric constant medium restricts the antenna radiation field less. Using this theory, the cell's phase change becomes gentler while the influence of surface wave is reduced.

C. Configuration of PRMS structure

In this section, a single-layer reflective metasurface structure with a square patch, a substrate and an air dielectric layer is designed. The side length of the patch is w, and the horizontal and vertical gap is g, as shown in Fig. 2. The patch unit cell is etched on one side of the dielectric board made out of a 2 mm thick FR4 substrate (ε_r = 4.4, tanδ = 0.018). When electromagnetic waves are incident on the surface of the periodic metal patch, the induced current is excited at the same time, causing the gap between two adjacent patches to generate a coupling capacitance *C*.

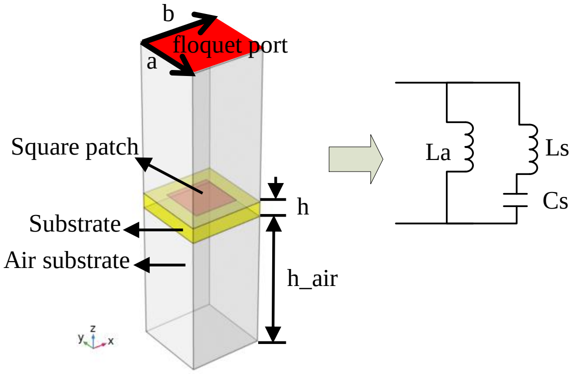

Fig. 2. Geometry settings of proposed metasurface unit and its equivalent circuit model.

The length of each patch generates an inductance, and the dielectric plate and the air layer generate the inductance is represented by *La*. Detailed equivalent circuit diagram of the partially reflective metasurface is shown in Fig. 3. Therefore, the total surface impedance can be expressed as [23]:

$$Z = Z_a//Z_s = jwL_a\frac{1-w^2L_sC_s}{1-w^2(L_s+L_a)C_s}, \tag{1}$$

where Z_s and Z_a are the equivalent impedances of the periodic patch and the total substrate, respectively, and the resonant frequency and reflection phase of the superstructure can be further calculated by the eq. (2):

$$f_s = \frac{1}{2\Pi\sqrt{(L_s+L_a)C_s}}, \tag{2}$$

$$j\Phi = \ln\Gamma = \ln\frac{Z-\eta_0}{Z+\eta_0}, \tag{3}$$

where η_0 is the free space wave impedance.

Although the square patch generates the LC equivalent circuit structure in series, the high impedance characteristic at resonance makes the superstructure show in-phase reflection characteristics. The incident wave cannot achieve the ideal total reflection or complete transmission.

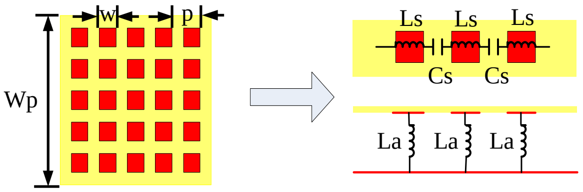

Fig. 3. Detailed equivalent circuit diagram of the partially reflective metasurface.

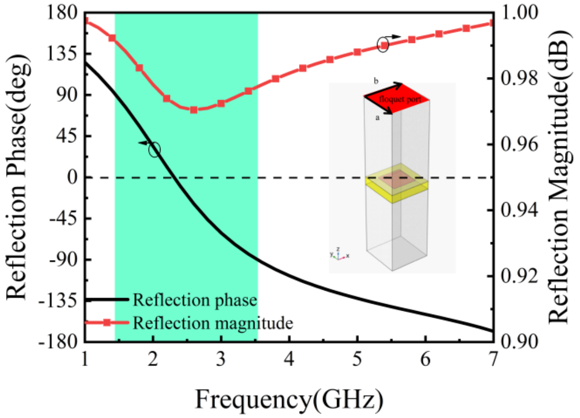

Fig. 4. Reflection phase and magnitude characteristics of the square patch metasurface. The blue band represents the ± 90° reflection phase bandwidth, suggesting the operating frequency of the metasurface.

The Floquet port method of HFSS simulation software is used to simulate the PRMS structure. Modeling of a cell set up around the master-slave boundaries to simulate infinite cycle and setting the floquet port on the upper surface for excitation. The reflection coefficient amplitude for one cell on PRMS structure changes with frequency curve is shown in Fig. 4. In the working frequency band (1.5-3.5GHz), metasurface reflection coefficient is between 0-1, which can realize the part of the electromagnetic wave reflection. The incident electric field is basically all reflected, which meets the needs of resonant cavity antenna. The designed PRMS structure in phase reflection bandwidth is basically consistent with the working bandwidth of the dipole antenna, thus the proposed structure can be used to improve the performance of the antenna.

Furthermore, the electromagnetic characteristics of metasurface are simulated by using CST. The electromagnetic wave incident to the near-zero refractive index metamaterial can be emitted almost perpendicular to the metamaterial surface and the antenna gain can be improved after the superposition of multiple reflected waves [19]. It can be seen from Fig. 5 that the magnetic permeability is close to zero at 3GHz.The relative permeability is -0.12+j0.05, which shows good space transmission performance of electromagnetic wave.

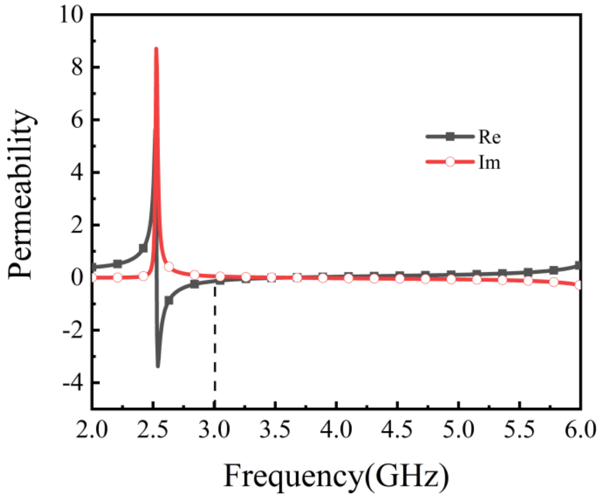

Fig. 5. Simulated permeability of metasurface unit.

III. OPTIMIZATION OF ANTENNA AND PRMS STRUCTURE

A. Analysis of the antenna parameter

The antenna is fed by a probe coupling, and the capacitance effect between the probe and the antenna radiator affects the working bandwidth of the antenna. Reasonable setting of the distance between the two can make the antenna achieve the best impedance matching. The simulation results of return loss under different spacing are shown in Fig. 6. It can be seen that with the increase of spacing, the capacitance value increases and the low-frequency resonance point gradually disappears. The impedance matching effect is the best when *R*=3.75mm. The spacing between dipole radiators also has a significant effect on antenna performance. When one pair of dipoles is excited, the other pair acts as a parasitic unit to extend the working bandwidth of the antenna, and the coupling current intensity can be adjusted by changing the distance between the dipoles. From Fig. 7, the simulated results show that the second resonant point is closely related to the spacing. When *d_gap* is 1.7 mm, the antenna has only one resonant point. With the increase of *d_gap*, the value of the first resonant point moves up.

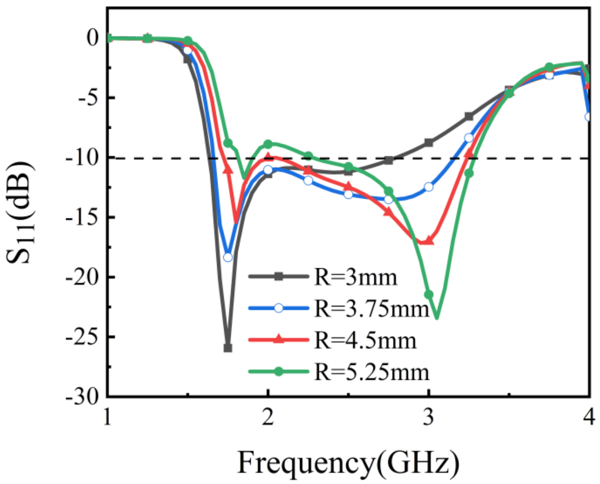

Fig. 6. Result of reflection with different *R*. The optimal bandwidth (1.67-3.17GHz) is achieved with *R=3.75*mm.

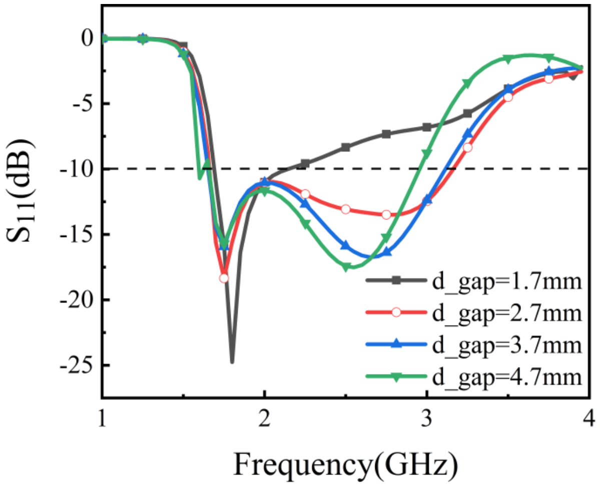

Fig. 7. Result of reflection with different *d_gap*. The optimal bandwidth (1.67-3.17GHz) is achieved with *d_gap*=2.7mm.

B. Optimization of the PRMS height

Eelectromagnetic waves are repeatedly reflected and transmitted through PRMS structure and the antenna, forming a resonant cavity. In the PRMS cavity, the antenna directivity coefficient (D_c) at the center frequency is indicated as follows [24]:

$$D_c = \frac{1+R}{1-R}, \tag{4}$$

where R is the magnitude of the PRMS reflection coefficient.

In the process of electromagnetic wave transmission, the signal energy in the resonant cavity is mitigated to different extend. The width of PRMS structure (*Wp*) and the height of PRMS structure (*h_gap*) all have great influence on the resonant cavity and then affect the antenna performance. We analysis two parameters (*Wp* and *h_gap*) separately.

The resonant point of the resonator cavity antenna is determined jointly by the height (*h_gap*), the reflecting phase of the PRMS structure (φ_1), and the reflective phase of the antenna bottom reflector (φ_2):

$$f = \frac{c}{2d}\left(\frac{\varphi_1+\varphi_2}{2n} - n\right),\ n = 0,1,2\ldots K. \tag{5}$$

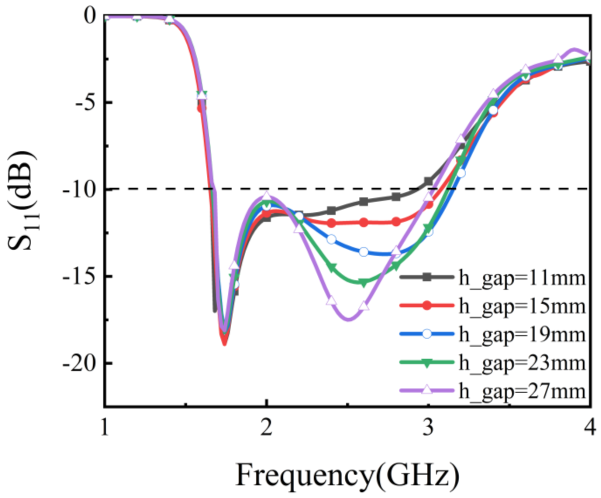

Fig. 8. Result of reflection with different *h_gap*. The optimal bandwidth (1.67-3.17GHz) is achieved with *h_gap*=19mm.

The parameters were analyzed using Ansoft HFSS simulation software. The antenna bandwidth is essentially stable with the different distance between the PRMS and the antenna. Fig. 8 shows the S11 simulation results by changing the height *h_gap*. When *h_gap* =19mm or 23mm, the -10dB impedance bandwidth of the antenna is 1.67 to 3.17GHz. Finally, Taking into account the size of the antenna, d=19mm is the optimal height which was established in further research.

C. Optimization of the dimension of PRMS structure

The number of PRMS patch cell equal to the size of PRMS structure (Wp) also has an effect on bandwidth [16]. In this section, we first keep the height *h_gap*=19mm is constant. After that, four groups of FSSs with varying cells which is 2×2 array (*Wp*=30mm), 5×5 array (*Wp*=56mm), 7×7 array (*Wp*=80mm) and 9×9 array (*Wp*=100mm) were chosen respectively to design the reflector surface and combine with the dipole antenna.

Figure 9 shows the return loss simulation results. It is demonstrated that the size of PRMS structure has a great influence on the impedance bandwidth and the high frequency resonant point. The operating frequency ban expands with the increase of PRMS dimension.

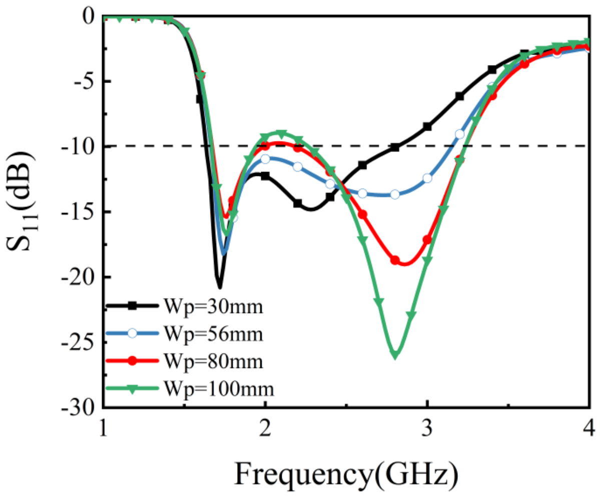

Fig. 9. Result of reflection with varying *Wp*. The widest -10dB impedance bandwidth is obtain when *Wp*=56mm

IV. RESULTS

To better demonstrate the effect of designing PRMS structure, we have compared the return loss results of only antenna, adding PRMS structure, adding quadrilateral bottom reflector (Abbreviated in the figure as reflector), and antenna with PRMS and reflector. Fig. 10 shows the simulation result. It can be seen that the input impedance of the antenna changes after loading part of the reflected surface, resulting in the decrease of resonant frequency with the bandwidth is 1.67-3GHz. The maximum working frequency is reduced from 3GHz to2.8GHz when the quadrilateral reflector is loaded. While the antenna added quadrilateral reflector and PRMS structure, the antenna has the best performance showing in a bandwidth increase of 61.2%.

Figure 11 shows the simulated results of antenna gain. The E-plane gain of antenna with PRMS structure is higher than that of antenna without PRMS structure within the operation band from 1.6-2.2GHz. Gain enhancement is very limited in other frequency. When the distance between antenna and metasurface is 18mm, the antenna gain increases significantly at 3GHz. The electromagnetic wave incident to the near-zero refractive index metamaterial can be emitted almost perpendicular to the metamaterial surface and the antenna gain can be improved after the superposition of multiple reflected waves. Adding quadrilateral reflector can effectively improve this deficiency. Moreover, the gain of the final proposed antenna is almost stable within the expect frequency band. It can be seen from Fig. 12 that the antennas with PRMS structure have a higher cross-polarization ratio at low frequencies and the beamwidth is slightly reduced. The performance of antenna with different structure was compared in Table 2.

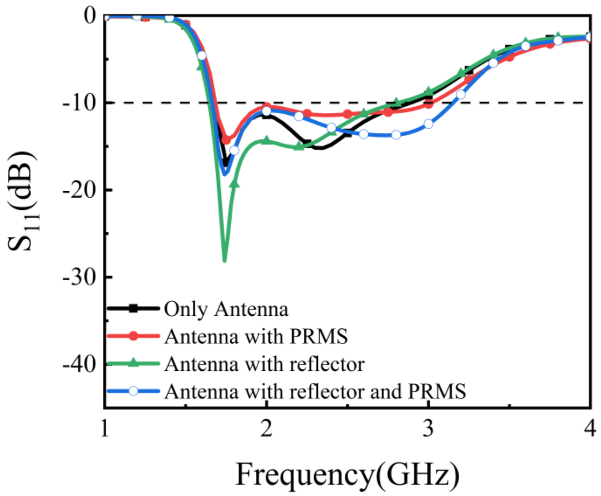

Fig. 10. Simulated reflection results with different antenna structure. Antenna with reflector and PRMS structure has the widest bandwidth.

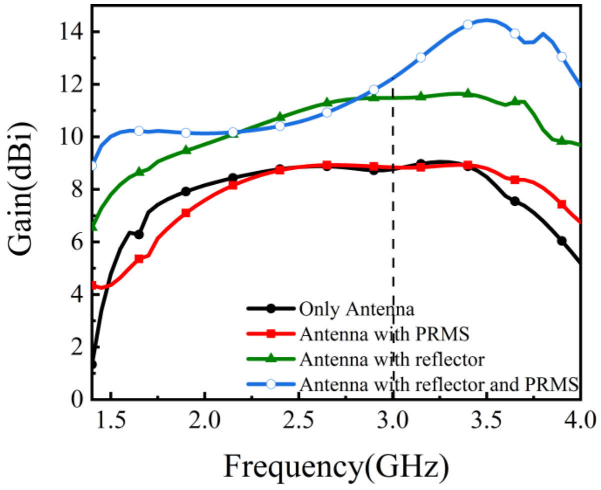

Fig. 11. Gain of antenna in E-plane in different antenna structure.

Therefore, we concluded that the gain enhancement method with PRMS structure is also efficiently to use in dipole antennas. The dipole antenna with PRMS structure is shown in Fig. 13. The space between the dipole antenna and the PRMS structure is supported by foam which acts as an air dielectric layer.

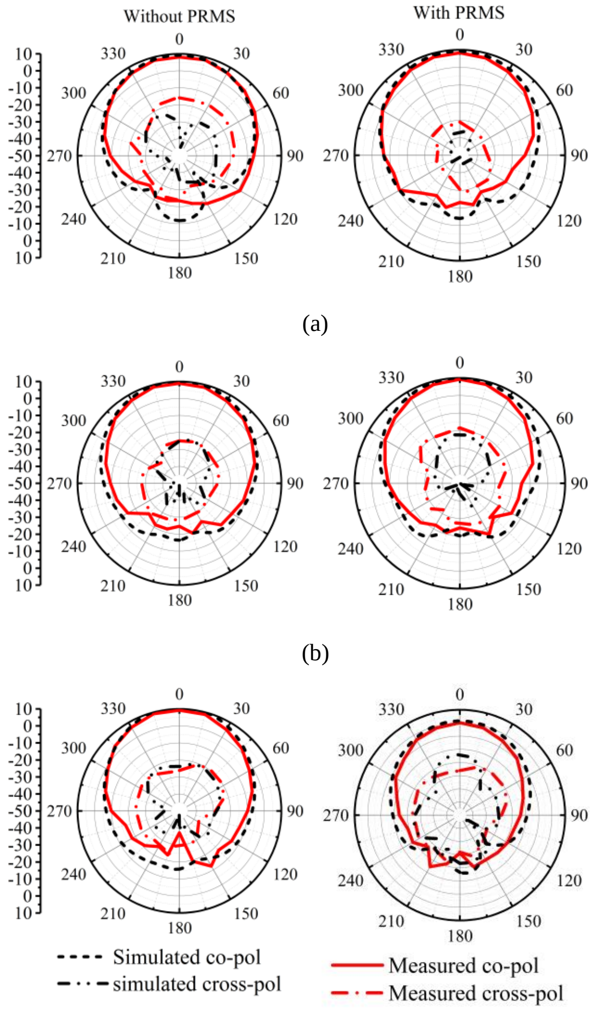

(a)

(b)

(c)

Fig. 12. Radiation patterns of the proposed metasurface antenna with reflector or without angular reflector at (a) 1.8GHz, (b) 2.2GHz, and (c) 2.8GHz.

Table 2: Comparison between the antenna with different structure

Antenna Structure	**-10dB Bandwidth (GHz)**	**Gain at 3GHz (dBi)**
Only antenna	1.6-2.8	7.6
Antenna with PRMS	1.6-2.97	7.6
Antenna with reflector	1.6-2.95	10.9
Antenna with reflector and PRMS	1.6-3.2	12.5

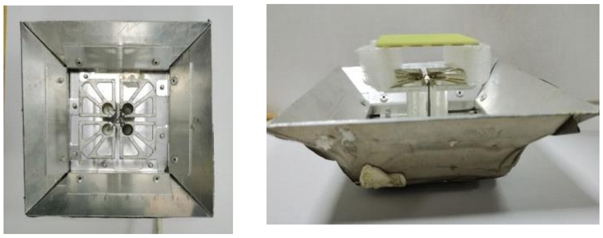
(a) (b)

Fig. 13. (a) Fabricated dual-polarized dipole antenna (top view), and (b) fabricated proposed antenna with PRMS structure.

The actual measurement is basically consistent with the simulated return loss. Due to processing error and the simulation does not consider the influence of the four foam spacers supporting PRMS on the antenna performance, the resonant frequency has a deviation of 0.1 GHz, which can be ignored theoretically (Fig. 14). In this paper, the gain and direction of the design antenna is further measured and analyzed.

Furthermore, the performance of antennas with New Electromagnetic Materials is compared which are listed in Table 3. It is obvious that they have similar performance, but the proposed antenna has a smaller aperture size, which is benefit for using array antenna and coupling effect can be ignored.

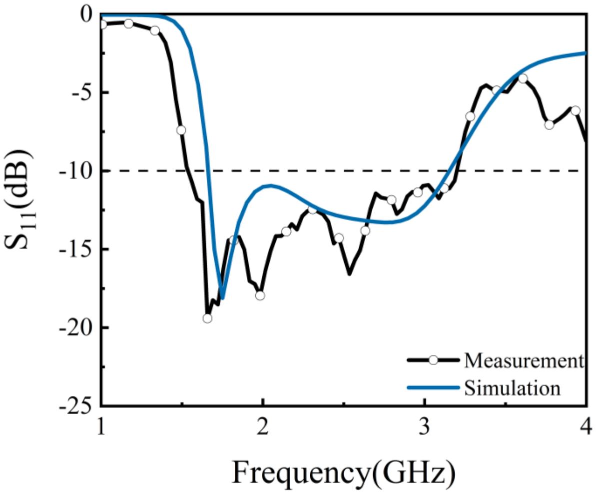

Fig. 14. Simulated and measured reflection results of proposed antenna.

Figure 15 shows the simulated and measured gain of the antenna. Because of the process error and test error, the measured gain is smaller than the simulation result. The measured efficiency is greater than 63% in the working frequency band, which meets the needs of practical engineering.

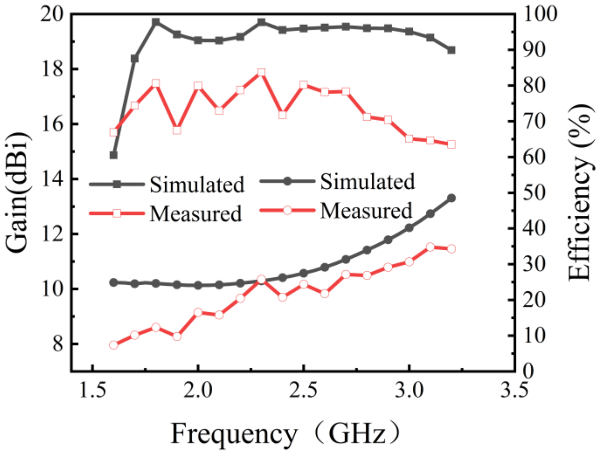

Fig. 15. Simulated and measured results of gain and efficiency.

Table 3: Comparison between the designed antenna and other high-gain antenna

Ref.	Antenna Type	-10dB Bandwidth (dB)	Maximum Gain (dBi)
[12]	Dual-polarized Fabry–Perot antenna	29.4%(8.7-11.7GHz)	15.7
[17]	Antenna Cavity resonator antenna	40.4% (8.1-12.2GHz)	12.5
[16]	Circularly polarized patch antenna	11% (2.34-2.64GHz)	9.1
[25]	Circularly polarized array	46.5% (1.9-3.05GHz)	12.8
This work	Dual-polarized dipole antenna	61.5%(1.6-3.1GHz)	12.7

Table 4: Comparison between the designed antenna and other base station antenna

Ref.	BW (GHz)	Isolation (dB)	Maximum Gain (dBi)	HPBW
[2]	1.7-2.7	＞30	8.9	65.2±5.6
[3]	1.427-2.9	＞20	8	66±3
[4]	4.5-5.0	＞27	10.3	58±4
[5]	1.55-2.75 3.3-3.8	＞30	7.6	68±5
[6]	1.71-2.71	＞30	9.9	65±4.5
[7]	3.14-3.81	＞43	12.5	64±3
This work	1.6-3.1	>28	12.7	65

As Table 4 shows the comparison between the antenna proposed in this paper and the existing base station antenna, it can be seen that the antenna proposed in this paper has a simple structure and the isolation degree meets the engineering needs while having the highest gain. While the disadvantage is that the operating bandwidth cannot completely cover the Sub-6G band, and the future work we will further optimize the antenna so that it can be used as a 5G base station. Therefore, the proposed antenna has a wider field of application.

V. CONCLUSION

In this paper, a quadrilateral reflector and PRMS structure are used to design a broadband dual-polarized antenna. The principle of PRMS structure is analyzed by LC equivalent circuit. Then we properly design the dimensions of square patch and the thickness of substrate to optimize the performance of antenna. Moreover, the antenna gain is greatly improved by the combination of the quadrilateral bottom reflector and PRMS structure. The bandwidth of the final design has increase by 15.8%. In addition, the maximum gain has improved 4.9dBi at 2.8GHz and the efficiency in the working frequency band is greater than 63%. Therefore, the method we presented to enhance the gain and broaden the bandwidth is suitable for dipole antenna which makes it very attractive to different type of base station antenna array.

ACKNOWLEDGMENT

Thanks to the support of Qingdao University in 2021. Thanks to the National Key Research and Development Program Strategic International Science and Technology Cooperation and Innovation Program (2018YFE0206500) for its funding support.

REFERENCES

[1] D. Z. Zheng and Q. X. Chu, "A wideband dual-polarized antenna with two independently controllable resonant modes and its array for base-station applications," *IEEE Transactions on Antennas and Propagation*, vol. 16, pp. 2014-2017, Apr. 2017.

[2] Y. He and Y. Yue, "A novel broadband dual-polarized dipole antenna element for 2G/3G/LTE base stations," *2016 IEEE International Conference on RFID Technology and Applications (RFID-TA)*, Foshan, pp. 102-104, Nov. 2016.

[3] Q. Zhang and Y. Gao, "A compact broadband dual-polarized antenna array for base stations," *IEEE Antennas and Wireless Propagation Letters*, vol. 17, no. 6, pp. 1073-1076, June 2018.

[4] B. Qiu, S. Luo, and Y. Li, "A broadband dual-polarized antenna for sub-6 GHz base station application," *2020 IEEE 3rd International Conference on Electronic Information and Communication Technology (ICEICT)*, pp. 273-275, Dec. 2020.

[5] Z. Li, J. Han, Y. Mu, X. Gao, and L. Li, "Dual-band dual-polarized base station antenna with a notch band for 2/3/4/5G communication systems," *IEEE Antennas and Wireless Propagation Letters*, vol. 19, no. 12, pp. 2462-2466, Dec. 2020.

[6] H. Sun, C. Ding, T. S. Bird, and Y. J. Guo, "A base station antenna element with simple structure but excellent performance," *2018 Australian Microwave Symposium (AMS)*, pp. 35-36, Apr. 2018.

[7] Y. Liu, S. Wang, X. Wang, and Y. Jia, "A differentially fed dual-polarized slot antenna with high isolation and low profile for base station application," *IEEE Antennas and Wireless Propagation Letters*, vol. 18, no. 2, pp. 303-307, Feb. 2019.

[8] Q. Zhang, L. Si, Y. Huang, X. Lv, and W. Zhu, "Low-index-metamaterial for gain enhancement of planar terahertz antenna," *AIP Advances*, vol. 4, pp. 037103, Mar. 2014.

[9] I. Yoo, M. F. Imani, T. Sleasman, and D. R. Smith, "Efficient complementary metamaterial element for waveguide-fed metasurface antennas," *Optics. Express*, vol. 24, no. 25, pp. 28686-28692, Dec. 2016.

[10] Y. Huang, L. Yang, J. Li, Y. Wang, and G. Wen, "Polarization conversing of metasurface for the application of wideband low-profile circular polarization slot antenna," *EJP Applied Metamaterials*, vol. 5, no. 11, pp. 1-13, Aug. 2018.

[11] N. Nasimuddin, Z. N. Chen, and X. Qing, "Bandwidth enhancement of a single-feed circularly polarized antenna using a metasurface: Metamaterial-based wideband CP rectangular microstrip antenna," *IEEE Antennas and Propagation Magazine*, vol. 58, no. 2, pp. 39-46, Apr. 2016.

[12] A. K. Singh, M. P. Abegaonkar, and S. K. Koul, "High-gain and high-aperture-efficiency cavity resonator antenna using metamaterial superstrate," *IEEE Antennas and Wireless Propagation Letters*, vol. 16, pp. 2388-2391, June 2017.

[13] Z. Liu, "Effect of primary source location on Fabry-Perot Resonator antenna," *2009 Asia Pacific Microwave Conference*, Singapore, pp. 1809-1812, Sept. 2009.

[14] K. L. Chung and S. Kharkovsky, "Metasurface-loaded circularly-polarized slot antenna with high front-to-back ratio," *Electronics Letters*, vol. 49, no. 16, pp. 979-981, Oct. 2013.

[15] S. Chaimool, K. L. Chung, and Prayoot Akkaraekthalin, "Simultaneous gain and bandwidths enhancement of a single-feed circularly polarized patch antenna using a metamaterial reflective surface," *Progress in Electromagnetics Research B*, vol. 22, pp. 23-37, Jan. 2010.

[16] S. Chaimool, K. L. Chung, and Prayoot Akkaraekthalin, "Bandwidth and gain enhancement of microstrip patch antennas using reflective metasurface," *IEICE Transactions Communication*, vol. E93-B, no. 10, Oct. 2010.

[17] F. Qin, S. Gao, G. Wei, Q. Luo, and J. Xu, "Array-fed dual-polarized wideband Fabry-Perot antenna based on metasurface," *Microwave and Optical*

Technology Letters, vol. 58, no. 10, pp, 2316-2321, Mar. 2016.

[18] L. Ji, Y. J. Guo, P. Qin, S. Gong, and R. Mittra, “A reconfigurable partially reflective surface (PRS) antenna for beam steering,” *IEEE Transactions on Antennas and Propagation*, vol. 63, pp. 2387-2395, June 2015.

[19] Y. Zhao, K. Yu, and Y. Li, “A high gain patch antenna using negative permeability metamaterial structures,” *2017 Progress in Electromagnetics Research Symposium - Fall (PIERS - FALL)*, pp. 119-123, Nov. 2017.

[20] D. Cure, T. M. Weller, and F. A. Miranda, “Non-uniform bias enhancement of a varactor-tuned FSS used with a low profile 2.4 GHz dipole antenna,” *Proceedings of the 2012 IEEE International Symposium on Antennas and Propagation*, Chicago, IL, pp. 1-2, Sept. 2012.

[21] F. Sultan and S. S. I. Mitu, “Superstrate-based beam scanning of a Fabry–Perot cavity antenna,” *IEEE Antennas and Wireless Propagation Letters*, vol. 15, pp. 1187-1190, Nov. 2016.

[22] J. Xue, W. Jiang, and S. Gong, “Wideband RCS reduction of slot-coupled patch antenna by AMC structure,” *Electronics Letters*, vol. 53, no. 22, pp. 1454-1456, Dec. 2017.

[23] M. Li, Q. L. Li, B. Wang, C. F. Zhou, and S. W. Cheung, “A low-profile dual-polarized dipole antenna using wideband AMC reflector,” *IEEE Transactions on Antennas and Propagation*, vol. 66, no. 5, pp. 2610-2615, Dec. 2018.

[24] T. Debogović and J. Perruisseau-Carrier, “Array-fed partially reflective surface antenna with independent scanning and beamwidth dynamic control,” *IEEE Transactions on Antennas and Propagation*, vol. 62, pp. 446-449, Oct. 2014.

[25] K. L. Chung, S. Chaimool, and C. Zhang, “Wideband subwavelength-profile circularly polarized array antenna using anisotropic metasurface,” *Electronics Letters*, vol. 51, no. 18, pp. 1403-1405, Sept. 2015.

[26] C. Wang, L. Zhang, S. Wu, S. Huang, C. Liu, X. Wu, “A Dual-band Monopole Antenna with EBG for Wearable Wireless Body Area Networks,” *ACES Journal*, vol. 36, no. 1, pp. 48-54, Jan. 2021.

Chenqi Li was born on July 8, 1997. She received the B.S. degrees from Qingdao University, Qingdao, China, in 2019. She is pursuing M.S. degree in Signal and Information Processing from Qingdao University at present.

Her current research interests include base station antenna and circularly polarized antenna. She attended the ICEICT Academic Conference in 2020.

Zhongsen Sun was born on July 11, 1980, in the P.R. of China. He received the M.S. and Ph.D. degrees in Radio Engineering from the Changchun Institute of Optics, Fine Mechanics and Physics, Chinese Academy of Sciences, 2004 and 2007 respectively. He received Professor in 2009. Winner of the award for the Best Scientific Work in Ministry of Industry and Information Technology of P.R. of China, 2018. His main research is in the area of Spectrum theory and adio communication.

Zhejun Jin received the B.S. degree in Electronics Engineering from the Yanbian University, China, in 2000, the M.S. degree in Electronics Engineering at Incheon University, South Korea, in 2006, and the Ph.D. degree from Hanyang University, Seoul, South Korea, in 2014. Since September 2014, he has been an Assistant Professor at Qingdao University, China. His research interests are antennas, microwave circuit design, microwave component modeling, and wireless communication systems.

Tian Liu was born in 1989. She received the B.S. in Advanced Materials Engineering from Chungbuk National University, Korea, in 2013. The M.S. and Ph.D. Degrees in Materials Engineering (Electronic Material Lab.) from Chungbuk National University, South Korea, in 2015 and 2020. In 2020, she joined the College of Microtechnology and Nanotechnology, Qingdao University, China, as an Assistant Professor. Her current research interests include areas of frequency selective surface, metamaterial, metasurface absorbers and microwave absorbers.

Leonid F. Chernjgor Full Professor, Fellow of Commission B (Fields and Waves) in the Ukrainian National URSI Committee, Fellow of the Scientific Council for Physics of the Ionosphere in Ukraine, Vice-President of the Academic Council conferring the Candidate of Science Degree (equivalent of American Ph.D.) and the Doctor of Science degree in Radio Science and a member of two other Academic Councils. Research Interests:

Nonstationary theory of the interaction between high-power radio emissions and near-earth plasmas. Large-scale (thousands of kilometers) perturbations launched by high-power HF and MF radio emissions in ionosphere-magnetosphere plasmas. Physical processes appearing in near-earth space from localized sources of energy of different physical nature (magnetic storms, solar terminator, solar eclipses, earthquakes, volcano eruptions, high-power explosions, rocket engine burns, etc.). Author and co-author of more than 700 scientific publications, including five science books and sixteen textbooks.

Yu Zheng received M.S. and Ph.D. degrees from V. N. Karazin Kharkiv National University, Kharkiv, Ukraine, in 1998 and 2006. Now he is working in College Electronic and Information, Qingdao University. In 2006 selected in corresponding member of Engineering Academy of Ukraine. His scientific interests include base Propagation of electromagnetic waves and RF technology.

Compact Wideband Dual-Band SIW Bandpass Filters

Yun Jiang, Lei Huang*, Zhaoyu Huang, Yuan Ye, Boyuan Liu, Wentao Yuan, and Naichang Yuan

State Key Laboratory of Complex Electromagnetic Environment Effects on Electronics and Information System
College of Electronic Science, National University of Defense Technology, Changsha, 410073, China
*huanglei_nudt@163.com

Abstract **─** A novel method to design compact wideband dual-band substrate integrated waveguide (SIW) bandpass filters (BPF) is proposed in this paper. By loading a novel beeline compact microstrip resonant cells (BCMRCs) with band-gap characteristics on top layer of SIW, two wide passbands separated by a stopband are generated. In order to enable the filter to have lower reflection coefficients in the two passbands, we use a tapered gradient line embedded with rectangular slots and loaded open stubs as the transition structure from microstrip line to SIW. The wideband dual-band BPF (DBBPF) is fabricated. The lower-band and upper-band fractional 3-dB bandwidths are 58.2% and 22.6%, while the measured minimum insertion losses (ILs) are 0.7 and 0.92 dB, respectively. The stepped-impedance open-loop ring resonator (SIOLRR) is introduced in order to improve the selectivity of the filter. The wideband DBBPF with SIOLRR is studied, simulated and measured. Two transmission zeros are generated in the stop band between the two passbands. Good agreement between simulated and measured results can be obtained.

Index Terms **─** Complementary split ring resonators, defected ground structure, dual-band bandpass filter, stepped-impedance open-loop ring resonator, substrate integrated waveguide.

I. INTRODUCTION

With the rapid development of wireless communication technologies, frequency spectrum resources have become increasingly scarce, thus dual-band system have received more and more attention. As an important passive component of wireless communication, DBBPF has been widely studied and developed [1-6]. But up to now, most DBBPFs are based on microstrip technology. Although they are simple structure and low in cost, disadvantages such as low power-banding capacity and poor performance limit their application [7-9]. Waveguide filters and dielectric resonator filters can effectively overcome the shortcomings mentioned above, but they are costly and bulky [10]. Fortunately, a new planar integration scheme called substrate integrated waveguide (SIW) has emerged and attracted tremendous attentions. It is a type of waveguide-like structure which enjoys not only the advantages of classical rectangular waveguide features, but also the benefits of planar circuit, thereby providing a promising platform to develop excellent filters which can satisfy the stringent requirements of modern wireless communication systems [11-13]. In [14] a dual-band SIW filter is obtained by loading E-shaped defected ground structure (DGS) on either top or bottom sides. In [15], two same or different sized complementary split ring resonators (CSRRs) are etched on the top side of SIW cavity to achieve a dual-band frequency response. The dual-band balanced SIW bandpass filter is demonstrated in [16], by vertically cascading two square SIW cavities. However, the all dual-band SIW filters mentioned above are narrow-bandwidth. As a result, they are not suitable in broadband wireless communication systems.

This paper presents a novel method to design compact wideband SIW DBBPFs. It combines the SIW and BCMRC technologies, which allow the implementation of two wide passbands. In order to improve the selectivity of the wideband SIW DBBPFs, the SIOLRRs are loaded on the input and output ports of the filter. Detailed working mechanisms and design method are explained as follows. For verification, two wideband SIW DBBPFs are proposed, fabricated and measured.

II. DUAL-BAND BANDPASS FILTERS STRUCTURE AND DESIGN

Figure 1 depcits the configuration and optimal physical parameters of the wideband DBBPF with SIOLRR. It directly excited by two 50 Ω standard microstrip feeding lines. The SIW structure consists of a dielectric substrate comprised between a pair of metal plates which are connected through via holes. The used substrate is Rogers 4350B with the thickness h=0.508 mm and its bottom is covered completely by a metal. A periodic BCMRCs unit is loaded on the top layer of the SIW. Electromagnetic waves are confined to the inside of

Submitted On: March 7, 2021
Accepted On: May 9, 2021

https://doi.org/10.47037/2021.ACES.J.360919

1054-4887 © ACES

SIW cavity, hence it can be considered as a planar circuit transformation of non-planar rectangular waveguide (RGW). If the electromagnetic waves are lower than the cutoff frequency, it will not be able to propagate in the SIW cavity. Since a periodic BCMRCs structure usually presents stopband characteristics, a compact DBBPF is obtained by combining the characteristics of SIW and BCMRCs. The DBBPF can be considered as a cascade connection of a highpass filter with a bandstop filter to form dual-passbands separated by a stopband, and the bandwidth of dual passbands is mainly determined by BCMRCs.

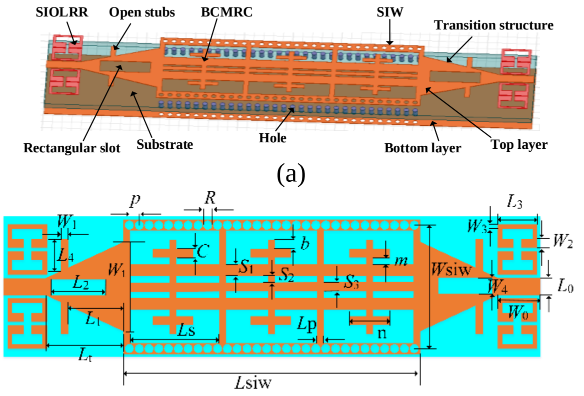

(a)

(b)

Fig. 1. Configuration of the wideband DBBPF with SIOLRR: (a) three-dimensional (3D) view, (b) planar view, where b=0.7 mm, C=0.5 mm, R=0.5 mm, p=0.9 mm, m=0.3 mm, n=1.5 mm, S_1=1.2 mm, S_2=0.3 mm, S_3=0.5 mm, W_0=3.5 mm, W_1=0.5 mm, W_2=0.75 mm, W_3=0.2 mm, W_4=1.7 mm, W_t=6.3 mm, W_{siw}=8.7 mm, Ls=8.37 mm, L_{siw}=27.1 mm, L_p=0.495 mm, L_t=2.6 mm, L_1=4.5 mm, L_2=5.2 mm, L_3=3 mm, L_4=1.675 mm.

A novel beeline structure is shown in Fig. 2, which is composed of five horizontal microstrip lines and one vertical microstrip line, and the three horizontal microstrip lines in the middle are connected in parallel and run through the entire unit structure. With the help of 3D simulation software HFSS, the simulated frequency response of a novel periodic BCMRCs unit with three beeline structure is shown in Fig. 3. As seen in Fig. 3, the BCMRCs structure plays not only the role of a low-pass, but also produces a passband.

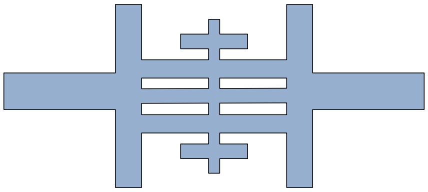

Fig. 2. The novel beeline structure.

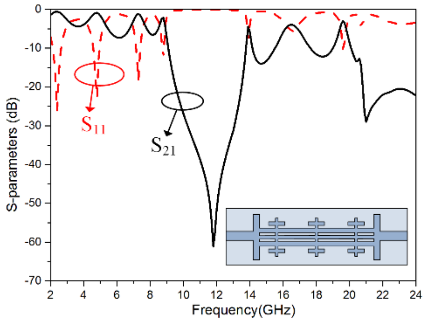

Fig. 3. Simulated results of a novel periodic BCMRCs unit.

It is well known that a SIW is similar to a RGW as a high-pass filter. According to the theory of typical RGW, the cutoff frequency of the fundamental mode in the SIW cavity can be calculated as:

$$f_{c10} = \frac{c}{2\sqrt{\varepsilon_r \mu_r}} \sqrt{\frac{1}{\left(W_{SIW} - \dfrac{d^2}{0.95p}\right)^2}}, \tag{1}$$

where c is the light velocity in vacuum, ε_r and μ_r are relative permittivity and relative permeability, W_{SIW} is the spacing between the rows of two metallic vias on the SIW, d is the diameter of metalized vias and p is the center-to-center pitch between adjacent via-holes. In addition, since the SIW is not an ideal homogenous rectangular waveguide, the gap between the aligned metallic vias may trigger frequency-dependent leakage loss. To prevent radiation loss, the parameters of the typical SIW structure must be sustained to meet the following condition [17]:

$$\begin{cases} d < 0.2\lambda_g \\ d < 0.2W_{SIW} \\ d > 0.5p \end{cases}. \tag{2}$$

Where λ_g can be calculated by:

$$\lambda_g = \frac{\lambda_0}{\sqrt{1 - \left(\dfrac{\lambda_0}{2\left(W_{SIW} - d^2/0.95p\right)}\right)^2}}, \tag{3}$$

where λ_0 is the free space wavelength. According to the target specifications and these relations mentioned above, all the examples presented in this paper are designed with d=0.5 mm and p=0.9 mm.

In order to verify the proposed design method, the prototype DBBPF is simulated by full-wave simulator HFSS. As seen in Fig. 4, due to the slow wave effect produced by the loaded BCMRCs, the cutoff frequency of the SIW of the same size has been moved from 9.7 GHz to 4.4 GHz. According to (1), the loaded BCMRCs reduces the equivalent width of SIW by about 55%. At the same time, by loading the BCMRCs with band-gap characteristics on top layer of SIW, two wide passbands separated by a stopband are generated.

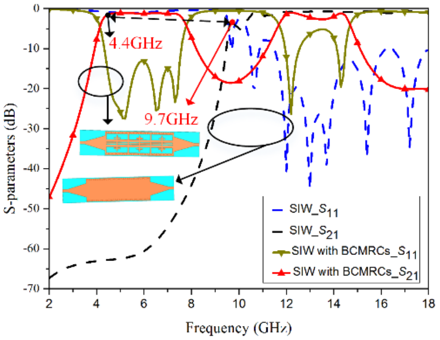

Fig. 4. Simulated S-parameters of the initial SIW and the SIW with BCMRCs.

In order to enable the wide DBBPF to have lower reflection coefficients, a tapered gradient line embedded with rectangular slots and open stubs are introduced. The simulated results of the dual-band filter with or without rectangular slots and open stubs in Fig. 5. As seen in Fig. 5, by loading rectangular slots and loaded open stubs on the transition structure of microstrip-SIW, the return losses of the two passbands are better than 10 dB.

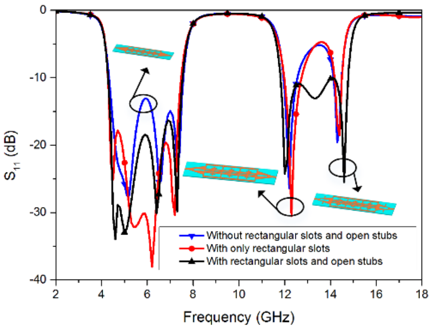

Fig. 5. Simulated frequency responses of the DBBPF with or without rectangular slots and open stubs.

The simulated results of the wideband DBBPF with rectangular slots and open stubs is shown in Fig. 6. The lower passband is from 4.2 GHz to 7.65 GHz, while the upper passband frequency covers from 11.65 GHz to 14.85 GHz. The simulated 3dB fractional bandwidths are 58.2% and 24.2%, and the return losses of the two passbands are below 10dB, respectively. The center frequency and bandwidth of the two passbands can be flexibly adjusted in this filter. As seen in Fig. 7, the bandwidth of two passbands decreases as *m* increases, while the upper passband has a greater change than the lower passband. Moreover, if L_s increases, the bandwidth of the two passbands becomes lager, but the lower passband changes more than the upper passband.

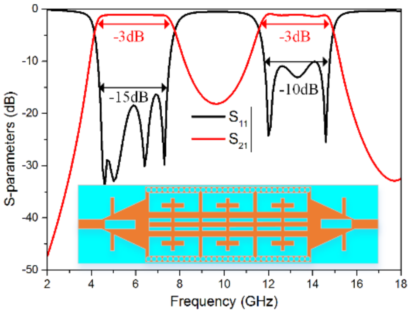

Fig. 6. Simulated results of the wideband DBBPF.

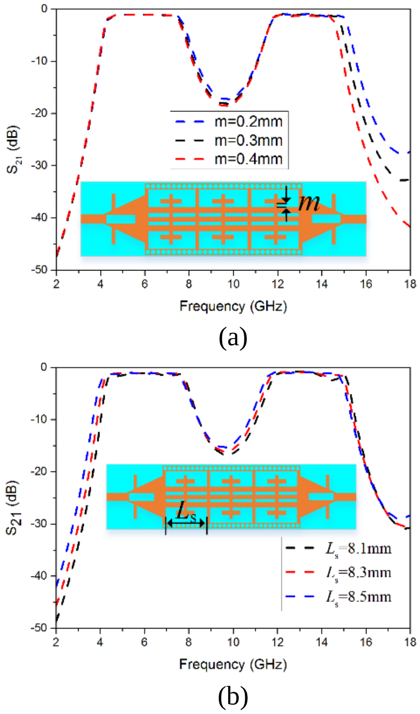

(a)

(b)

Fig. 7. Simulated frequency responses of: (a) *m* and (b) L_s.

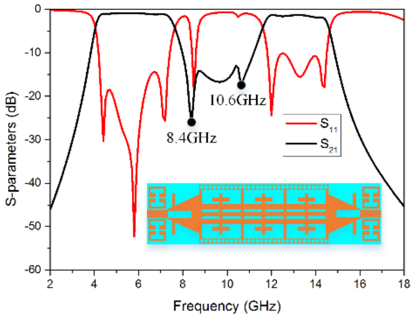

Fig. 8. Simulated frequency responses of the wideband DBBPF with SIOLRR.

However, the DBBPF have poor frequency selectivity between two bands. In order to improve the frequency selectivity, the SIOLRRs is loaded on both sides of the input and output ports of the filter, and its frequency response results are shown in Fig. 8. As seen in Fig. 8, two transmission points are generated in the stop band between the two passbands, and it is obvious that the wideband DBBPF with SIOLRR has a better frequency selectivity.

III. EXPERIMENTAL RESULTS

According to the analysis and discussion above, the two prototype wideband DBBPFs are designed, fabricated and measured. Figure 9 shows the photograph of the fabricated filters. The overall circuit size of the DBBPF is 9.7 mm×45.7 mm (0.26 λ_g×1.22 λ_g), and the size of the DBBPF with SIOLRR is 9.7 mm×49.7 mm (0.26 λ_g×1.35 λ_g), where λ_g is the guided wavelength in the substrate at center frequency (CF) of the first passband.

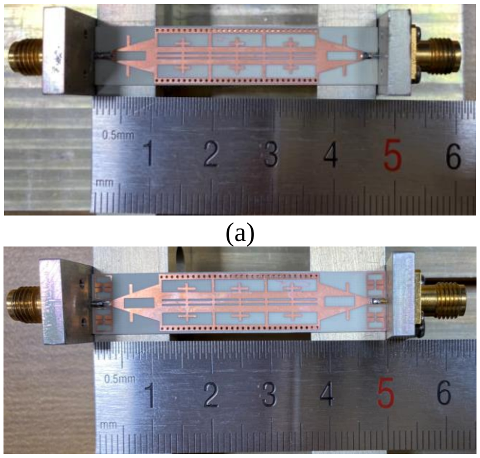

(a)

(b)

Fig. 9. Photograph of the fabricated DBBPFs: (a) the DBBPF without SIOLRR, and (b) the DBBPF with SIOLRR.

The simulated and measured results are shown in Fig. 10. In Fig. 10 (a), the lower-band and upper-band of the proposed DBBPF have the measured CFs at the 5.93 and 13.35 GHz with 3 dB fractional bandwidths of 3.45 and 3 GHz (58.2% and 22.5%), while the measured minimum ILs are 0.7 and 0.92 dB, respectively. In Fig. 10 (b), the measured minimum ILs are 0.55 and 1.4 dB in the lower and upper passbands centered at 5.8 and 13.05 GHz with 3 dB relative bandwidths of 58.6% and 20.7%, while two transmission points are generated in the stop band between the lower and upper passbands, respectively. Good agreements between the simulated and measured results are obtained both in the DBBPF and the DBBPF with SIOLRR.

Table 1 illustrates the comparisons of our presented SIW DBBPFs with other reported advanced ones. Compared with the designs in [9]-[11], our proposed ones provide more widely bandwidths, smaller size and widely separated passbands from SIW and BCMRCs technology. Compared to the designs in [12], our proposed DBBPFs provide more widely bandwidths and lower ILs.

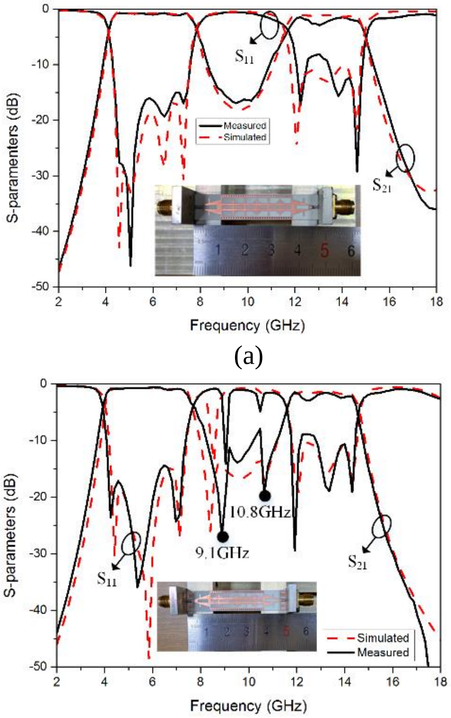

(a)

(b)

Fig. 10. Simulated and measured S-parameters of: (a) the DBBP without SIOLRR, and (b) the DBBPF with SIOLRR.

Table 1: Performance comparisons with some previous DBBPFs

	f_1/f_2 (GHz)	$k=f_2/f_1$	3-dB FBW (%) 1st /2nd	IL (dB) 1st /2nd	Size ($\lambda_g{}^2$)
[11]	20/21	1.05	1.5/1.43	1.37/1.1	2.18×1.44
[12]-A	12/14	1.167	5.53/4.04	1.21/1.34	1.15×1.10
[12]-B	12/16	1.333	3.8/3.47	1.79/1.76	2.16×1.25
[13]-A	12/16	1.333	8.75/7.06	1.07/0.95	1.12×1.71
[13]-B	12/15	1.25	7/6.6	1.24/0.85	1.66×1.29
[14]	2.4/5.2	2.25	5.8/6.45	3.6/3.1	0.15×0.16
This work without SIOLRR	**5.9/13.4**	**2.27**	**58.2/22.5**	**0.70/0.92**	**0.26×1.22**
This work with SIOLRR	**5.8/13.1**	**2.26**	**58.6/20.7**	**0.55/1.4**	**0.26×1.35**

IV. CONCLUSION

In this paper, two compact SIW DBBPFs with wide bandwidths and wide separated passbands has been proposed. The structure and design strategy have been analyzed in detail. The SIW provides a highpass performance and the BCMRCs generates a bandstop characteristic. They can be effectively combined to obtain a wideband dual-band filter. Finally, the simulations and measurements of the demonstrative filters are in good agreement, while the measured separated passbands are much wider than those of the previous reported works.

REFERENCES

[1] U. Naeem, S. Bila, M. Thevenot, T. Monediere, and S. Verdeyme, "A dual-band bandpass filter with widely separated passbands," *IEEE Trans. Microw. Theroy Tech.*, vol. 62, no. 3, pp. 450-456, Mar. 2014.

[2] K. D. Xu, H. Luyen, and N. Behdad, "A decoupling and matching network design for single- and dual-band two-element antenna arrays," *IEEE Trans. Microw. Theory Tech.*, vol. 68, no. 9, pp. 3986-3999, Sep. 2020.

[3] J. Shi, L. L. Lin, J. X. Chen, H. Chu, and X. Wu, "Dual-band bandpass filter with wide stopband using one stepped-impedance ring resonator with shorted stubs," *IEEE Microw. Wireless Compon. Lett*., vol. 24, no. 7, pp. 442-444, July 2014.

[4] Y. J. Guo, X. H. Tang, and K. D. Xu, "Dual high-selectivity band-notched ultra-wideband filter with improved out-of-band rejection," *Applied Computational Electromagnetics Society Journal*, vol. 31, no. 9, pp. 1072-1078, Sep. 2016.

[5] S. Y. Zheng, "A dual-band antenna across micro-wave and millimeter-wave frequency bands," *2018 International Applied Computational Electromagnetics Society Symposium (ACES)*, Beijing, China, pp. 1-2, Aug. 2018.

[6] Y. Z. Zhu, W. X. Xie, X. Deng, and Y. F. Zhang, "Compact modified quarter mode substrate integrated waveguide resonator and its application to filters design," *Applied Computational Electromagnetics Society Journal*, vol. 32, no. 2, pp. 163-168, Feb. 2017.

[7] D. Li and K. D. Xu, "Compact dual-band bandpass filter using coupled lines and shorted stubs," *Electron. Lett.*, vol. 56, no. 14, pp. 721-724, July 2020.

[8] J. T. Kuo, T. H. Yeh, and C. C. Yeh, "Design of microstrip bandpass filter with a dual-passband response," *IEEE Trans. Microw. Theory Tech.*, vol. 53, no. 4, pp. 1331-1337, Apr. 2005.

[9] S. B. Zhang and L. Zhu, "Synthsis design of dual-band bandpass filters with *λ/4* stepped-impedance resonators," *IEEE Trans. Microw. Theory Tech.*, vol. 61, no. 5, pp. 1812-1819, May 2013.

[10] X. Cao, Z. Tang, and J. Bao, "Design of a dual-band waveguide filter based on micromachining fabrication process," *IET Microw. Antennas Propag.*, vol. 10, no. 4, pp. 459-463, Mar. 2016.

[11] X. P. Chen and K. Wu, "Dual-band and triple-band substrate integrated waveguide filters with chebyshev and quasi-elliptic response," *IEEE Trans. Microw. Theory Tech.*, vol. 55, no. 12, pp. 2569-2578, Dec. 2007.

[12] K. Zhou, C. X. Zhou, and W. Wu, "Resonance characteristics of substrate-integrated rectangular cavity and their applications to dual-band and wide-stopband bandpass filters design," *IEEE Trans. Microw. Theory Tech.*, vol. 65, no. 5, pp. 1511-1524, May 2017.

[13] K. Zhou, C. X. Zhou, and W. Wu, "Substrate-integrated waveguide dual-mode dual-band band-pass filters with widely controllable band-width ratios," *IEEE Trans. Microw. Theory Tech.*, vol. 65, no. 10, pp. 3801-3812, Oct. 2017.

[14] S. S. Xu, K. X. Ma, F. Y. Meng, and K. S. Yeo, "Novel defected ground structure and two-side loading scheme for miniaturized dual-band SIW bandpass filter designs," *IEEE Microw. Wireless Compon. Lett.*, vol. 25, no. 4, pp. 217-219, Apr. 2015.

[15] Y. Dong and T. Itoh, "Miniaturized dual-band substrate integrated waveguide filters using complementary split-ring resonators" *IET Microw. Antennas Propag.*, vol. 6, no. 6, pp. 1-4, June 2011.

[16] P. Li, H. Chu, D. Zhao, and R. S. Chen, "Compact dual-band balanced SIW bandpass filter with improved common-mode suppression," *IEEE Microw. Wireless Compon. Lett.*, vol. 27, no. 4, pp. 347-349, Apr. 2017.

[17] J. C. Rautio, "Publishing at IWS–Part I," *IEEE Microw. Mag.*, vol. 14, no. 4, pp. 162-163, June 2013.

Yun Jiang was born in Hunnan Provence, China. He received the M.S. degrees in Electronic Engineering from the University of Electronic Science and Technology of China (UESTC), Chengdu, China, in 2017, and currently he is working toward the Ph.D. degree in National of Defense University. His research interests include RF/millimeter-wave components and circuits.

Lei Huang was born in 1990. He received the B.S. degree in Vacuum Electronic Technology from University of Electronic Science and Technology of China, Chengdu, China, in 2014, the M.S. degree in Electromagnetic Field and Microwave Technique from National University of Defense Technology, Changsha, China, in 2017. He is currently working toward the Ph.D. degree in Electromagnetic Field and Microwave Technique at the National University of Defense Technology. His current research interests are microwave and millimeter-wave circuits and systems.

Zhaoyu Huang was born in 1992. He received the M.S. degree in Electronics and Communication Engineering from the University of Electronic Science and Technology of China, Chengdu, China in 2018, where he is currently pursuing Ph.D. degree with the College of Electronic Science and Engineering, National University of Defense Technology, Changsha, China. His current research interests include passive RF/microwave circuits, microstrip antennas and wireless communication.

Yuan Ye was born in Guangxi, China. She received the M.S. degree in Sun Yat-sen University, Guangzhou, China, in 2012, and currently she is working toward the Ph.D. degree in National University of Defense Technology. Her current research interests include ultra-wideband antenna Arrays and reconfigurable antenna.

Boyuan Liu was born in 1991. He has received Master's degree from University of Electronic Science and Technology, China and now proceed to Doctor's degree in National University of Defense Technology. His research interests are microwave and millimeter wave circuits and system, Radar guidance, electronic countermeasures and electromagnetic technology. He joined in researches such as Design of Capacitance quickly charging based on the technology of coupling resonance, Design and Implementation of X-band Single Road's Frequency Mixer Channel Based on MEMS Filter, which were finally published on national core periodicals. He is now engaged in one project of Natural Science Foundation of China, named Structure Unit Design of Compound Electromagnetic Material of Graphene Selective Surface, and one innovation project of Research on Multiple-Element Linear Retrodirective Cross-Eye Jamming.

Wentao Yuan was born in 1990. He received his M.S. degree in Computer Science and Technology from the Anhui Normal University in 2016. Currently he is working towards the Ph.D. degree in the College of Electronic Science and Engineering, National University of Defense Technology, Changsha, Hunan, China. His research interests include passive microwave circuits design and wireless communication.

Naichang Yuan was born in Anhui, China, in 1965. He received the M.S. and Ph.D. degrees in Electronic Science and Technology from the University of Electronic Science and Technology of China in 1991 and 1994, respectively. He is currently a Professor with the National University of Defense Technology. His research interests include array signal processing, radar system design, SAR/ISAR imaging and electronic countermeasures.

Broadband Multimode Antenna for Sub-6 GHz Base Station Applications

Weifeng Lin [1], Kang Rong [1], Qiming He [1], Zhenjun Chen [1], Bei Huang [2], and Jun Zhang [1*]

[1] School of Information Engineering
Guangdong University of Technology, Guangzhou, 510006, People's Republic of China
linweifeng@mail2.gdut.edu.cn, 2111903136@mail2.gdut.edu.cn, 2111903142@mail2.gdut.edu.cn,
2111903097@mail2.gdut.edu.cn, *junzhang@gdut.edu.cn

[2] School of Electronic and Information
Guangdong Polytechnic Normal University, Guangzhou, 510665, People's Republic of China
13247166166@163.com

Abstract **─** In this paper, a novel dual-polarized multimode antenna is presented for sub-6 GHz base station applications. Two pairs of slotted patches act as the main radiator to excite two modes, and they are coupled with each other to bring the resonant frequency of the two modes together. Two baluns are orthogonally placed between the main radiator and the ground plane for impedance transforming and introducing a new mode at the lower frequency. The ends of the slotted patches are connected with a reversed T-shaped dipole to optimize the current path and introducing a new mode at the higher frequency. Measured results show that the prototype antenna can achieve a 15-dB impedance bandwidth of 2.30 ~ 3.96 GHz (53.1%) and an average gain of 9.67 ± 0.33 dBi in the operating band. The isolation is greater than 28.0 dB with a half-power beamwidth of around 64° among the operating frequency band. The proposed antenna can be a promising candidate for the fifth-generation communication in the sub-6 GHz band.

Index Terms **─** Base station antennas, broadband antenna, multimode antenna.

I. INTRODUCTION

With the development of the fifth-generation (5G) mobile communication, there has been an increased demand for dual-polarized base station antennas with low cost, compact size, stable gain, and stable radiation patterns. In recent years, various types of structures have been developed to meet the requirements. Multi-mode antennas are a promising candidate for the base station application because of their broadband and compact size. Traditional antennas can increase space and energy utilization by introducing additional parts to realize multimode operation. For instance, additional loops were embedded into the original loop antenna [1]. A short-circuit stub and an open-circuit stub were loaded by the original dipole [2]. And two pairs of slot stubs were loaded along the original slot antenna [3]. Another way to realize multimode operation is by integrating several types of antennas with carefully selected feed structures. For example, feeding by a pair of dipoles, an elliptical patch with an elliptical slot can generate three different modes in a compact aperture [4]. A bow-tie dipole enclosed by an octagonal-ring patch and fed by an inverted-F antenna also can form a multimode operation [5]. Also, a pair of folded dipoles fed by an L-shaped microstrip line can realize multimode in a simple structure [6]. By combining a magnetic dipole and an electric dipole, the magneto-electric antenna owns the merits of low cross-polarization, low back radiation, stable radiation patterns, and broad bandwidth [7].

Recently, a Sakura-shaped antenna was designed to work in N78 band for Sub-6GHz base station application [8]. A dual-band antenna with a notched band was produced by introducing a mouse-ear-shaped arm at the edge of the radiator for covering 2/3/4/5G bands [9].

A broadband dual-polarized antenna was proposed in [10], where the bandwidth is enhanced by introducing four parasitic metal disks above the antenna with a U-shaped slot in each patch to increase the electrical length of the current path, which achieves a bandwidth of 67% for reflection coefficients < –15-dB, with a size of $0.464\,\lambda_0 \times 0.464\,\lambda_0 \times 0.35\,\lambda_0$ (λ_0 is the wavelength in the free space at the center of the operating frequency). However, the antenna has a large profile and a cavity-shaped reflector. To this end, a dual-polarized multimode antenna with a size of $0.470\,\lambda_0 \times 0.470\,\lambda_0 \times 0.207\,\lambda_0$ is proposed in this paper. The baluns are used to enhance the stability of radiation patterns and transform the impedance of the proposed antenna. The reversed T-shaped dipoles are connected to the end of slotted patches by metal holes, introducing additional resonance to broaden the impedance bandwidth. Because of its simple structure and easy assembly, the proposed antenna is suitable for base station applications.

Submitted On: October 5, 2020
Accepted On: August 13, 2021

https://doi.org/10.47037/2021.ACES.J.360920

II. ANTENNA DESIGN

Figure 1 is the configuration of the broadband multimode antenna. The antenna is composed of four substrates, including the main radiator, two orthogonal balun structures, and a flat reflector. The substrate is FR4 material with a dielectric constant of 4.33, a loss tangent of 0.02, and a thickness of 0.762 mm. The sizes of the main radiator and the flat reflector are 60 mm × 60 mm and 150 mm × 150 mm, respectively. Other detailed dimensions of the proposed antenna are listed in Table 1.

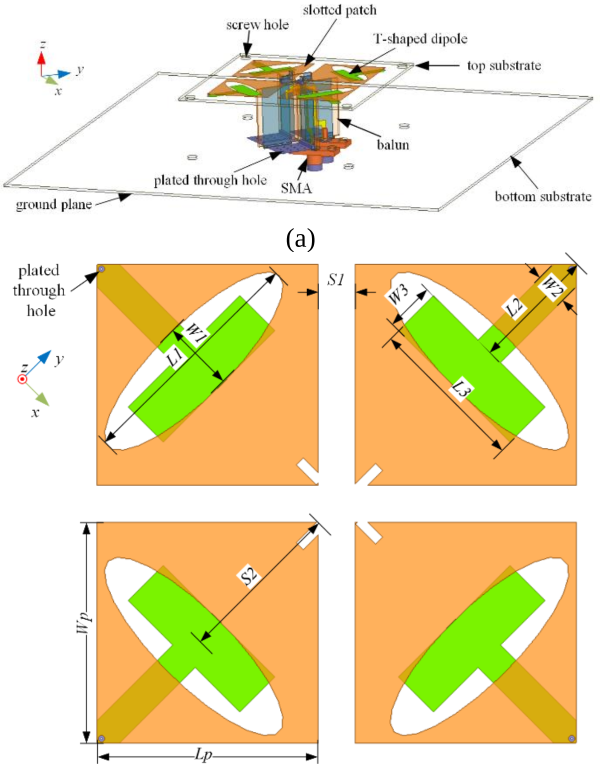

(b)

Fig. 1. Configuration of the proposed antenna: (a) 3D view and (b) main radiator.

Table 1: Dimensions of the proposed antenna

Parameter	L_1	L_2	L_3	L_4	L_5	L_6
Value (mm)	11.5	11.7	15	25	19.8	3
Parameter	L_7	L_8	L_9	L_{10}	L_{11}	L_{12}
Value (mm)	6.3	5	8.5	3.7	5.5	1.55
Parameter	L_{13}	L_{14}	W_1	W_2	W_3	W_4
Value (mm)	3	1.8	3.45	3	4.7	19.2
Parameter	W_5	W_6	W_7	W_8	W_9	W_{10}
Value (mm)	20	2.5	1.5	4.5	0.9	1
Parameter	W_{11}	W_{12}	W_{13}	W_{14}	L_p	W_p
Value (mm)	1	0.85	0.6	1	21	21
Parameter	S_1	S_2	S_3	S_4	S_5	S_6
Value (mm)	3.5	16.7	1.99	0.76	2.1	17.3

A pair of crossed slotted patches are printed on the upper side of the main radiator to realize the dual-polarization, and the elliptical slots inside are designed for increasing the current path as well as keeping the radiation aperture. Crossed T-shaped dipoles are reversely printed on the lower side of the main radiator and electrically connected to the end of slotted patches by plated through holes.

The configuration of the baluns is displayed in Fig. 2. The baluns are composed of a Γ-shaped microstrip line printed on one side and two rectangular patches printed on the other side. An SMA located under the reflector is connected to the end of the Γ-shaped feeding line. The top and bottom sides of rectangular patches are respectively connected to the main radiator and the flat reflector (ground plane).

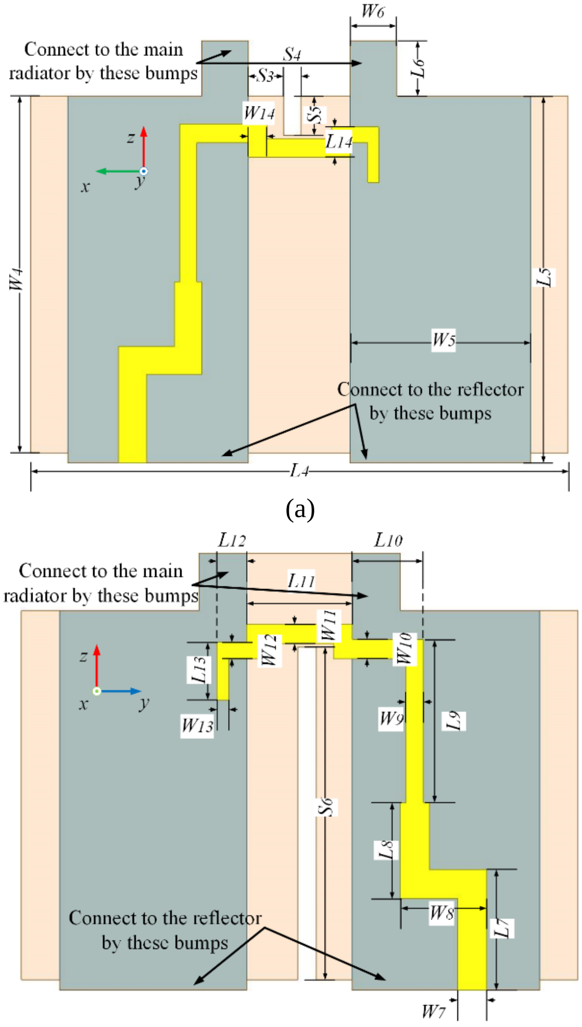

(b)

Fig. 2. Configuration of the balun: (a) balun of xoz plane and (b) balun of yoz plane.

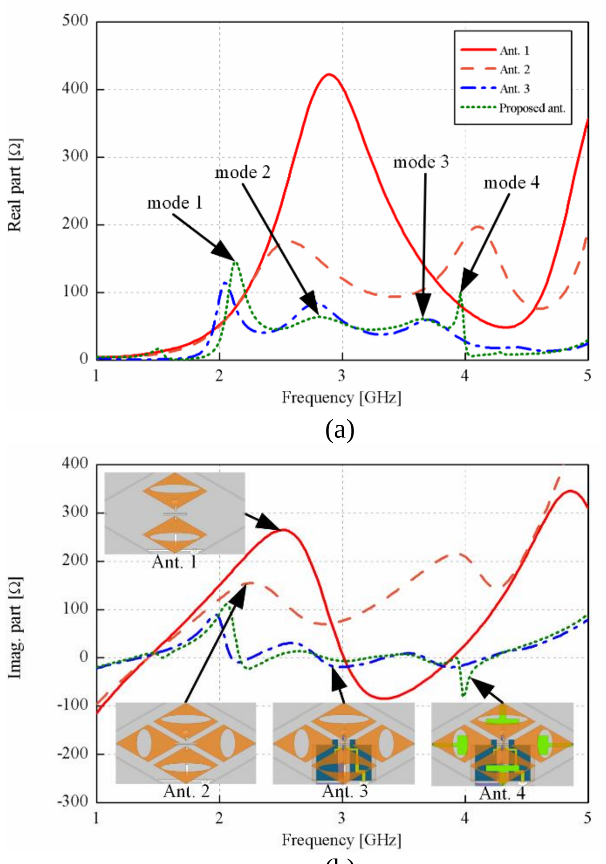

(a)

(b)

Fig. 3. Evolution of the proposed antenna: (a) real part of input impedance, and (b) imaginary part of input impedance, where the mode 1 is dominated by the balun, the modes 2 & 3 are dominated by the slotted patches and the mode 4 is dominated by the T-shaped dipoles.

The numerical method based on finite element (FEM) is used to simulate and analyze the proposed antenna with the input of the model. The evolution of the proposed antenna is shown in Fig. 3 for a better understanding of the operating mechanism. When one pair of slotted patches are excited, the other one is coupled and acts as a parasitic element. By properly adjusting the gap between the slotted patches, the second mode located at the higher frequency can be shifted toward the first mode, while the first mode will stay at the original frequency. These two adjacent modes are the modes 2 and 3 of the proposed antenna. The balun can balance the current and transform the antenna impedance. Meanwhile, the shorted patches of balun act as a magnetic dipole to provide an additional resonance for broadening the matching, dominating the mode 1 of the proposed antenna. At last, the T-shaped dipoles are introduced to create a new mode at the higher frequency and it is the mode 4 of the proposed antenna. It is found that at the high frequency, the current distributions on the slotted patches are accumulated along the edge of patches and surrounded by the elliptical slot once the T-shaped dipoles were introduced, as illustrated in Fig. 4.

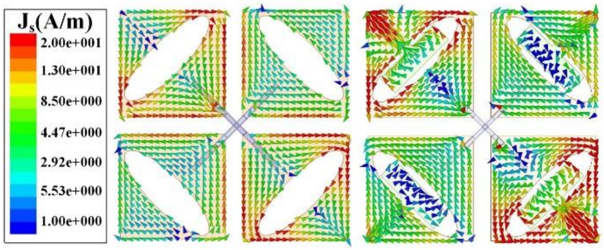

(a) (b)

Fig. 4. Effect of the reversed T-shaped dipoles on current distributions of the slotted patches at 3.9 GHz: (a) the slotted patches without reversed T-shaped dipoles, and (b) the slotted patches with reversed T-shaped dipoles.

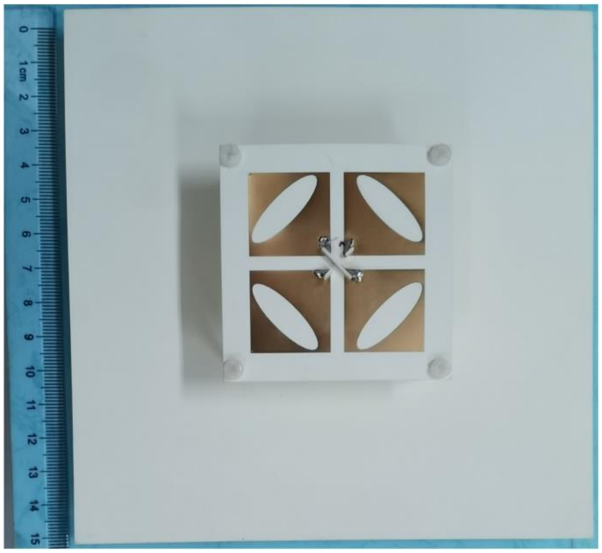

Fig. 5. Photograph of the prototype antenna.

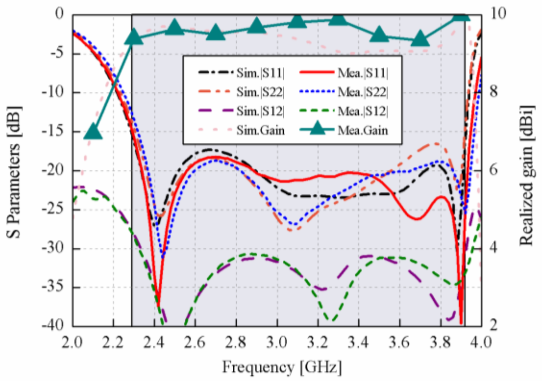

Fig. 6. Simulated and measured S parameters and realized gain of the broadband multimode antenna.

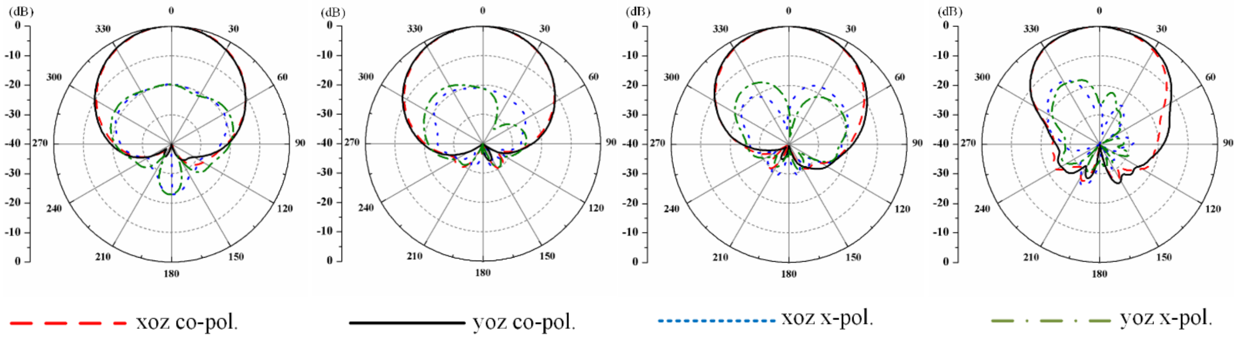

(a) (b) (c) (d)

Fig. 7. Measured radiation patterns of the proposed antenna: (a) 2.5 GHz, (b) 3.1 GHz, (c) 3.5 GHz, and (d) 3.9 GHz.

Table 2: Performance comparison of the proposed antenna with the state-of-the-art work

Ref.	Main Radiator ($\lambda_0 \times \lambda_0 \times \lambda_0$)	Bandwidth (GHz)	Gain (dBi)	Isolation (dB)	FBR (dB)	Half-power Beam Width (°)	
						E-plane	H-plane
[10]	0.46× 0.46 × 0.35	1.39~2.80 (67.3%) (RL>15)	9.0	>30.0	20.0	65.0 ± 5.0	
[11]	0.39 × 0.39 × 0.25	1.68~2.83 (51.1%) (VSWR<1.5)	8.8 ± 0.7	>28.5	18.0	65.4 ± 2.4	
[12]	0.38 × 0.38 × 0.17	1.58~2.75 (54.0%) (VSWR<2)	9.0 ± 1.0	>30.0	19.5	76.0	52.0
[13]	0.37 × 0.37 × 0.27	3.14~5.04 (46.5%) (VSWR<1.5)	8.0 ± 0.3	>32.5	—	71.8 ± 2.5	
[14]	0.56 × 0.54 × 0.15	1.22~2.00 (48.4%) (VSWR<2)	9.4 ± 1.7	>28.0	19.0	53.3	58.3
This work	0.47 × 0.47 × 0.21	2.30~3.96 (53.1%) (RL>15)	9.7 ± 0.3	>28.0	25.3	63.2 ± 3.6	64.6 ± 2.9

III. RESULT AND DISCUSSION

A prototype of the proposed antenna is fabricated to verify the simulated results, as shown in Fig. 5. Nylon screws are used to fix the top and bottom substrates. The simulated and measured S parameters of the broadband multimode antenna are presented in Fig. 6. The antenna achieves a 15-dB impedance bandwidth of about 52.9% (2.28 ~ 3.92 GHz) for simulation and a relative bandwidth of 53.1% (2.30 ~ 3.96 GHz) for measurement. Simulated and measured isolations are greater than 27.6 dB and 28.0 dB while the simulated and measured gains are about 9.48 ± 0.50 dBi and 9.67 ± 0.33 dBi, respectively. The operating band covers both the 2.515 ~ 2.675 GHz (n41) and 3.3 ~ 3.6 GHz (n78) in sub-6 GHz bands, which is suitable for 5G communication.

Four typical measured radiation patterns of the prototype antenna are displayed in Fig. 7. It is observed that the half-power beamwidths of the prototype antenna at 2.5 GHz, 3.1 GHz, 3.5 GHz, and 3.9 GHz are 63°, 65°, 63°, and 61° for xoz-polarization and 63°, 67°, 67°, and 65° for yoz-polarization, respectively. The difference in radiation patterns between two polarizations may be caused by the asymmetry in the feeding structures.

Table 2 shows the performance and size comparison between the antenna proposed in this paper and the state-of-the-art work. The half-power beam width in the table takes the average value in the frequency band. We can see that the proposed antenna has competitive relative bandwidth and port isolation while maintaining small size and profile as well as in-band gain and pattern stability. The operating frequency band covers the two sub-6 GHz bands of 2.515 GHz ~ 2.675 GHz (n41) and 3.3 GHz ~ 3.6 GHz (n78).

IV. CONCLUSION

In this paper, a broadband multimode dual-polarized antenna operating in sub-6 GHz band has been proposed. By utilizing the balun feeding structures as a magnetic dipole and guiding the current path of the main radiator through T-shaped dipoles, additional two modes are introduced to realize a multimode function. The dual-polarized multimode antenna achieves a 15-dB impedance bandwidth from 2.30 to 3.96 GHz with a gain of 9.67 ± 0.33 dBi. The proposed base station antenna can be a low-cost element for ubiquitous deployments in macro- or micro-cell scenarios.

ACKNOWLEDGMENT

This work was supported in part by the National Key Research and Development Program of China (Grant 2018YFB1802100), and in part by the National Natural Science Foundation of China (Grants 61701120 and 61974035).

REFERENCES

[1] D. Z. Zheng and Q. X. Chu, "A multimode wideband +/- 45 degrees dual-polarized antenna with embedded loops," *IEEE Antennas and Wireless Propagation Letters*, vol. 16, pp. 633-636, 2017.

[2] Q. X. Chu, D. L. Wen, and Y. Luo, "Principle of multimode broadband antennas with resonator-loaded dipole," in *2015 International Workshop on Antenna Technology*, pp. 45-47, 2015.

[3] X. K. Bi, G. L. Huang, X. Zhang, and T. Yuan, "Design of wideband and high-gain slotline antenna using multi-mode radiator," *IEEE Access*, vol. 7, pp. 54252-54260, 2019.

[4] B. Huang, W. F. Lin, J. L. Huang, J. Zhang, G. Zhang, and F. G. Wu, "A patch/dipole hybrid-mode antenna for sub-6GHz communication," *Sensors*, vol. 19, no. 6, Mar. 2019.

[5] J. Zhang and Z. X. Shen, "Dual-band shared-aperture UHF/UWB RFID reader antenna of circular polarization," *IEEE Transactions on Antennas and Propagation*, vol. 66, no. 8, pp. 3886-3893, Aug. 2018.

[6] Y. H. Cui, R. L. Li, and P. Wang, "A novel broadband planar antenna for 2G/3G/LTE base stations," *IEEE Transactions on Antennas and Propagation*, vol. 61, no. 5, pp. 2767-2774, May 2013.

[7] K. M. Luk and B. Q. Wu, "The magnetoelectric dipole-A wideband antenna for base stations in mobile communications," *Proceedings of the IEEE*, vol. 100, no. 7, pp. 2297-2307, July 2012.

[8] P. Chen, L. Wang, and T. Ding, "A dual-polarized Sakura-shaped base station antenna for 5G communications," *Applied Computational Electromagnetics Society Journal*, vol. 35, no. 5, pp. 567-571, May 2020.

[9] Z. L. Li, J. Q. Han, Y. J. Mu, X. H. Gao, and L. Li, "Dual-band dual-polarized base station antenna with a notch band for 2/3/4/5G communication systems," *IEEE Antennas and Wireless Propagation Letters*, vol. 19, no. 12, pp. 2462-2466, Dec. 2020.

[10] Y. H. Cui, L. J. Wu, and R. L. Li, "Bandwidth enhancement of a broadband dual-polarized antenna for 2G/3G/4G and IMT base stations," *IEEE Transactions on Antennas and Propagation*, vol. 66, no. 12, pp. 7368-7373, Dec. 2018.

[11] D. Z. Zheng and Q. X. Chu, "A wideband dual-polarized antenna with two independently controllable resonant modes and its array for base-station applications," *IEEE Antennas and Wireless Propagation Letters*, vol. 16, pp. 2014-2017, 2017.

[12] K. M. Mak, H. W. Lai, and K. M. Luk, "A 5G wideband patch antenna with antisymmetric L-shaped probe feeds," *IEEE Transactions on Antennas and Propagation*, vol. 66, no. 2, pp. 957-961, Feb. 2018.

[13] H. Tang, X. Z. Zong, and Z. P. Nie, "Broadband dual-polarized base station antenna for fifth-generation (5G) applications," *Sensors*, vol. 18, no. 8, Aug. 2018.

[14] C. Ding and K. M. Luk, "A low-profile dual-polarized magneto-electric dipole antenna," *IEEE Access*, vol. 7, pp. 181924-181932, 2019.